

INVESTIGATION OF PLANAR FRESNEL ZONE PLATE ANTENNAS

By

Sara Stout-Grandy, B.Eng (EE), M.Eng (EE)

A thesis submitted to the Faculty of Graduate Studies
in partial fulfillment of the requirements
for the degree of

DOCTOR OF PHILOSOPHY

Ottawa-Carleton Institute for Electrical and Computer Engineering
Department of Electronics
Carleton University
Ottawa, Ontario, Canada

Copyright © Sara Stout-Grandy, 2008



Library and
Archives Canada

Bibliothèque et
Archives Canada

Published Heritage
Branch

Direction du
Patrimoine de l'édition

395 Wellington Street
Ottawa ON K1A 0N4
Canada

395, rue Wellington
Ottawa ON K1A 0N4
Canada

Your file Votre référence
ISBN: 978-0-494-40538-3
Our file Notre référence
ISBN: 978-0-494-40538-3

NOTICE:

The author has granted a non-exclusive license allowing Library and Archives Canada to reproduce, publish, archive, preserve, conserve, communicate to the public by telecommunication or on the Internet, loan, distribute and sell theses worldwide, for commercial or non-commercial purposes, in microform, paper, electronic and/or any other formats.

The author retains copyright ownership and moral rights in this thesis. Neither the thesis nor substantial extracts from it may be printed or otherwise reproduced without the author's permission.

AVIS:

L'auteur a accordé une licence non exclusive permettant à la Bibliothèque et Archives Canada de reproduire, publier, archiver, sauvegarder, conserver, transmettre au public par télécommunication ou par l'Internet, prêter, distribuer et vendre des thèses partout dans le monde, à des fins commerciales ou autres, sur support microforme, papier, électronique et/ou autres formats.

L'auteur conserve la propriété du droit d'auteur et des droits moraux qui protègent cette thèse. Ni la thèse ni des extraits substantiels de celle-ci ne doivent être imprimés ou autrement reproduits sans son autorisation.

In compliance with the Canadian Privacy Act some supporting forms may have been removed from this thesis.

Conformément à la loi canadienne sur la protection de la vie privée, quelques formulaires secondaires ont été enlevés de cette thèse.

While these forms may be included in the document page count, their removal does not represent any loss of content from the thesis.

Bien que ces formulaires aient inclus dans la pagination, il n'y aura aucun contenu manquant.


Canada

ABSTRACT

The possibility of using the Fresnel zone plate antenna (FZPA) as an alternate antenna candidate for future satellite communication systems in the Ka-band (26GHz – 40GHz) was investigated. Various parameters of the FZPA were identified and studied as a potential means to improve its performance or enhance its capability.

The planar conventional FZPA requires an improvement in the aperture efficiency and a reduction in the physical volume in order to compete with existing planar antenna technologies. This research work addressed both deficiencies. A reflector-backed FZPA was conceived which enhanced the antenna aperture efficiency by 33%. The large physical volume was addressed by developing low profile arrays. This yielded an overall antenna package with profile comparable to traditional planar technology.

A new technique was devised to more accurately create the Fresnel zones which takes into account the interference between the multiple feeds of the array. Using this technique, various linear and planar FZPA arrays were studied and shown to perform well despite the large element spacings inherent with their physical size. A comparison between FZPA array and microstrip patch array losses was also performed at 30GHz. It was shown that the FZPA has significantly less loss.

Several other aspects of the FZPA were investigated which were found to add enhanced capability. First, a parameter called reference phase, when chosen properly, was shown to substantially reduce sidelobes in the radiation patterns of the FZPA. Second, changing the shape of the FZPA zones to hexagonal enabled sidelobe control by rotating the zones with respect to each other. Finally, the spatial resolution of the FZPA with sub-wavelength focal distance was investigated for the first time and shown to be comparable to dielectric lenses.

ACKNOWLEDGEMENTS

I would like to take this opportunity to thank all the people who assisted me throughout the course of this degree. I am most grateful to Dr. Jim Wight, Dr. Aldo Petosa, Dr. Igor Minin, and Dr. Oleg Minin for their valuable support and guidance. Thank-you Jim for allowing me the freedom to choose my own path and for providing me with whatever I needed to follow that path. Thank-you Aldo for putting up with me as an office mate and for taking my questions seriously no matter how valid they were. Thanks also to Michel Cuhaci for allowing me to do my work at the Communications Research Centre (CRC). Also, the financial support of NSERC is gratefully acknowledged. Without this support I would not have been able to leave a well paying job to enter the life of a student again.

I am also most grateful to have had Nicolas Gagnon and Soulideth Thirakoune as office mates at CRC. I would not have learned the ways of Empire without them and would certainly not have had as much fun! Nicolas was particularly helpful when I encountered Matlab coding difficulties and he turned out to be a fabulous paper and thesis editor. Special thanks to John Bradley and David Lee for coming to my rescue on countless occasions. John saved me whenever my computer stopped functioning properly and was also fundamental in my efforts to learn how to use DW2000. David made me see how a well designed test fixture can make all the difference.

Finally, I would like to recognize the unwavering support of my family. I would never have been able to do this if it weren't for the encouragement of my husband, Trevor, who somehow saw that the sacrifice would be worth it. Trevor, I am indebted to you for helping me to achieve this goal. You have been a constant source of counsel, inspiration and understanding. Thanks also to my 3 year old daughter Alena, who was a continual reminder of the important things in life. A final special thanks to the unrelenting motivation and constant flow of good vibes from my parents. Mom and Dad, it's been a long road, but you can now call me DOCTOR!

TABLE OF CONTENTS

ABSTRACT	iii
ACKNOWLEDGEMENTS	iv
TABLE OF CONTENTS	v
LIST OF FIGURES	xi
LIST OF TABLES	xvii

CHAPTER 1: INTRODUCTION **1**

1.1	Target Application and Current Challenges	1
	1.1.1 Problem Statement	1
	1.1.2 Challenges with Traditional Methods	2
1.2	Motivation	3
1.3	Thesis Objective	4
1.4	Thesis Organization	5

CHAPTER 2: PLANAR FZPA TECHNOLOGY **9**

2.1	Introduction	9
2.2	Basic Lens Theory	9
	2.2.1 Shaped Dielectric and Fresnel Lens Operation	9
	2.2.2 Phase Correcting Fresnel Lens Operation	12
	2.2.3 Huygens' Principle & Diffraction.....	15
	2.2.4 Construction of Fresnel Zones	16
	2.2.5 Circular FZPL Antenna	18

2.2.6	Fresnel Zone Radii	22
2.2.7	Circular FZPA Radiation Characteristics	25
2.2.8	FZPA Focal Fields	29
2.2.9	Spatial Resolution	31
2.3	Types of FZPAs	33
2.3.1	Reflecting FZPAs	33
2.3.2	Layered FZPA	37
2.3.3	Offset FZPA	39
2.3.4	Square & Polygonal FZPA	41
2.4	Lens Array Antennas	44
2.5	Alternate High Gain Antenna	48
2.5.1	Microstrip Patch Array	48
2.5.2	Planar Antenna with Partially Reflective Surface.....	50
2.6	Conclusion	52

CHAPTER 3: FZPA ANALYSIS TECHNIQUES 54

3.1	Introduction	54
3.2	Huygen's-Fresnel's Principle	54
3.3	Scalar Kirchhoff's Diffraction Theory	57
3.4	Vectorial Kirchhoff's Diffraction Theory	63
3.5	Finite-Difference Time-Domain (FDTD) Method	64
3.6	Conclusion.....	68

CHAPTER 4: OPTIMAL REFERENCE PHASE 69

4.1	Introduction	69
4.2	Reference Phase Formulation	70
4.3	Simulated Reference Phase Results	73
4.3.1	Simulation Parameters	73
4.3.2	Simulation Results	75
4.3.2.1	Peak Directivity	77
4.3.2.2	First Sidelobe Level	79
4.3.2.3	Maximum Sidelobe Level	82
4.3.2.4	Half-Power (3dB) Beamwidth	83

4.3.2.5	Maximum Cross-Polarization	83
4.4	Measurement Results	84
4.4.1	Antenna Fabrication and Test Set-up	84
4.4.2	Radiation Patterns of the Feed	85
4.4.3	Comparison of Measured and Simulated Results	86
4.4.3.1	General Radiation Patterns.....	86
4.4.3.2	Peak Gain	89
4.4.3.3	Measurement Discussion.....	90
4.5	Physical Meaning	90
4.6	Conclusion	91

CHAPTER 5: RESOLUTION & FOCAL FIELDS 92

5.1	Introduction	92
5.2	Resolution of the FZPA	93
5.2.1	Focal Distance $> \lambda$	94
5.2.2	Focal Distance $< \lambda$	95
5.2.3	Resolution Comparison with Phase Correcting Fresnel Antenna.....	99
5.3	Focal Intensity of the FZPA with Reference Phase	100
5.4	Conclusion	103

CHAPTER 6: CONTROL OF FZPA RADIATION PATTERNS 104

6.1	Introduction	104
6.2	Hexagonal and Circular FZPA Comparison	105
6.2.1	Hexagonal Geometry	105
6.2.2	Simulations of the Hexagonal FZPA	107
6.2.3	Discussion	111
6.3	FZPA with Alternating Hex-Cut Zones	111
6.3.1	Creation & Simulation of Alternating Hex-Cut Zones	112
6.4	FZPA with Rotated Alternating Hex-Cut Zones	115
6.5	Measurement Results	119
6.6	Conclusion	122

CHAPTER 7: REFLECTOR-BACKED FZPA 124

7.1	Introduction	124
7.2	Reflector-Backed FZPA Geometry & Modeling	126
7.3	Simulation Results	126
	7.3.1 Feed Radiation Patterns	126
	7.3.2 Reflector-Backed FZPA Radiation Patterns	128
	7.3.3 Circular Ground Plane	131
7.4	Measurement Results	133
7.5	Conclusion	134

CHAPTER 8: LOW-PROFILE FZPA 136

8.1	Introduction	136
8.2	FZPA with Small Focal Distances	137
	8.2.1 Simulation Model	139
	8.2.2 Focal Spacing Decrement Considerations	140
	8.2.3 Peak Directivity vs. Number of Metal Zones	143
	8.2.4 Peak Directivity Bandwidth	145
	8.2.5 Aperture Efficiency vs. Number of Metal Zones	146
	8.2.6 Discussion	149
8.3	Single-Zone FZPA Compared with Superstrate Antenna	149
8.4	Measurement Results	153
	8.4.1 Antenna Fabrication and Test Set-Up	153
	8.4.2 Measurement Test Results	154
	8.4.2.1 Feed Alone	154
	8.4.2.2 $F=3.0\lambda$ Single-Zone FZPA With Ground Plane	156
	8.4.2.3 $F=3.0\lambda$ Single-Zone FZPA Without Ground Plane ...	159
	8.4.2.4 $F=0.5\lambda$ Single-Zone FZPA With Ground Plane	160
	8.4.2.5 Superstrate	162
	8.4.3 Discussion	163
8.5	Conclusion	164

9.1	Introduction	165
9.2	Conversion from Feed Phase to FZPA Zones	166
	9.2.1 Phase of a Single Waveguide	167
	9.2.2 Phase Contours	170
	9.2.3 'Modified' Zones Based on Phase Contours	172
	9.2.4 Discussion	175
9.3	FZPA Linear 2-Element Array	175
	9.3.1 Phase Contours & 'Modified' Zone Determination	176
	9.3.2 Circular Zone Determination	177
	9.3.3 'Modified' and Circular Zone 2-Element Array Patterns	179
	9.3.4 Discussion	182
9.4	FZPA Planar Arrays	182
	9.4.1 Array Lattice Determination	183
	9.4.2 Grating Lobe Analysis	187
	9.4.3 Phase Contours & 'Modified' Zone Determination	188
	9.4.4 Circular Zone Determination	189
	9.4.5 'Modified' and Circular Zone 2x2 Element Array Patterns	190
	9.4.6 4x4 Array	193
	9.4.7 Discussion	196
9.5	FZPA Arrays with Different Elements	197
	9.5.1 Arrays with Different Reference Phase Elements	198
	9.5.2 Arrays with Rotated Hex-Cut & Hexagonal Elements	203
	9.5.3 Discussion	209
9.6	FZPA Array & Microstrip Patch Array Losses	210
	9.6.1 Estimated Loss in T-Junctions	210
	9.6.2 Estimated Path Loss	213
	9.6.3 Total Estimated Loss	213
	9.6.4 Gain vs. Loss/Junction	215
	9.6.5 Discussion	217
9.7	Conclusion	218

CHAPTER 10: CONCLUSIONS & FUTURE RESEARCH	220
10.1 Summary of Conclusions	220
10.2 Thesis Contributions	223
10.3 Future Research	224
REFERENCES	226

LIST OF FIGURES

Figure 2-1:	Lens Operation in (a) Transmit Mode and (b) Receive Mode	10
Figure 2-2:	Side view of (a) Hyperbolic Dielectric Lens, (b) Fresnel Lens	11
Figure 2-3:	Grooved Phase Correcting Fresnel Antenna with 180° Phase Correction.	13
Figure 2-4:	Quarter-Wave Phase Correcting Fresnel Antenna	14
Figure 2-5:	Huygens' Principle	15
Figure 2-6:	Construction of Fresnel Zones	17
Figure 2-7:	Circular FZPA: (a) Front View, (b) Side View.....	20
Figure 2-8:	Side View of Circular FZPA Illustrating 180° Phase Sub-Zones	21
Figure 2-9:	Fresnel Lens Diagram	23
Figure 2-10:	Geometry of the FZPA for Far-Field Computation	26
Figure 2-11:	Typical Circular FZPA Radiation Patterns, H-Plane	28
Figure 2-12:	Circular FZPA in Receive Mode	30
Figure 2-13:	Typical Focal Fields of Circular FZPA	31
Figure 2-14:	Two Monochromatic Spectral Components	32
Figure 2-15:	(a) CFZPL Antenna, (b) Reflecting FZPA	34
Figure 2-16:	Normalized Radiation Patterns for the Reflecting and Conventional FZPAs	35
Figure 2-17:	Integrated Reflecting FZPA	36
Figure 2-18:	Layered FZPAs (a) Double Layer, (b) Enhanced Double Layer, (c) Four Layer	37
Figure 2-19:	Geometry for the Offset FZPA	39
Figure 2-20:	Elliptical Fresnel Zones with (a) $\theta_o=0^\circ$, (b) $\theta_o=0^\circ$, (c) $\theta_o=50^\circ$	40
Figure 2-21:	Improved Zoning Rule Geometry for Square FZPA	42

Figure 2-22:	Normalized Radiation Patterns for Square and Circular FZPAs	43
Figure 2-23:	Fresnel Lens Array Depth Reduction Concept: (a) Single Lens, (b) Lens Array	44
Figure 2-24:	Array of Circular FZPAs	46
Figure 2-25:	Array of Hexagonal FZPAs	47
Figure 2-26:	12x12 Printed Planar Antenna	49
Figure 2-27:	32x32 Printed Planar Antenna	50
Figure 2-28:	Planar Antenna with Partially Reflective Surface	51
Figure 3-1:	Geometry used to Derive Fresnel's Version of Huygen's Principle	55
Figure 3-2:	Geometry used to Derive Scalar Kirchhoff's Diffraction Theory	58
Figure 3-3:	Geometry of FZPA for Scalar Kirchhoff's Diffraction Theory	62
Figure 3-4:	Focal Field Intensity Comparison Between Methods	65
Figure 3-5:	Focal Field Intensity Comparison Between Methods	67
Figure 4-1:	Lens Antenna Diagram Showing Phase Offset	71
Figure 4-2:	Front View of Circular FZPA	75
Figure 4-3:	Typical Radiation Patterns with Varying Reference Phase, H-Plane	76
Figure 4-4:	Typical Radiation Patterns with Varying Reference Phase, E-Plane	77
Figure 4-5:	Normalized Peak Directivity vs. Reference Phase	78
Figure 4-6:	Relative 1 st Sidelobe Level with Varying Reference Phase, H-Plane	79
Figure 4-7:	Relative 1 st Sidelobe Level with Varying Reference Phase, E-Plane	80
Figure 4-8:	Maximum Relative Sidelobe Level with Varying Reference Phase	82
Figure 4-9:	Half-Power Beamwidth with Varying Reference Phase, H-Plane	83
Figure 4-10:	Test-Set-up in the Near-Field Anechoic Chamber	85
Figure 4-11:	Normalized Measured vs. Simulated Feed Patterns	86
Figure 4-12:	Normalized Measured vs. Simulated Patterns with $\Phi_0=0^\circ$, H-Plane	87
Figure 4-13:	Normalized Measured vs. Simulated Patterns with $\Phi_0=0^\circ$, E-Plane	87
Figure 4-14:	Normalized Measured vs. Simulated Patterns with $\Phi_0=60^\circ$, H-Plane	88
Figure 4-15:	Normalized Measured vs. Simulated Patterns with $\Phi_0=60^\circ$, E-Plane	88
Figure 5-1:	Geometry of the FZPA for Focal Field Simulation	93
Figure 5-2:	Average Power Density Along z-Axis at $x=y=0$	94
Figure 5-3:	Normalized Average Power Density Along the x- and y-axis at $z=3.75\lambda$	95
Figure 5-4:	Average Power Density Along z-Axis at $x=y=0$	96

Figure 5-5:	Normalized Average Power Density Along the x - and y -axis at $z=0.64\lambda$	97
Figure 5-6:	Peak Average Power Density vs. Frequency	98
Figure 5-7:	Intensity Along z -axis at $x=y=0$ for all Reference Phases	101
Figure 5-8:	Magnified Version of Figure 5-7	101
Figure 6-1:	Arrays of (a) Circles and (b) Hexagons	105
Figure 6-2:	(a) Circular FZPA, (b) Hexagonal FZPA	106
Figure 6-3:	Optimum Hexagon Derivation	107
Figure 6-4:	Co-polarized Radiation Pattern Comparison	109
Figure 6-5:	(a) Circular Zone FZPA, (b) Hexagonal Zone FZPA, (c) Alternating Hex-Cut Zone FZPA	112
Figure 6-6:	Method for Creating the Hex-Cut Zones	113
Figure 6-7:	Comparison Between Circular and Alternating Hex-Cut FZPAs, H-Plane	114
Figure 6-8:	Comparison Between Circular and Alternating Hex-Cut FZPAs, E-Plane	114
Figure 6-9:	FZPA with Rotated Alternating Hex-Cut Zones	116
Figure 6-10:	Effect of Zone Rotation on Sidelobe: (a) Case B, (b) Case E, (c) Case J	118
Figure 6-11:	Comparison of Measured vs. Simulated Results for Case A, H-Plane	120
Figure 6-12:	Comparison of Measured vs. Simulated Results for Case B, H-Plane	120
Figure 6-13:	Comparison of Measured vs. Simulated Results for Case J, H-Plane	121
Figure 7-1:	(a) Conventional FZPA, (b) Reflecting FZPA, (c) Reflector-Backed FZPA	125
Figure 7-2:	Radiation Patterns of the Waveguide With and Without the Ground Plane	127
Figure 7-3:	Radiation Patterns of the FZPA with Original and Smaller Waveguide	128
Figure 7-4:	10-Zone FZPA With and Without the Ground Plane, H-Plane	129
Figure 7-5:	10-Zone FZPA With and Without the Ground Plane, E-Plane	130
Figure 7-6:	Peak Directivity vs. Frequency With and Without Ground Plane, H-Plane	131
Figure 7-7:	10-Zone FZPA with Circular and Square Ground Plane, H-Plane	132
Figure 7-8:	Comparison Between Measured and Simulated Results, H-Plane	133
Figure 7-9:	Comparison Between Measured and Simulated Results, E-Plane	134

Figure 8-1:	(a) Aperture Illumination Issue, (b) Ground Plane Reflection Issue	138
Figure 8-2:	FZPA with Ground Plane Surrounding Waveguide Aperture	140
Figure 8-3:	Peak Directivity vs. Frequency for F with Even Multiples of 0.25λ	141
Figure 8-4:	Peak Directivity vs. Frequency for F with Odd Multiples of 0.25λ	142
Figure 8-5:	Peak Directivity vs. # Metal Zones With Ground Plane	144
Figure 8-6:	Peak Directivity vs. # Metal Zones With No Ground Plane	145
Figure 8-7:	Peak Directivity vs. Frequency for $F=3.75\lambda$ and 1.25λ Cases	146
Figure 8-8:	Aperture Efficiency vs. # Metal Zones With Ground Plane	148
Figure 8-9:	$\lambda/4$ Superstrate Spaced $\lambda/2$ Above a Ground Plane	150
Figure 8-10:	Comparison Between FZPA and Superstrate at 30GHz, H-Plane	151
Figure 8-11:	Bandwidth Comparison Between the FZPA and the Superstrate	152
Figure 8-12:	FZPA Test Set-Up for $F=3.0\lambda$	153
Figure 8-13:	FZPA Test Set-Up for the Superstrate	154
Figure 8-14:	Measured and Simulated Results for WR28, H-Plane	155
Figure 8-15:	Measured and Simulated Results for WR28, E-Plane	155
Figure 8-16:	Measured and Simulated Results for $F=3.0\lambda$ FZPA, H-Plane	156
Figure 8-17:	Radiation Patterns With and Without Foam for $F=3.0\lambda$, H-Plane	157
Figure 8-18:	Bandwidth Comparison With and Without Foam for $F=3.0\lambda$, H-Plane	158
Figure 8-19:	Frequency Sensitivity Comparison Between $F=1.75\lambda$ and 2.0λ , H-Plane	159
Figure 8-20:	Measured and Simulated Results Without Ground Plane, $F=3.0\lambda$, H-Plane	160
Figure 8-21:	Measured and Simulated Results for $F=0.5\lambda$, E-Plane	161
Figure 8-22:	Measured and Simulated Results for Superstrate, H-Plane	163
Figure 9-1:	Geometry of Single Waveguide for Phase Computation	167
Figure 9-2:	E_y Phase at $z=0.7\lambda$ from Waveguide, $y=0$ cut	168
Figure 9-3:	Normalized E_y Phase at $z=0.7\lambda$ from Waveguide, $y=0$ cut	169
Figure 9-4:	Magnified Version of Figure 9-3	169
Figure 9-5:	Phase Contours in the x - y Plane at $z=0.75\lambda$ from the Waveguide	171
Figure 9-6:	180° Phase Contours from Figure 9-5	172
Figure 9-7:	(a) 'Modified Zone FZPA Based on 180° Contours, (b) 'Modified' and Circular Geometry Comparison	173
Figure 9-8:	Comparison of 'Modified' vs. Circular Zone FZPAs, H-Plane	174
Figure 9-9:	Comparison of 'Modified' vs. Circular Zone FZPAs, E-Plane	174

Figure 9-10:	180° Phase Contours of 2 Waveguides with Separation=31.62mm	176
Figure 9-11:	'Modified' Zone 2-Element FZPA: (a) 2 Metal Zones, (b) 3 Metal Zones	177
Figure 9-12:	Circular Zone 2-Element FZPA: (a) 2 Metal Zones, (b) 3 Metal Zones ..	178
Figure 9-13:	(a) Ring Subtraction Approach, (b) Priority Approach	179
Figure 9-14:	'Modified' and Circular Zone 2-Element Array Patterns, 2 Metal Zones, H-Plane	180
Figure 9-15:	3 Metal Zones with Ring Subtraction Approach for Circular Case, H-Plane.....	181
Figure 9-16:	3 Metal Zones with Priority Approach for Circular Case, H-Plane	181
Figure 9-17:	Lattice Configurations: (a) Rectangular, (b) Equilateral Triangular	184
Figure 9-18:	Radiation Patterns of No Overlap Case, H-Plane	185
Figure 9-19:	Radiation Patterns of No Overlap Case, E-Plane	185
Figure 9-20:	Radiation Patterns of 1 Metal Zone Overlapped Case, H-Plane	186
Figure 9-21:	Radiation Patterns of 1 Metal Zone Overlapped Case, E-Plane	187
Figure 9-22:	'Modified' Zone 2x2 Element FZPA: (a) 2 Metal Zones, (b) 3 Metal Zones.....	188
Figure 9-23:	Circular Zone 2x2 Element FZPA: (a) 2 Metal Zones, (b) 3 Metal Zones	189
Figure 9-24:	Radiation Patterns of 2 Metal Zone 2x2 Array, H-Plane	190
Figure 9-25:	Radiation Patterns of 2 Metal Zone 2x2 Array, E-Plane	191
Figure 9-26:	Radiation Patterns of 3 Metal Zone 2x2 Array, H-Plane	192
Figure 9-27:	Radiation Patterns of 3 Metal Zone 2x2 Array, E-Plane	192
Figure 9-28:	4x4 Array Geometry: (a) $F=0.75\lambda$, (b) $F=1.25\lambda$	194
Figure 9-29:	Radiation Patterns of 2 Metal Zone $F=0.75\lambda$ 4x4 Array	195
Figure 9-30:	Radiation Patterns of 2 Metal Zone $F=1.25\lambda$ 4x4 Array	196
Figure 9-31:	Array Geometry: (a) No Reference Phase, (b) Progressive Reference Phase.....	199
Figure 9-32:	All Elements with 0° Reference Phase, H-Plane	200
Figure 9-33:	Progressive Reference Phase (1) 0°, (2) 60°, (3) 120°, (4) 180°, H-Plane	200
Figure 9-34:	3D Far-Field Patterns: (a) 0° Reference Phase, (b) Progressive Reference Phase (1) 0°, (2) 60°, (3) 120°, (4) 180°	201
Figure 9-35:	Empire vs. Array Factor (AF) Pattern for Identical Elements, H-Plane ..	202
Figure 9-36:	Radiation Patterns of Various Reference Phase Cases, H-Plane	203

Figure 9-37: Element Pattern (all circular zones) vs. Array Factor, H-Plane	204
Figure 9-38: Element Pattern (alternating hex-cut zones) vs. Array Factor, H-Plane	205
Figure 9-39: Element Pattern (all hexagonal zones) vs. Array Factor, H-Plane	205
Figure 9-40: Element Pattern (2 alternating hex-cut zones) vs. Array Factor, H-Plane	206
Figure 9-41: Element Pattern (3 alternating hex-cut zones) vs. Array Factor, H-Plane	207
Figure 9-42: 3D Far-Field Patterns: (a) No Rotation, (b) Rotation <i>A</i> , (c) Rotation <i>B</i> (d) Rotation <i>C</i> , (e) Rotation <i>D</i>	209
Figure 9-43: Geometry of the $\epsilon_r=10$ T-Junction	211
Figure 9-44: Geometry of the $\epsilon_r=3.5$ T-Junction	211
Figure 9-45: Return Loss and Insertion Loss for Both T-Junctions	212
Figure 9-46: Gain vs. Junction Loss for 12dB/m Line Loss ($\epsilon_r \approx 3$)	216

LIST OF TABLES

Table 3-1:	Comparison of Results Between Empire and [3-5]	67
Table 4-1:	Simulation Parameters for each F/D in the $\Phi_0 = 0^\circ$ Case	74
Table 4-2:	Normalized Min. Sidelobe (SLB) Level, Decrease & Reference Phase ...	81
Table 4-3:	Antenna Cases that were Fabricated for Testing	84
Table 4-4:	Peak Gain with Varying Reference Phase	89
Table 5-1:	Comparison Between FZPA & Dielectric PC Fresnel Antenna	99
Table 5-2:	Results of Peak Intensity with Varying Reference Phase	102
Table 6-1:	Model Parameters for Each F/D	108
Table 6-2:	Summary of Circular FZPA Simulation Results	110
Table 6-3:	Summary of Hexagonal FZPA Simulation Results	110
Table 6-4:	Summary of Simulation Results	115
Table 6-5:	Summary of Zone Rotation Simulation Results	117
Table 6-6:	Summary of Measured Results	121
Table 8-1:	Single Metal Zone Small Focal Distance Simulation Results	147
Table 9-1:	Comparison of Metal Zone Widths	170
Table 9-2:	Summary of Simulation Results	193
Table 9-3:	Summary of Simulation Results	196
Table 9-4:	Summary of Results for Rotated Alternating Hex-Cut Zone FZPA Array	208

Table 9-5:	Substrate Material Data	210
Table 9-6:	Total Estimated Loss for 12dB/m Line loss Substrate ($\epsilon_r \approx 3$)	214
Table 9-7:	Total Estimated Loss for 39dB/m Line loss Substrate ($\epsilon_r \approx 10$)	214
Table 9-8:	Total Estimate Loss for 12dB/m Line Loss ($\epsilon_r \approx 3$)	217

CHAPTER 1

INTRODUCTION

1.1 Target Application and Current Challenges

1.1.1 Problem Statement

Wireless and satellite communications are vital in the daily activities of the average individual and business. Most services can now be received from anywhere at anytime. Location is irrelevant and communication is constant. These services must deliver wireless high-bandwidth multi-media signals which provide reliable simultaneous access to voice, fax, high-speed internet, and video. Antennas represent a critical technology in any of these wireless systems. Not only do they directly affect the received power of the system, they are also typically the largest and most visible part.

With the huge growth in wireless systems in recent years, space on towers and building roofs for locating antennas is at a premium and customers are not interested in mounting large antennas on their homes. This trend is driving the design of physically small antennas that are low profile, light weight, and aesthetically pleasing. Significant research has been devoted to making antennas smaller with varying degrees of success. However,

reducing antenna size always comes with trade-offs in performance.

One way to automatically reduce the size of the antenna is to design the system at a higher frequency. This is not a novel idea. In the last decade, the Ka-band (26GHz – 40GHz) received significant attention in the research world. At that time, researchers were looking into the proposed local multi-point communication/distribution systems (LMCS/LMDS) which would incorporate much smaller antennas than the traditional sizes inherent in lower frequency applications. Interest in these systems dwindled over the last five years due primarily to issues with high propagation losses at these frequencies for non line-of-sight configurations. Although the antenna research did not stop, most businesses turned away from the Ka-band.

Recently, however, the Ka-band has regained momentum with the launch of the Telesat Anik F2 Satellite in 2004. It operates in the Ka-band and is considered the world's largest commercial communication satellite. It offers two-way broadband services, such as high-speed internet, and enables direct line-of-sight which overcomes the propagation issues. There are many services that can make use of this satellite and other satellites that will be launched in the near future. At these frequencies, the services will provide broadband signals to the home or business. All will require some form of low-cost (<\$100US), low-profile (<4cm), and light-weight (<4.5kg) antenna in the Ka-band.

1.1.2 Challenges with Traditional Methods

Achieving a low-cost, low-profile, and light-weight antenna in the Ka-band is not trivial. The core problem is generally that existing low-profile technologies have low radiation efficiencies. Traditional high-gain and high-efficiency antennas such as the parabolic

reflector, reflectarray, and dielectric hyperbolic lens are not low profile. Each one consists of a feed placed in front of the aperture by a certain distance which causes the antenna depth to be large even at Ka-band. There are also stringent tolerance issues that exist in each of their construction, which make them costly to fabricate at these high frequencies. Fresnel lens antennas, including Fresnel zone plates in their current state of technology, are also not very low profile due to their feed being placed at the focal point in front of the aperture in a similar manner to the other high gain antennas.

The most common low-profile technology is the microstrip patch antenna, which is typically used in an array to achieve higher gain. At higher frequencies, such as those in the Ka-band, the microstrip array feed network is very lossy, which seriously degrades the aperture efficiency. The slotted waveguide array is another potential low-profile antenna option, but its cost is prohibitive owing to the tight fabrication tolerances required at these frequencies. Another alternative low profile antenna is the dielectric grating but, similar to the slotted waveguide array, fabrication becomes more complex and costly in the Ka-band. The last potential low-profile option is the partially reflective surface array, described in Chapter 2, which achieves reasonable gain and aperture efficiency, but has a very narrow bandwidth.

1.2 Motivation

A potential solution to the low-profile, light-weight and low-cost antenna problem at Ka-band lies in using lens technology in an array. By replacing a large diameter lens with an array of smaller lenses, the overall profile of the resulting array can be significantly reduced from that of the single element. Since they have less elements than an equivalent

microstrip patch array, lens arrays would require a simpler feed network with reduced line loss, presuming the lens has a printed feed.

The Fresnel zone plate antenna (FZPA) is an interesting candidate for the lens array element since it is the lowest cost and lightest weight antenna in the lens family. The aperture of the FZPA also has a very low profile because it is simply printed on a thin substrate which does not need to be of microwave grade. This also makes the FZPA aperture inexpensive to fabricate in comparison with other structures which require expensive microwave grade substrates.

The FZPA array offers tremendous benefits in the Ka-band compared to existing technologies. To be a viable alternative to existing planar antenna technology, however, the FZPA must compete with the higher aperture efficiency of the planar technology. Although the aperture efficiency of the FZPA can be increased, the overall FZPA array profile must be made lower and it must have less loss than the planar technology to be competitive. Also, if the FZPA array could offer a unique radiation characteristic, then it would be a more attractive option for antenna suppliers to bundle with their receivers in future satellite communication systems.

1.3 Thesis Objective

The overall objective of this thesis is to explore the possibility of making the FZPA a viable and attractive alternate antenna option for future satellite communication systems in the Ka-band. This involves identifying various parameters and studying their effects to see how the FZPA performance can be improved. This also involves investigating the

performance of the FZPA as an array element.

Some specific questions that need to be resolved in order to address the primary objective are the following:

1. Are there any properties of the FZPA that can add enhanced capability?
2. What is the resolution of a low-profile FZPA?
3. Is there a more desirable FZPA zone shape in terms of performance?
4. Can the efficiency of the FZPA be improved without increasing the profile?
5. How low profile can the FZPA be made?
6. How does FZPA element overlap affect array performance?
7. How do different elements perform in a FZPA array?
8. How does the loss of the FZPA array compare to an equivalent planar array?
9. What is the relative cost of the FZPA compared to an equivalent planar array?
10. What is the relative weight of the FZPA compared to an equivalent planar array?
11. What is the aesthetic and relative fabrication complexity of the FZPA?

The properties of the FZPA are investigated by designing, performing numerical modeling, fabricating, and testing prototypes. The data collected is used to evaluate the performance of the various FZPA properties and determine their applicability for Ka-band satellite communication systems.

1.4 Thesis Organization

This thesis is organized into ten chapters which describe the various FZPA investigations performed during the course of the research. This section will outline how the thesis is

organized and highlight the contents of each chapter.

The second chapter opens with a review of the basic theory of operation for the FZPA. An overview of the current state of planar FZPA technology is then provided. Each variation of the FZPA is explained and performance parameters are given. The chapter concludes with a review of lens arrays and a description of two competing high gain antennas.

The third chapter provides a brief review of several common analysis techniques for the FZPA. The discussion begins with a description of the Huygens'-Fresnel's principle, then the scalar and vectorial Kirchhoff's Diffraction Theory, and ends with a discussion related to the commercial finite-difference time-domain (FDTD) software that was used to analyze the FZPAs.

The fourth chapter summarizes the effects of a parameter called reference phase on the performance of the FZPA. The chapter opens with a definition of reference phase, which is followed by a review of the simulation results.

The fifth chapter investigates the FZPA resolution by examining the focal fields of the FZPA. The highlight of the chapter is the resolution result for FZPAs designed with sub-wavelength focal distances, which has never been determined for this structure. How the focal fields change with reference phase is also presented in this chapter.

The sixth chapter investigates a method for controlling the radiation patterns, specifically the sidelobe levels and their locations. The hexagonal FZPA is introduced as an element

geometry that will allow for this pattern control by rotating the hexagonal zones with respect to each other. The hexagonal FZPA is initially compared to the circular FZPA in terms of the most important radiation characteristics. It is shown that the hexagonal geometry does not perform as well as the conventional design. As a result, the FZPA with alternating hex-cut zones is introduced. It is a compromise between the hexagonal and circular structures to enable pattern control with radiation characteristics close to that of the conventional circular FZPA. The chapter also includes a comparison between measured and simulated results.

The seventh chapter introduces the new reflector-backed FZPA. It consists of a ground plane at the aperture of the waveguide feed. This approach not only improves the FZPA directivity and aperture efficiency, but it also enables the FZPA to possibly have a more compact package. This chapter reviews the simulation and measurement results.

The eighth chapter investigates the effect of decreasing the FZPA profile by reducing the focal distance. Simulation results highlight the effect on peak directivity and aperture efficiency as the focal distance is decreased. A comparison is made to the superstrate antenna, an alternative low-profile antenna, and trade-offs between the two structures are outlined. The chapter concludes with a review of the measurement results, where some interesting observations are made.

The ninth chapter deals with FZPA arrays. The chapter starts by describing an innovative approach to compute the FZPA zones. The approach is applied to a selection of linear and planar arrays and results are compared to the conventional FZPA arrays. Two arrays with different elements are also investigated, one method having elements with different

reference phases, and one method having elements with different zone rotation configurations. The chapter concludes with a comparison between the FZPA array and microstrip patch array losses.

Finally, the tenth chapter will conclude the thesis. A summary of the final conclusions is presented and the primary contributions of the thesis are outlined. This chapter ends with a discussion of the direction for possible future research on this topic.

CHAPTER 2

PLANAR FZPA TECHNOLOGY

2.1 Introduction

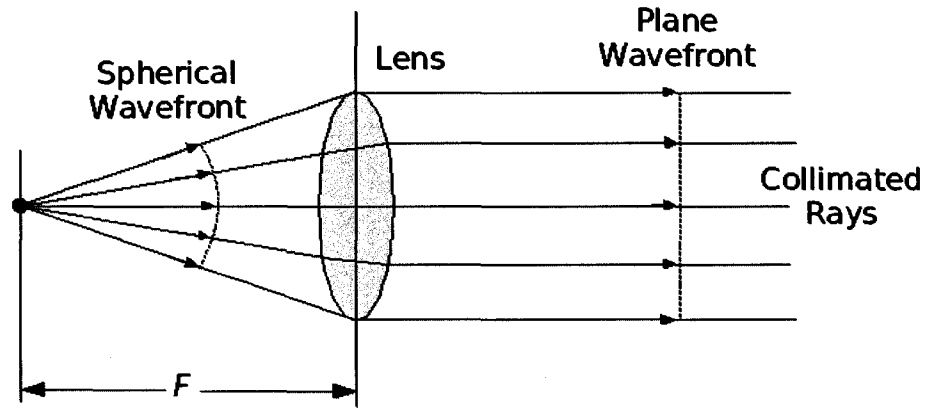
This chapter will establish the current state of planar FZPA technology by providing important background information. Basic lens theory will be reviewed where the operation mechanism of the FZPA will be explained. Various types of planar FZPA structures from the literature will be presented and their performance parameters will be outlined. A brief description of lens arrays will also be given, and then the chapter will conclude by outlining the performance of two competing high gain antennas.

2.2 Basic Lens Theory

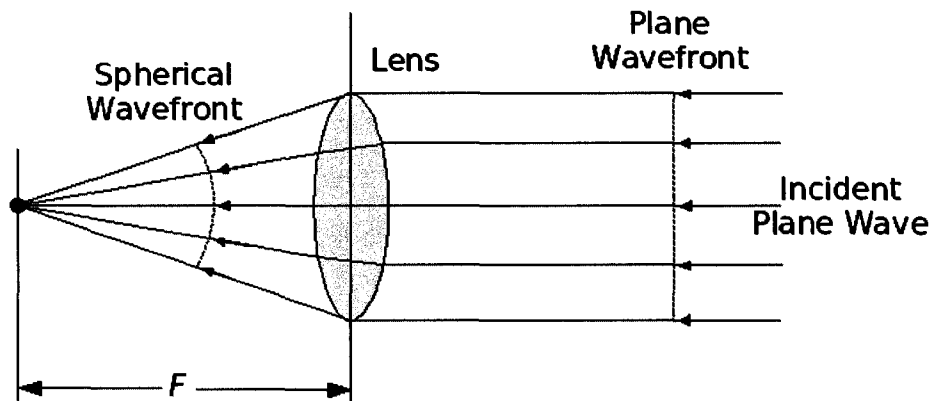
2.2.1 Shaped Dielectric and Fresnel Lens Operation

A lens is a device which focuses electromagnetic (EM) energy. Lenses are used in combination with transmitting or receiving antennas, placed at the lens focal point, to create a lens-antenna system. In this system, the lens performs a phase transformation. For example, as illustrated in Figure 2-1(a), a lens in transmit mode can transform the phase of a spherical wave originating from its focal point into a collimated beam or plane

wave on the opposite side of the lens. The lens accomplishes this phase transformation by introducing an appropriate phase change to the wavefront as it passes through the lens such that when the wavefront leaves the lens all parts of it will be in phase [2-1].



(a)



(b)

Figure 2-1: Lens Operation in: (a) Transmit Mode and (b) Receive Mode

Similarly, as illustrated in Figure 2-1(b), the lens in receive mode performs the opposite task of transforming an incoming plane wave into a spherical wave at the focal point. The lens-antenna system is also capable, in receive mode, of focusing to a line, a plane, or any arbitrary surface.

In the case of a shaped dielectric lens, the collimation occurs because the EM waves refract and change velocity as they pass through the dielectric material. The amount that the wave changes upon entering the lens depends on where it hits the surface of the lens. This can be more easily understood by considering the ray model of light, which assumes that the waves follow straight line paths called rays. The shape of the lens used in a transmit mode system is therefore such that the total phase of any ray leaving the lens is equal to the phase of any other ray also leaving the lens. A dielectric lens with a hyperbolic surface, as shown in Figure 2-2(a), performs this function by transforming the phase perfectly over its whole aperture. Typically, the aperture efficiency of the hyperbolic dielectric lens is around 50-60%. This type of shaped lens has many applications in the optical world and comes in several different forms.



Figure 2-2: Side View of (a) Hyperbolic Dielectric Lens, (b) Fresnel Lens

The Fresnel lens, as conceived by Augustin Fresnel in the early 1800's [2-2], is different from the shaped dielectric lens in that the phase transforming surface is broken down into Fresnel zones (defined in Section 2.2.4), or concentric circular sections. Although the sections have discontinuities between them, each section maintains the surface curvature

of the original shaped dielectric lens, but with significantly less dielectric material as shown in Figure 2-2(b). The smaller lens profile is made possible by removing material such that the difference between ray paths on each side of the step is a full wavelength.

Fresnel came up with this idea because he needed to construct a large lens with an appropriate focal length for a lighthouse but was unable to use the traditional shaped dielectric lens due to its excessive weight and size. Fresnel had reasoned that it was the surface curvature of the shaped dielectric lens which gave it the focusing power so he instead reproduced the surface curvature in small sections. In this way he was able to maintain the same focal length while reducing the weight and size of the lens significantly.

The Fresnel lens operation, like the shaped dielectric lens, depends on wave refraction and velocity changes in the material to perform proper focusing. Unfortunately, compared to the hyperbolic lens, the Fresnel lens is less efficient at focusing the energy from the source since the discontinuities in the aperture cause scattering and shadowing effects [2-1]. Also, the Fresnel lens antenna has a more narrow band of operation since the bandwidth is inversely related to the number of zones. The efficiency and bandwidth are thus traded off against the improvement in size and weight.

2.2.2 Phase Correcting Fresnel Lens Operation

The phase correcting Fresnel lens is an alternative to the Fresnel lens described in the previous section. It transforms the phase at discrete intervals across the antenna aperture such that the phase transforming surface does not maintain the curvature of the original hyperbolic dielectric lens. The most common version of this antenna is the grooved phase

correcting Fresnel lens [2-1]. The zones are made by cutting circular grooves, with a fixed depth, s , into a slab of dielectric material at the appropriate Fresnel radii. The groove depth is important since, when chosen correctly, it will cause the radiation passing through the groove to undergo the proper phase shift. In this way, the radiation that hits the grooves will be corrected and will be in phase with the radiation that exits in the adjacent zone. This concept is illustrated in Figure 2-3.

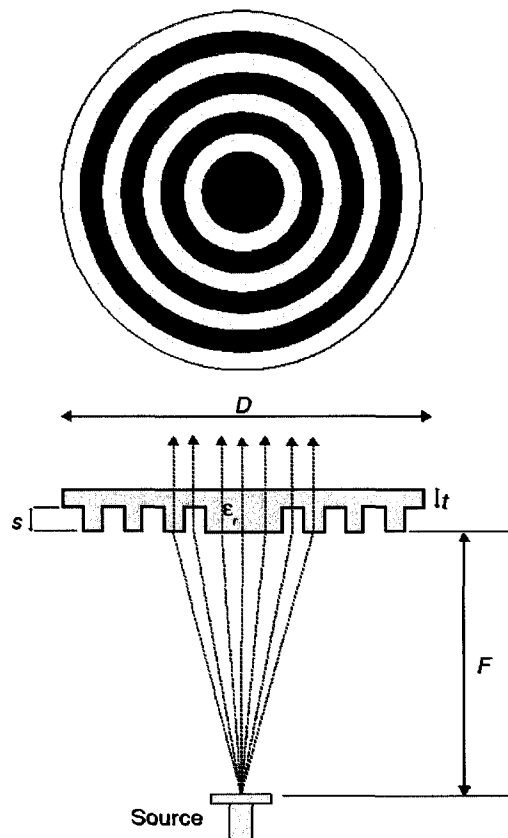


Figure 2-3: Grooved Phase Correcting Fresnel Antenna with 180° Phase Correction (from [2-1])

In 1898, Robert W. Wood designed the first phase correcting Fresnel lens at optical frequencies by using half-period (180°) phase correction [2-2]. The aperture efficiency of the 180° grooved phase correcting Fresnel antenna is typically on the order of 15-20% depending on the focal-length-to-diameter ratio (F/D) and frequency [2-1]. However, by

dividing the half-period (180°) sub-zones into smaller sub-zones, each with specific phase correction, it is possible to achieve better aperture efficiencies. By making smaller sub-zones, the grooved phase correcting Fresnel lens will better approximate the cross-section of a Fresnel lens of the same F/D . Figure 2-4 illustrates a quarter-wave (90°) phase correcting Fresnel antenna where the phase correction of each level in the dielectric is specifically stated.

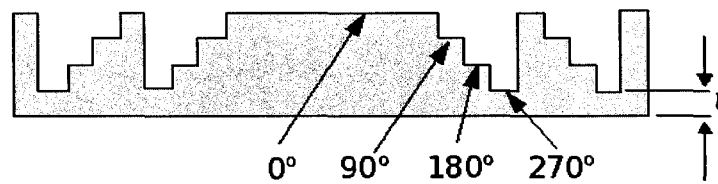


Figure 2-4: Quarter-Wave Phase Correcting Fresnel Antenna (from [2-1])

In [2-3], it was shown that a grooved 90° phase correcting Fresnel antenna has a focus intensity only 1dB below the same F/D Fresnel lens. Also, a grooved 90° phase correcting Fresnel antenna design shown in [2-1] at 30GHz with $F/D=1$ and $D=15.8\text{cm}$ achieved a 43% aperture efficiency. These aperture efficiencies may be further degraded by mismatch losses at the air-dielectric interfaces of the lens and by the effects of shadow blockage [2-1]. Both of these effects are more serious with smaller F/D designs.

There is, however, a limit to how much phase correction can be realistically achieved. The authors in [2-1] indicated that using a phase correction beyond quarter-wave (90°) would not be worth the extra fabrication complexity and lens thickness required.

A recent paper by Reid and Smith [2-4] showed numerical results of the grooved phase correcting Fresnel antenna which was analyzed using the body-of-revolution FDTD method. The authors provided a parametric study on the effects of focal length, diameter,

number of zones, thickness of lens, as well as the number of phase correction zones. These results represent a good summary of the state of this technology and provide useful guidelines for the designer of these antennas.

2.2.3 Huygens' Principle & Diffraction

In the late seventeenth century, Christiaan Huygens developed a model for wave propagation which today is the basis of the surface equivalence theorem. Huygens' principle states that "each point on a primary wavefront can be considered to be a new source of a secondary spherical wave and that a secondary wavefront can be constructed as the envelope of these secondary spherical waves" [2-5]. This concept is illustrated in Figure 2-5 where the initial spherical wave originates from the point source.

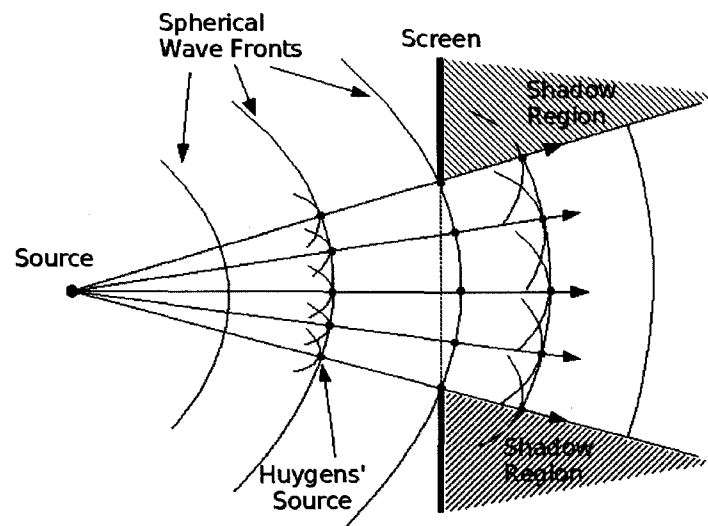


Figure 2-5: Huygens' Principle (from [2-6])

The wave propagates toward the screen by creating wavefronts. Each wavefront consists of sources, referred to as Huygens' sources, which radiate new spherical mini-waves (wavelets). The envelope of these mini-waves and the sum of the sources creates the new wavefront. The wavefronts are perpendicular to the optical rays and therefore the wave

propagates in straight lines.

The screen in the path of the propagating wavefronts of Figure 2-5 is present to illustrate the diffraction mechanism. Since the Huygens' sources are located on the optical rays that go through the aperture in the screen, certain sources will follow a path that takes them behind the screen. This presence of rays behind the obstacle is called diffraction. In terms of waves instead of rays, diffraction occurs when the waves encounter an obstacle and spread out or bend around it. The waves cannot fill the area behind the screen entirely though, so shadow regions are created where the waves do not penetrate. Diffraction is the basis for the operation of the FZPA.

2.2.4 Construction of Fresnel Zones

The concept of Fresnel zones originated in the early nineteenth century from the work by Augustin Fresnel [2-7]. Fresnel expanded on Huygens' work by taking into account the space and time periodicity of light waves. He was interested in the interference and diffraction of light and was the first to use a geometrical construction of zones to solve what is now referred to as the Huygens'-Fresnel integral [2-8]. Although these zones, which later became known as the "Fresnel zones", can be applied to different shaped surfaces [2-6], discussion in this work will be limited to a planar surface since it is the most appropriate for FZPAs.

Figure 2-6 illustrates the construction of Fresnel zones on a planar surface which is normal to the direction of propagation, i.e. the z -axis. A spherical wave emanates from a source, S , located a distance F from the planar surface, centered at O .

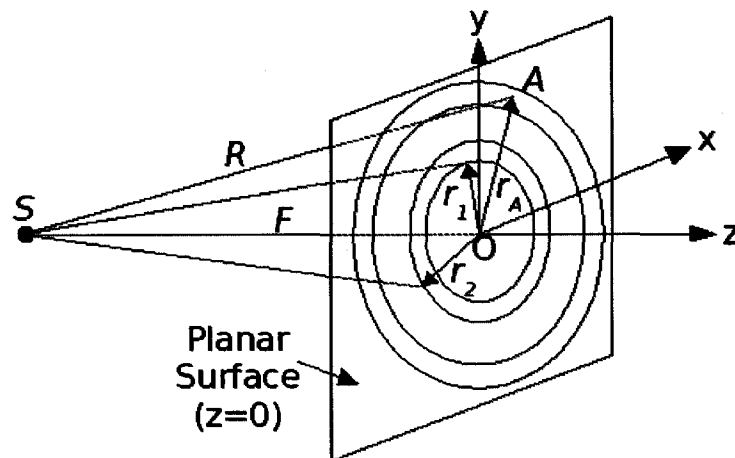


Figure 2-6: Construction of Fresnel Zones

The phase of the wave on the surface is what determines the zones. The phase at any given location on the surface can be calculated by first tracing rays from the source to the specific point on the surface. As shown in Figure 2-6, if the point on the surface is A, this creates a triangle between the rays SO , SA , and the radius r_A . The electrical path difference between SA and SO results in a relative phase difference between points O and A . Since the source wave is spherical, all rays from the source to points on the surface at constant radii from O will have the same path difference. This results in constant phase spheres centered around O which form circles on the planar surface. These circles represent constant phase contours.

Mathematically, the phase, ϕ , at an arbitrary point on the surface, A , is computed according to Equation 2-1, where δ is the difference in path lengths between SO and SA and λ_o is the free space wavelength. The path difference is computed according to Equation 2-2, where F is the distance SO , R is the distance SA , and r_A is the radius from O to A on the planar surface.

$$\phi = 2\pi \frac{\delta}{\lambda_o} \quad (2-1)$$

$$\delta = R - F = \sqrt{(r_A^2 + F^2)} - F \quad (2-2)$$

By knowing the phase values for every point on the surface, it is possible to define the zones. The first zone, from O to r_1 in Figure 2-6 moving radially outward, contains the phases from 0° to 360° where the phase 0° is arbitrarily set to 0° . The second zone, which covers the area between the first and second rings, r_1 to r_2 , has phases between 360° and 720° . The third zone has phases between 720° and 1080° , and so on. A complete zone therefore contains a 360° phase range.

It is also possible to define sub-zones where the phase from one sub-zone to the next ranges by an amount less than 360° . It is common to break the 360° phase range in half so that each sub-zone covers 180° . This is based on the half-period zone theory which Fresnel founded when he noted that light emerging from adjacent 180° zones will be opposite in phase. This concept is utilized in the construction of the FZPA.

2.2.5 Circular Fresnel Zone Plate Antenna

The optical Fresnel zone plate lens, although named after Fresnel, was neither designed by him nor any way related to the Fresnel lens described in Section 2.2.1. The idea for the zone plate lens originated from Fresnel's half-period zone concept, described briefly in Section 2.2.4. Fresnel had observed that light waves having phases in the sub-zone 0° to 180° will add destructively and cancel with waves having phases in the sub-zone from 180° to 360° .

Lord Rayleigh used Fresnel's observation to create the first optical zone plate lens in the

late nineteenth century. He showed that, by blocking the light waves from alternating 180° sub-zones, the light that emerged would add constructively and combine to increase focus intensity [2-2]. Although he created the first optical zone plate lens, it was not until 1875 that it became public knowledge. At that time, Jacques-Louis Soret was the first to publish a paper on the optical Fresnel zone plate. The Soret lens consisted of concentric black rings corresponding to the alternate 180° phase sub-zones that were "blacked-out" [2-2].

The FZPA, as conceptualized by Soret and Rayleigh at optical frequencies, was first used as an antenna in the microwave band in the early twentieth century by Western Electric [2-2]. In transmit mode, the FZPA required that a feed generating spherical waves be placed at the focal point of the lens so that a collimated beam would result in the far field on the other side of the lens. The rings that were blackened by Soret to prevent light from getting through, were made metallic to reflect the microwaves. The resulting FZPA, as illustrated in Figure 2-7, consisted of planar circular rings which alternated between transparent and opaque (metal) and became known as the circular FZPA.

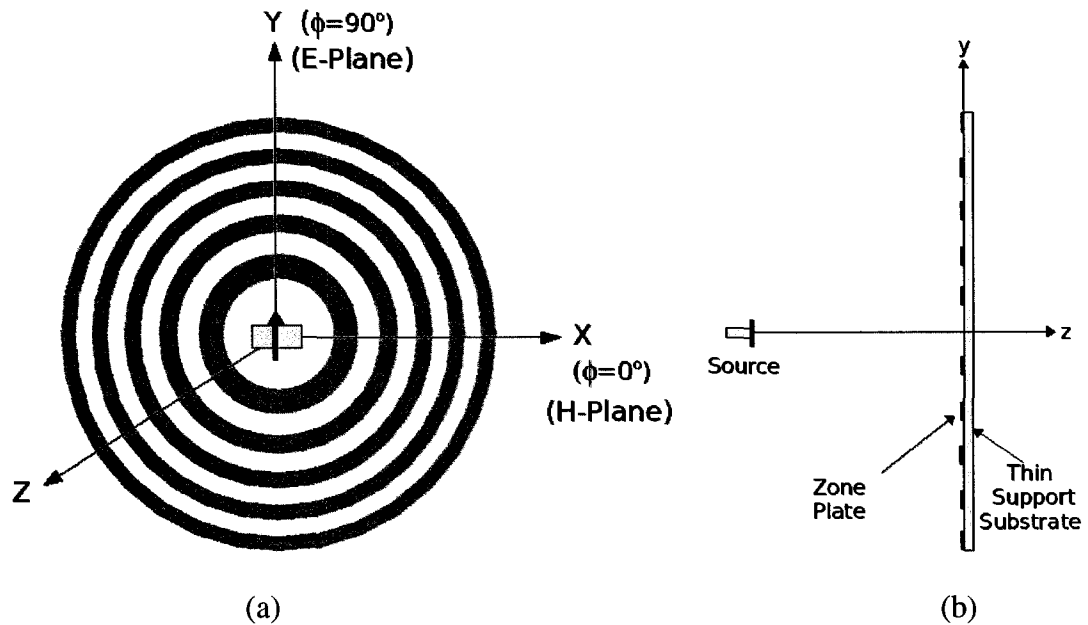


Figure 2-7: Circular FZPA: (a) Front View, (b) Side View

The circular geometry, as described in Section 2.2.4, stems from the fact that the spherical waves from the feed create constant phase zones on the planar surface that are circular. The metal rings coincide with the alternating 180° phase sub-zones on the surface of the antenna aperture as detailed in Figure 2-8. The EM waves that hit the transparent regions diffract through and combine to collimate a beam in the far field. This operation mechanism is different from the refraction and wave velocity method of the Fresnel and shaped dielectric lenses.

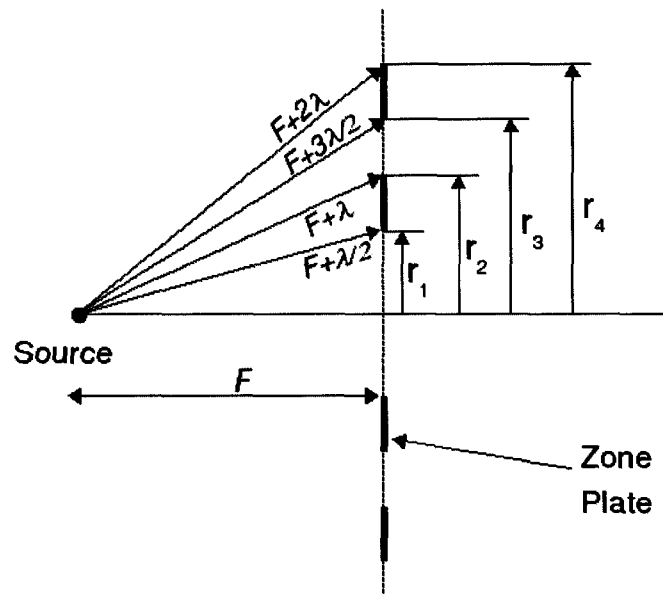


Figure 2-8: Side View of Circular FZPA Illustrating 180° Phase Sub-Zones

An interesting property of the circular FZPA is that, if there are a large number of zones, it does not matter whether the first sub-zone is transparent or opaque. The zone plate lens will perform the same in either case since it can focus both in the transmit and receive modes. This means that the FZPA has multiple foci, a fact that is exploited in the reflector FZPA which will be discussed in Section 2.3.1.

The circular FZPA was the topic of extensive research in the 1940s and early 1950s. Both Bell Telephone Labs and the National Research Lab in Washington, D.C. [2-2] were actively investigating the circular FZPA although neither group published their work. Boivin et al. from Laval University, Canada, published a paper in 1956 outlining results of their measurements at 24GHz on the FZPA [2-9]. In 1960, Sobel et al. [2-3] were the first to perform measurements at millimeter frequencies, but most of their work was in regards to the phase correcting Fresnel antenna discussed in Section 2.2.2. In 1961, Buskirk and Hendrix [2-10] performed novel work on the FZPA at X-band (7–12.5GHz).

There were no further publications until 1968 when Sanyal and Singh [2-11] published an extensive paper outlining their theoretical and experimental work on FZPAs. Their work was also at X-band and provided significant insight into the focal fields of these antennas.

For the next 15 years, very little research activity occurred in this field. Starting in the early 1980s, interest in exploring the FZPA was rekindled due to the increasing need for small, inexpensive antennas. Of note was a paper in the early 1990s by Guo and Barton [2-12]. They investigated the sidelobe performance of the circular FZPA and found that the sidelobe level of a fixed aperture circular FZPA with constant aperture field taper decreased as the number of full wave zones increased. This meant that smaller F/D circular FZPAs should produce lower close-in sidelobes. Around the same time, Baggen and Herben [2-13] combined all known results on circular FZPAs and developed a design procedure. The procedure incorporated specific design rules and showed that it is possible to optimize the circular FZPA performance given the diameter of the lens.

2.2.6 Fresnel Zone Radii

Design equations for the Fresnel zone radii are established based on the lens antenna geometry shown in Figure 2-9. The lens aperture has a diameter, D , and the source is located at the focal point which is a distance F from the lens. The source generates spherical waves, which are represented in Figure 2-9 by the hemispherical wavefront. The waves that hit the center of the lens have a different phase relative to the waves that hit the other parts of the lens. This is due to the varying path lengths from the source to the lens aperture.

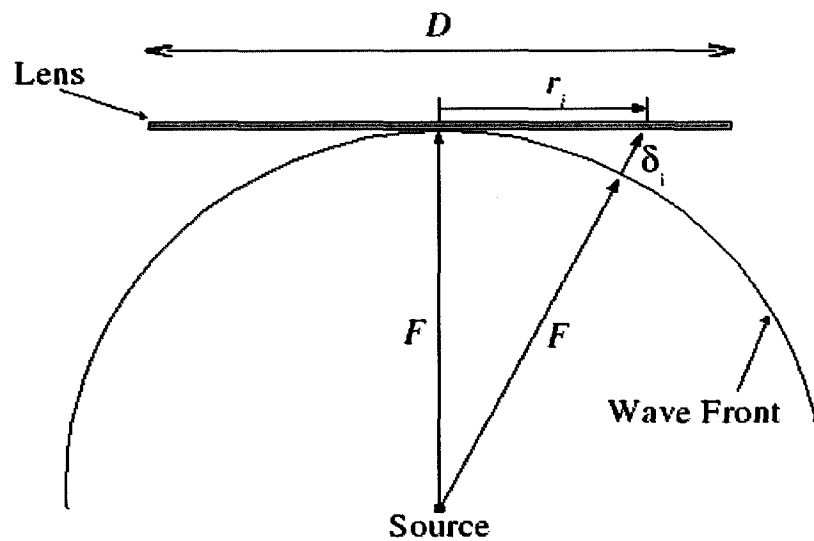


Figure 2-9: Fresnel Lens Diagram

In Section 2.2.4, this path difference was derived and expressed in Equation 2-2. Rearranging this equation and solving for the zone radii yields Equation 2-3, where r_i represents the radius of the i^{th} zone and N is the total number of zones.

$$r_i = \sqrt{2Fi\delta + (i\delta)^2} \quad i=1,2,3,\dots,N \quad (2-3)$$

Equation 2-1 from Section 2.2.4 also needs to be re-written in order to account for the number of sub-zones, P , into which the lens is divided. The number of sub-zones is related to the phase by Equation 2-4(a) where the phase, ϕ , is in radians.

$$P = \frac{2\pi}{\phi} \quad (a)$$

$$\text{Therefore: } \delta = \frac{\lambda_o}{P} \quad (b) \quad (2-4)$$

As an example, if the lens is broken down into 180° sub-zones, $\phi = \pi$ and therefore $P=2$. If

full zones are used, $\phi=2\pi$ and $P=1$. Generally, as P gets larger, the lens will have more sub-zones and the phase error, ϕ , will decrease. It is common to re-write Equation 2-3 as shown in Equation 2-5(a), to include P by substituting the relation for δ from Equation 2-4(b) into Equation 2-3. Since all FZPAs considered in this work will have $P=2$, Equation 2-5(b) will be the standard equation for computing the zone radii. From this point forward, a “zone” will refer to a 180° sub-zone.

$$r_i = \sqrt{\left(F + i \frac{\lambda_o}{P}\right)^2 - F^2} \quad i=1,2,3,\dots, N \quad (a)$$

(2-5)

$$r_i = \sqrt{\left(F + i \frac{\lambda_o}{2}\right)^2 - F^2} \quad i=1,2,3,\dots, N \quad (b)$$

Since this equation was derived based on a ray-tracing approach, it is only valid for large focal distances. This is because the principle of ray-tracing requires that the rays make small angles with the focal axis so that they can be paraxial. This fact will become important when considering FZPA designs with small focal distances as will be discussed in Chapter 8.

In order to better understand certain characteristics of lens behavior, Equation 2-1 can be normalized with respect to the lens diameter, D . The expression for δ from Equation 2-2 is substituted into Equation 2-1 and then all the terms are divided by the diameter resulting in Equation 2-6 where r_i is the radius of the i^{th} zone.

$$\frac{\phi}{D} = \left[\sqrt{\left(\frac{r_i}{D}\right)^2 + \left(\frac{F}{D}\right)^2} - \left(\frac{F}{D}\right) \right] \frac{2\pi}{\lambda_o} \quad (2-6)$$

From this expression, it can be seen that, if the (r_i/D) term is fixed (i.e. for a specific zone radius and diameter of the lens) and the F/D decreases, the normalized phase error, ϕ/D , will increase. This implies that, to maintain a given phase error at a fixed diameter with a decreasing focal length, more sub-zones are required.

2.2.7 Circular FZPA Radiation Characteristics

Determining the actual far-field radiation patterns for the circular FZPA involves the standard approach of finding the solution to the vectorial wave equations in the far field. In the case of FZPAs, this is complicated by the fact that the antenna influences the incident waves. Because the antenna reflects some of the waves back toward the source, the problem is too complicated to solve using standard methods [2-6]. Kirchhoff's Diffraction Theory must be used instead.

In studying this problem, Kirchhoff made some simplifying assumptions which allowed him to approximate the far-field radiation patterns. This method is outlined in [2-6] and described in Chapter 3 for both the scalar and vectorial far-field equations. Using either approach, the first step is to compute the field distribution for a single zone on the lens aperture. This process is repeated for the other zones and then the total aperture field is determined by summing the contributions from all of the zones. Once the total aperture field is known, it can be integrated using the Fresnel-Kirchhoff integral to determine the radiation patterns in the far field.

The following method and equations are taken from the paper by Baggen, Jeronimus and Herben [2-14] who derived an estimate of the far-field gain function for the circular FZPA. They used the scalar Kirchhoff's Diffraction Theory and applied it to the geometry

shown in Figure 2-10. This figure shows the source, S , located in an offset position at the focal point of the lens which is a distance F' and angle σ away from the lens. The offset position from the lens axis allows for scanning capability and allows for a more general solution.

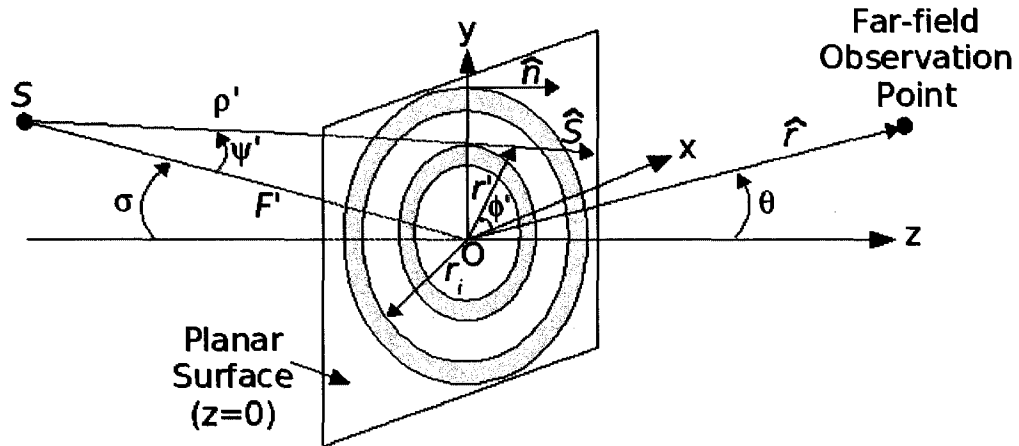


Figure 2-10: Geometry of the FZPA for Far-Field Computation

Several simplifying assumptions were made in this analysis including the gain function of the feed which is given by Equation 2-7, where n is any number representing the order of the cosine and ψ' is the angle describing the location of the offset source from the focal axis F' .

$$G_{feed}(\psi', n) = \begin{cases} 2(n+1) \cos^n(\psi') & 0 \leq \psi' < \frac{\pi}{2} \\ 0 & \frac{\pi}{2} \leq \psi' < \pi \end{cases} \quad (2-7)$$

The fields on the lens aperture are given by:

$$g(r', \phi', \theta) = \left[E'_f(r', \phi') (\cos(\theta) + \hat{n} \cdot \hat{S}(r', \phi')) \right] \cdot r' \quad (2-8)$$

where:

$$E'_f(r', \phi') = \sqrt{\frac{(F' - r' \sin(\sigma) \cos(\phi'))^n}{(F'^2 + r'^2 - 2r'F' \sin(\sigma) \cos(\phi'))^{(1+\frac{n}{2})}}} \quad (2-9)$$

and

$$\hat{n} \cdot \hat{S}(r', \phi') = \frac{F' \cos(\sigma)}{\sqrt{F'^2 + r'^2 - 2r'F' \sin(\sigma) \cos(\phi')}} \quad (2-10)$$

In Equation 2-8 the coordinates r' and ϕ' describe points on the planar surface of the lens, θ is one of the spherical coordinates of the far-field observation point, \hat{n} is the unit vector normal to the lens surface, and \hat{S} is the Poynting vector of the radiation fields from the feed.

The gain function in the far field is obtained by integrating the field expression from Equation 2-8 over the clear zones of the lens aperture resulting in:

$$G_{ff}(\theta) = \left(\frac{n+1}{2\lambda^2} \right) \left| \sum_i \int_0^{2\pi r_{2i+1}} \int_{r_{2i}} g(\phi', r') e^{jkh(\phi', r', \theta)} dr' d\phi' \right|^2 \quad (2-11)$$

where:

$$h(r', \phi', \theta) = -\sqrt{F'^2 + r'^2} \sqrt{1 - W(r', \phi') \cos(\phi') + r' \sin(\theta) \cos(\phi')} \quad (2-12)$$

and

$$W(r', \phi') = \frac{2r'F' \sin(\sigma)}{F'^2 + r'^2} \quad (2-13)$$

and where r_i is the radius of the i^{th} zone, and k is the wave number.

Using the above equations, typical far-field radiation patterns for a FZPA, having 10

circular zones with $F/D=0.237$, $F=3.75\lambda$, and $D=15.8\text{cm}$ at 30GHz, were computed and are shown in Figure 2-11 for the H-plane. The results in the E-plane are identical due to symmetry. The gain is shown to be approximately 22dB, the 3dB beamwidth is about 4.5° and the sidelobe level is about 20dB below the main beam.

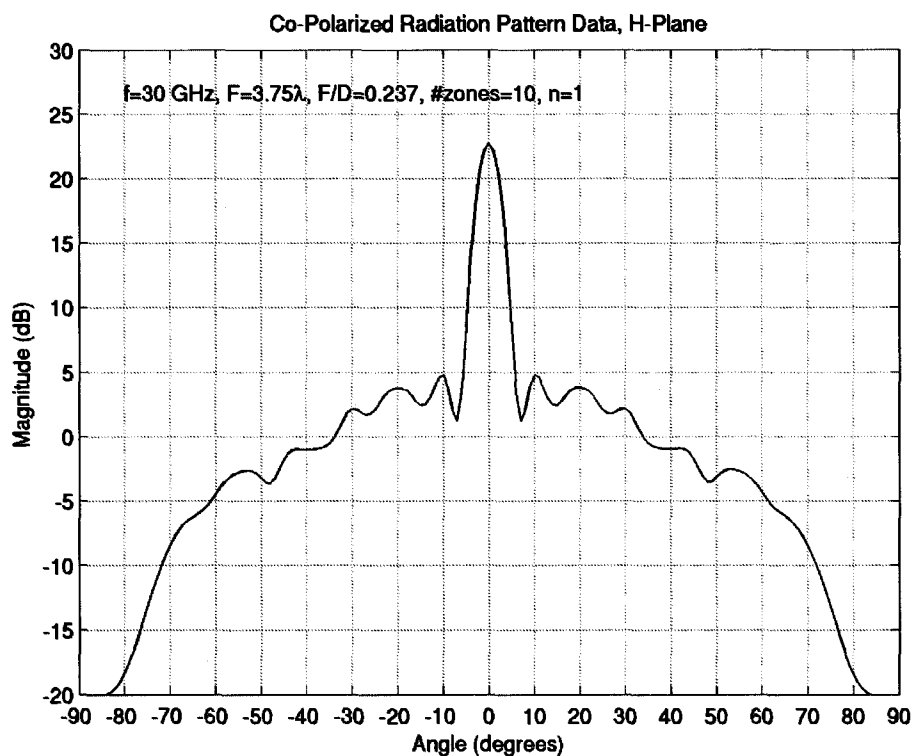


Figure 2-11: Typical Circular FZPA Radiation Patterns, H-Plane

Due to the inherent nature of the circular FZPA, researchers proved that it was not as efficient as the Fresnel lens, dielectric shaped lens, or the parabolic reflector antenna. A significant portion of energy from the source is reflected back by the metal zones of the FZPA instead of contributing to the collimated beam on the other side. This is a serious disadvantage for the FZPA since many applications require aperture efficiencies to be higher than 50% instead of around 10% as is the case with the circular FZPA.

Researchers devised several methods to improve the FZPA aperture efficiency [2-15] and

most will be discussed later in this chapter. Recently, for example, Zhang [2-16] proposed a new zoning rule for the FZPA which is an improvement over Equation 2-5. It is based on a quantitative analysis of the Fresnel integral and effectively performs a superposition of in-phase contributions from each zone. The improved zone radii calculation was shown to enhance antenna gain by about 1dB. Most methods to improve efficiency, however, involve compromising aspects of the circular FZPA that are advantageous such as its low profile, low weight, low cost, and simplistic construction.

2.2.8 FZPA Focal Fields

The previous discussion involved the FZPA system being operated in transmit mode. In this section, the opposite scenario will be discussed where the antenna is now in receive mode. This is the case where the receiver is located at the focal point of the lens and the plane waves passing through the lens are diffracted in such a way that they focus to the receiver. Figure 2-12 illustrates this situation where the plane wave is normally incident on the aperture from the left. By analyzing the FZPA in this mode, it is possible to observe the fields at the focal point. Guo et al. acknowledged this fact in their paper [2-17] where they derived equations for analyzing the diffraction field in front of the FZPA in receive mode.

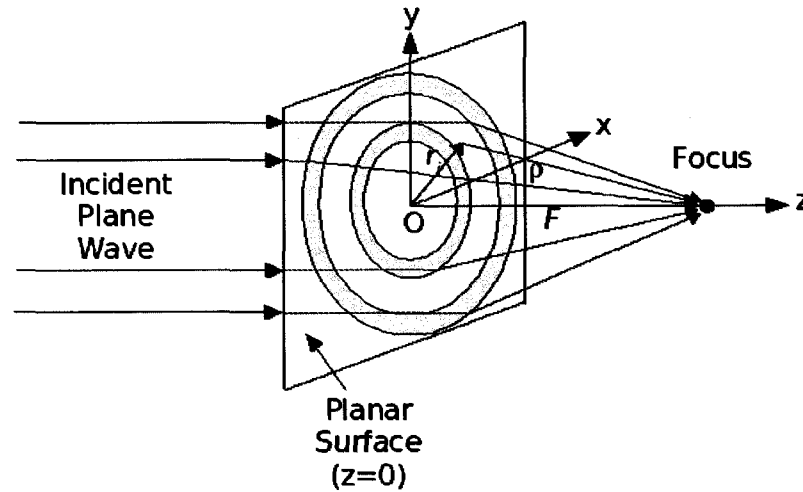


Figure 2-12: Circular FZPA in Receive Mode

By looking at the focal fields, it is possible to confirm the location of the lens focal point. The focal field intensity, I , along the z -axis is computed via Equation 2-14 where N is total number of zones, k is the wave number, r_i are the zone radii, ρ is the distance from the point on the lens surface to the focus, and $\Phi(\rho)$ is the phase correction function which is used for phase correction lenses.

$$I(z) = \frac{j\pi}{\lambda} \sum_{i=1}^N \int_{\rho_{i-1}}^{\rho_i} e^{j(\Phi(\rho) - k\rho)} \left(1 + \frac{z}{\rho}\right) d\rho \quad (2-14)$$

where: $\rho_i = \sqrt{z^2 + r_i^2}$

Figure 2-13 shows simulated results for the focal field intensity plotted against distance in the z -direction for a 10 zone circular FZPA with $F/D=0.237$, $F=3.75\lambda$, and $D=15.8\text{cm}$ at 30GHz. If the lens is designed correctly, there will be a peak at the desired focal point. In Figure 2-13, this peak occurs at $z=3.75\lambda$ and the lens is located at $z=0\lambda$. This means that the focal distance is 3.75λ which is correct based on the given F/D and diameter.

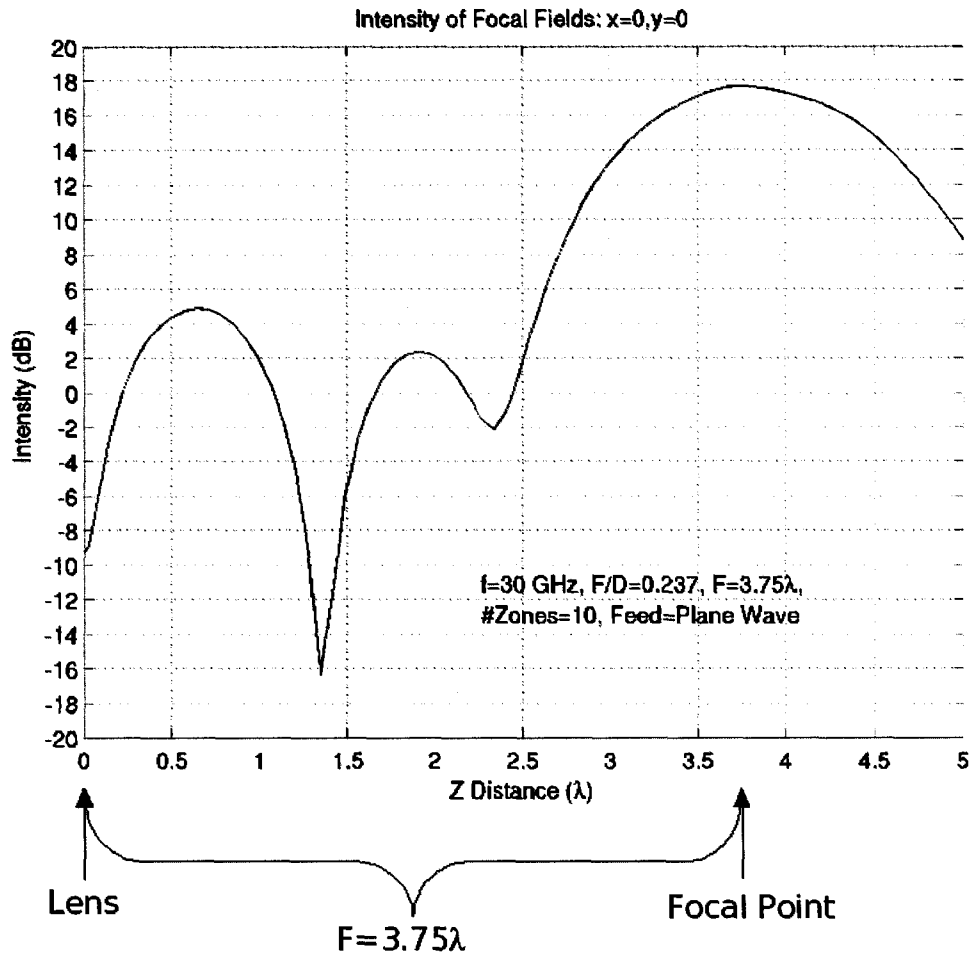


Figure 2-13: Typical Focal Fields of Circular FZPA

2.2.9 Spatial Resolution

Spatial resolution is a measure of the resolving power of a lens or other optical device. In the case of the lens, the resolving power is limited by diffraction since the lens aperture creates a circular diffraction pattern, also called an Airy pattern [2-18].

In 1879, Lord Rayleigh introduced a criterion for resolution in a diffraction-limited optical (quasi-optical) system which has become known as the Rayleigh criterion. Rayleigh considered two equal intensity monochromatic spectral components to be resolved when the intensity maximum of one is located where the first intensity minimum

of the second one occurs [2-19]. This concept is illustrated in Figure 2-14 where I represents the intensity.

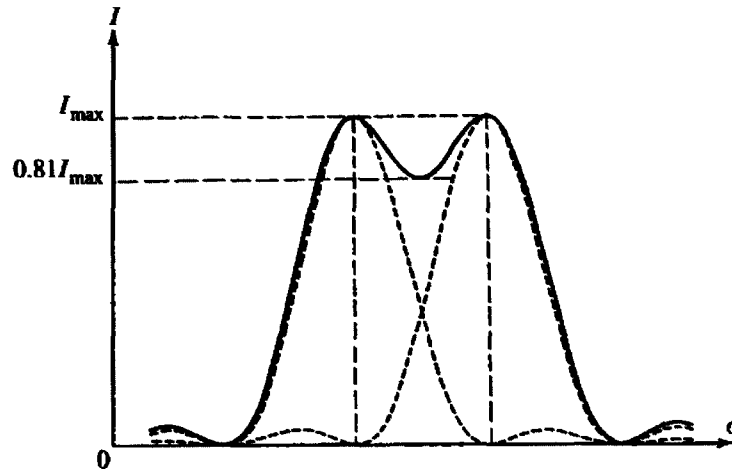


Figure 2-14: Two Monochromatic Spectral Components (from [2-19])

For an ideal lens having a focal distance F and diameter D , the Rayleigh criteria can be expressed mathematically as the minimum spatial resolution shown in Equation 2-15.

$$\Delta = 1.22 \lambda \frac{F}{D} \quad (2-15)$$

The factor of 1.22 in Equation 2-15 comes from the computed position of the first dark ring in the diffraction pattern which surrounds the central ring of the Airy pattern. The spatial resolution, Δ , is the radius of the smallest spot that a collimated beam of light can be focused to. It is proportional to both the wavelength and the F/D , implying that a decrease in the F/D would yield a smaller spatial resolution. However, diffraction-limited optical systems are typically limited to having an $F/D \geq 0.5$ [2-20] due to the limitations caused by the paraxial approximation. In these cases, the spatial resolution is therefore limited to $\Delta = 0.61\lambda$.

Spatial resolution has also been specified for ideal optical systems by Ernst Abbe to be a half wavelength ($\Delta = 0.5\lambda$) [2-19]. There is no special significance given to this or the Rayleigh criteria since both are used and others have been proposed.

At optical frequencies, due to the small wavelength values, lenses are typically designed with an F/D much larger than one. This leads to spatial resolutions that are greater than a wavelength. At microwave frequencies, however, lens antennas can be designed with a much smaller F/D including $F/D < 0.5$. With F/D values this small, the criterion given in Equation 2-15 is no longer valid since the paraxial approximation is exceeded. In this case, the spatial resolution limits are relatively unknown. Kearey et al. [2-21] investigated small diameter Fresnel lenses at microwave frequencies, but they did not study the spatial resolution effects. Minin et al. [2-22] recently presented some spatial resolution results with small F/D values for the dielectric phase correcting Fresnel lens. They found that a spatial resolution less than 0.5λ could be achieved for $F/D < 0.2$ and $F < 2\lambda$. To date, the spatial resolution of FZPAs has not been investigated. Chapter 5 will expand on this topic.

2.3 Types of FZPAs

2.3.1 Reflecting FZPA

The reflecting or folded version of the FZPA is more efficient than the conventional circular FZPA. A ground plane is placed behind the lens to reflect the waves that had diffracted through so that they can now contribute to the overall radiation. This concept was first introduced by Buskirk and Hendrix in 1961 [2-10] as an alternative to the parabolic reflector antenna and has since been investigated in more detail by several other researchers [2-12, 2-23, 2-24, 2-25]. The reflecting FZPA is shown in Figure

2-15(b) in comparison with the conventional circular FZPA in Figure 2-15(a).

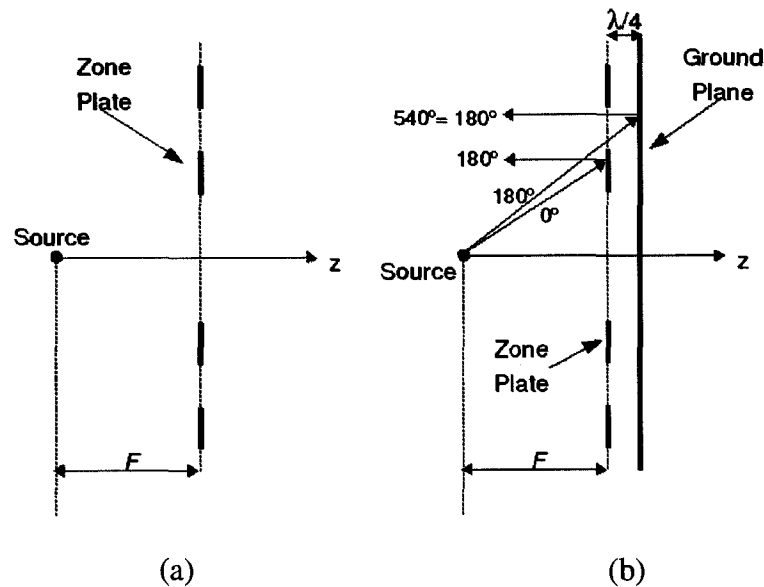


Figure 2-15: (a) Circular FZPA, (b) Reflecting FZPA

The efficiency is improved because, unlike the conventional FZPA, the reflecting FZPA makes use of the energy that reflects off the metal rings. The placement of the ground plane is important since it must cause the radiation that is reflected to be in phase with the radiation that originally reflected off the metal rings, as illustrated in Figure 2-15. The radiation that reflects off the metal rings incurs a 180° change in phase when it gets reflected. The same is true for the radiation that diffracts through the transparent rings and reflects off the ground plane. The difference, however, is that this radiation must travel a distance equal to the gap between the zone plate and the ground plane both before and after the reflection occurs. To ensure that the radiation from both parts of the lens is in phase when it reaches the focal point, the gap distance must be a quarter wavelength in order to force a second 180° phase reversal. The additional phase reversal is required because the radiation in the zones that are blocked is already 180° out of phase with the radiation from the transparent zones. In this way, the two sets of radiation will

add constructively.

Figure 2-16 illustrates the normalized simulated radiation patterns in the H-plane for both the circular FZPA and reflecting FZPAs. The directivity of the reflecting FZPA is about 27dB, which is 3dB higher than the conventional FZPA. The half-power beamwidth of the two structures was very close at about 4.3° and the maximum relative sidelobe level of the reflecting FZPA was better by nearly 5dB. The aperture efficiency of the reflecting FZPA was about 22% compared to 10% for the circular FZPA.

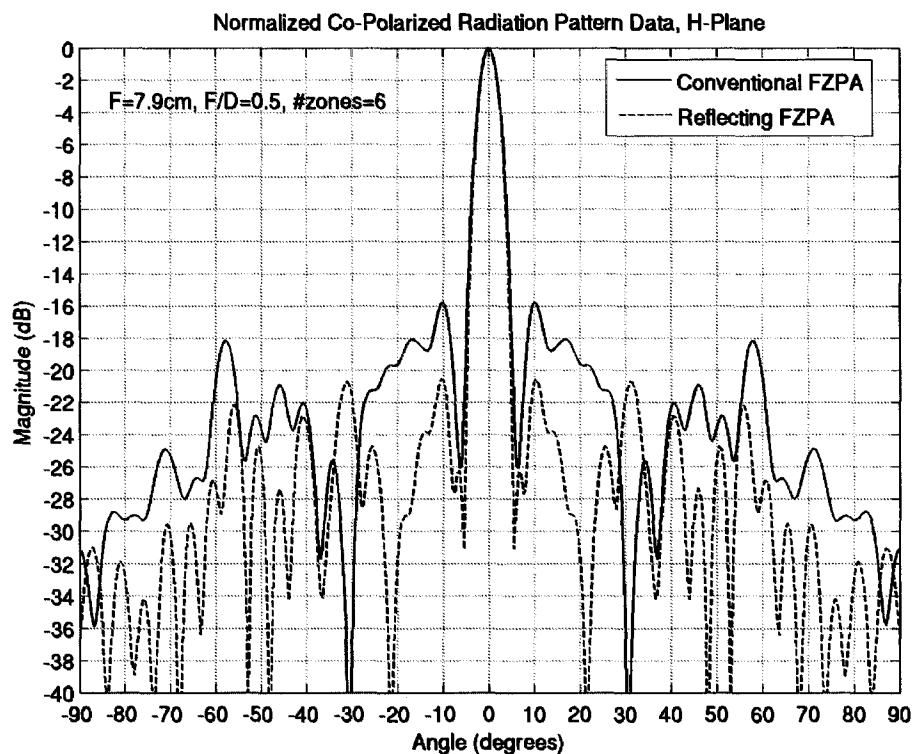


Figure 2-16: Normalized Radiation Patterns for the Reflecting and Conventional FZPAs

These results compared well with the results from [2-23] where it was reported that the aperture efficiency of a reflecting FZPA with $F/D=0.64$, $F=80\text{mm}$, $f=94\text{GHz}$ was on the

order of 20%. The reflecting FZPA directivity is therefore about a two-fold improvement over the conventional FZPA.

An interesting application for the reflecting FZPA was described by Gouker and Smith in [2-24]. They used the reflecting FZPA in an integrated circuit at 230GHz. The reflecting FZPA, as illustrated in Figure 2-17, is located on one side of the substrate and is fed by a strip dipole antenna located on the other side of the substrate at the focal point. The idea behind this structure was to create an antenna with higher gain than the dipole by itself. They experimented with different F/D geometries and found a significant range of performance characteristics. They also developed a theory for predicting the gain, beamwidth, and sidelobe levels for zone plates with focal lengths greater than $8-9\lambda$.

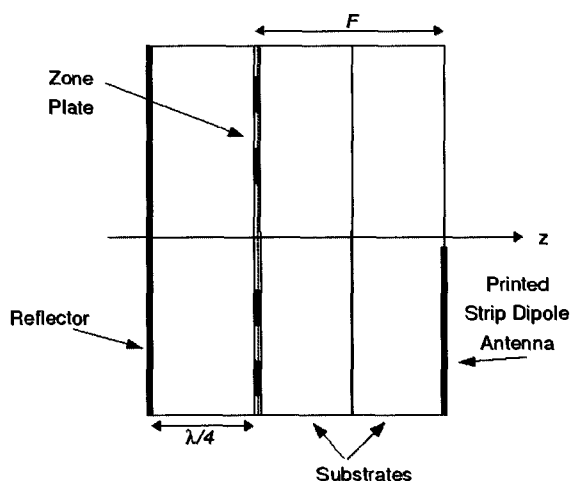


Figure 2-17: Integrated Reflecting FZPA (from [2-24])

Ji and Fujita worked on the reflecting FZPA at both 30GHz and 60GHz [2-25]. They developed an analytical model to compute the fields of the reflecting FZPA based on the scalar Kirchhoff's Diffraction Theory. They looked at the reflecting FZPA both with and without dielectric material between the lens and reflecting plate and found good agreement with the results from [2-24]. Based on their numerical results, they presented a

design procedure for the reflecting FZPA.

Guo and Barton in [2-12] showed that the sidelobe level of the reflecting FZPA was reduced in comparison with the conventional FZPA by about 5dB. They also showed that the number of full wave zones included on the antenna had a significant bearing on the sidelobe level of both the reflecting FZPA and the conventional FZPAs. As the number of zones increased, the sidelobes decreased. They found that there was a limit to how high the number of zones could be increased since more zones caused the F/D to decrease (since D is increasing), which decreased the overall antenna efficiency.

2.3.2 Layered FZPA

As a means of improving the aperture efficiency, Jiang and Zhang [2-26] proposed a double FZPA. The idea was to improve the gain of the conventional FZPA by using the second lens to compensate for, or simply to cancel, the reflection off the metal zones from the first lens. This antenna geometry consisted of two conventional FZPAs separated by a specific distance, d_o , as illustrated in Figure 2-18(a).

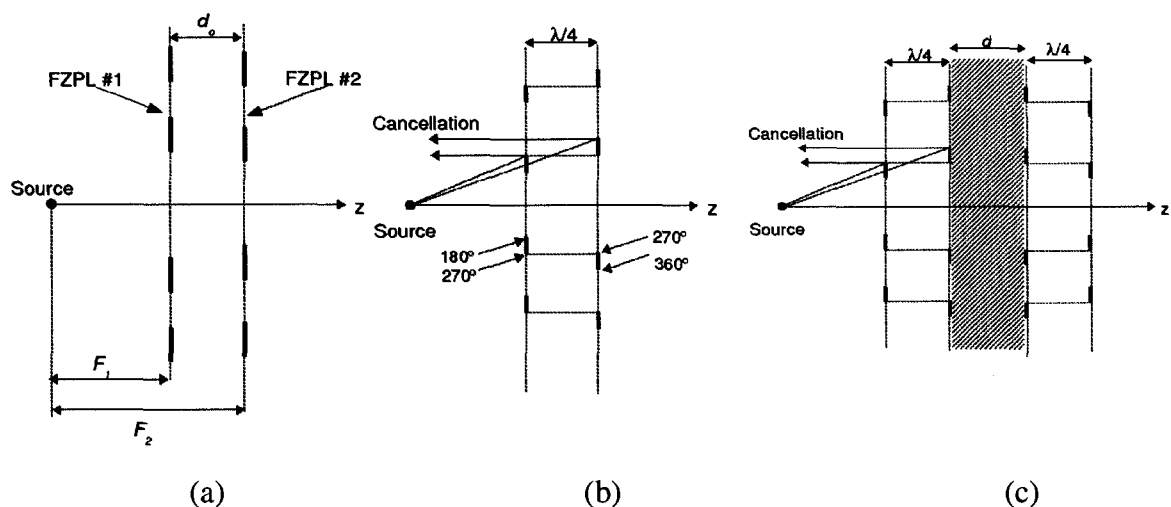


Figure 2-18: Layered FZPAs (from [2-26, 2-27])
 (a) Double Layer, (b) Enhanced Double Layer, (c) Four-Layer

Since both lenses must have the same focus, the authors defined the focal distance, F_2 , of the second lens to be:

$$F_2 = F_1 - d_o \quad (2-16)$$

where F_1 is the focal distance of the first lens. The difference in focal lengths implies that the radii of the zones in each lens will be slightly different. The authors simplified their analysis by considering only the case where the space between the lenses was air instead of dielectric to avoid reflections from the dielectric interface. By modeling the normalized scattered field at the focus, they showed that about a 2dB improvement in gain could be achieved by selecting d_o to be an odd multiple of $\lambda/4$.

Jiang and Zhang [2-27] also improved the backward radiation of the double FZPA by halving the radii of the rings on the first layer and then placing the other half on the second layer a distance $\lambda/4$ away. By doing this, the radiation will reflect as per normal off the metal rings of the first lens sub-zone with phases 180° to 270° . The radiation that reflects off the metal ring on the second layer, with phases 270° to 360° , will be exactly out of phase with the reflected radiation from the first layer. The two radiations will cancel and greatly decrease the backward radiation of the antenna. Unfortunately, the sidelobe levels were found to increase substantially in this version of the double FZPA in comparison to the conventional FZPA. This structure is shown in Figure 2-18(b).

Jiang and Zhang [2-27] further improved the performance of the double FZPA by designing a four-layered version. This structure is shown in Figure 2-18(c) and consists of two double FZPAs with improved backward radiation separated by a specific distance. Numerical results revealed a 3.1dB gain enhancement over the conventional FZPA.

However, this structure achieved improvement at the cost of an increase in size and complexity.

2.3.3 Offset FZPA

Guo and Barton were the first to propose the offset FZPA [2-28, 2-29]. They were motivated by two factors: avoiding the feed blockage present with FZPAs in reflecting mode, and enabling a non-normally directed signal to be effectively received at the antenna when it is mounted on a building wall. The offset FZPA solves both of these problems.

The zone boundaries in the offset FZPA structure are more complicated than in the conventional FZPA due to the requirement to maintain constructive interference at the focal point. The geometry is shown in Figure 2-19 where the feed is located at S , the lens is located at O , F is the focal length, and θ_o is the offset angle.

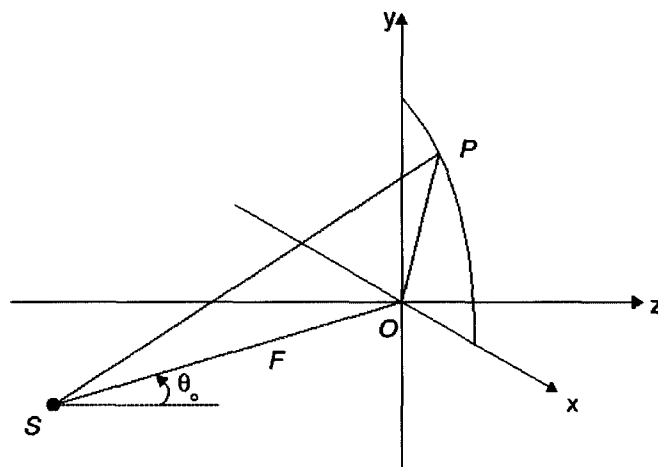


Figure 2-19: Geometry for the Offset FZPA (from [2-28])

Similar to the conventional FZPA, the shortest ray is still SO and the requirement that the

zone boundaries be separated by half wavelength path differences still holds. This results in elliptical zones. The size and center of the ellipses will vary depending on the offset angle, θ_o , and the specific zone number respectively. The bigger the offset angle, the more the ellipse center shifts down. This effect is illustrated in Figure 2-20 for a few offset values.

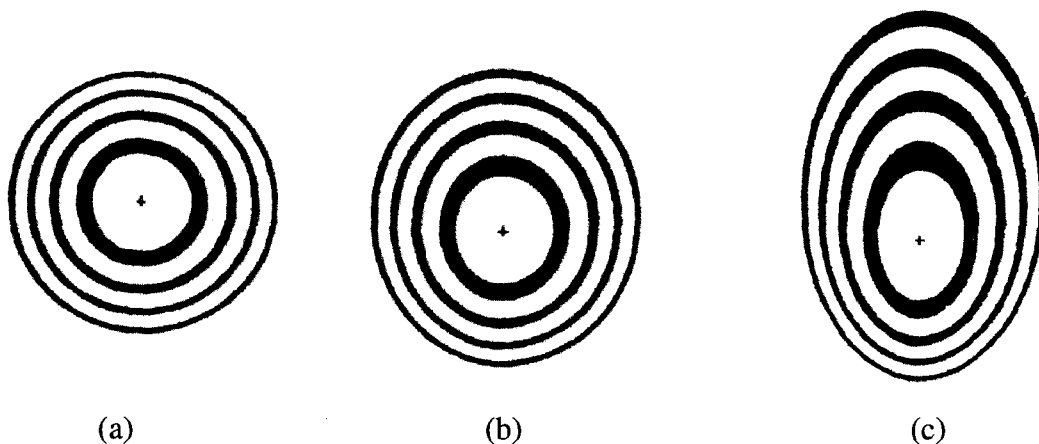


Figure 2-20: Elliptical Fresnel Zones with
(a) $\theta_o = 0^\circ$, (b) $\theta_o = 25^\circ$ and (c) $\theta_o = 50^\circ$ (from [2-28])

In [2-29], the authors presented numerical and measured results for the offset FZPA at 10.39GHz with a 20° offset angle. They showed that, if the offset angle was kept below 40° , the antenna radiation characteristics, particularly the main beam and sidelobe levels, remained constant. They extended the offset FZPA concept in [2-30] to a multilayer reflecting structure incorporating phase correction and achieved a 61% aperture efficiency.

Hoashi and Onodera [2-31, 2-32] also explored the offset FZPA. They developed an analytical model in [2-31] based on Kirchhoff's Diffraction Theory to compute the power level around the focal point for broadcast satellite applications. The receiving power at the focal point was found to be constant as long as the feed offset angle was less than 60° .

In [2-32], they looked at 90° offset angles and various focal lengths at 11.92GHz, the operating frequency for satellite TV. They measured the aperture efficiency of the offset FZPA to be around 24% which was effectively the same as the reflecting FZPA.

2.3.4 Square & Polygonal FZPA

The square FZPA was first investigated by Janecijevic in 1982 [2-33]. He studied the diffraction characteristics of the square FZPA where he considered the square FZPA as a 2D version of the linear zone plate.

Square zones were not studied again until 2004, when Gonzalez et al. compared the square geometry to the conventional circle for application in an antenna-coupled infrared-detector [2-34]. The square FZPAs were designed to have the same area as the corresponding circle according to Equation 2-17, where L_i is the half side of the square and r_i is the radius of the circle [2-34].

$$L_i = \frac{r_i \sqrt{\pi}}{2} \quad (2-17)$$

The authors in [2-34] showed experimentally that the circle performed better than the square, which confirmed their theoretical analysis. They argued that this was because the square zones did not coincide as well with the actual Fresnel zones.

In 2005, Minin et al. presented the square FZPA as a structure that would allow for a significant sidelobe level reduction [2-35]. They proposed that the square Fresnel zones could be rotated with respect to each other such that the diffraction mechanism contributed to a decrease in the sidelobe level. They showed that the amount of zone

rotation was limited to being below 15° for the zones beyond the first few, which could be rotated by about 30° . Their numerical results indicated a sidelobe level improvement of about 50% for five zones and about 40% as the number of zones increased beyond seven.

The same authors devised an improved zoning rule for the square FZPA which is shown in Equation 2-18 where, again, L_i is the half side of the square and r_i is the radius of the circular zone [2-36].

$$L_i = r_i \cos\left(\frac{\pi}{8}\right) \quad (2-18)$$

The improvement comes from the fact that the square intersects the corresponding circle in eight equally spaced locations as shown in Figure 2-21.

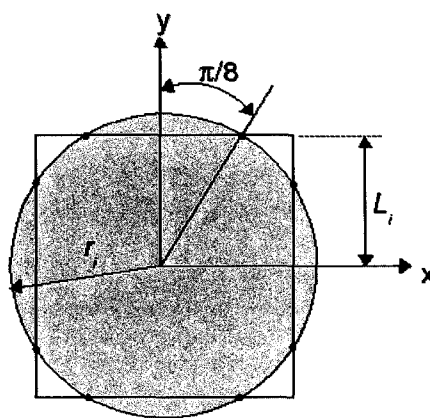


Figure 2-21: Improved Zoning Rule Geometry for Square FZPA

At 30GHz, this new zoning rule achieved a 1.2dB peak gain improvement over the standard zoning methods for the square FZPA and was shown to enhance focusing characteristics. Despite these improvements, however, the square FZPA performance was

quite poor in comparison to the conventional circular version. The gain was about 8.5dB less and the sidelobes were significantly worse. Figure 2-22 shows a normalized comparison of radiation patterns between the square and circular FZPAs in both planes using the improved zoning rule for the square. The focal distance was 3.75λ and the F/D was 0.237 in each case.

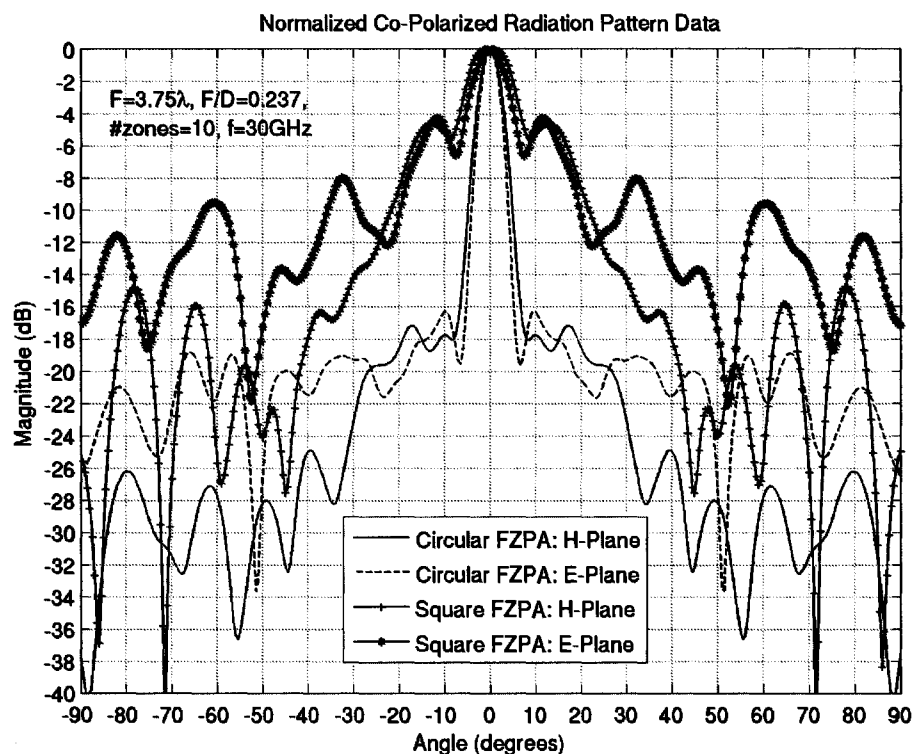


Figure 2-22: Normalized Radiation Patterns for Square FZPA and Circular FZPAs

The authors in [2-37] extended the work on the square FZPA to include polygonal shapes. They looked at octagonal and hexadecagon shapes as well and confirmed the fact that the approximation to the circular FZPA improved when the polygon has many sides. They also investigated the use of adding a dielectric phase profile, a phase screen, in front of the square FZPA to correct the phase from the square zones and improve the radiation

patterns. They found that the performance improved slightly, but the profile of the structure increased significantly.

2.4 Lens Array Antennas

Arrays of lens antennas are attractive since they enable a more compact antenna while maintaining the same overall diameter of the equivalent single lens antenna. The size reduction occurs in the depth of the antenna and is made possible by the fact that each array element can be a portion, x , of the single antenna diameter, D . This means that the diameter of the array element would be $d=D/x$. The focal distance of each array element is reduced by the same portion, $f=F/x$, in order to maintain the $F/D=f/d$ of the single lens antenna. This concept is illustrated in Figure 2-23 where the single lens diameter is divided into four array elements and the $F/D=1$.

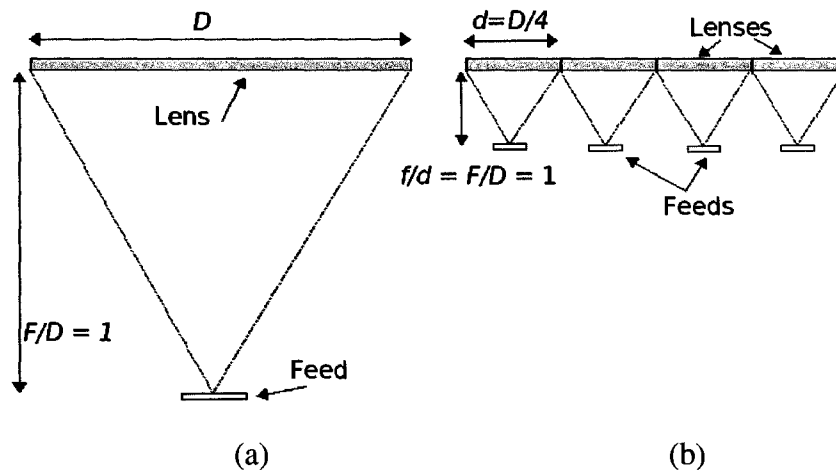


Figure 2-23: Fresnel Lens Array Depth Reduction Concept (from [2-1])
(a) Single Lens, (b) Lens Array

Arraying of lenses is used extensively at optical frequencies for imaging applications [2-8, 2-39, 2-40]. In these cases, the lens array elements are typically being used to create a series of spot beams where detectors are placed to pick up the light and create an image.

At microwave frequencies, antenna arrays are used to enhance gain by focusing the radiation of all elements to the same point. Lenses have been used in various antenna arrays over the years but these lenses are not of the Fresnel lens types discussed in this chapter. In fact, only recently has a Fresnel antenna been used as an element in an array. Petosa and Ittipiboon investigated an array of perforated dielectric phase correcting Fresnel antennas in 2004 [2-41], and in 2006, Petosa et al. designed an hexagonal shaped FZPA array [2-42].

The hexagonal FZPA geometry is an interesting candidate for an array element since hexagonal elements can be packed closer together than circular elements. This is important because FZPA elements are large, on the order of a wavelength or more, which means that some degree of element overlap is required in order to minimize grating lobes in the array. Figure 2-24 shows the array spacing for a triangular lattice when overlapping is avoided. This results in a minimum spacing of $0.5D$ between centers of elements in the vertical direction and $0.866D$ (using Pythagorean theorem) in the horizontal direction. These large element spacings will yield poor grating lobe performance. The hexagonal geometry is therefore potentially beneficial since it does not require as much overlap as the circular geometry to achieve the same element spacing. In this way, it may offer some advantages in terms of array performance.

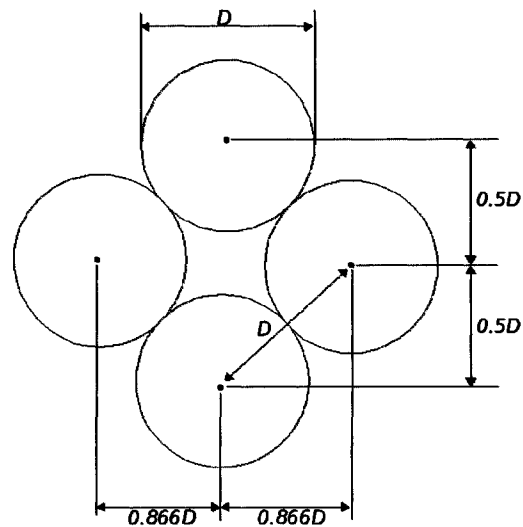


Figure 2-24: Array of Circular FZPAs (from [2-1])

The hexagonal FZPA array designed by Petosa et al. in [2-42], consisted of 2x2 single-zone elements. The authors reduced the inter-element spacing by overlapping the adjacent zones of each element as shown in Figure 2-25. The FZPA elements, printed on a Fiberglass substrate having a thickness of 0.008", were suspended above the feed network with foam spacers. The FZPA array was fed with an array of four aperture-coupled microstrip patches printed on a 0.02" thick substrate having $\epsilon_r=3.5$, which was bonded to a 0.1" thick substrate with $\epsilon_r=3.5$ containing the feed lines. The authors showed that the overall profile of the array was 2.5 times smaller than that of a single lens having an equivalent beamwidth and F/D .

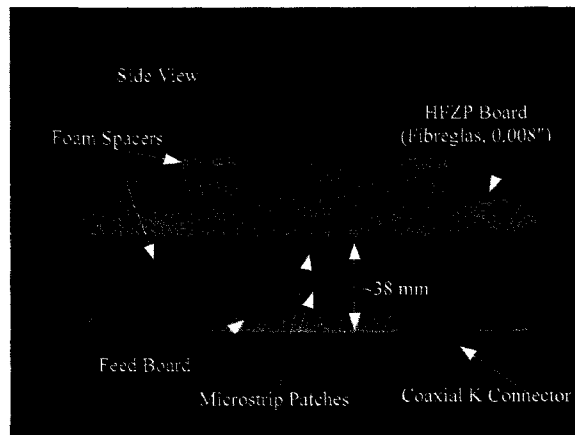


Figure 2-25: Array of Hexagonal FZPAs (from [2-42])

The physical arrangement of elements in the array is also important. The hexagonal FZPA array in Figure 2-25 has the elements arranged in a triangular lattice since the packing efficiency was higher. Another benefit of the triangular lattice is that it has better grating lobe performance than the same elements arranged in a square lattice [2-1]. This is because of the smaller element spacing.

The FZPA array, similar to any array, has added complexity that is required to handle feeding each element. Microstrip technology for a FZPA array feed structure is preferable to using horns or other feed methods due to the planar topology, which does not detract from the compactness of the FZPA array. Microstrip lines, however, exhibit significant loss in the Ka-band. This fact makes the FZPA array more attractive than the microstrip patch array since the FZPA array would have less elements for the same array area. This translates to less feed lines and junctions, which means the amount of loss in the feed lines of the FZPA array feed will be less than the equivalent microstrip patch array.

2.5 Alternate High Gain Antennas

2.5.1 Microstrip Patch Array

Microstrip patch arrays have been the leading planar technology in the microwave frequency band since the 1980s. This technology offers high gain with a very low-profile and cost effective structure. At millimeter wave frequencies, such as Ka-band, the microstrip patch array suffers from significant loss in the feed lines, which results in a low radiation efficiency. For this reason, very few microstrip patch arrays have been designed at Ka-band. In the early 1980s, however, two groups of researchers published their attempts to design effective microstrip patch arrays at Ka-band.

J.C. Williams from the Phillips Research Laboratory in England published a printed planar array at 36GHz [2-43]. This array consisted of 16x16 elements printed on a 0.8mm copper-clad polythetyene. The substrate was bonded to a 1.6mm thick sheet of aluminum to provide rigidity. The array was cross-fed with a central feed point via coaxial connector and is shown in Figure 2-26 for a 12x12 array. The array was found to provide 25dB of gain with sidelobes better than -20dB and beamwidths around 8°. The author calculated the radiation efficiency to be 60%. He also investigated a larger array, 24x24 elements, but found that the gain only increased to 26dB owing to the excessive dielectric losses.

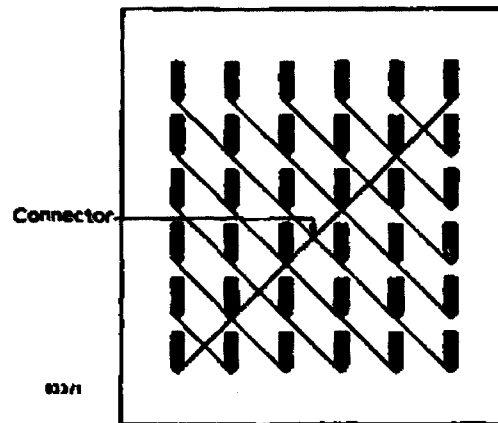


Figure 2-26: 12x12 Printed Planar Antenna (from [2-43])

M.A. Weiss from Ball Aerospace Systems in Colorado published a paper outlining his design of several millimeter wave planar printed arrays [2-44]. He first looked at a 4x4 array at 35GHz. The elements were etched on a 0.001" Teflon/fiberglass substrate having $\epsilon_r=2.2$ with a 0.0014" copper cladding. The measured array performance revealed a gain of 16dBi at 36.6GHz. The losses were estimated at 0.7dB, yielding a radiation efficiency of 77%. Weiss then investigated a 32x32 element patch array at 38GHz. The elements were printed on a 0.005" thick substrate with a 0.25" thick aluminum base. He used a -25dB Taylor sidelobe taper and in order to minimize the feed network losses he used a feed system which combined waveguide and microstrip. The final array is shown in Figure 2-27.

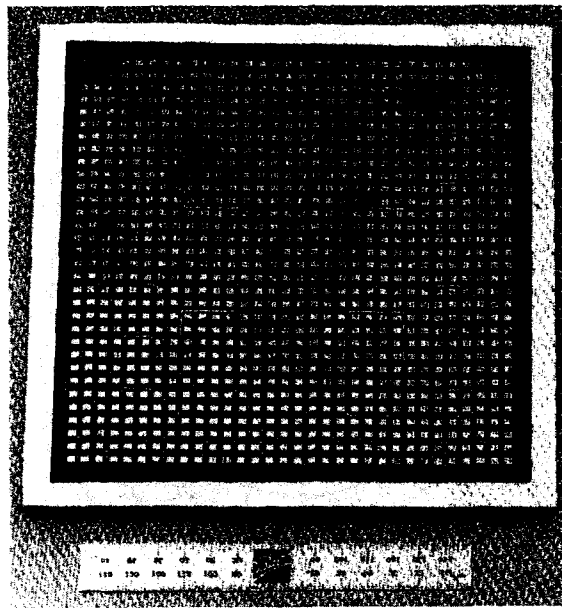


Figure 2-27: 32x32 Printed Planar Antenna (from [2-44])

Although the efficiency and array dimensions were not given, the array was found to achieve a gain of 29dBi at 38.4GHz, but the sidelobes were poor in both planes. Weiss attributed the sidelobe deterioration to the mismatches in the microstrip feed network due to substrate etching non-uniformity. This was not an uncommon finding at millimeter waves, even the slightest non-uniformity in the etching process could have serious implications at these high frequencies.

2.5.2 Planar Antenna with Partially Reflective Surface

Feresidis and Vardaxaglou designed a high gain planar antenna which utilizes a single layer partially reflective array of dipoles [2-45]. The structure they used is illustrated in Figure 2-28.

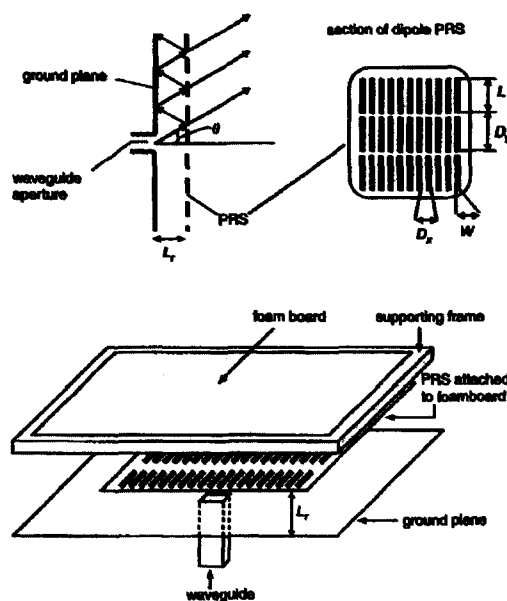


Figure 2-28: Planar Antenna with Partially Reflective Surface (from [2-45]): (Top Left) Side View, (Top Right) Partially Reflective Surface, (Bottom) Exploded View

A ground plane was placed at the aperture of an open-ended waveguide which was used as the primary antenna. A partially reflective surface was placed a distance L_r away from the waveguide to introduce a leaky wave. The basic operation of the antenna depends on the interference between the waves that emerge from the waveguide and the waves that are reflected by the reflecting surface. The waves that are transmitted through the surface determine the radiation patterns of the antenna. The interesting part of the design is how to configure the partially reflecting surface so as to achieve a desired reflection coefficient. The authors spent significant effort on this optimization before establishing the best dipole and unit cell dimensions.

Feresidis and Vardaxaglou performed both simulations and measurements on their design. The dipole surface was set at 10cm x 10cm square, L_r was set at 1mm from the waveguide, and the ground plane was set at 30cm x 30cm square. They achieved a

maximum gain of 21.9dBi and an aperture efficiency of 54% at 14.275GHz. The 3dB bandwidth was found to be only 1.2% though, which they claim could be improved by using multiple layers of partially reflecting surfaces.

2.6 Conclusion

This chapter opened with a review of basic lens theory. The basic Fresnel lens was described and shown to be different from the FZPA. The method of operation of the FZPA was outlined and basic radiation pattern characteristics were discussed. Other important concepts such as focal fields and spatial resolution were described.

The bulk of this chapter summarized the state of planar FZPA technology. The various planar FZPA structures that have been published were discussed along with their origins and their associated operation mechanisms. It was shown that the FZPA has an aperture efficiency of about 10%, but was found to be simple to fabricate and low in profile compared to dielectric Fresnel lens antennas. The reflecting FZPA and double FZPA were developed as alternatives to the conventional FZPA with improved aperture efficiencies. Unfortunately, in all cases, the increase in aperture efficiency came at the expense of increased cost, complexity and size of the antenna.

Basic Fresnel antenna array theory was presented and shown to enable much smaller focal distances than can be achieved with a single lens. This was shown to yield a smaller overall antenna package but the complexity would increase due to the requirement to feed each element in the array. The fact that the FZPA would require less elements compared to a microstrip patch array was highlighted as an advantage since the FZPA array would

have less feed line loss.

Finally, the chapter concluded by outlining two alternative low-profile, high-gain antennas. Microstrip patch arrays were very low profile but suffered from significant feed line losses at Ka-band. The partially reflective surface antenna was also fairly low-profile, but was not able to produce radiation characteristics as good as the microstrip patch array. These two technologies warrant comparison to the planar FZPA technology.

CHAPTER 3

FZPA ANALYSIS TECHNIQUES

3.1 Introduction

This chapter will outline the derivations for the analytical methods used to analyze the FZPA. These methods provide valuable insight and relatively quick approaches to finding the fields of the FZPA under certain limiting conditions.

The most accurate method, however, is to perform a full 3D numerical analysis of the structure. A brief description of the modeling tool selected for this thesis will be provided. The accuracy of the FZPA model will be verified in comparison with approximate methods and results from references in the literature which use other numerical techniques.

3.2 Huygens'-Fresnel's Principle

The Huygens'-Fresnel's principle is a combination of the work by both Huygens and Fresnel. Huygens defined a wavefront as being made up of secondary wavelets, which in turn radiate and create the next wavefront (Section 2.2.3). Fresnel furthered Huygens'

work by giving the wavelets amplitudes and directions and quantifying the interference between them. This principle is fundamental for solving wave diffraction problems.

Fresnel's formulation of the Huygens' principle yields an integral which can be used to determine the electric field at a point, P_2 , located at some distance away from a source at P_1 . Figure 3-1 illustrates these points.

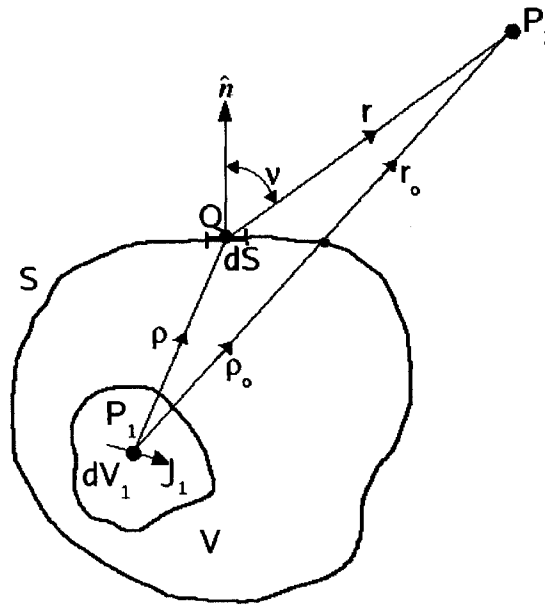


Figure 3-1: Geometry used to Derive Fresnel's Version of Huygens' Principle [2-6]

Following Huygens' principle, the source is surrounded by a closed surface, S , of arbitrary shape. The source has a current density, J_1 , in a volume dV_1 . Once the field on the surface is found, then the source can be removed. The surface is now a Huygens' source which radiates secondary wavelets. The surface is divided into small radiating elements of area, dS , each producing an elementary electric field $dE(P_2)$. The sum of these elementary electric fields yields the electric field at P_2 . This elementary electric field can be written as shown in Equation 3-1, where E_S is the amplitude of the electric field vector on the surface at point Q and Ψ_S is the phase of the electric field vector on the

surface at point Q . $I(\nu)$ is the inclination factor, which is determined by the angle between the unit normal and direction to point P_2 .

$$dE(P_2) = E_s(Q) e^{j\Psi_s(Q)} \frac{e^{-j\beta r}}{r} I(\nu) dS \quad (3-1)$$

Integrating the differential electric field from Equation 3-1 over the whole surface performs the required summation to yield the total electric field at P_2 . This result is shown in Equation 3-2.

$$E(P_2) = \iint_S E_s(Q) e^{j\Psi_s(Q)} \frac{e^{-j\beta r}}{r} I(\nu) dS \quad (3-2)$$

Fresnel simplified this expression by using a spherical surface instead of an arbitrary surface. The origin of the sphere was located at P_1 and the radius was ρ_o . This simplification meant that the surface fields at point Q , both amplitude and phase, can be replaced by the far-field component of the incident spherical wave, Equation 3-3, which is radiated from a point source at P_1 . In this expression, A_1 represents the amplitude at a distance $\rho_o=1$ from the source.

$$E_s(Q) e^{j\Psi_s(Q)} \Rightarrow A_1 \frac{e^{j\beta \rho_o}}{\rho_o} \quad (3-3)$$

The total electric field at P_2 can now be written as shown in Equation 3-4. This is the final result of the Huygens'-Fresnel's Principle.

$$E(P_2) = A_1 \iint_S \left[\frac{e^{j\beta \rho_o}}{\rho_o r} I(\nu) \right] dS \quad (3-4)$$

3.3 Scalar Kirchhoff's Diffraction Theory

Gustav Kirchhoff later developed an alternative approximate diffraction method to determine the total electric field at P_2 . This method is very similar to the Huygens'-Fresnel's principle, but gives a more accurate meaning to the inclination factor. The scalar Kirchhoff's Diffraction Theory outlined in this section follows [2-6] and assumes that all diffracted fields are of the same polarization.

Equation 3-5 was derived from the Helmholtz wave equation and the second Green theorem. In this equation, $E(P_2)$ is the scalar component of the electric field at P_2 , $E(Q)$ is the component of the electric field at point Q on the surface, $\Phi(r)$ is the spherical wave function, and n is along the direction of the unit vector \hat{n} which is normal to the surface element dS .

$$E(P_2) = \frac{1}{4\pi} \iint_s \left[\Phi(r) \frac{\partial E(Q)}{\partial n} - E(Q) \frac{\partial \Phi(r)}{\partial n} \right] dS \quad (3-5)$$

where $\Phi(r) = e^{\frac{-j\beta r}{r}}$

This equation was based on the geometry shown in Figure 3-2 which is very similar to Figure 3-1 except that there is an open portion of the surface, S_o . The remainder of the surface, S_c , is closed or screened.

$$\text{On } S_c: \quad E(Q)=0$$

$$\frac{\partial E(Q)}{\partial n}=0$$

$$\text{On } S_o: \quad E(Q)=E_i(Q)$$

$$\frac{\partial E(Q)}{\partial n}=\frac{\partial E_i(Q)}{\partial n} \quad (3-7)$$

$$\text{where} \quad E_i(Q)=A_1 \frac{e^{-j\beta\rho}}{\rho}$$

In these equations, E_i is the incident spherical wave radiated by a source at P_1 , $\rho \gg \lambda$, and Q is a point in the far field of P_1 . These boundary conditions are intuitive. The fields are set to zero on the screened portion since they are considered to be ideally absorbed inside the screen. The fields over the aperture (i.e. the opening) are set to what they would be if the screen was not present. The first condition means that the screened portion of the surface can be neglected in the integration, and the second condition allows for the disturbance incident on the aperture to be determined by considering only the portion of the integration surface lying within the aperture itself [3-1]. These boundary conditions are the primary source of the approximation in this method. In reality, the screen will inevitably have an effect on the fields in the aperture and the screen could never be perfect, which implies that there will be fields behind the screen. Kirchhoff's basis for these assumptions are that, if the aperture size was large compared to the wavelength, then the assumptions would become more valid.

Equation 3-5 can be simplified since the gradient of $E(Q)$ is in the direction of $\hat{\rho}$. This simplification is shown in Equation 3-8(a) & (b) which yields the relation in Equation 3-8(c) where the $1/\rho$ term is neglected compared to $\beta=2\pi/\lambda$.

$$\frac{\partial E_i(Q)}{\partial n} = \frac{\partial E_i(Q)}{\partial \rho} \cos(n, \rho) \quad (a)$$

$$\frac{\partial E_i(Q)}{\partial n} = -A_1 \frac{e^{-j\beta\rho}}{\rho} \left(j\beta + \frac{1}{\rho}\right) \cos(n, \rho) \quad (b) \quad (3-8)$$

$$\frac{\partial E_i(Q)}{\partial n} \approx -j\beta A_1 \frac{e^{-j\beta\rho}}{\rho} \cos(n, \rho) \quad (c)$$

The second derivative in Equation 3-5 is simplified in a similar manner resulting in Equation 3-9. In this equation, r is much larger than the wavelength and the size of the aperture.

$$\frac{\partial \Phi(r)}{\partial n} = \frac{\partial}{\partial n} \left(\frac{e^{-j\beta r}}{r} \right) \approx -j\beta \frac{e^{-j\beta r}}{r} \cos(n, r) \quad (3-9)$$

After simplifying the derivatives in Equation 3-5, the resulting scalar diffraction integral becomes:

$$E(P_2) = \frac{j}{2\lambda} A_1 \iint_S \left[\frac{e^{-j\beta(\rho+r)}}{\rho r} [\cos(n, \rho) - \cos(n, r)] \right] dS \quad (3-10)$$

Comparing this equation with Equation 3-4 reveals that the inclination factor comprises the cosine terms.

$$I(v) \approx (\cos(n, \rho) - \cos(n, r)) \quad (3-11)$$

However, the cosine terms can be rewritten to be more related to the angles in Figure 3-2. There are two angles of particular interest, v' and v . v' is the angle between the normal unit vector, \hat{n} , and the radial unit vector $\hat{\rho}$. v is the angle between the normal unit vector, \hat{n} and the unit vector in direction of P_2 , \hat{r} . Equation 3-12 shows how using these angles simplifies the cosine terms and thus more clearly defines the inclination factor.

$$\text{Let : } \cos(n, r) = \cos(\pi - \nu) = -\cos(\nu)$$

$$\text{Let : } \cos(n, \rho) = \cos(\nu')$$
(3-12)

$$\text{Therefore : } I(\nu, \nu') = \frac{1}{2}(\cos \nu' + \cos \nu)$$

Equation 3-10 can be re-written as shown in Equation 3-13 which now has a format very similar to Equation (3-4):

$$E(P_2) = \frac{j}{2\lambda} A_1 \iint_S \left[\frac{e^{-j\beta(\rho+r)}}{\rho r} I(\nu, \nu') \right] dS$$
(3-13)

This is the final expression of the scalar Kirchhoff's Diffraction Theory. As was done in Section 3.2, a further simplification could be made if the surface of integration were chosen to be a sphere with radius ρ_o . From Figure 3-2, it can be seen that by using a sphere, the unit normal and radial unit vector are in the same direction thus making $\nu' = 0$ and $\cos \nu' = 1$. This simplifies the inclination factor and provides more insight into the appearance of the Huygens' source radiation pattern.

Equation 3-13 can be interpreted as meaning that the field at P_2 is comprised of the summation of all the fictitious secondary point sources located within the aperture [3-1]. These point sources have amplitudes and phases which depend on the source wavefront and also the angles for which the wavefront arrives and is observed. Specifically, the secondary source at P_2 has a complex amplitude which is related to the excitation at P_1 . Also, the amplitude is inversely proportional to the wavelength, the phase leads the phase of the incident wave by 90° , and the secondary source has a directivity pattern associated with the inclination factor [3-1].

To apply this method to the FZPA, the scalar Kirchhoff's Diffraction Theory integral must be modified to accommodate an annular slot aperture with inner and outer radii. The geometry for this special case is illustrated in Figure 3-3 where the focus is located on the z -axis.

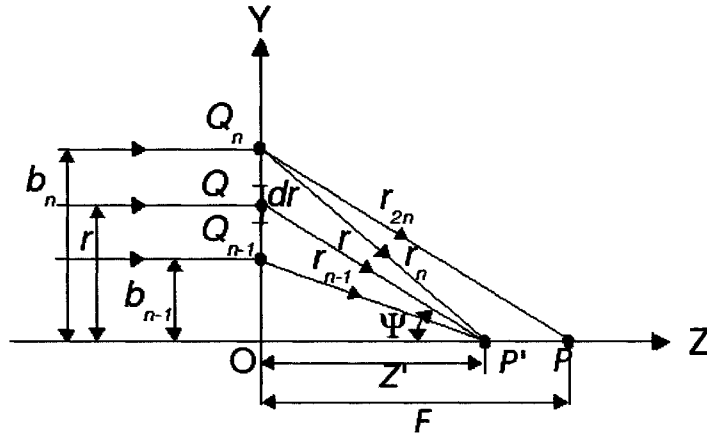


Figure 3-3: Geometry of FZPA for Scalar Kirchhoff's Diffraction (from [2-6])

The derivation for the diffraction equation is outlined in [2-6] and the final form is shown in Equation 3-14 where E_o is the field of the incident plane wave, z is the distance from the lens along the z -axis, b_n is the n th Fresnel zone radius and r_n is the length of the ray that goes from the n th zone to the peripheral focus, P' . The peripheral focus is different from the paraxial focus, P , because of spherical aberrations inherent with the lens [2-6]. This equation assumes a normally incident plane wave.

$$E(z) = \sum_n \frac{j\pi}{\lambda} E_o(P) \int_{r_{n-1}}^{r_n} \left(1 + \frac{z}{r}\right) e^{-j\beta r} dr \quad (3-14)$$

$$\text{where: } r_n = \sqrt{z^2 + b_n^2}$$

The power of the scalar Kirchhoff's Diffraction Theory integral is that it allows diffraction problems to be solved without paying attention to the physical details of

exactly what is happening at the aperture. The use of the method, however, is limited since it is not accurate for observation points that are further from the aperture than about a wavelength.

3.4 Vectorial Kirchhoff's Diffraction Theory

At radio wave frequencies, the polarization of the diffracted fields is important and must be taken into account. To that end, the scalar Kirchhoff's Diffraction Theory equation from Section 3.3 must be modified to include vectors. Equation 3-4 is re-written to show the vectors.

$$\mathbf{E}(P_2) = \frac{1}{4\pi} \iint_S \left[\Phi(r) \frac{\partial \mathbf{E}(Q)}{\partial n} - \mathbf{E}(Q) \frac{\partial \Phi(r)}{\partial n} \right] dS \quad (3-15)$$

This equation is only valid for the rectangular coordinate system and it is now only applicable to a closed surface of integration that bounds a space without a source. When an aperture is present, the equation must be modified to include two line integrals around the edge of the aperture which has a length, L [2-6]. These changes are shown in Equation 3-16.

$$\begin{aligned} \mathbf{E}(P_2) = & \frac{1}{4\pi} \iint_S \left[\Phi(r) \frac{\partial \mathbf{E}(Q)}{\partial n} - \mathbf{E}(Q) \frac{\partial \Phi(r)}{\partial n} \right] dS \\ & + \frac{j}{4\pi\epsilon_0} \oint_L \nabla \Phi(r) \mathbf{H} dl' - \frac{1}{4\pi} \oint_L \Phi(r) \mathbf{E} dl' \end{aligned} \quad (3-16)$$

This represents the vectorial Kirchhoff's Diffraction Theory. It completely satisfies Maxwell's equations, but is far more complicated to solve analytically than the scalar version.

3.5 Finite-Difference Time-Domain (FDTD) Method

Since it is a complex matter to solve the vectorial Kirchhoff's Diffraction Theory equation, numerical modeling is required. There are many techniques available to perform this modeling, all with varying degrees of accuracy. The modeling technique used in this thesis was the 3D FDTD method. The method solves the space and time partial derivatives of the time dependent Maxwell's equations by discretizing the equations and using a central difference approximation. The equations are solved in a leap-frog type manner according to Yee's algorithm [3-2]. In other words, the electric field vector of a certain volume of space is solved at a particular instant in time, then the same thing is done for the magnetic field vector but at the next instant in time. The process repeats itself throughout the entire volume and time until the desired electromagnetic behavior is reached.

The commercial software, Empire [3-3], was chosen as a cost effective tool to perform the FDTD computation on the FZPAs in this work. Although the software's ability to correctly model the FZPAs is continually verified through comparison with experimental measurements, it was important to first establish how well the model performed in comparison with other models in the literature as well as with the scalar Kirchhoff's Diffraction Theory model. For this purpose, two papers were chosen to perform a comparison.

In [3-4] the authors compared the scalar Kirchhoff's Diffraction Theory result to their 3D method of moments (MoM) model. The MoM is different from the FDTD method in that it solves a direct boundary integral equation by breaking the integral down into a set of

linear algebraic equations. The authors in [3-4] computed the relative focal field intensity along the z-axis from the FZPA. They used a FZPA with a focal distance of 5cm and 10 zones at a frequency of 11.92GHz. Their computed MoM data was extracted from the paper and overlaid with Empire FDTD method simulated results for the same lens. The resulting focal field intensity curves are shown in Figure 3-4 where the lens is located at $z=0\text{cm}$. The Empire FDTD predicted a higher intensity at the focus, but the overall curve shape was similar.

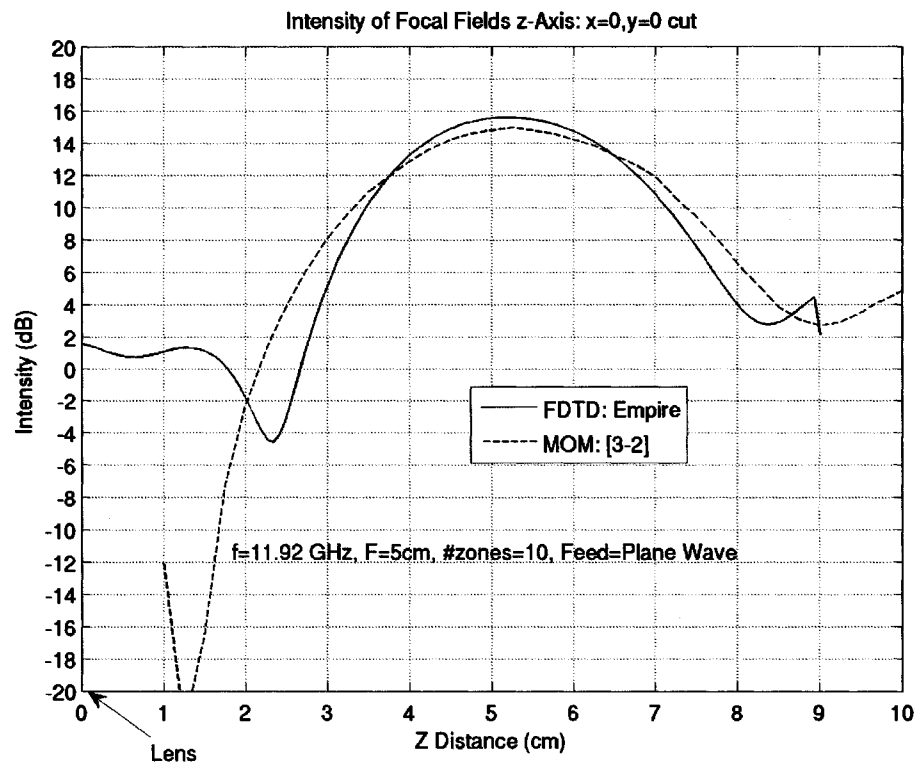


Figure 3-4: Focal Field Intensity Comparison Between Methods

In [3-5] the authors analyzed the conventional FZPA using a body-of-revolution (BOR) FDTD approach. The benefit of the BOR-FDTD method is that it exploits the rotational symmetry of the FZPAs to reduce the computation time. They compared their results to the approximate scalar Kirchhoff's Diffraction Theory (KDT). Their results showed how

the accuracy of the approximate theories was dependent on the focal lengths used. The focusing gain of the approximate theories diverged from the BOR-FDTD method and overestimated the focusing gain when the F/D became small. This made sense because the paraxial approximation does not apply in these cases. Also, the scalar Kirchhoff's Diffraction Theory approximation depends on the assumption that the incident field is reflected unperturbed by the metal zones, a fact which loses accuracy as the zones become closer together when the F/D decreases.

Figure 3-5 illustrates three cases modeled in Empire that were also modeled in [3-5] using the BOR-FDTD method at 30GHz. The focal distance was set at 3λ and the number of zones was decreased from 14 to 4. The focal field intensity was observed in order to determine the peak intensity for comparison with [3-5]. Table 3-1 summarizes the results for Empire FDTD, BOR-FDTD, and the scalar Kirchhoff's Diffraction Theory.

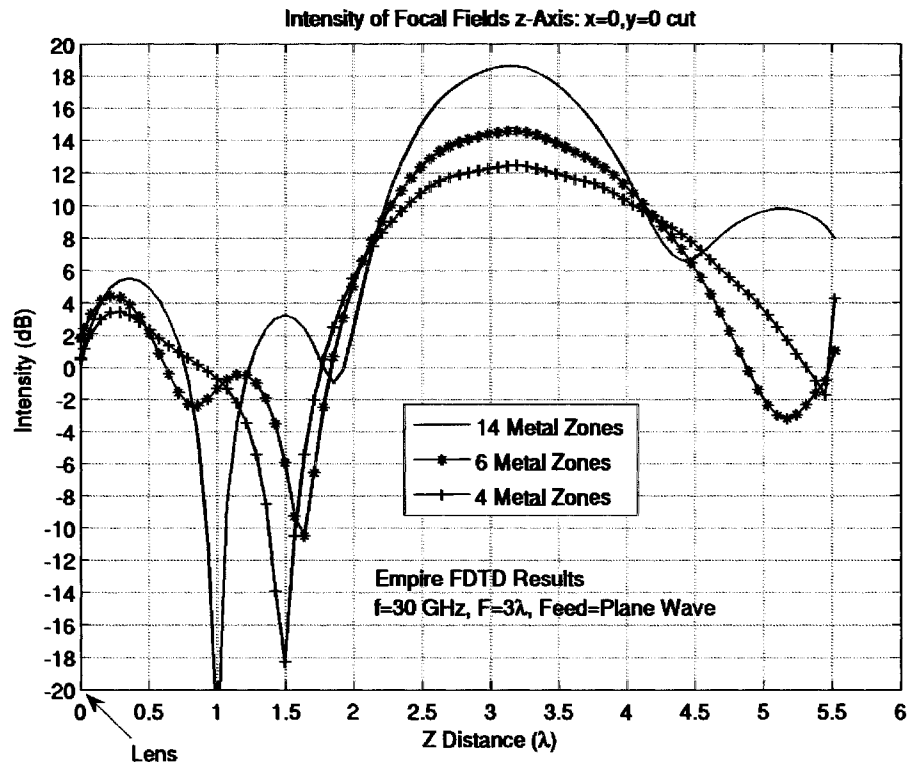


Figure 3-5: Focal Field Intensity Comparison Between Methods

# Metal Zones	Diameter (cm)	F/D	Peak Intensity Empire FDTD (dB)	Peak Intensity BOR-FDTD [3-5] (dB)	Peak Intensity Scalar KDT (Eqn.3-14) (dB)
14	19.08	0.157	18.62	18.75	21.64
6	10.40	0.288	14.55	14.50	16.50
4	8.00	0.375	12.44	12.50	11.20

Table 3-1: Comparison of Results Between Empire and [3-5]

These results showed very good agreement between the two FDTD models for all F/D cases. As expected, the scalar Kirchhoff's Diffraction Theory results were not as accurate for the smaller F/D cases (i.e. $F/D=0.157$ and 0.288) and generally overestimated the peak intensity in these cases.

3.6 Conclusion

This chapter began by highlighting the development of the approximate Kirchhoff's Diffraction Theory for computing the fields of FZPAs. The method was shown to be derived from Huygens' principle and was highly influenced by Fresnel before being completed by Kirchhoff. The scalar approach was shown to provide a good approximation for large F/D cases, but not for small F/D cases. Full 3D EM analysis remains the only sure method to accurately model FZPAs with small F/D configurations.

The FZPA models in the commercial FDTD software tool, Empire, were verified against other published methods and shown to provide accurate results. Also, as will be shown in future chapters, measurement results have also verified the accuracy of the FZPA simulation model. Empire was thus chosen for all modeling in this thesis unless stated otherwise.

CHAPTER 4

OPTIMAL REFERENCE PHASE

4.1 Introduction

A recent paper by Minin et al. [4-1] highlighted the existence of a free parameter in the design of FZPAs. This parameter is the reference phase (originally introduced in [4-2]) and, when properly chosen, was shown to improve certain aspects of antenna performance. The reference phase work in [4-1] was based on a single F/D case at 39GHz. Also, their results were derived using geometrical optics, scalar Kirchhoff's Diffraction Theory, and experimental verification.

In this chapter, the findings from [4-1] will be expanded upon by using FDTD simulation software to systematically vary the reference phase for several different F/D cases [4-3]. The antennas were analyzed to determine how the peak directivity, 3dB beamwidth, sidelobe level, and maximum cross-polarization levels changed with varying reference phase. Measurements were also carried out on various circular FZPA prototypes to verify the simulation results. Typical measured radiation patterns of the prototypes will be

shown along with a summary of their performance. A comparison between the measured and simulated results will also be presented and discussed.

4.2 Reference Phase Formulation

Though fundamentally the same, reference phase in this thesis is defined slightly differently than in [4-1]. This work deals with the specific case of a Fresnel zone plate used as an antenna. That is, it creates a plane wave in the far field in transmit mode with a source such as a waveguide placed at its focal point. The more general treatment in [4-1] involved spherical waves from an arbitrary point source on one side of the lens being focused to an arbitrary point on the other side of the lens. The two cases become the same when the arbitrary focus point in the general case is moved to infinity.

Consider again the lens geometry from Section 2.2.6, which is redrawn in Figure 4-1 to specifically indicate the phase. As described previously, the fields from the source travel varying distances before reaching the lens surface. The shortest distance traveled is F with all other paths being longer by δ_i , the path difference. The phase of the shortest path is ϕ_o and the fields that hit any point on the lens surface will have a radius, r_i , and a phase ϕ_i .

Historically, the radius of the first zone was chosen such that the phase difference, $\phi_i - \phi_o$, was 180° . This decision was made to simplify calculations and ensure that the out-of-phase waves from 180° to 360° were blocked in order to achieve constructive interference in the far field. However, this phase difference does not have to be 180° and can actually be any value between 0° and 180° . Phases between 180° and 360° are the dual

of the 0° to 180° cases wherein the opaque and transparent regions are simply inverted.

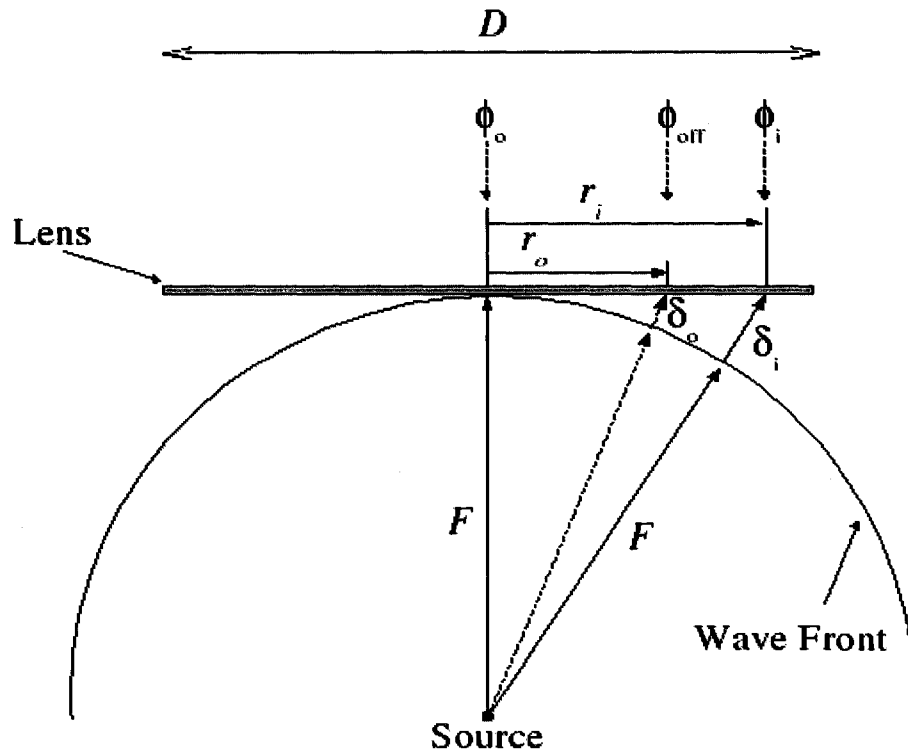


Figure 4-1: Lens Antenna Diagram Showing Phase Offset

Changing the phase difference between ϕ_i and ϕ_o creates a new first zone with radius r_o and offset phase ϕ_{off} , as illustrated in Figure 4-1. This causes a shift in the phase of all the other zone radii by the amount of the phase offset since ϕ_i , now the phase of the second zone, must be 180° from ϕ_{off} and the phase of the third zone is 180° from the second zone, and so on for the other zones. The creation of the new zone can be thought of as a form of phase correction because, instead of allowing the phase difference (or error) to reach 180° , it is corrected at a value less than 180° while still maintaining constructive interference in the far field. Equation 4-1(a) shows how the phase offset is included in the standard phase difference expression.

$$\begin{aligned}
(\phi_i - \phi_o) &= i\pi + \phi_{off} \quad i=1,2,\dots,N & (a) \\
\text{Let: } \Phi_o &= \phi_o + \phi_{off} & (b) \\
\text{Therefore: } (\phi_i - \Phi_o) &= i\pi \quad i=1,2,\dots,N & (c)
\end{aligned}
\tag{4-1}$$

As a simplifying measure, the sum of ϕ_o and ϕ_{off} will be represented by Φ_o which is defined as the reference phase and is expressed mathematically in Equation 4-1(b). Since ϕ_o is typically chosen to be 0° , the reference phase becomes equal to the offset phase. Substituting the reference phase into Equation 4-1(a) yields Equation 4-1(c).

Antenna designs take this parameter into account by including it in the computation of the Fresnel zone radii. The derivation of this new expression begins with an analysis of the trigonometry in Figure 4-1. Equation 4-2 is a rearrangement of Equation 2-1 from Section 2.2.4.

$$r_i^2 + F^2 = (F + \delta_i)^2 \tag{4-2}$$

Recognizing that ϕ_i is actually the electrical length of δ_i , then Equation 4-3 is simply another version of Equation 4-1(c).

$$\begin{aligned}
\frac{2\pi}{\lambda} \delta_i &= \phi_i = i\pi + \Phi_o \\
\text{Therefore: } \delta_i &= \frac{\lambda}{2\pi} (i\pi + \Phi_o)
\end{aligned}
\tag{4-3}$$

Substituting δ_i from Equation 4-3 into Equation 4-2 yields the result of Equation 4-4, which is the final expression for zone radii when reference phase is included. The zone index begins at zero instead of one in this case in order to include the additional zone. Careful inspection of Equation 4-4 confirms that increasing the reference phase causes the radii of the Fresnel zones to increase and hence the overall diameter of the lens also

increases.

$$r_i = \sqrt{\left[F + \frac{\lambda_o}{2\pi} (i\pi + \Phi_o) \right]^2 - F^2} \quad i=0,1,2,3,\dots,N \quad (4-4)$$

It can be shown that, if $\Phi_o=0^\circ$, the familiar expression of Equation 4-5 results with $r_o=0$. This expression was derived in Section 2.2.6 as Equation 2-5 with $P=2$ for 180° phase sub-zones.

$$r_i = \sqrt{\left(F + i \frac{\lambda_o}{2} \right)^2 - F^2} \quad i=0,1,2,3,\dots,N \quad (4-5)$$

The realization that the reference phase can be chosen to be any value between 0° and 180° is significant since it provides designers with another parameter to control and adjust antenna performance. In the specific case outlined in [4-1], it was shown that the peak-to-sidelobe-ratio is maximized and the gain is optimum for non-standard reference phases.

4.3 Simulated Reference Phase Results

4.3.1 Simulation Parameters

Simulations in this work were performed at 30GHz and the circular FZPAs were modeled with perfectly conducting metal for the opaque zones. The lens parameters for each F/D simulation are shown in Table 4-1. Each one was analyzed with the following nine different reference phases: $\Phi_o = 0^\circ, 30^\circ, 45^\circ, 60^\circ, 75^\circ, 90^\circ, 120^\circ, 150^\circ, 180^\circ$. The number of zones was kept constant with increasing reference phase, which meant that the radii of the zones was increasing slightly. The radii of the Fresnel zones in each case

were computed using Equation 4-4.

Nominal F/D	F (cm)	D (cm) Desired	D (cm) Actual	# Total Zones
0.237	3.75	15.8	15.05	10
0.35	5.53	15.8	15.49	8
0.5	7.9	15.8	15.02	6
1.0	15.8	15.8	16.39	4

Table 4-1: Simulation Parameters for each F/D in the $\Phi_o = 0^\circ$ Case

Since it was desirable to have a consistent aperture size for comparison purposes, the lens diameters were chosen to be as close to 15.8cm as possible for the $\Phi_o = 0^\circ$ case, while still maintaining an integer number of zones. This meant that careful consideration of the number of zones was required for each F/D to match the desired diameter of the last zone. This resulted in actual lens diameters that were not exactly 15.8cm as shown in Table 4-1 for the $\Phi_o = 0^\circ$ case. Since the radii increased with an increase in the reference phase, the F/D inherently decreased by a small amount as Φ_o changed from 0° to 180° . This was found to have very little effect on the antenna performance.

The lenses were fed with an open-ended WR28 waveguide placed at their focal point. The waveguide was oriented such that the electric field vector was along the y-axis as indicated by the coordinate system in Figure 4-2. Radiation patterns of the isolated feed were simulated and shown to have a peak directivity of about 7dB with 10dB beamwidths of 120° in the H-plane and 194° in the E-plane. Despite the inherently

unequal H- and E-plane patterns, this feed was well suited to achieving the required 10dB edge taper for an F/D of 0.237. The 10dB edge taper is commonly used as a compromise between spillover and taper illumination for the parabolic reflector and is also a good compromise for the FZPA. It was shown in [2-13] that the optimum edge taper for the FZPA is 12dB. Also, the open-ended waveguide was chosen since it would be used as the feed for the prototype lenses.

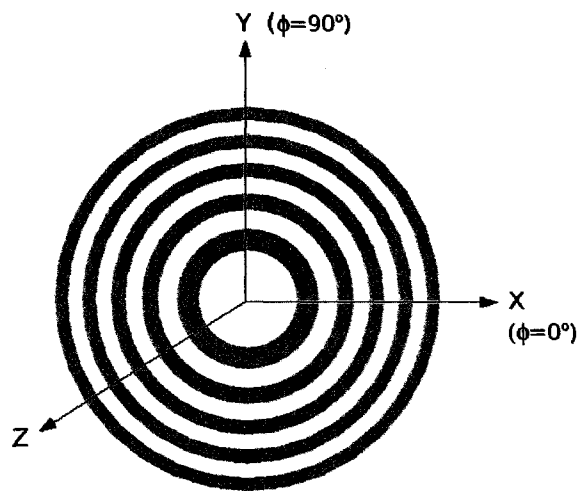


Figure 4-2: Front View of Circular FZPA

4.3.2 Simulation Results

Preliminary simulation results and expectations based on the findings in [4-1] indicated that the following antenna parameters would be affected by varying the reference phase:

- Peak Directivity
- Sidelobe (SLB) Level
- Half-Power Beamwidth (BW)
- Maximum Cross-Polarization

Figures 4-3 and 4-4 illustrate how typical co-polarized radiation patterns in the H- and

E-planes vary with reference phase in the $F/D=0.237$ case. In order to accentuate the inner sidelobes in these figures, the angle range is limited to the first 50° from boresight. As the reference phase increased from $\Phi_o = 0^\circ$ up to 180° , the radiation pattern changed shape and dropped in level. The discussion that follows will give a more detailed analysis on the effect of reference phase for the four different antenna configurations listed in Table 4-1.

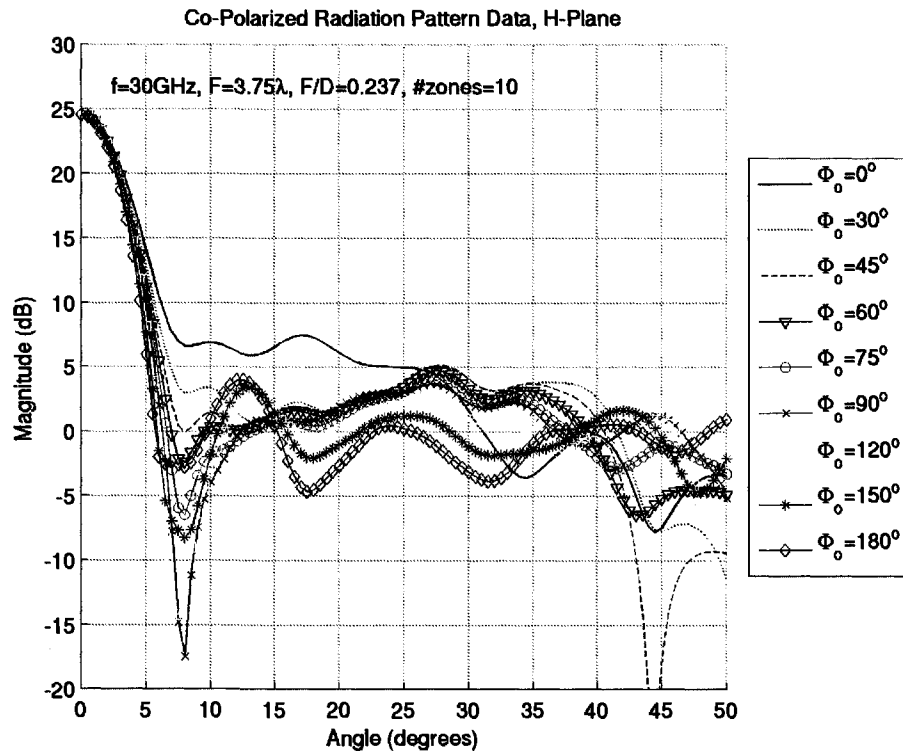


Figure 4-3: Typical Radiation Patterns with Varying Reference Phase, H-Plane

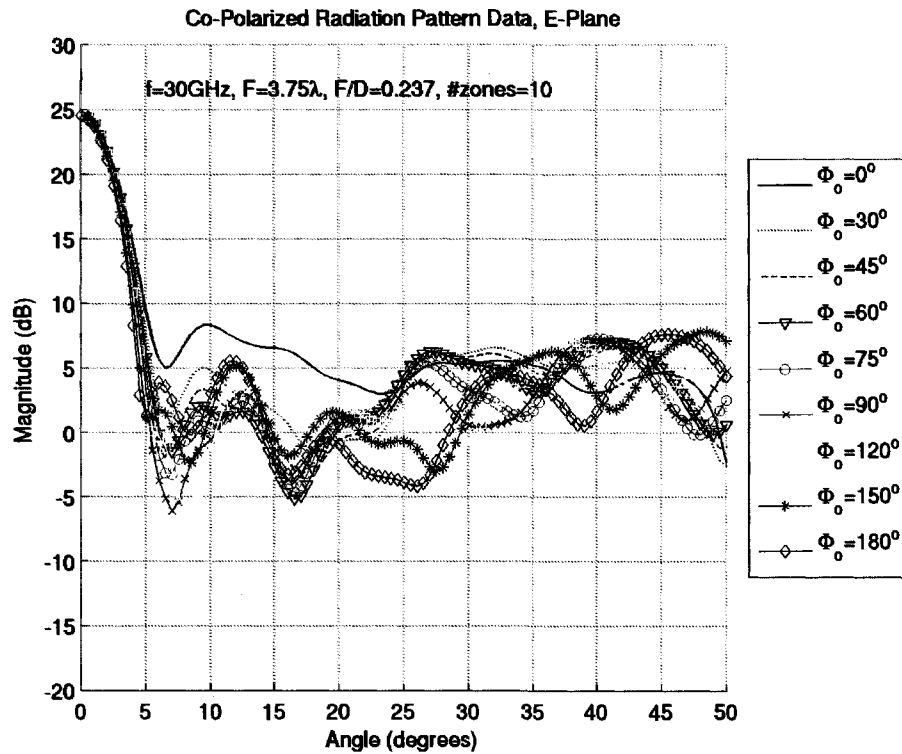


Figure 4-4: Typical Radiation Patterns with Varying Reference Phase, E-Plane

4.3.2.1 Peak Directivity

The simulated peak directivity was confirmed to occur at the designed center frequency of 30GHz for the smaller F/D cases (0.237, 0.35). This was not true for the larger F/D cases, however, where the frequency of the peak directivity was observed to shift closer to 31GHz. This increase in antenna center frequency was likely related to the feed not being as optimal for the lens in the larger F/D cases (0.5, 1.0). The feed was designed to be optimal for the $F/D=0.237$ case so that when the F/D was increased, the feed's 10dB beamwidth was much larger than that required for the 10dB edge taper and therefore significant spillover resulted.

The normalized peak directivity for each F/D case is shown in Figure 4-5. The curves

were normalized to the peak of the $\Phi_o = 0^\circ$ case to compensate for the feed not being optimal in the larger F/D cases. The variation of the peak directivity with reference phase was related to the fact that changing the reference phase altered the diffraction pattern of the lens in a complex fashion. This caused the sidelobes to shift and change in level, thus impacting the peak gain.

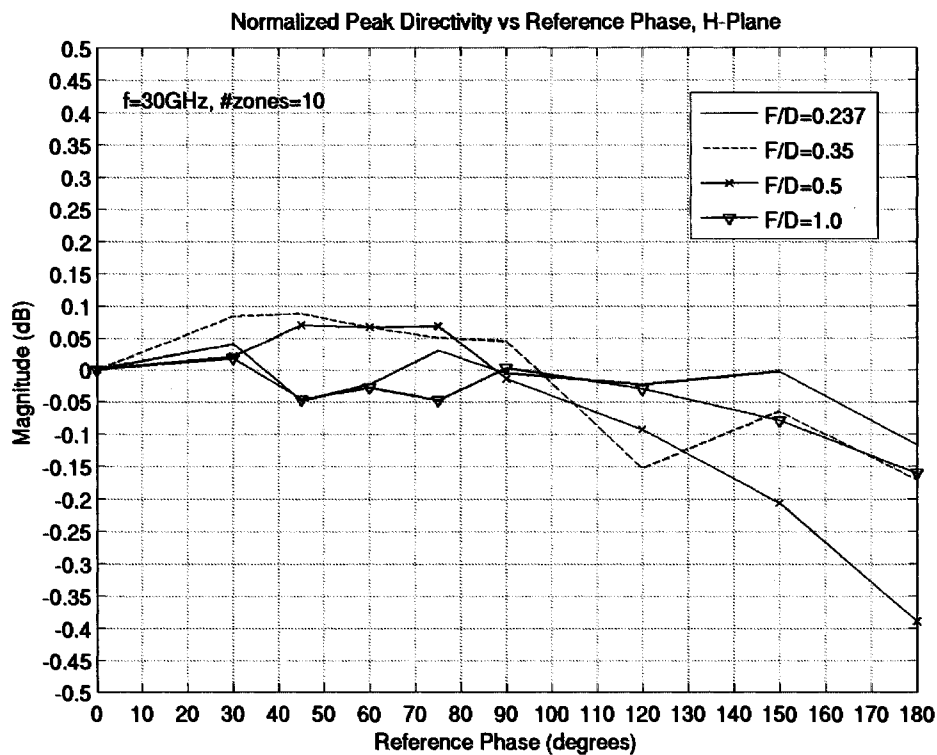


Figure 4-5: Normalized Peak Directivity vs. Reference Phase

The curves of Figure 4-5 demonstrate that the average change in peak directivity was 0.23dB as the reference phase increased from 0° to 180° . This meant that the reference phase had very little effect on the peak directivity. The gain was also computed from these results based on the simulated losses in the structure, which include material loss, mismatch loss at the excitation port, and loss due to surface resistance. It was found that

there was a 2.45dB difference between the directivity and gain for the $F/D=0.237$ case. This difference dropped to 1.23dB for the $F/D=1.0$ case.

4.3.2.2 First Sidelobe Level

The level of the first sidelobe was affected significantly by the change in reference phase. Figures 4-6 and 4-7 illustrate the first sidelobe trends for the H- and E-planes respectively, where the curves in both figures are relative to the peak directivity. The sidelobe levels were generally better for the smaller F/D values. This was particularly true when the reference phase was 0° .

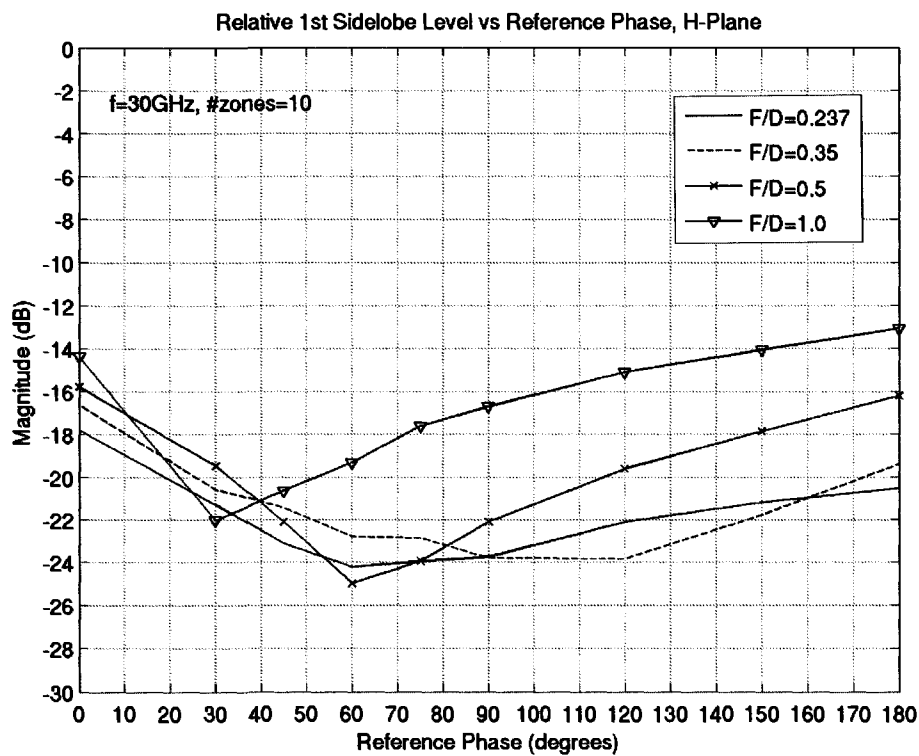


Figure 4-6: Relative 1st Sidelobe Level with Varying Reference Phase, H-Plane

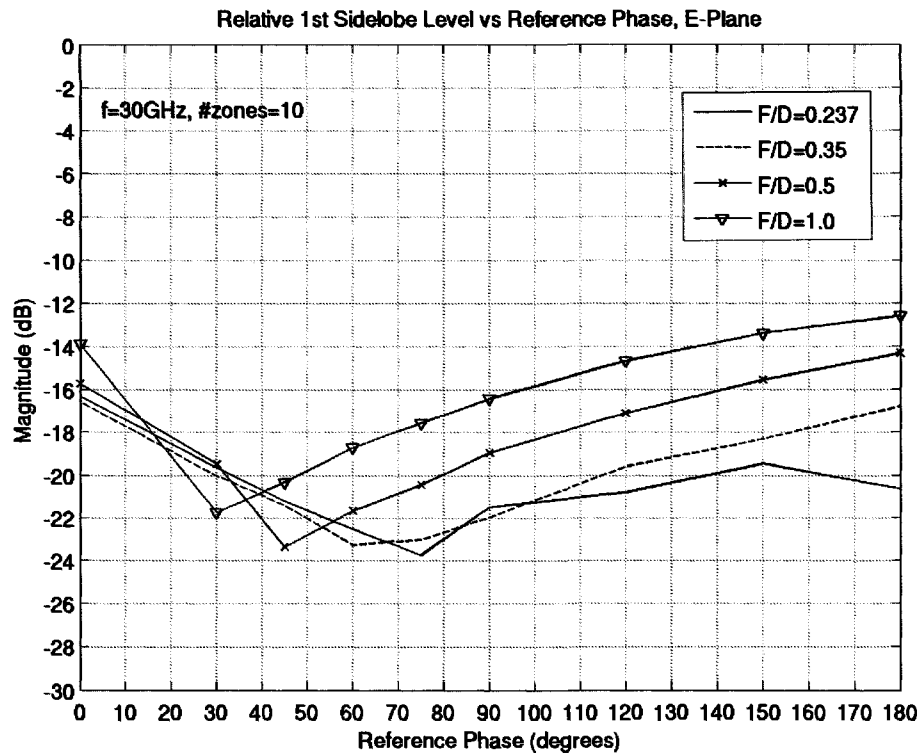


Figure 4-7: Relative 1st Sidelobe Level with Varying Reference Phase, E-Plane

In both the H- and E-planes, all F/D cases exhibited a similar trend in that the level of the first sidelobe decreased as the reference phase increased from 0° through to about 60° . When the reference phase increased beyond 60° , the sidelobe level also increased such that, at 180° , the sidelobe level was nearly the same as it was at 0° . The overall decrease in sidelobe level, as well as the normalized minimum relative first sidelobe level and the reference phase where this minimum occurred, are shown in Table 4-2 for each F/D case.

<i>F/D</i>	H-Plane Min. SLB (dB)	H-Plane SLB Decrease (dB)	H-Plane Ref. Phase (deg)	E-Plane Min. SLB (dB)	E-Plane SLB Decrease (dB)	E-Plane Ref. Phase (deg)
0.237	-24.22	6.44	60	-23.79	7.47	75
0.35	-23.85	7.23	120	-23.31	6.78	60
0.5	-25.08	9.29	60	-23.46	7.72	45
1.0	-22.08	7.69	30	-21.78	7.89	30

Table 4-2: Normalized Minimum Sidelobe (SLB) Level, Decrease & Reference Phase

Table 4-2 and Figures 4-6 and 4-7 indicate that a drop of at least 6dB in the level of the first sidelobe can be expected by changing the reference phase from 0° to a more optimal value. At best, this drop could be as much as nearly 9.3dB in the H-plane. The minimum first sidelobe occurred at 60° in two of the four *F/D* cases which was similar to the result in [4-1].

The case where the optimum reference phase was 120° (*F/D*=0.35) was a case where the first sidelobe had shifted in relation to the sidelobes formed by the other reference phase cases. This seemed to be a common effect caused by the increase in reference phase. At first, the sidelobes would decrease and then they would diminish completely and reform another sidelobe further away from boresight.

Overall, these simulations showed that there was no single value of reference phase which resulted in the best first sidelobe level for all of the lens designs considered. Therefore, although the level of the first sidelobes can be improved from the 0° reference phase case, the optimized value must be determined for each specific value of *F/D* and will be design dependent.

4.3.2.3 Maximum Sidelobe Level

The maximum relative sidelobe level was determined by analyzing the pattern levels that were computed over all ϕ angles. It was found that the maximum sidelobe level was only slightly affected by the changing reference phase and was nearly independent of the F/D under consideration. Figure 4-8 illustrates these results.

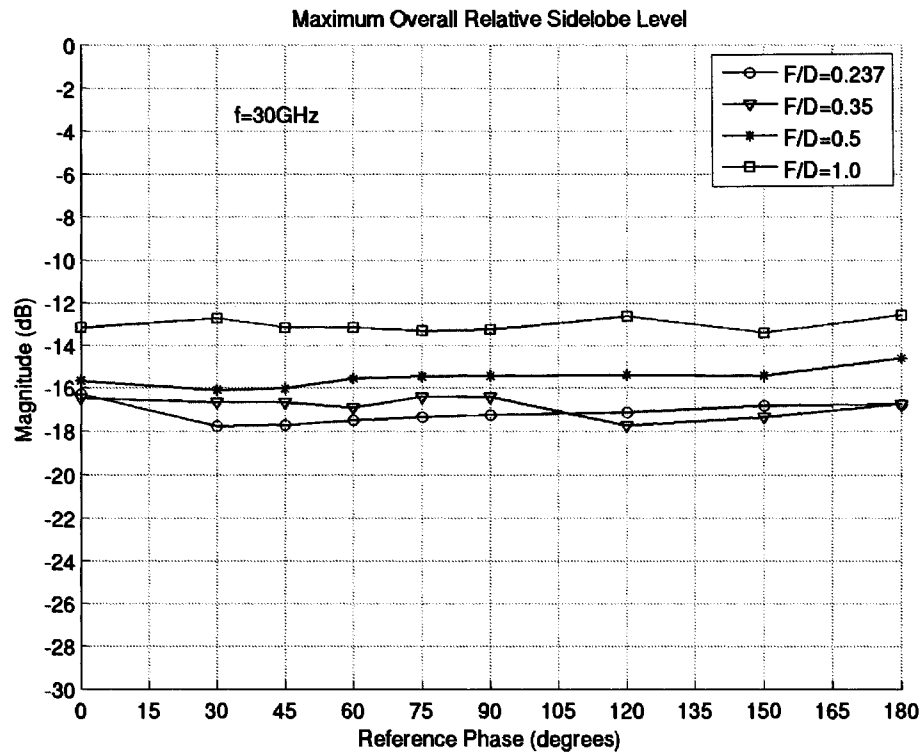


Figure 4-8: Maximum Relative Sidelobe Level with Varying Reference Phase

In all F/D cases, by changing the reference phase it was possible to achieve a slightly improved overall maximum relative sidelobe level. The best improvement was with the $F/D=0.237$ case where the maximum sidelobe level improved by about 1.5dB when the reference phase was 30° .

4.3.2.4 Half-Power (3dB) Beamwidth

The half-power beamwidth in all F/D cases was found to decrease with increasing reference phase as shown in Figure 4-9 for the H-plane. A small part of this was expected due to the increasing diameter of the antenna aperture as the reference phase increased. However, it was found that the change in diameter could only account for about 0.2° of the overall change, which was typically about 0.5° . Therefore, by increasing the reference phase, a small narrowing in the 3dB beamwidth can be expected. This effect is also visible in Figures 4-3 and 4-4.

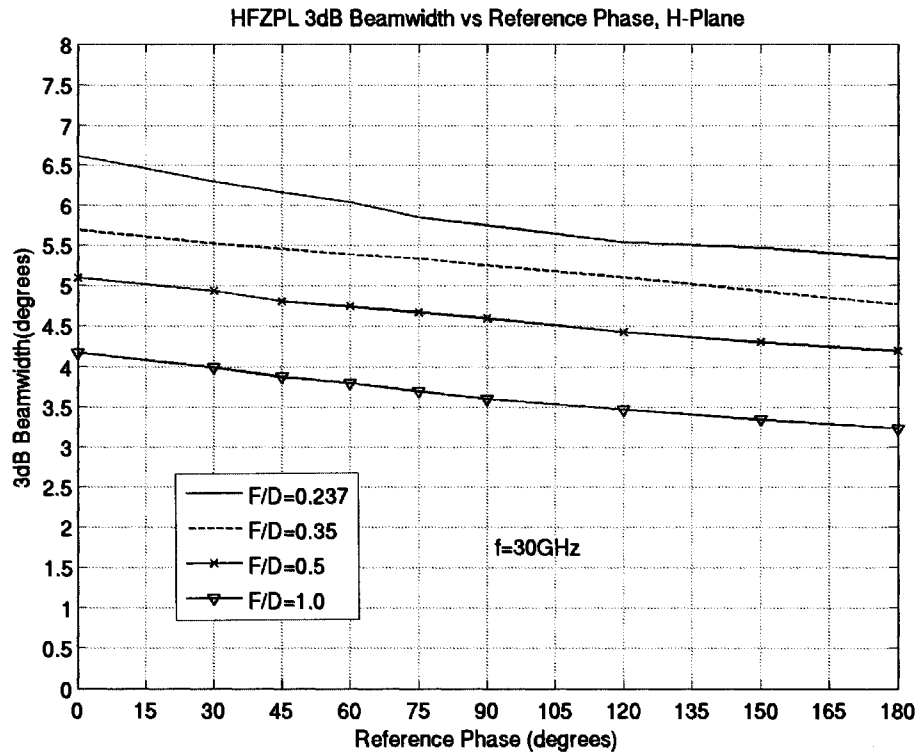


Figure 4-9: Half-Power Beamwidth with Varying Reference Phase, H-Plane

4.3.2.5 The Maximum Cross-Polarization

Cross-polarization for a FZPA is very low in the principle planes due to the symmetry of the structure which causes the cross-polarized fields to cancel each other. For all cases,

changing the reference phase had only a small effect on the cross-polarization levels in the principle planes. Generally, the simulated levels were all very low and on the order of -60dB to -100dB in these planes.

4.4 Measurement Results

Experimental testing was implemented to verify the FDTD simulation results and confirm that the observed trends discussed in the previous sections were accurate. The measurements were performed in a calibrated near-field anechoic chamber, which was used to determine the far-field radiation patterns.

Two of the simulated circular FZPAs were selected for fabrication. Table 4-3 lists these antennas and their associated reference phases.

<i>F/D</i>	Reference Phase (deg)
0.237	0
0.237	60

Table 4-3: Antenna Cases that were Fabricated for Testing

4.4.1 Antenna Fabrication and Test Set-up

Each FZPA aperture was made using the same zone radii as in the simulations. The metal zones were etched on a 0.005" FR4 substrate material and were attached with masking tape to a vertical piece of 3mm thick foam for support. The structure was then situated on a custom-made test fixture at the proper location away from a tapered open-ended WR28 waveguide feed. The tapered waveguide was used instead of the standard waveguide to provide more stable and smooth patterns over all angles. The actual taper in the

waveguide affects only the outer wall thickness which was reduced from 0.04" to 0.02".

The test fixture was specially designed to minimize the scattering effects that were shown to be substantial in earlier far-field measurements which used a plastic fixture. The horizontal location of the feed on the test fixture was controlled by a precision positioning device. The lens was manually centered on the foam with respect to the feed. The set-up is shown in Figure 4-10.

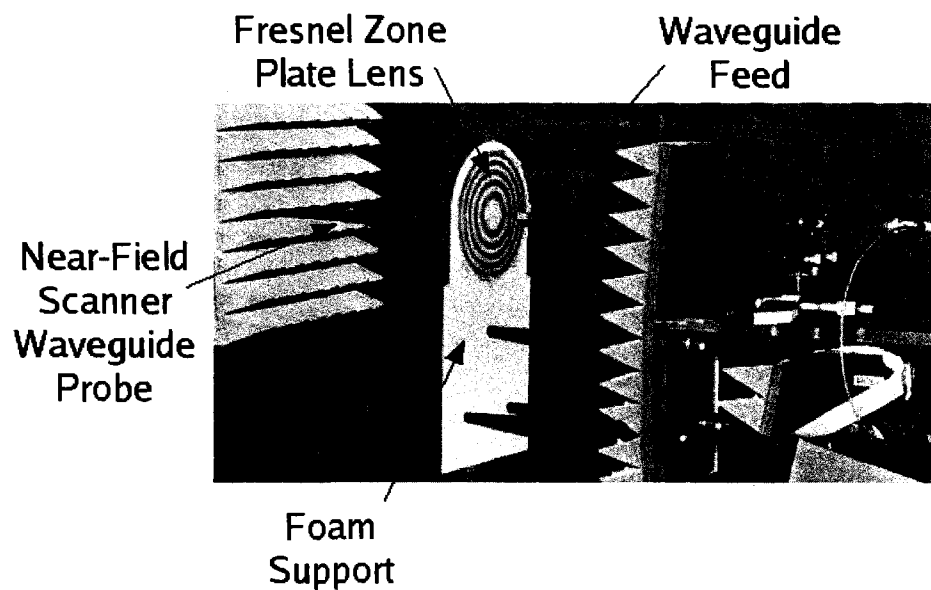


Figure 4-10: Test Set-up in the Near-Field Anechoic Chamber

4.4.2 Radiation Patterns of the Feed

Prior to testing the antennas, the radiation patterns of the feed were measured. To perform this test, the waveguide was placed in the far-field chamber since its gain was too low for measurement in the near-field chamber. Figure 4-11 illustrates the normalized measured and simulated radiation patterns for the tapered waveguide in both the H- and E-planes. The measurements matched the simulations very closely.

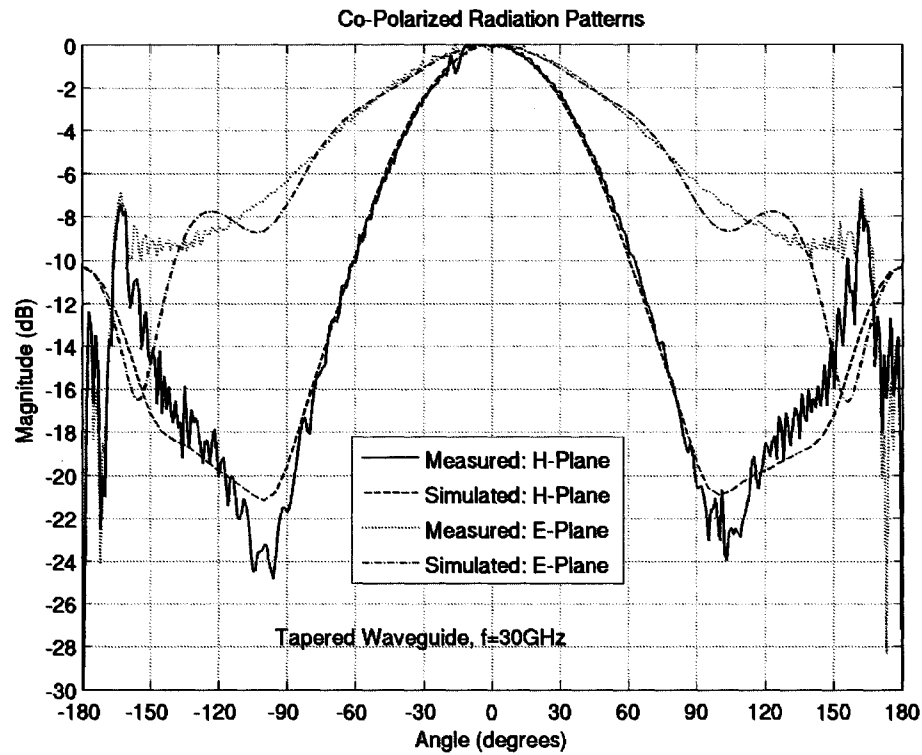


Figure 4-11: Normalized Measured vs. Simulated Feed Patterns

4.4.3 Comparison of Measured and Simulated Results

4.4.3.1 General Radiation Patterns

For the case when $F=3.75\lambda$, $F/D=0.237$ and $\Phi_o=0^\circ$, Figures 4-12 and 4-13 show a direct comparison of the normalized measured radiation pattern compared to the same normalized simulated pattern in the H- and E-planes respectively. Figures 4-14 and 4-15 show the same comparison, but for the $\Phi_o=60^\circ$ case.

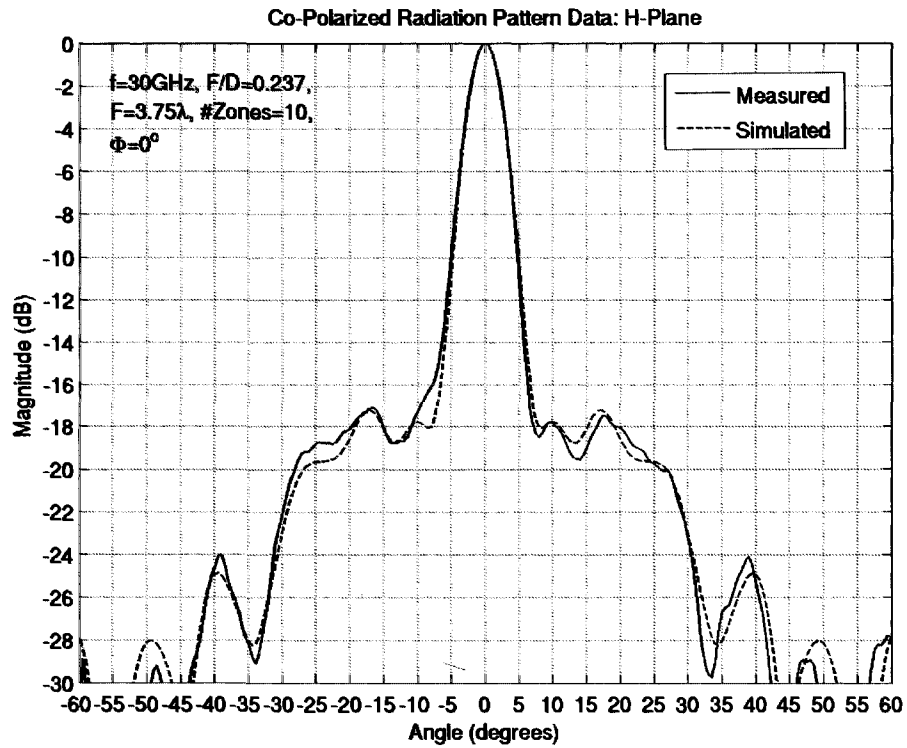


Figure 4-12: Normalized Measured vs. Simulated Patterns with $\Phi_0=0^\circ$, H-Plane

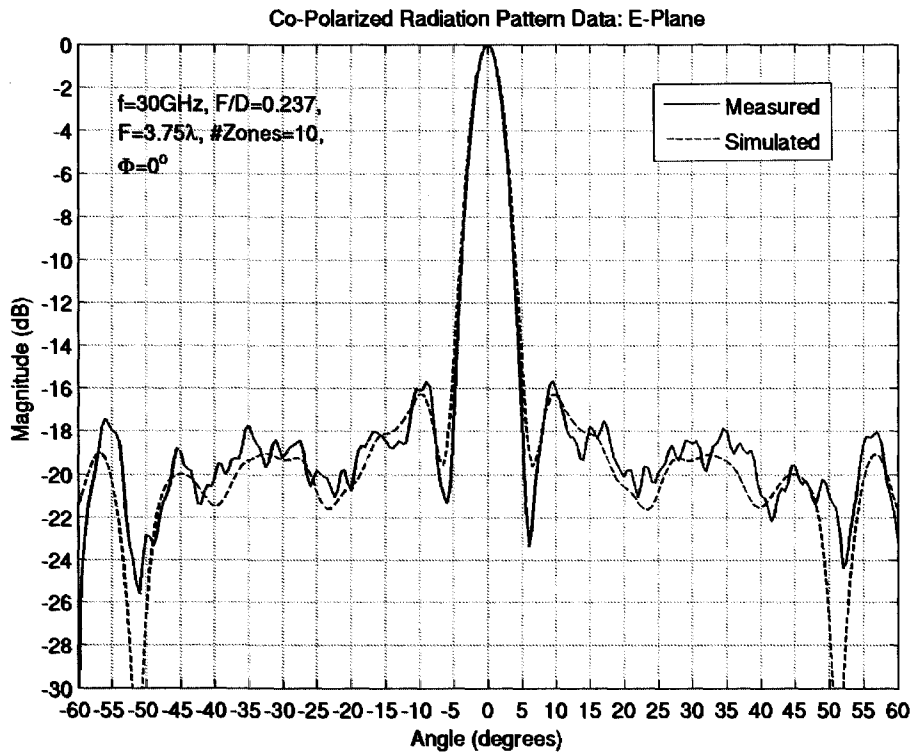


Figure 4-13: Normalized Measured vs. Simulated Patterns with $\Phi_0=0^\circ$, E-Plane

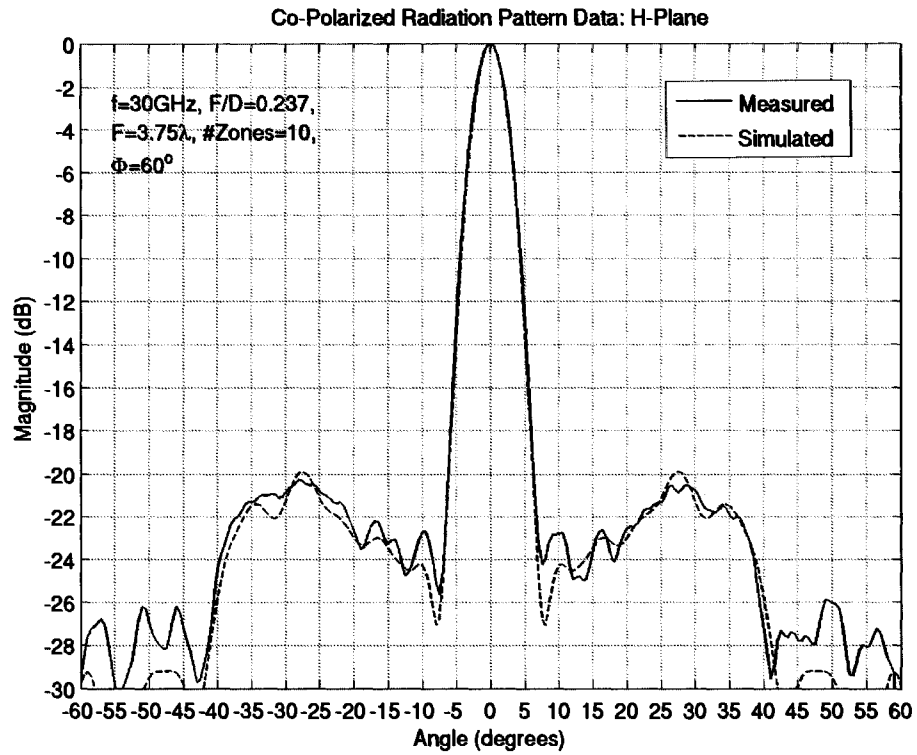


Figure 4-14: Normalized Measured vs. Simulated Patterns with $\Phi_0=60^\circ$, H-Plane

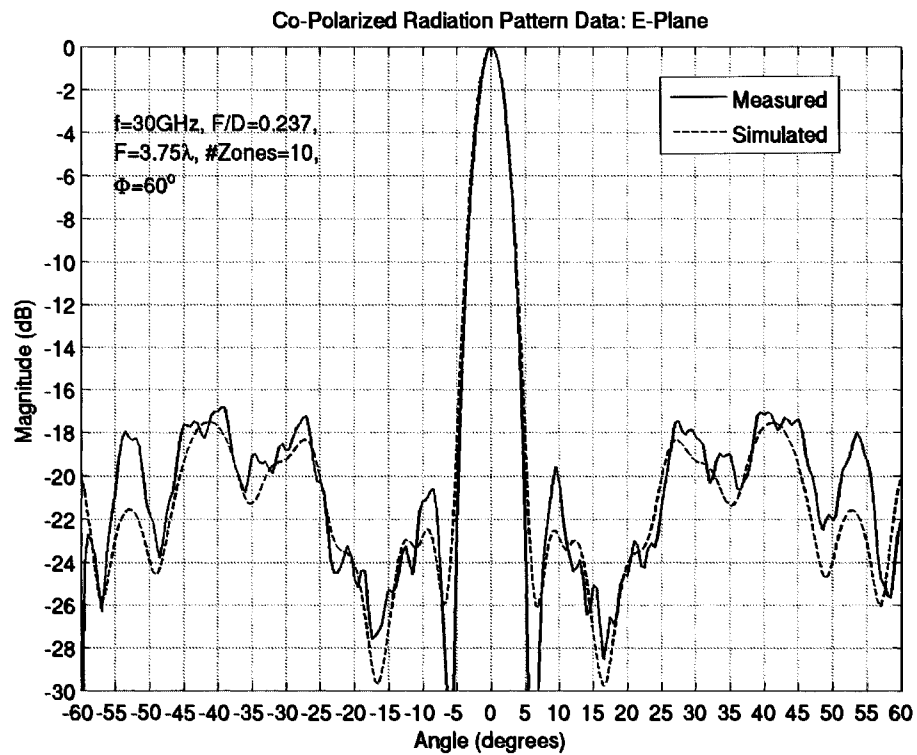


Figure 4-15: Normalized Measured vs. Simulated Patterns with $\Phi_0=60^\circ$, E-Plane

These figures demonstrate how the simulated patterns predicted the shape of the measured patterns with a high degree of accuracy even in the sidelobe region for both antennas. The minor differences between the measured and simulated patterns could be attributed to the fact that neither the FR4 material onto which the FZPA apertures were printed nor the foam support onto which they were mounted were included in the simulations.

4.4.3.2 Peak Gain

A comparison between measured and simulated peak gain is shown in Table 4-4 for each antenna that was measured. The simulated peak gain values were obtained by subtracting the simulated losses from the simulated directivity. The slight differences were again attributed to the simulation model not including the FR4 material or the test fixture. Despite these minor differences, the results verified the simulation accuracy since the measured gain was close to the simulated gain and followed the same trend. This also confirmed that the gain was essentially unaffected by the changing reference phase.

<i>F/D</i>	Reference Phase (deg)	Gain Simulated (dBi)	Gain Measured (dBi)
0.237	0	22.20	21.07
0.237	60	22.18	20.55

Table 4-4: Peak Gain with Varying Reference Phase

The frequency of the peak gain was 30GHz in both simulation and measurement. This is a further indication of the accuracy of the simulation model for this structure.

4.4.3.3 Measurement Discussion

The above noted measurement results successfully verified the accuracy of the simulation model for FZPAs. It is therefore appropriate to conclude that the trends observed in simulation are an accurate reflection of the actual FZPA performance. Further improvement in accuracy may be achieved by including the FR4 material and the aspects of the test fixture in the model.

4.5 Physical Meaning

This work has shown that by carefully selecting the reference phase for a FZPA, the level of the inner sidelobe can be substantially improved in a specific plane while having a minimal impact on the peak directivity, half-power beamwidth, and cross-polarization. It was also shown that the exact improvement is highly dependent on the configuration of the design since there was no single value of reference phase and F/D which yielded the best results. The reasoning for this can be interpreted physically by considering the FZPA as a diffractive grating element with a non-periodic structure [2-18]. This is a valid assumption for FZPAs with small number of zones ($N < 100$). Such an element produces output beams having several diffractive orders, the interference of which yields the beam pattern in the far field. When the reference phase is altered, a new zone is created which increases the spatial frequency of the zones in the structure thus resulting in a somewhat larger lens. A change to the spatial frequency causes a change in the intensity of the various diffractive orders which redefines the output beam power from the FZPA surface into space. The resulting beam patterns are formed based on this new interference pattern.

Changing the reference phase is thus a means of changing the diffraction and interference

patterns of the antenna. Due to the complicated nature of these effects, it is difficult to predict how the radiation patterns of the antenna will be affected without electromagnetic simulations. However, it is intuitive that the antenna's exact geometry is important in forming the diffraction patterns since constructive and destructive addition of waves will be different in each case thus affecting the sidelobe levels and locations. This also explains why the optimum reference phase is different for each F/D antenna configuration.

4.6 Conclusion

A systematic study investigating the effect of varying reference phase and F/D on the performance of FZPAs was presented. Simulations were performed at 30GHz using an FDTD software package and prototypes were measured for comparison. The measured results verified the simulation results, which revealed that by changing the reference phase from the standard 0° to some other value between 0° and 180° , there was a drop in the level of the 1st sidelobe between 6.5dB and 9.3dB depending on the reference phase.

This finding is significant since the sidelobe improvement comes with very little impact on either the peak gain or the cross-polarization levels and a small decrease in the 3dB beamwidth. The trend was also found to exist with other F/D values but the optimum reference phase changed with each antenna configuration. This approach of optimizing the reference phase to improve the sidelobe level performance should also be applicable to various types of phase correcting Fresnel lenses whose radiation efficiencies will be significantly better than the FZPA.

CHAPTER 5

RESOLUTION & FOCAL FIELDS

5.1 Introduction

When operating the FZPA in receive mode, the antenna receives a signal from a far-away source which appears as an incident plane wave at the aperture of the antenna. The FZPA then focuses the waves to the focal point. This basic concept was discussed in Section 2.2.8. Operating the FZPA in this mode is the basis for many imaging applications such as optical microscopy, micro-optics, and tomography, particularly at optical frequencies.

Alternately, at microwave frequencies, the FZPA can be arrayed and used in this mode for spatial power combining applications. In such a case, the plane wave front is incident on the elements in the FZPA array which have corresponding amplification devices. The antenna creates an array of spot beams where detectors would be placed. The narrower the spot beam, the higher the intensity. This enables the detectors to capture the most amount of energy possible. The width of the spot beam is therefore not only a measure of resolution, but is also a measure of the antenna's efficiency.

This chapter will begin by analyzing the focal fields and determining the resolution of the FZPA with a focal distance greater than a wavelength. This work will then be extended to the sub-wavelength focal distance range where the results will be compared to those from the phase correcting dielectric Fresnel antenna. Focal distances in this range are important for creating compact FZPAs. Finally, this chapter will conclude with a review of how the focal field intensity changes with reference phase.

5.2 Resolution of the FZPA

Determining the resolution of the FZPA is accomplished by observing the focal fields and was described in Section 2.2.9. This involved illuminating the FZPA aperture with an incident plane wave propagating in the $+z$ -direction and polarized in the y -direction as shown in Figure 5-1. Owing to the symmetry of the FZPA, the polarization of the wave in the x - or y -directions would yield the same results.

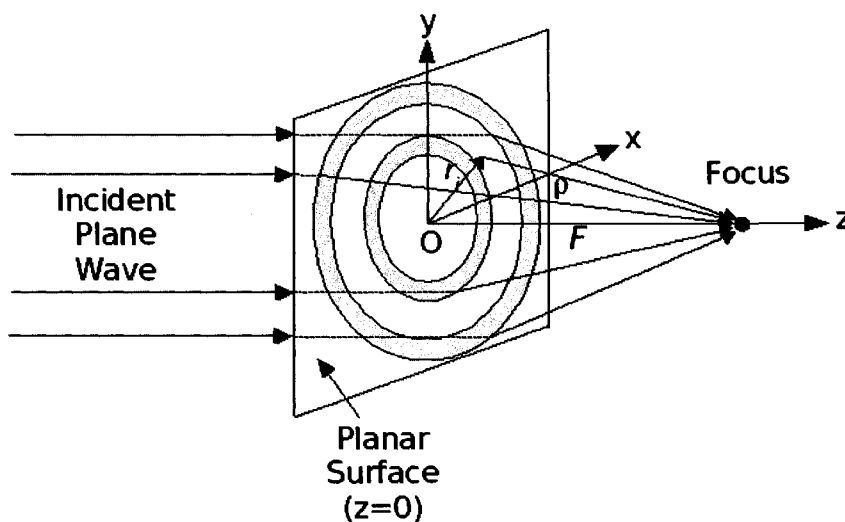


Figure 5-1: Geometry of the FZPA for Focal Field Simulation

To determine the location of the focus, the average power density (S_z) along the z -axis ($x=y=0$) was computed using Empire [3-3] and plotted so that the peak could be

observed. The normalized average power density was then plotted along the x - and y -axes at the z location of the focus. The resolution was computed from the distance between the peak and the location of the first nulls in the spot-beam.

5.2.1 Focal Distance $> \lambda$

With focal distances greater than the wavelength, it was expected that the computed FZPA resolution would be within the Abbe criteria where the resolution is greater than 0.5λ , as outlined in Section 2.2.9. For this computation, a 10-zone, $F=3.75\lambda$, $F/D=0.237$ FZPA was modeled at 30GHz. The resulting average power density is shown in Figure 5-2 where the lens is located at $z=0\lambda$ and the focal point is located at $z=3.75\lambda$. The peak average power density is -11.14dB/m^2 .

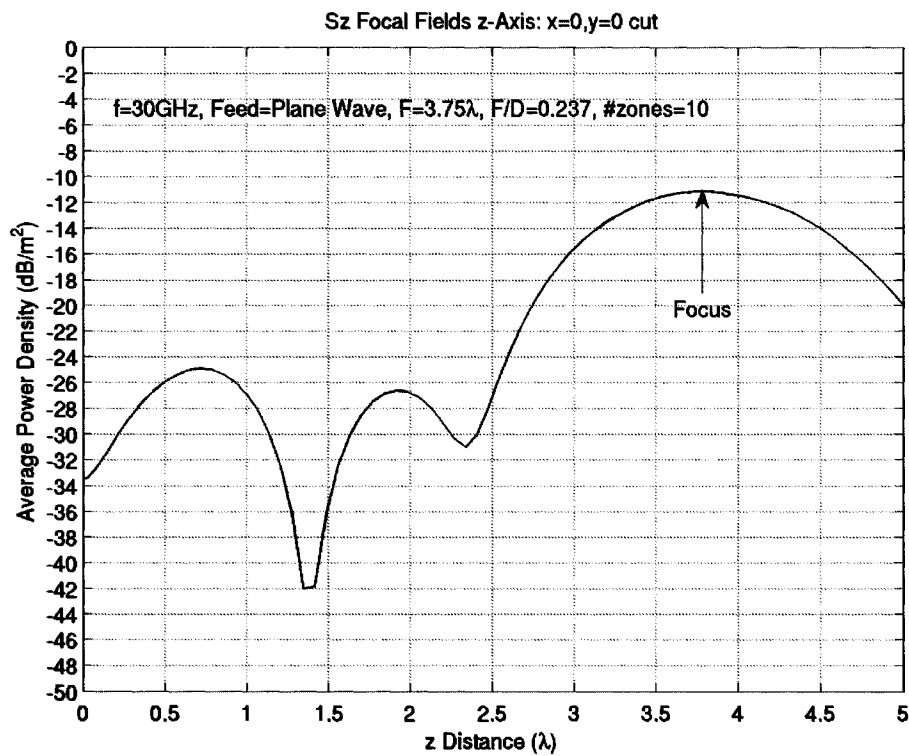


Figure 5-2: Average Power Density Along z -Axis at $x=y=0$

Figure 5-3 shows the normalized magnitude of the spot beam at $z=3.75\lambda$ along the x - and y -axes overlaid together with associated resolutions noted. The x - and y -axis cuts were not the same because the polarization of the plane wave created a different interaction along each cut. The resolution along the x -axis was 0.56λ and along the y -axis was 0.64λ . These results are standard for FZPAs with focal distances greater than a wavelength.

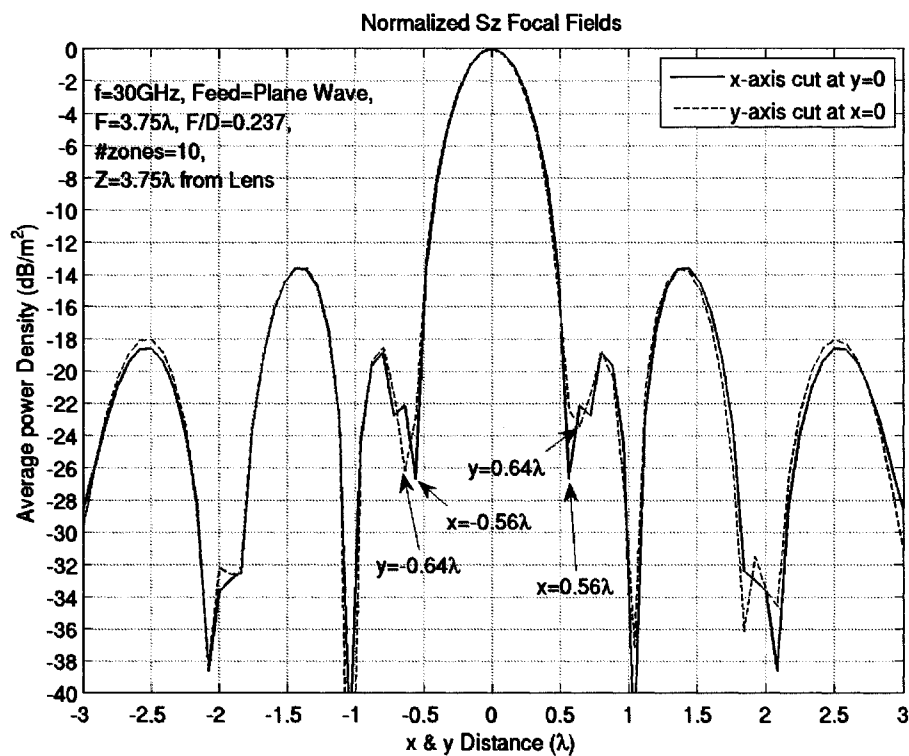


Figure 5-3: Normalized Average Power Density Along the x - and y -axis at $z=3.75\lambda$

5.2.2 Focal Distance $< \lambda$

With sub-wavelength focal distances, the standard equations for spatial resolution given in Section 2.2.9 are no longer valid. That is, the Rayleigh and Abbe limits cannot be used to predict what resolutions are achievable in sub-wavelength configurations. Until

recently, the resolution of the FZPA with sub-wavelength focus remained unknown [5-1]. For this computation, a 10-zone, $F=0.5\lambda$ and $F/D=0.045$ FZPA was analyzed at 30GHz. After simulation with the plane wave incident on the FZPA aperture, the average power density was found to be as shown in Figure 5-4. In this figure, the lens was located at $z=0\lambda$ and the focus was to the right of the lens at $z=0.64\lambda$. This yielded a focal distance of 0.64λ , which was slightly different from the intended $F=0.5\lambda$.

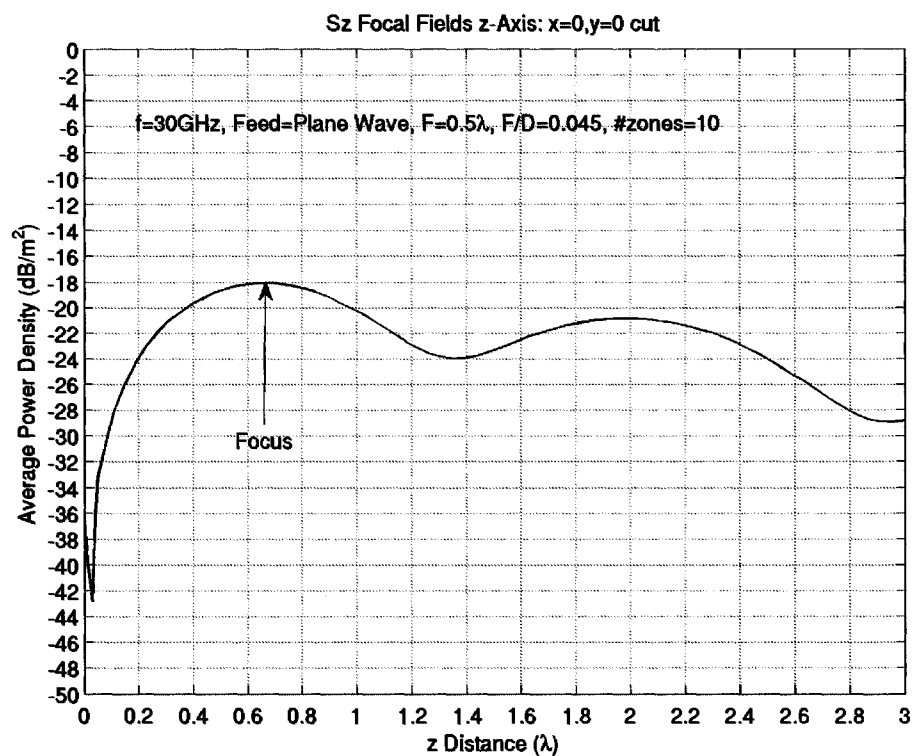


Figure 5-4: Average Power Density Along z -Axis at $x=y=0$

Figure 5-5 shows the normalized magnitude of the spot beam along the x - and y -axes overlaid together with associated resolutions noted. The resolution along the x -axis was 0.429λ and along the y -axis was 0.416λ (average of both the left and right of the spot beam) which represented a spatial resolution less than 0.5λ . The resolution was not

symmetrical along y -axis due to the spot beam being located in the reactive near field of the antenna.

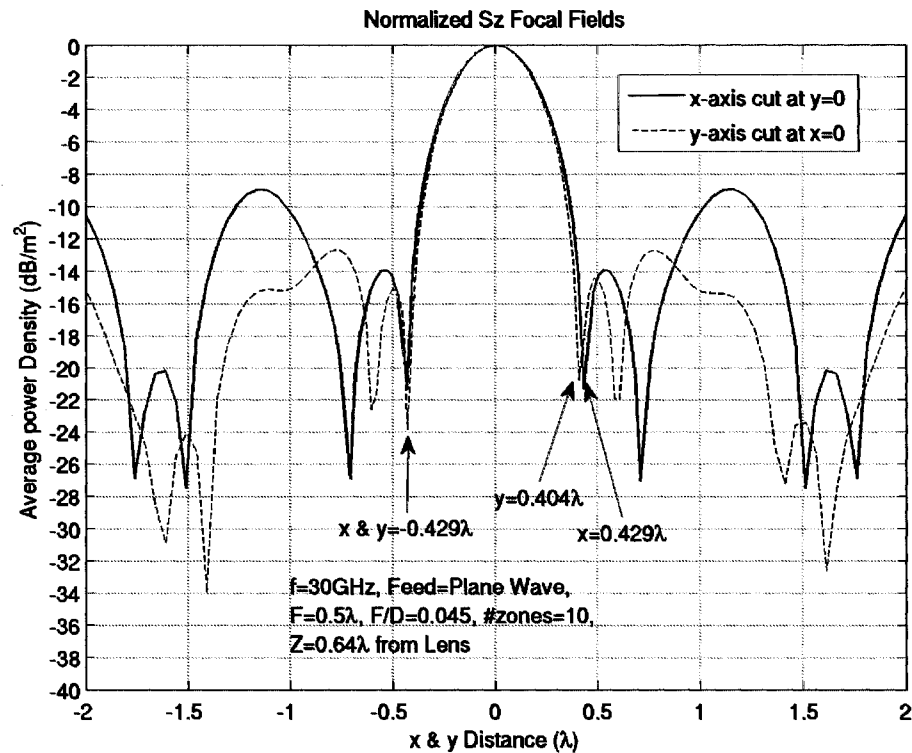


Figure 5-5: Normalized Average Power Density Along the x - and y -axis at $z=0.64\lambda$

Figure 5-6 shows how the peak average power density varied with frequency. Since the focus moved with frequency, the figure shows two curves. The first curve represents the peak intensity and reveals that the peak actually occurs at 34.5GHz instead of 30GHz. The second curve represents the intensity at the 0.64cm focus, which is the focus at 30GHz. This curve is important in most practical applications since the receiver is typically fixed at a certain focus. In this case, the 1dB power density bandwidth was found to be 3GHz or 9.8%.

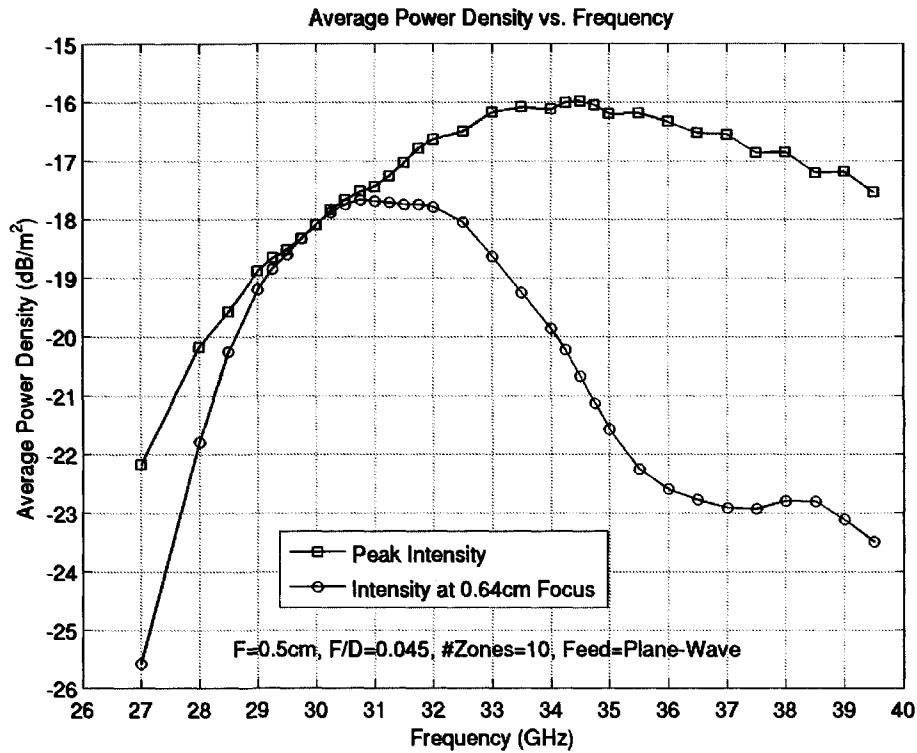


Figure 5-6 Peak Average Power Density vs. Frequency

The x -axis resolution ($y=0$ cut) was also observed, at the location of the peak average power density, as the frequency changed from 27 to 40GHz. The x -axis resolution improved to 0.404cm at 34.5GHz, which was the frequency of the peak average power density from Figure 5-6. This effect can be explained by the fact that the wavelength decreased as the frequency increased, which yielded a smaller focal length. The smaller focal length meant that the feed would be closer to the aperture and thus further into the near fields. When the antenna operation depends more on the near fields than on the radiative fields, the Rayleigh and Abbe's limits do not apply [5-2]. In this way, sub-wavelength focusing can exceed the standard limits.

5.2.3 Resolution Comparison with Phase Correcting Fresnel Antenna

As briefly described in Section 2.2.9, Minin et al. published their recent work on the computation of resolution for phase correcting Fresnel antennas with small F/D and sub-wavelength focal distances [2-22]. The phase correcting (PC) dielectric lens in their work had parameters: $\epsilon_r=4$, $t=\lambda/2$, $F=0.5\lambda$, and 10 zones. These parameters were well suited for a direct comparison to the results from the previous section. Table 5-1 summarizes the results of the comparison where it can be seen that the spatial resolution of the FZPA is also under 0.5λ and is close to that of the dielectric phase correcting Fresnel antenna. The y-axis resolution is stated as being the average of the left and right sides of the focal field curves along the x- and y-axes.

<i>Antenna Type ($F=0.5\lambda$)</i>	<i>x-Axis Resolution (λ)</i>	<i>y-Axis Resolution (avg. left & right) (λ)</i>	<i>Peak Power Density (dB/m^2)</i>
Fresnel Zone Plate	0.429	0.416	-18.08
Dielectric PC Fresnel Antenna ($\epsilon_r=4$)	0.410	0.370	-13.90

Table 5-1: Comparison Between FZPA & Dielectric PC Fresnel Antenna

The dielectric phase correcting Fresnel antenna, however, still has a much higher peak intensity than the FZPA at 30GHz. Despite this, the fact that the spatial resolution of the FZPA was shown to be nearly the same as that of the dielectric phase correcting Fresnel antenna for sub-wavelength focal distances and small F/D cases provides further motivation to design compact FZPAs.

5.3 Focal Intensity of the FZPA with Reference Phase

After having studied how the reference phase affected the radiation patterns of the FZPA in Chapter 4, it was natural to extend this work to observe how the focal intensity changed with reference phase. For this computation, the FZPA was again modeled with 10 zones, $F=3.75\lambda$, and $F/D=0.237$, but this time the zone radii were calculated using Equation 4-4 instead of Equation 2-5 in order to include the reference phase.

Seven different reference phases were chosen for this analysis (0° , 30° , 60° , 90° , 120° , 150° , and 180°) which resulted in seven different structures to simulate. Each antenna was modeled at 30GHz similar to the others described in this chapter with a y-polarized plane wave incident on the aperture of the antenna. The resulting average power density for all reference phases is shown in Figure 5-7 where the FZPA aperture is located at $z=0\lambda$. Figure 5-8 is a magnified version of Figure 5-7 where the actual differences in the peak intensity can be observed.

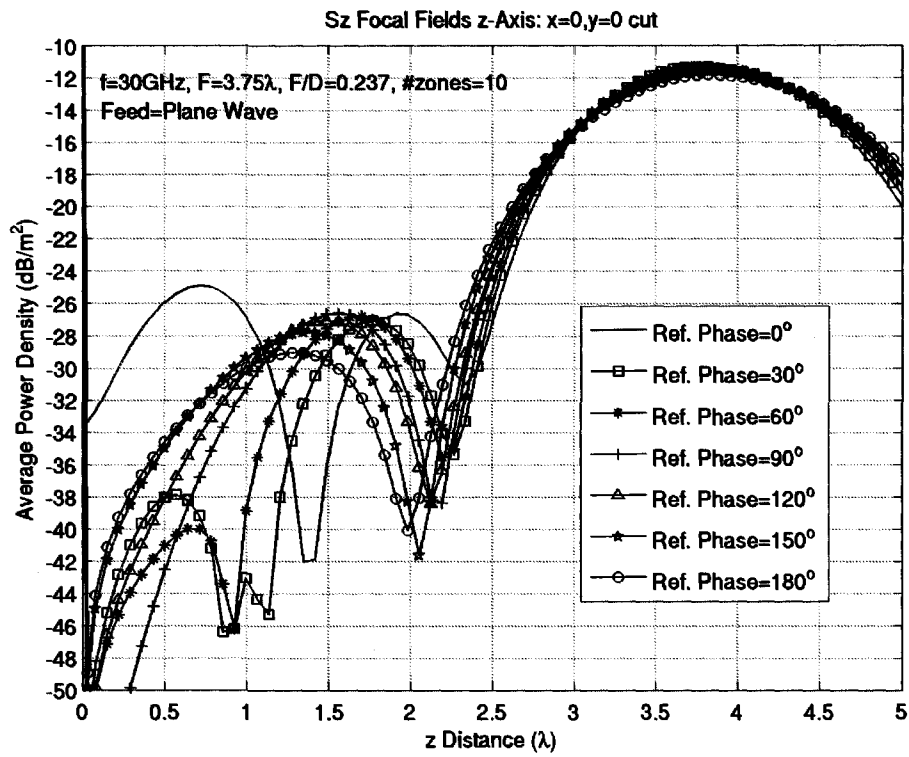


Figure 5-7: Intensity along z -Axis at $x=y=0$ for all Reference Phases

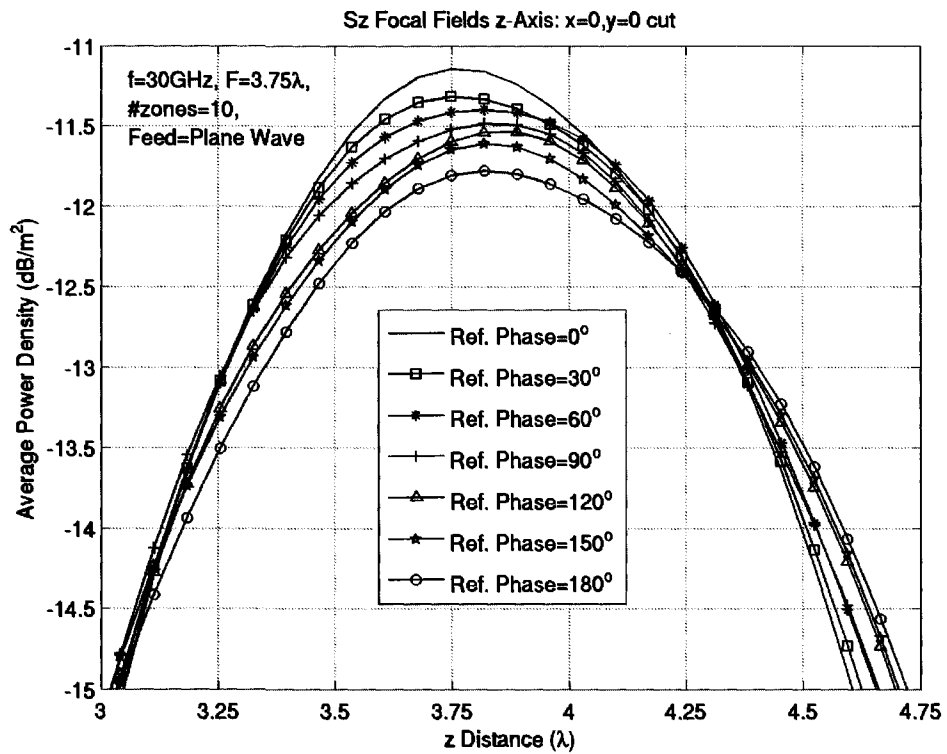


Figure 5-8: Magnified Version of Figure 5-7

Table 5-2 summarizes these results and also includes the average resolutions for the $x=0$ (y -axis) and $y=0$ (x -axis) cuts. Again, the resolution numbers are an average of the left and right sides of the spot beam.

Reference Phase (degrees)	Peak Power Density (dB/m²)	Focus Location (λ)	Avg. x-Axis Resolution (λ)	Avg. y-Axis Resolution (λ)
0	-11.16	3.75	0.640	0.560
30	-11.32	3.75	0.596	0.636
60	-11.40	3.82	0.510	0.645
90	-11.49	3.82	0.532	0.573
120	-11.54	3.89	0.525	0.566
150	-11.61	3.82	0.513	0.474
180	-11.78	3.82	0.560	0.480

Table 5-2: Results of Peak Intensity with Varying Reference Phase

The peak intensity dropped only slightly as the reference phase increased. The highest peak intensity was at 0° reference phase and the lowest was at 180° . There was no real advantage to changing the reference phase from 0° in order to improve the peak intensity. The resolution, however, was more affected by the reference phase than the peak intensity, but not in a predictable manner. Generally, the resolution along both axes was less when the reference phase was 180° than when it was 0° .

5.4 Conclusion

This chapter investigated the resolution and focal fields of the FZPA. In the first part of the chapter, it was shown that FZPAs, like dielectric phase correcting Fresnel antennas, can yield a resolution less than 0.5λ with a sub-wavelength focal length. This was an important finding since the FZPA with sub-wavelength focus and fine resolution allows designers to create very compact antennas that will be more attractive for future wireless applications in the Ka-band. The second part of the chapter investigated how the focal field intensity changed with reference phase. It was concluded that the reference phase had very little effect on the the focal field intensity. This result enables designers to use reference phase to optimize sidelobe levels and locations without sacrificing focal field intensity.

CHAPTER 6

CONTROL OF FZPA RADIATION PATTERNS

6.1 Introduction

In this chapter, hexagonal zones will be presented as an alternative to the conventional circular zones in the FZPA. The hexagonal geometry is interesting because the zones are no longer circularly symmetric. They can therefore be rotated with respect to each other and provide control over certain characteristics of the radiation pattern. The hexagonal shape is also beneficial when the FZPA elements are used in an array as shown in Figure 6-1. Because the FZPA elements are several wavelengths in size, overlapping is required in order to maintain appropriate element spacing so as to minimize grating lobes. The hexagonal geometry helps to minimize this overlap by allowing a closer element to element spacing.

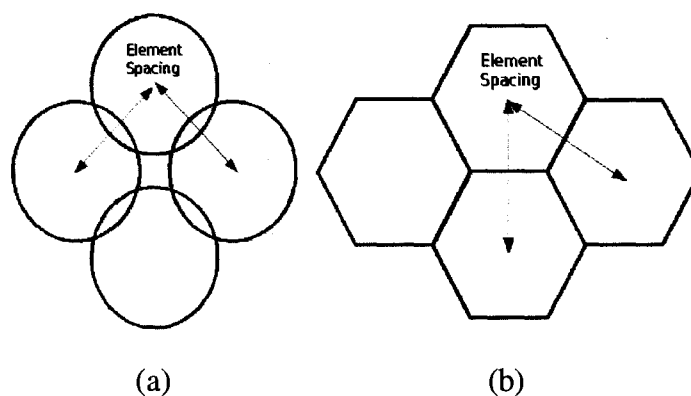


Figure 6-1: Arrays of (a) Circles and (b) Hexagons

However, since the hexagonal FZPA is inherently an approximation to the circular FZPA, it was expected that the circular geometry would have superior radiation pattern characteristics. For this reason, the first section of this chapter will outline the direct comparison between the hexagonal and circular FZPAs. Then, in order to maintain the hexagonal shape but bring the radiation characteristics closer to those of the circular FZPA, a method involving alternating hex-cut zones was proposed. This structure will be presented and compared to both the hexagonal and circular FZPAs in Section 6.3. Finally, control over the radiation patterns was achieved by rotating the zones of the alternating hex-cut FZPA with respect to each other. This method will be demonstrated and analyzed in Section 6.4.

6.2 Hexagonal and Circular FZPA Comparison

6.2.1 Hexagonal Geometry

In the conventional configuration, FZPAs consist of planar circular rings which alternate between transparent and metal as shown in Figure 6-2(a). The circular geometry stems from the fact that the spherical waves from the feed create constant phase zones on a planar surface that are circular. These rings coincide with the Fresnel zones on the

aperture of the antenna.

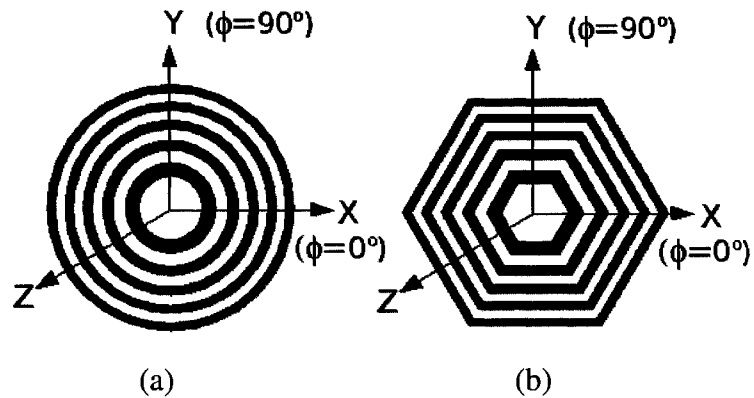


Figure 6-2: (a) Circular FZPA, (b) Hexagonal FZPA

The circular geometry is inconvenient, however, when used as an element in an array, due to the significant overlap areas. Square FZPAs were investigated as being better array packing elements, but their performance was significantly worse than the circular FZPA [2-34, 2-35]. The hexagonal FZPA was thus introduced as a closer alternative to the circular FZPA for use in arrays [6-1]. When the hexagonal shape is used in an array it removes some potential problems associated with overlapping elements in an array, which may occur with circular FZPAs.

The hexagonal FZPA operates in the same way as the circular FZPA. The metal hexagonal zones are centered in the same position as the alternating 180° circular phase zones on the surface of the antenna aperture. However, since the hexagon is inherently an approximation to the circle, the hexagonal zones will not cover the entire constant circular phase zones. Making the hexagonal geometry as close to the circular geometry as possible was important to yield the best results.

In order to best approximate the circle, a technique based on the method presented for a square geometry [2-36] was used. The optimum hexagon was derived by ensuring that each hexagonal edge intersected the equivalent circle at two points per side as shown in Figure 6-3.

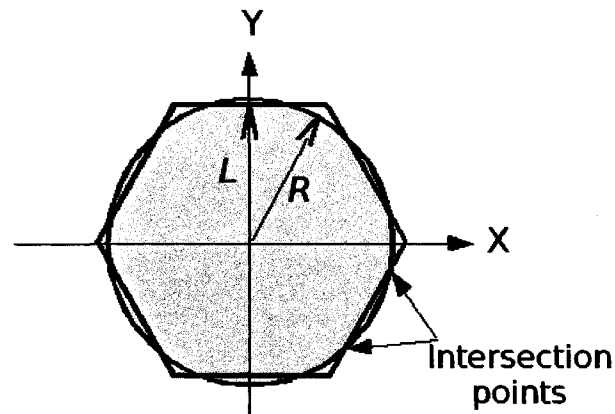


Figure 6-3: Optimum Hexagon Derivation

Using this method and simple trigonometry, the distance from the center of the hexagon to the center of the i^{th} zone edge, L_i , was related to the radius of the circle, R_i , by:

$$L_i = 0.966 R_i \quad \text{where } i=1,2,3,\dots,N \quad (6-1)$$

In order to determine the hexagonal zone radii, the circular Fresnel zone radii must first be computed according to Equation 2-5 from Section 2.2.6. Once the circular radii are known, then the hexagon parameter, L_i , can be computed from Equation 6-1.

6.2.2 Simulations of the Hexagonal FZPA

Simulations were again performed at 30GHz and the lens parameters for each simulation in this comparison are summarized in Table 6-1. These parameters were computed via Equation 6-1 based on the circular diameters, D_i , which were chosen to be as close to

15.8cm as possible.

Nominal <i>F/D</i>	<i>F</i> (λ)	<i>D</i> (cm) Desired	<i>D</i> (cm) Actual	<i>L</i> (cm) Actual	# Total Zones
0.237	3.75	15.8	15.05	7.64	10
0.35	5.53	15.8	15.49	7.48	8
0.5	7.9	15.8	15.02	7.25	6
1.0	15.8	15.8	16.39	7.92	4

Table 6-1: Model Parameters for Each *F/D*

The FZPAs were fed with the same open-ended WR28 waveguide placed at their focal point as was used in previous chapters. Since the hexagonal FZPA was not rotationally symmetric, it was necessary to determine which orientation of the FZPA aperture with respect to the vertically oriented feed would produce the best results. Initially, the lens was oriented such that a flat edge was perpendicular to the *y*-axis, as shown in Figure 6-2. The aperture was then progressively rotated until the next edge became perpendicular with the *y*-axis. It was found that the sidelobe levels degraded by several decibels as the lens orientation was rotated away from the initial position. Therefore the FZPA aperture was oriented with an edge perpendicular to the *y*-axis and the waveguide was oriented such that the electric field vector was along the *y*-axis (see Figure 6-2 for the coordinate system).

The hexagonal and circular FZPAs were compared by analyzing the peak directivity, the

first sidelobe level, the half-power beamwidth, and the maximum cross-polarization level. Figure 6-4 illustrates a typical comparison of the co-polarized radiation patterns between the hexagonal and the circular FZPAs in both planes. Both structures were configured for the 10-zone, $F=3.75\lambda$, $F/D=0.237$ case. In order to better see the effect on the inner sidelobes, the angle range was limited to the first 50° from boresight.

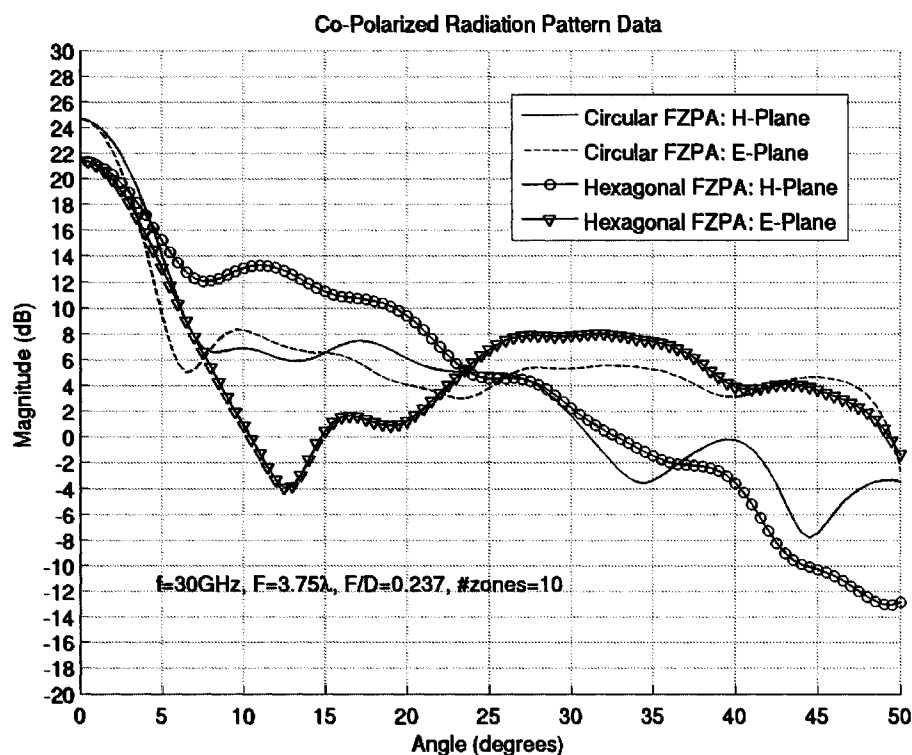


Figure 6-4: Co-polarized Radiation Pattern Comparison

This figure highlights the primary differences between the two structures. The hexagonal FZPA had a lower peak directivity by about 3dB compared to the circular version and the hexagonal FZPA was found to have a larger half-power beamwidth than the circular version in both planes. The level of the first sidelobe in the H-plane was generally much higher for the hexagonal FZPA, but the level of the first sidelobe in the E-plane was actually better than the circular FZPA first sidelobe for some F/D cases. The location of

the first sidelobe was not the same in the H- and E-planes for the hexagonal FZPA, whereas the locations were nearly the same for the circular version. This was because of the asymmetrical structure of the hexagon relative to the feed in each plane compared to the circular structure. Tables 6-2 & 6-3 summarize the comparison results for the circular and hexagonal FZPAs.

<i>F/D</i>	Peak	1 st SLB Level	3dB BW
	Directivity (dB)	H-Plane / E-Plane (dB)	H-Plane / E-Plane (deg)
0.237	24.65	-17.8 / -16.3	5.2 / 4.4
0.35	24.67	-16.6 / -16.6	4.6 / 4.2
0.5	23.63	-15.8 / -15.8	4.4 / 4.1
1.0	21.12	-14.4 / -13.8	3.8 / 3.6

Table 6-2: Summary of Circular FZPA Simulation Results

<i>F/D</i>	Peak	1 st SLB Level	3dB BW
	Directivity (dB)	H-Plane / E-Plane (dB)	H-Plane / E-Plane (deg)
0.237	21.41	-8.2 / -19.8	6.3 / 5.4
0.35	21.63	-7.7 / -22.8	5.7 / 5.3
0.5	21.11	-7.8 / -24.8	5.1 / 4.8
1.0	19.84	-8.2 / -13.5	4.2 / 4.1

Table 6-3: Summary of Hexagonal FZPA Simulation Results

As expected, the maximum cross-polarization levels were generally higher for the

hexagonal FZPA than for the circular version, particularly when comparing the H-plane. Also, the maximum cross-polarization levels in both planes of the hexagonal FZPA were close in value whereas, in the case of the circular FZPA, the maximum levels in the two planes were significantly different. The cross-polarization results are not shown in the table since the exact simulated values are so low that they have little meaning in terms of what would be expected experimentally.

6.2.3 Discussion

The hexagonal FZPA was compared to the circular FZPA in terms of the primary antenna performance characteristics. As expected, the circular FZPA had better radiation characteristics than the hexagonal FZPA. The directivity and sidelobe levels in the H-plane represented the most significant difference between the two structures.

The simulation results also showed that the hexagonal structure displayed the same general trends with increasing F/D . The peak directivity dropped, the first sidelobe levels increased, and the half-power beamwidths decreased.

6.3 FZPA with Alternating Hex-Cut Zones

In order to make a closer approximation to the circular FZPA, the hexagonal geometry was applied to the conventional FZPA in a different manner [6-2]. Starting from the outermost zone, alternate circular zones were trimmed, or cut, by an optimum hexagon. In this way, the actual shape of the zones becomes a mixture of the hexagonal and circular geometries. Figure 6-5(c) illustrates the alternating hex-cut zone FZPA in comparison with the circular FZPA (Figure 6-5(a)), and the hexagonal FZPA (Figure 6-5(b)).

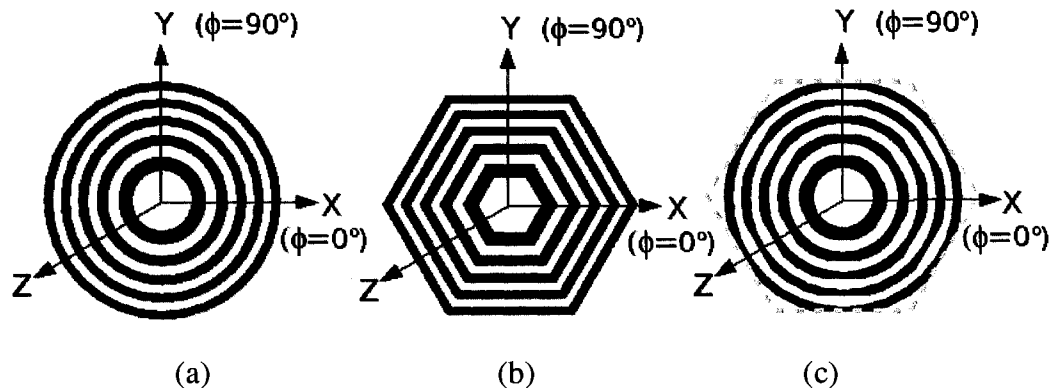


Figure 6-5: (a) Circular Zone FZPA, (b) Hexagonal Zone FZPA, (c) Alternating Hex-Cut Zone FZPA

There are several benefits to the alternating hex-cut zone approach. First, because the trimmed zones continue to have partial circularity and only alternate zones are cut, the radiation patterns and gain will not be significantly degraded from the conventional circular FZPA. Second, because the outer zone is trimmed to have hexagonal sides, the overlap problem is still minimized when the antenna is used as an element in an array. Finally, because some of the zones are not circularly symmetric, zone rotation is still possible for achieving the sidelobe control as will be demonstrated later in this chapter. This approach will therefore yield a FZPA which will have similar radiation performance to the conventional FZPA, but will have the added benefit of sidelobe control and will avoid overlap regions when used as an element in an array.

6.3.1 Creation & Simulation of Alternating Hex-Cut Zones

As in Section 6.2.1, the creation of the hex-cut zones required the determination of both the circular and hexagonal Fresnel zone dimensions. Once these dimensions were known, the two structures were overlaid and the perimeter of the circle was trimmed where it

intersected the hexagonal sides. Figure 6-6 illustrates this process by showing a single hexagonal zone overlaid on the circular one in (a), the circular zone being trimmed by the hexagon in (b), and the resulting hex-cut circular zone in (c). Applying this process to the alternate zones of a 10-zone, $F=3.75\lambda$, $F/D=0.237$ FZPA resulted in the geometry which was shown in Figure 6-5(c).

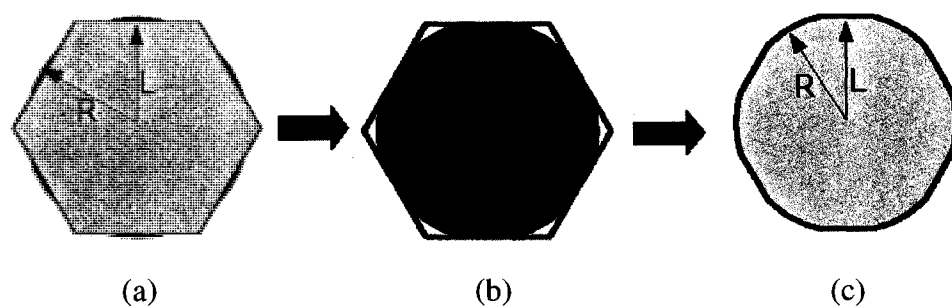


Figure 6-6: Method for Creating the Hex-Cut Zones

Simulations involved the antenna being again fed with an open-ended WR28 waveguide placed at the focal point and oriented such that the electric field vector was along the y -axis (Figure 6-2). Simulation results for the FZPA with alternating hex-cut zones were tabulated and compared to the results obtained for the conventional FZPA under similar simulation conditions. The primary parameters under investigation were the peak directivity and the relative maximum sidelobe level over all ϕ angles. Figures 6-7 and 6-8 illustrate this comparison in the H- and E-planes respectively.

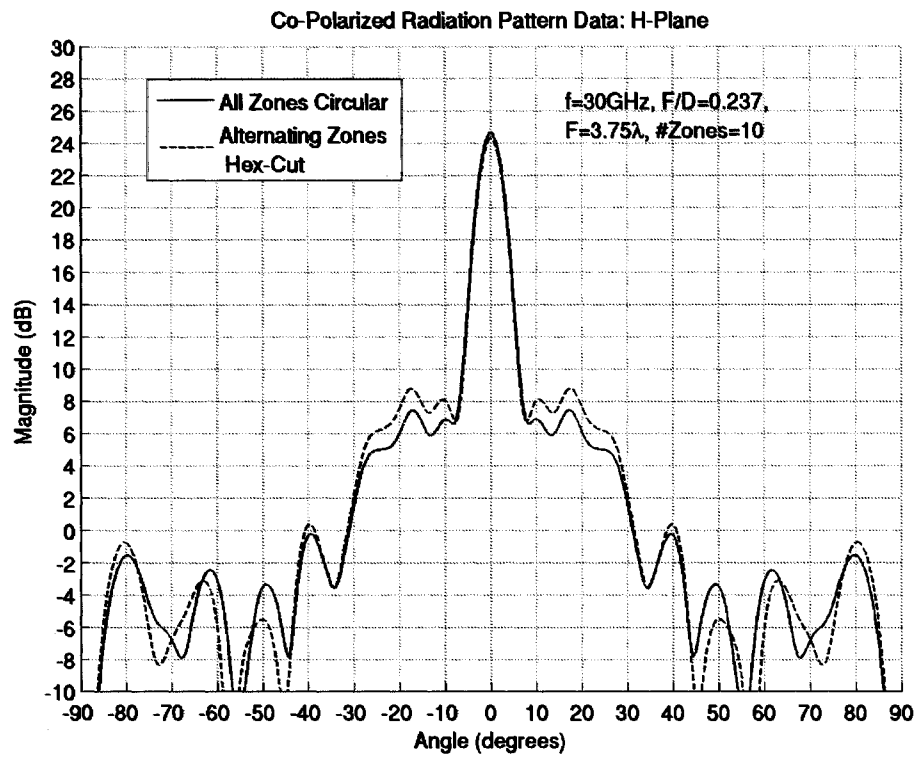


Figure 6-7: Comparison Between Circular and Alternating Hex-Cut FZPAs, H-Plane

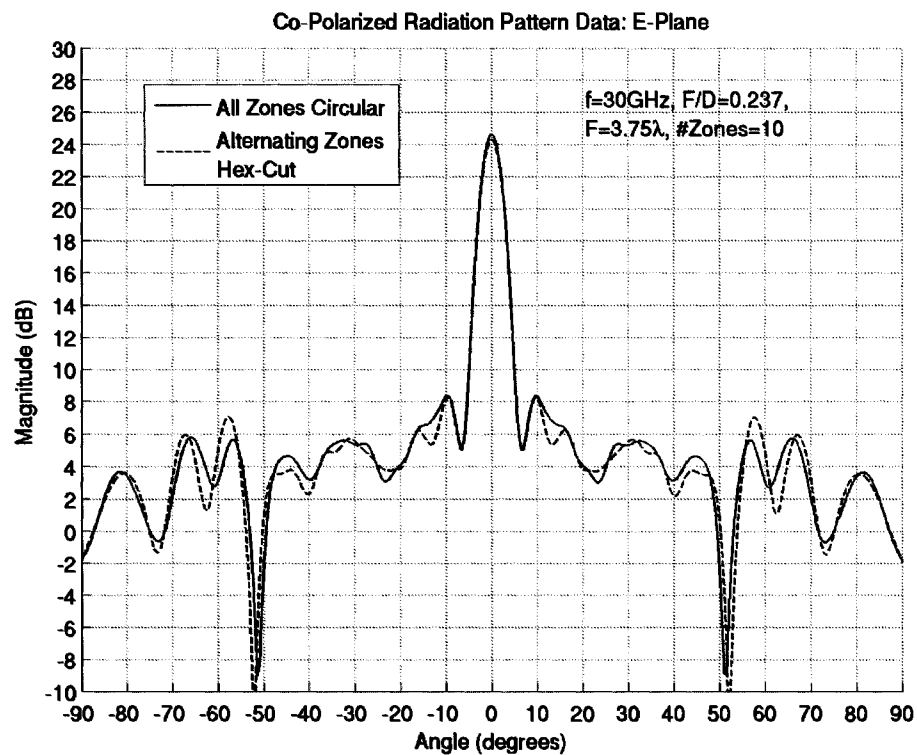


Figure 6-8: Comparison Between Circular and Alternating Hex-Cut FZPAs, E-Plane

Compared to the circular zone version, the FZPA with alternating hex-cut zones had a decreased peak directivity of only 0.32dB and it had an overall increased sidelobe level by only 0.73dB. These numbers were a significant improvement over those of the FZPA with hexagonal zones as reported in Section 6.2.2. Table 6-4 summarizes these results.

FZPA Configuration	Peak Directivity (dB)	Gain (dBi)	Relative Max. SLB over all ϕ (dB)
Conventional Circular Zones	24.65	22.19	-16.30
All Hexagonal Zones	21.52	19.00	-8.57
Alternating Hex-Cut Zones	24.33	21.92	-15.57

Table 6-4: Summary of Simulation Results

Simulation results also revealed that the size of the hexagon used to trim the circular zones had an impact on the peak directivity of the FZPA with alternating hex-cut zones. Removing too much of the circular zones would cause a decrease in the peak directivity. This was not surprising since removing more of the circular zones would leave less metal area which significantly changes the diffraction patterns. The optimal hexagon was found to yield the least amount of impact to the directivity.

6.4 FZPA with Rotated Alternating Hex-Cut Zones

The primary advantage of the alternating hex-cut zone FZPA configuration lies in the ability to control the sidelobe levels, something which cannot be done using conventional circular zones. The sidelobe control comes from rotating the alternating hex-cut zones with respect to each other. This concept was recently introduced in [2-35] for a square FZPA and is illustrated in Figure 6-9 for the 10-zone, $F=3.75\lambda$, $F/D=0.237$ case where

the alternating zones are hex-cut and rotated 0° , 30° , 15° , 30° , 0° from the outer most hex-cut zone to the inner most hex-cut zone.

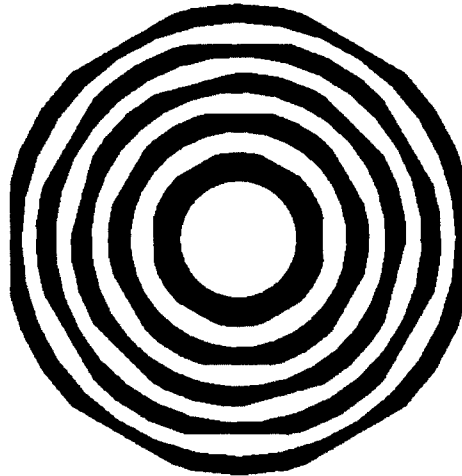


Figure 6-9: FZPA with Rotated Alternating Hex-Cut Zones

Many FZPAs with alternating hex-cut (AHC) zones were simulated with varying configurations of zone rotation to observe the effect on the peak directivity, sidelobe (SLB) levels, and cross-polarization (Xpol). All simulations involved the same antenna parameters: 10 zones, $F=3.75\lambda$, $F/D=0.237$. The same open ended WR28 waveguide was used to feed the lenses. It was placed at the focal point and again oriented such that the electric field vector pointed in the y-direction.

The maximum angle of zone rotation was 60° due to the symmetry of the structure. Table 6-5 summarizes a selection of these simulated results where the listings of rotation angles go from outer hex-cut zone to inner hex-cut zone. All rotations in the table are clockwise. It was found that rotations in the counter-clockwise direction produced the same results as those in the clockwise direction. Mixing the rotation direction from alternate hex-cut zone to alternate hex-cut zone did not produce desirable results. Each rotation in the

alternate direction effectively undid the effect from the previous rotation direction. Also, rotating only one zone, particularly the outer zones, proved to have very little effect on the sidelobes.

	FZPA Rotation Configuration	Peak Directivity (dB)	Relative Max. SLB over all ϕ (dB)	Relative Max. Xpol H/E-Plane (dB)
<i>A</i>	Conventional Circular Zones	24.65	-16.30	118.8 / 71.1
<i>B</i>	AHC: No Rotation	24.33	-15.57	125.9 / 73.2
<i>C</i>	AHC: All Rotated 30°	24.34	-16.03	56.4 / 54.1
<i>D</i>	AHC: 40°, 30°, 20°, 10°, 0°	24.36	-15.56	34.4 / 36.1
<i>E</i>	AHC: 0°, 10°, 20°, 30°, 40°	24.35	-15.53	34.5 / 36.1
<i>F</i>	AHC: 0°, 30°, 30°, 30°, 30°	24.34	-16.19	57.1 / 53.4
<i>G</i>	AHC: 0°, 0°, 0°, 0°, 30°	24.33	-16.23	121.7 / 73.1
<i>H</i>	AHC: 0°, 30°, 30°, 30°, 0°	24.33	-15.93	57.6 / 52.7
<i>J</i>	AHC: 0°, 30°, 15°, 30°, 0°	24.34	-16.42	40.4 / 40.9
<i>K</i>	AHC: 0°, 30°, 0°, 30°, 0°	24.34	-16.25	57.4 / 55.6

Table 6-5: Summary of Zone Rotation Simulation Results

The following observations were made from these results:

- The peak directivity was virtually unaffected by zone rotation.
- Rotation configuration *J* achieved a maximum sidelobe level over all ϕ better than the conventional circular FZPA by 0.12dB.
- The relative maximum cross-polarization level increased from the no rotation case where it was effectively in the noise. However, this maximum cross-polarization level was expected since without the symmetry, the

cross-polarization in the H- and E-planes would not cancel as it normally does in the symmetrical case.

Another interesting effect was that if the rotation was progressive from alternate hex-cut zone to alternate hex-cut zone, the sidelobes were found to form a pin-wheel around the main beam while smearing along the direction of zone rotation. However, if the rotation was not progressive, the sidelobe smearing would not occur. Figure 6-10 illustrates this effect by showing a 3D far-field radiation pattern for three different cases, each cut at -18.5dB from the normalized peak. Figure 6-10(c) shows the case that achieved the best overall sidelobe level (case *J*). In this case, the sidelobe smearing was minimal, but there was a slight tilt in the rotation direction instead.

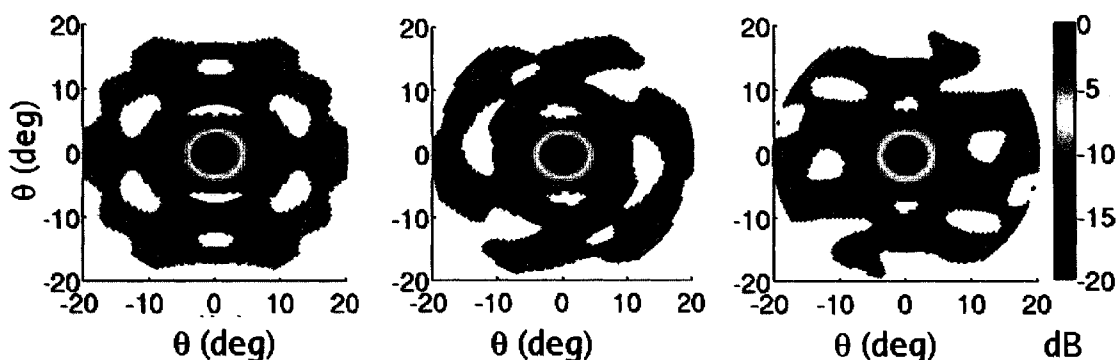


Figure 6-10: Effect of Zone Rotation on Sidelobe: (a) Case *B*, (b) Case *E*, (c) Case *J*

These simulation results showed that the conventional FZPA can have enhanced capability when alternate zones are hex-cut and then specifically rotated with respect to each other. Depending on the exact rotation configuration of the hex-cut zones, the sidelobes can be moved in nearly any direction and can also be smeared with one another. In this way, the designer can effectively place the sidelobes in a desired location.

Also, the enhanced capability comes with virtually the same radiation pattern characteristics as the conventional FZPA. Rotating the alternate hex-cut zones does not significantly degrade the radiation patterns or gain of the FZPA. This could be quite useful for antennas in applications where a specific sidelobe template is required.

6.5 Measurement Results

Three FZPAs were selected from Table 6-5 for fabrication and testing. The first was the conventional circular FZPA (case *A*), the second consisted of alternating hex-cut zones (case *B*), and third represented the best sidelobe case of the alternating hex-cut zone rotation configurations (case *J*). Each antenna was made in a similar fashion to the antennas in Chapter 4. They used the same zone radii as in the simulations and were etched on a 0.005" thick FR4 material. The antennas were mounted on the same custom-made test fixture as in Chapter 4 and also used the same tapered open-ended WR28 waveguide feed. Figure 4-10 in Chapter 4 shows an illustration of the test set-up and the measured feed patterns.

Figures 6-11, 6-12, and 6-13 show a direct comparison between the normalized measured radiation pattern compared to the same normalized simulated pattern in the H-plane. Figure 6-11 is the case of the conventional circular zones (case *A*), Figure 6-12 is the case of the no-rotation FZPA with alternating hex-cut zones (case *B*), and Figure 6-13 is the case of the FZPA with rotated hex-cut zones (case *J*). The simulated patterns in all cases predicted the shape of the measured radiation pattern with a high degree of accuracy, even in the sidelobe region. The minor differences between the two curves was likely due to the fact that the FR4 and the test fixture were not included in the simulations.

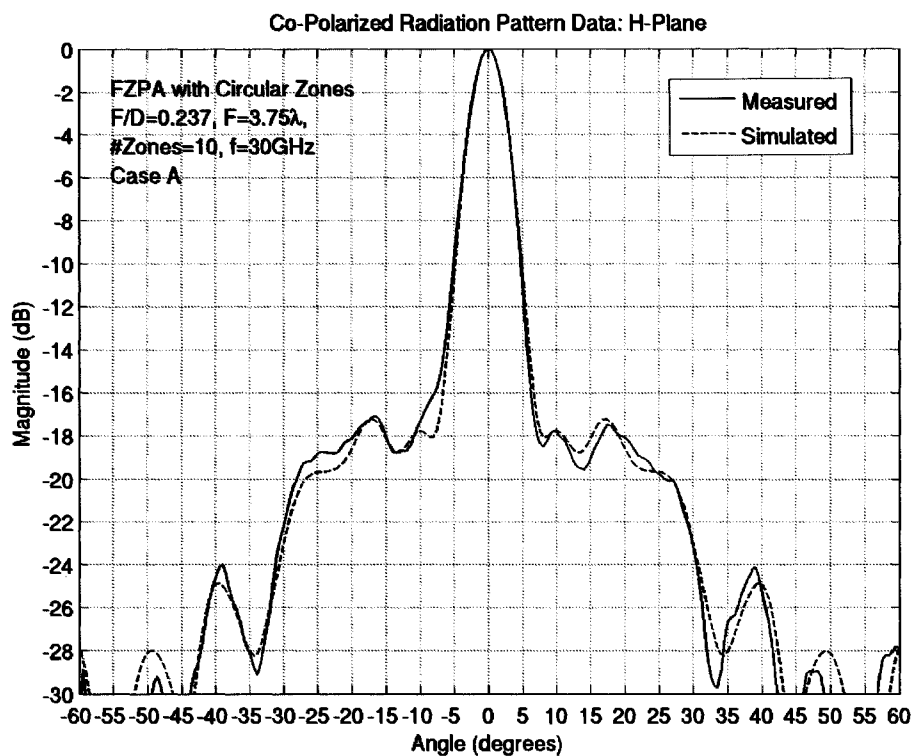


Figure 6-11: Comparison of Measured vs. Simulated Results for Case A, H-Plane

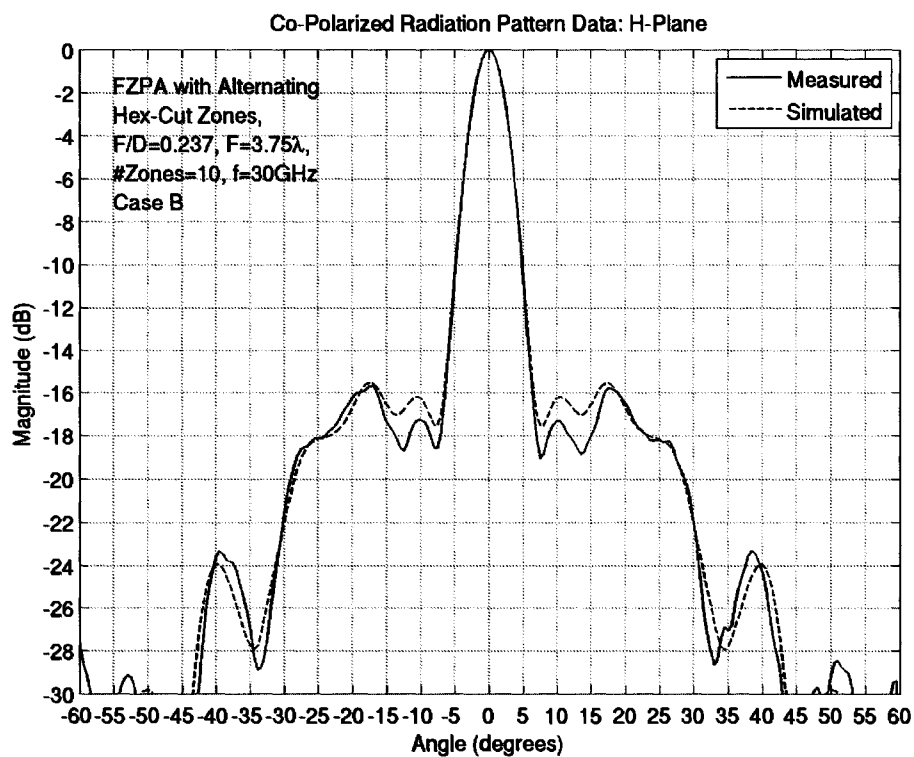


Figure 6-12: Comparison of Measured vs. Simulated Results for Case B, H-Plane

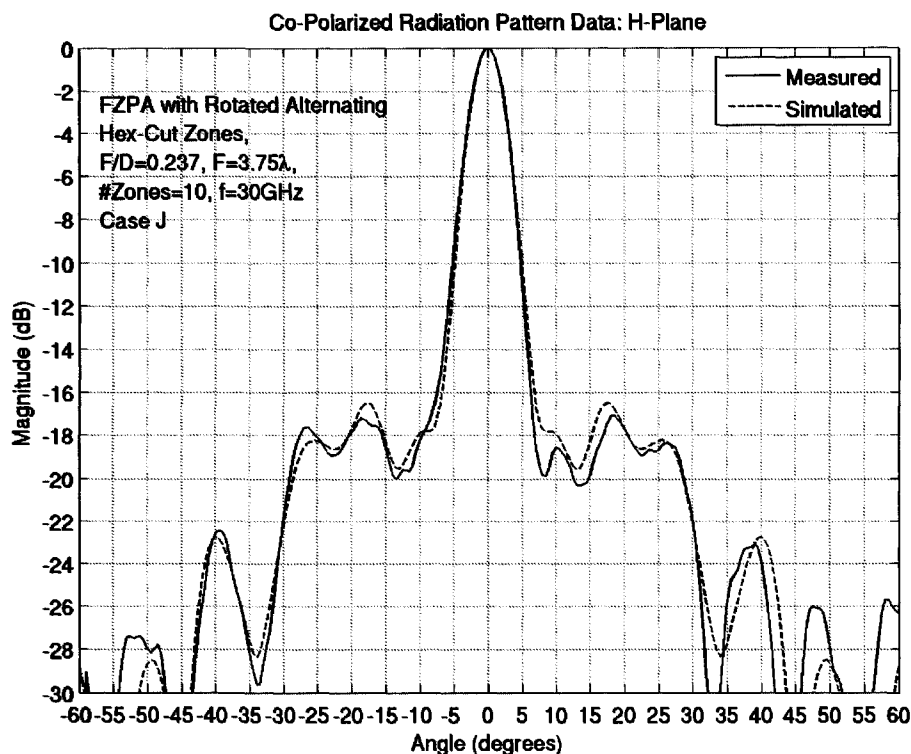


Figure 6-13: Comparison of Measured vs. Simulated Results for Case *J*, H-Plane

Table 6-6 shows a summary of the measured results for the three antenna configurations at 30GHz. These results can be compared to those in Tables 6-4 and 6-5. The measured results confirmed that the gain was minimally affected by the zone rotation and that the rotation case *J* yielded the best overall sidelobe level and the highest overall cross-polarization level compared to the conventional circular FZPA version.

FZPA Configuration	Peak Gain (dBi)	Relative Max. SLB over all ϕ (dB)
Conventional Circular Zones (Case A)	21.07	-15.28
No Rotation AHC Zones (Case B)	20.76	-15.68
Rotated AHC (Case J)	20.77	-16.00

Table 6-6: Summary of Measured Results

6.6 Conclusion

This chapter investigated the performance of the FZPA with hexagonal and alternating hex-cut zones. The idea behind changing the zone shape from circular to hexagonal was to enable both sidelobe control and better packing for elements in an array. However, since the hexagonal FPZA was inherently only an approximation to the circular FZPA, it had a lower directivity, higher sidelobe levels, larger 3dB beamwidths, and higher cross-polarization levels compared to the circular version.

In order to maintain the benefits of the hexagonal shape but bring the radiation characteristics closer to those of the circular FZPA, alternating hex-cut zones were proposed. The concept of trimming the standard circular zones by an optimum hexagon was explained. Simulations were performed which showed that the radiation patterns and gain for the alternating hex-cut zone FZPA were very close to the circular zone version. This confirmed that hex-cut circular zones, as opposed to hexagonal zones, would not excessively degrade the radiation patterns.

Once the FZPA with alternating hex-cut zones was proven to be similar to the circular FZPA, attention was turned to modifying this structure to control the sidelobe levels and locations. This control was achieved by rotating the alternate hex-cut zones with respect to each other. Simulations of the FZPA with rotated alternating hex-cut zones revealed that the level and location of the inner sidelobes can be controlled under certain rotation configurations. The simulations also revealed that this control comes without sacrificing the antenna's radiation pattern characteristics. Measurements were performed and were found to match closely with the simulated results. This work confirmed that the FZPA

with alternating hex-cut zones offers a sidelobe control advantage over the conventional FZPA for applications in terrestrial wireless and satellite.

CHAPTER 7

REFLECTOR-BACKED FZPA

7.1 Introduction

In its conventional orientation, the FZPA has a low aperture efficiency (on the order of 10%) compared to shaped lenses, parabolic reflectors, and planar arrays. This is a result of the significant amount of EM waves that are blocked by the metal zones. Several methods have been developed over the last few decades to improve the aperture efficiency of the FZPA [2-15, 2-16]. One method of particular interest involved a reflecting surface placed a quarter wavelength behind the FZPA aperture. This structure was outlined in Section 2.3.1 and is formally known as the reflecting or folded FZPA. The reflecting surface effectively converts the antenna into a reflector, similar to a parabolic antenna. The radiation that diffracts through the transparent zones is reflected so that it is in phase with the radiation that was reflected off the metal zones. This technique enhances the aperture efficiency by about two-fold since there is less wasted radiation [2-10, 2-23, 2-24, 2-25]. The reflecting FZPA is shown in Figure 7-1(b) compared to the conventional transmission mode version in Figure 7-1(a). Despite this improvement, however, the reflecting FZPA is still not very attractive due to the

blockage created by the feed and the additional support arm required to hold the feed and the ground plane in place.

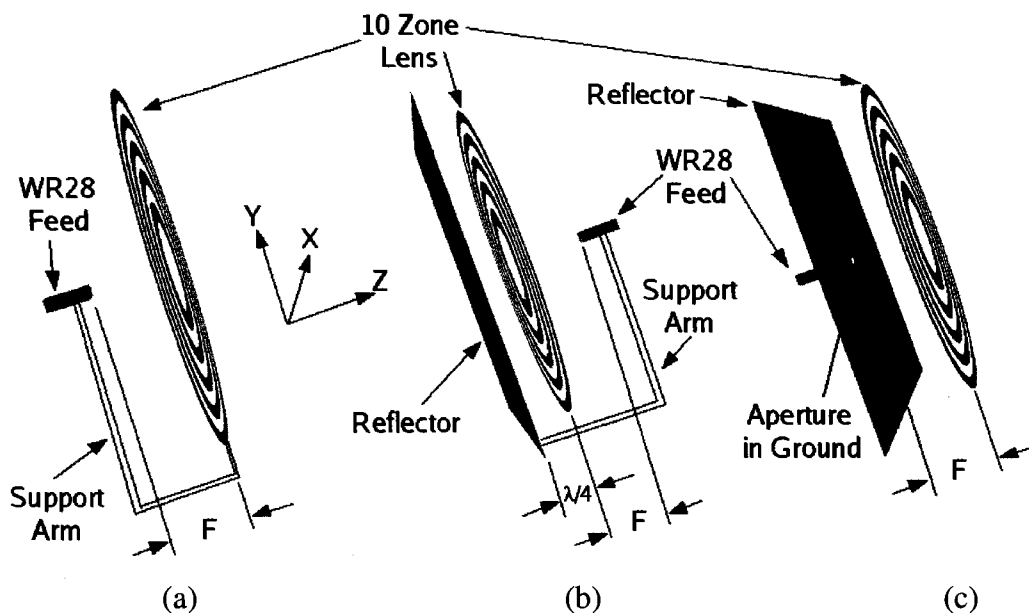


Figure 7-1: (a) Conventional FZPA, (b) Reflecting FZPA, (c) Reflector-Backed FZPA

In this chapter, an alternative feed method will be described which enhances the aperture efficiency of the FZPA in transmit mode, eliminates the support arm for the feed and also allows for a potentially significant reduction in profile. This new antenna is called the reflector-backed FZPA [7-1]. Instead of placing a reflecting surface behind the FZPA, it was placed at the aperture of the feed antenna as shown in Figure 7-1(c). With this geometry, the FZPA could be fed using a planar antenna such as a microstrip patch array. In this way, if the focal distance was decreased, the feed, a layer of foam to act as an air spacer, and the lens could all be sandwiched together to yield an attractive compact package, which would be comparable to a planar array in profile.

7.2 Reflector-Backed FZPA Geometry & Modeling

The FZPA used in this investigation consisted of 10 zones with $F=3.75\lambda$ and $F/D=0.237$. The radii of the FZPA zones were determined using Equation 2-5. The FZPAs were designed and modeled at 30GHz with perfect conductors for the metal zones and reflecting surface.

An open-ended WR28 waveguide with a ground plane around the aperture was used to feed the FZPAs and was placed at the lens focal point. A waveguide feed was again chosen to simplify the model and focus on the effect of the ground plane. The ground plane size was set at 15.8cm x 15.8cm square, where each side corresponded to the diameter of the outer zone of the 10-zone FZPA. The waveguide was oriented such that the electric field vector was along the y-axis, as defined in Figure 7-1.

7.3 Simulation Results

7.3.1 Feed Radiation Patterns

The simulated radiation patterns for the isolated waveguide feed with and without the ground plane are shown in Figure 7-2. The peak directivity of the feed at 30GHz, without the ground plane, was about 7.2dB with 10dB beamwidths of 122° in the H-plane and 196° in the E-plane. When the ground plane was included the directivity of the waveguide at 30GHz dropped to 6.3dB (avg.) with a 0.9dB peak-to-peak ripple. The ripples were due to the scattering from the edges of the finite ground plane. Also, the 10dB beamwidths changed to 126° and 187° in the H- and E-planes respectively.

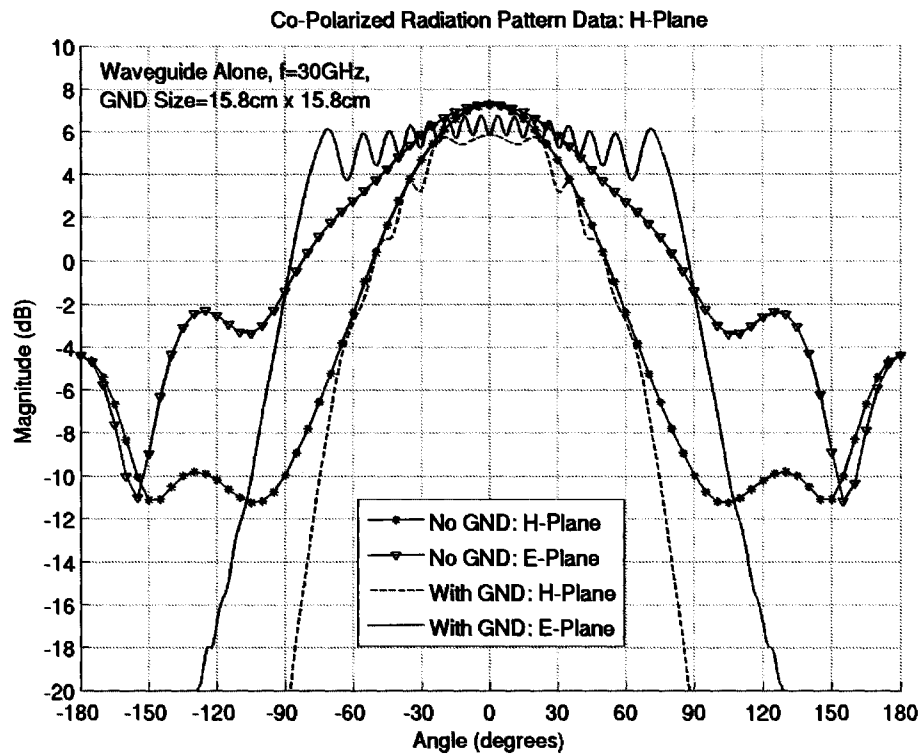


Figure 7-2: Radiation Patterns of the Waveguide With and Without the Ground Plane

Since the 10dB beamwidths were slightly different with the ground plane than without the ground plane, it was important to verify that the change in directivity was caused by the ground plane and not by the change in beamwidth. To that end, a smaller waveguide was modeled to have the same directivity as it would in the infinite ground plane case. This waveguide was then used to feed a FZPA without a ground plane having 10 zones, $F=3.75\lambda$, $F/D=0.237$. Figure 7-3 shows this result where it can be seen that there is virtually no difference between the two directivities.

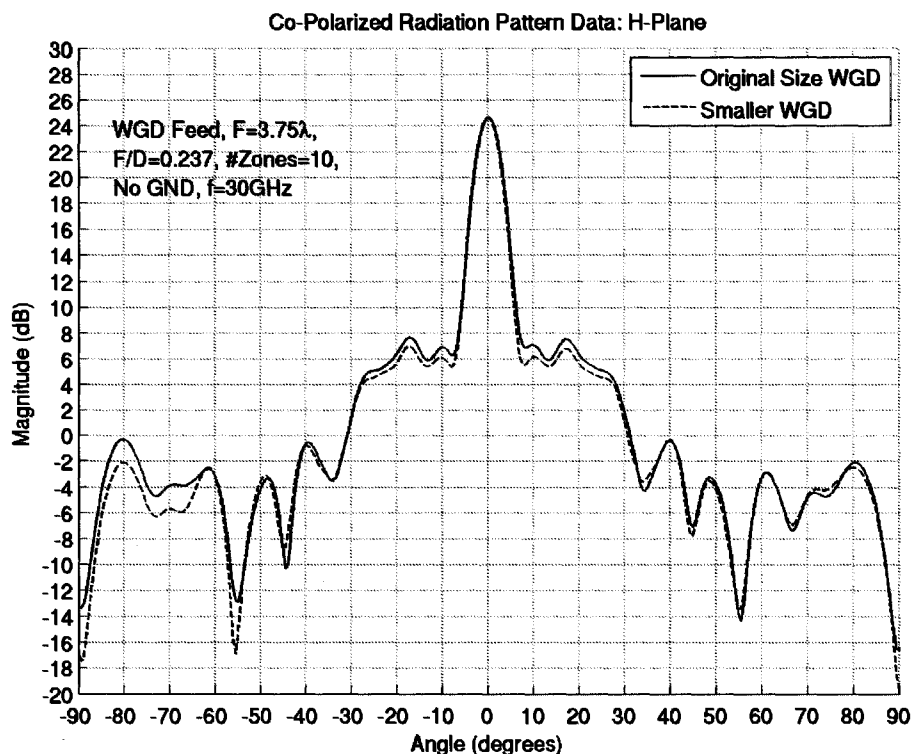


Figure 7-3: Radiation Patterns of the FZPA with Original and Smaller Waveguide

This result means that the directivity change was related to the addition of the ground plane and not the change in beamwidth of the waveguide. In other words, the differences in beamwidth between the waveguide with and without the ground plane were found to have very little impact on the directivity of the FZPA.

7.3.2 Reflector-Backed FZPA Radiation Patterns

Figures 7-4 and 7-5 show a simulated comparison at 30GHz of the H- and E-plane radiation patterns between two identical 10-zone FZPAs where one has the ground plane at the aperture of the waveguide feed and the other does not have the ground plane. The addition of the ground plane improved the peak directivity at 30GHz by about 1.3dB. It also lowered the overall sidelobe level by nearly 2dB and lowered the sidelobes in the

principle planes by 3dB. As a result of the directivity improvement, the aperture efficiency also improved from 12% to 16% when the ground plane was included.

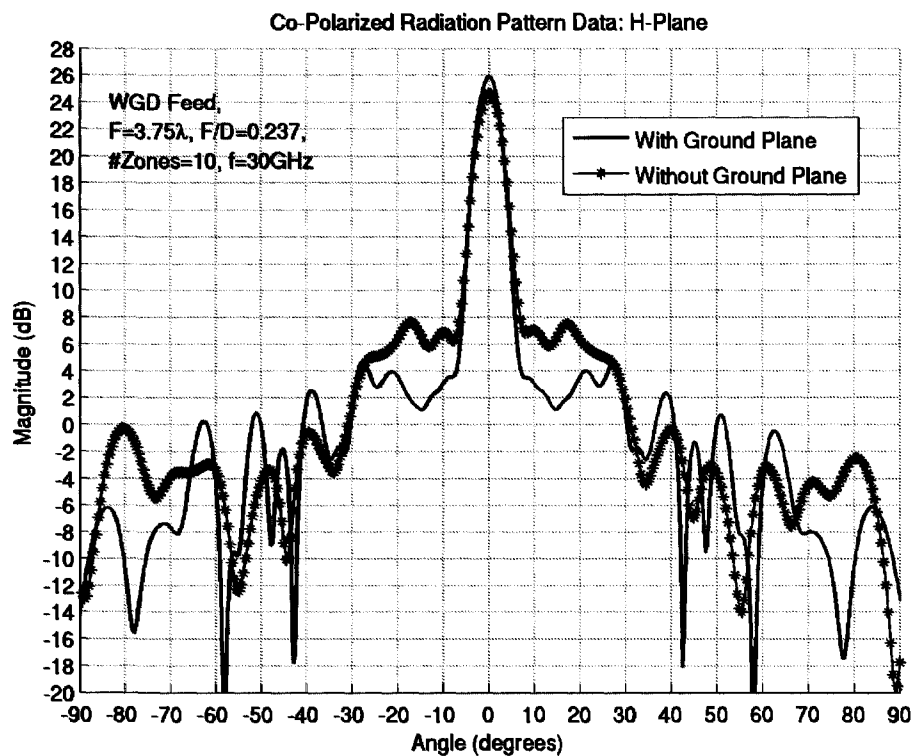


Figure 7-4: 10-Zone FZPA With and Without the Ground Plane, H-Plane

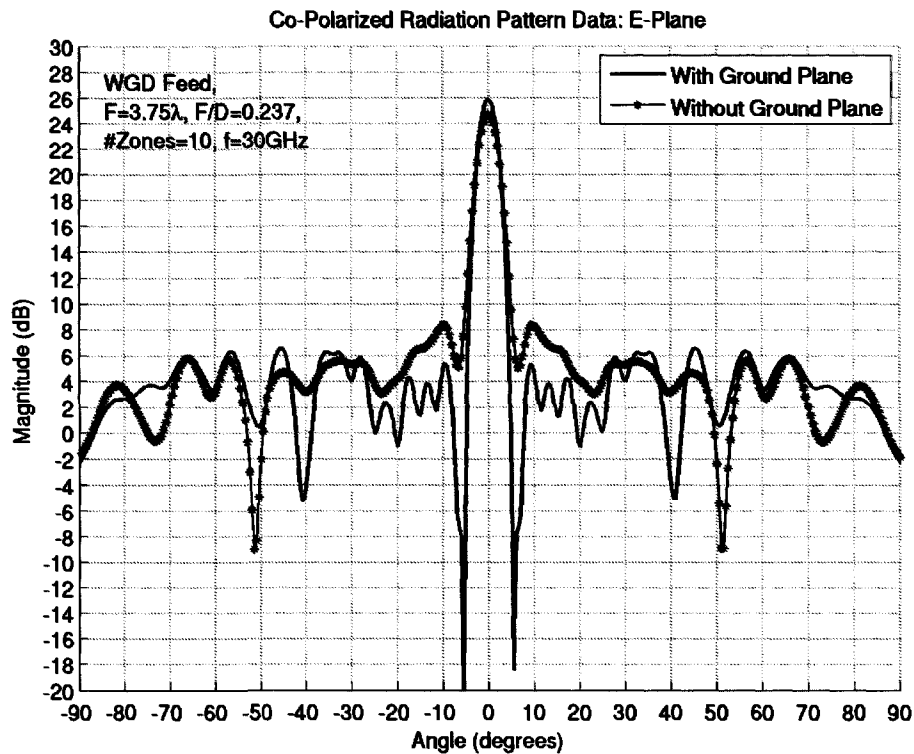


Figure 7-5: 10-Zone FZPA With and Without the Ground Plane, E-Plane

The improvement was related to the interference of the re-scattered fields from the ground plane. The fields that were initially reflected off the metal zones of the FZPA were being re-reflected by the ground plane and then either diffracted through the air zones or reflected again off the metal zones. The re-reflected fields that diffracted through the air zones contributed to the increase in peak directivity and the re-reflected fields that reflected again off the metal zones caused further interference of fields between the lens and ground plane.

Figure 7-6 shows how the peak directivity varied with frequency. When the ground plane was included, the frequency response of the peak directivity was not smooth as in the case without the ground plane. The cause of this was related to the fact that the fields

between the FZPA and the ground plane were adding constructively and destructively depending on the frequency. This indicated that the antenna's ability to focus the incoming radiation was more frequency sensitive when there was a ground plane.

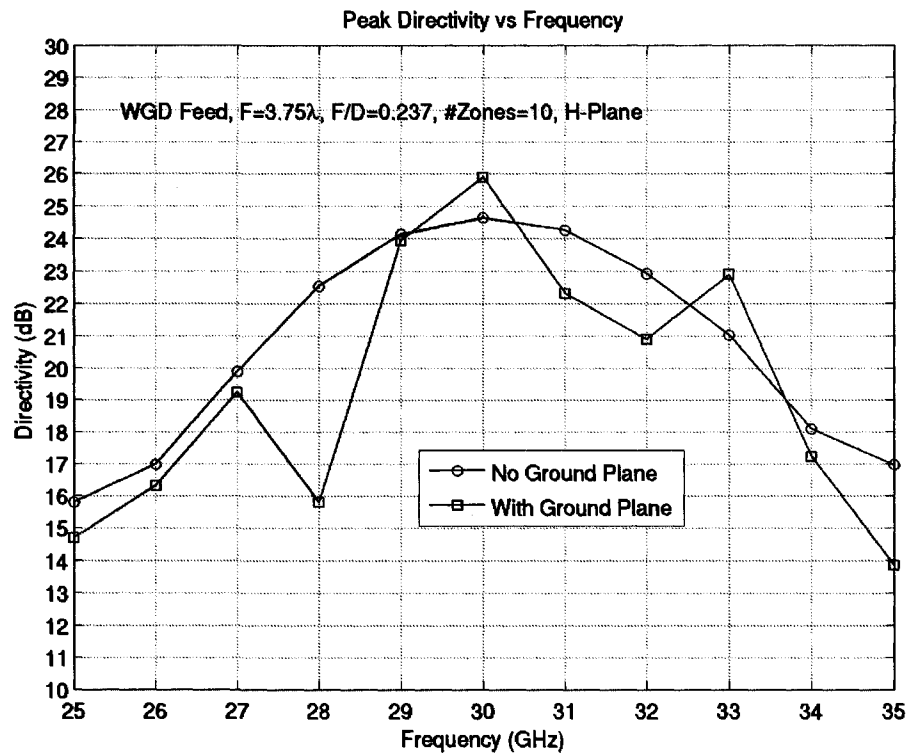


Figure 7-6: Peak Directivity vs. Frequency With and Without Ground Plane, H-Plane

7.3.3 Circular Ground Plane

The shape of the ground plane used in the previous sections was square since the original idea was derived from using a microstrip patch array feed. However, there was no reason that the ground plane must remain square. A more compact package for a FZPA with circular zones would likely involve a circular ground plane.

Several simulations were undertaken to investigate the difference between the square and

circular ground planes. The circular ground plane was given a diameter equal to the outer zone of the FPZA, which corresponded to the side of the original square shaped ground plane. In this configuration, the square ground would have slightly more area which could lead to as much as 1dB more directivity.

The simulations showed that the square version had higher directivity by 0.5dB as shown in Figure 7-7 for the H-plane. Since 0.5dB was less than the 1dB that was possible based on the area difference, other factors contributed to making the radiation patterns different such as the different scattering off the ground plane edges. In any case, the results revealed that there was very little difference between the two after the area differences were accounted for. The square ground plane was thus used in all future simulation work due to modeling simplicity.

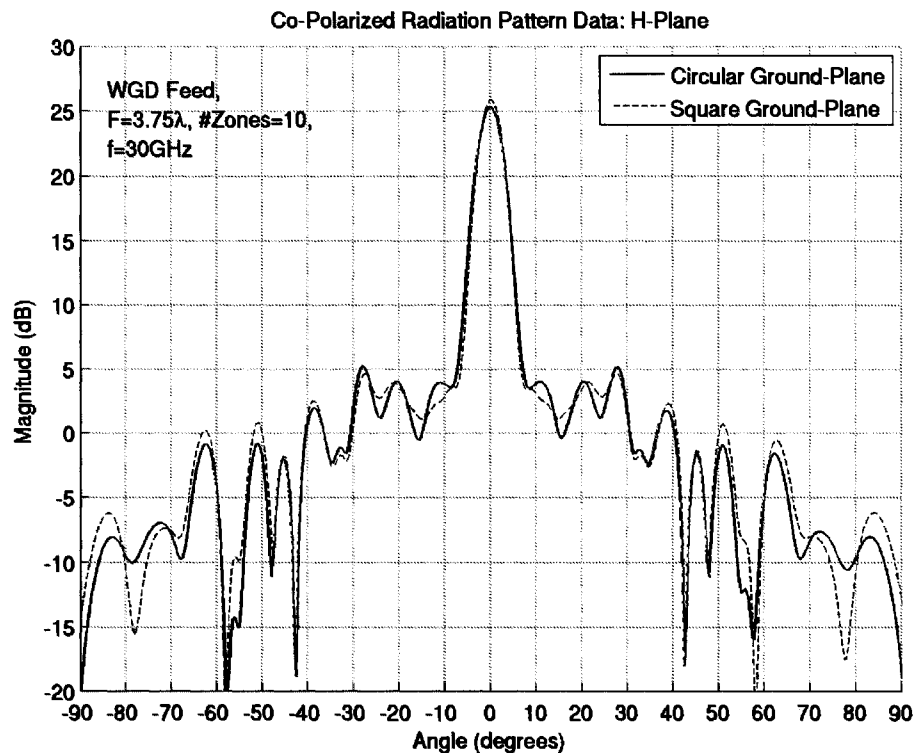


Figure 7-7: 10-Zone FZPA With Circular and Square Ground Plane, H-Plane

7.4 Measurement Results

In order to verify the simulated results, the 10-zone, $F=3.75\lambda$, $F/D=0.237$ FZPA was fabricated. The antenna was fabricated in the same way as was done in Chapter 4 and was tested using the same custom-made test fixture and tapered open-ended WR28 waveguide feed. The test set-up in the near-field chamber was also illustrated in Chapter 4.

Figures 7-8 and 7-9 show a normalized comparison between the measured and simulated results of the 10-zone FZPA without the ground plane in the H- and E-planes respectively. Generally, the two curves matched very closely, particularly in the area of the main beam. The measured peak gain was lower by about 1dB compared to the simulated gain.

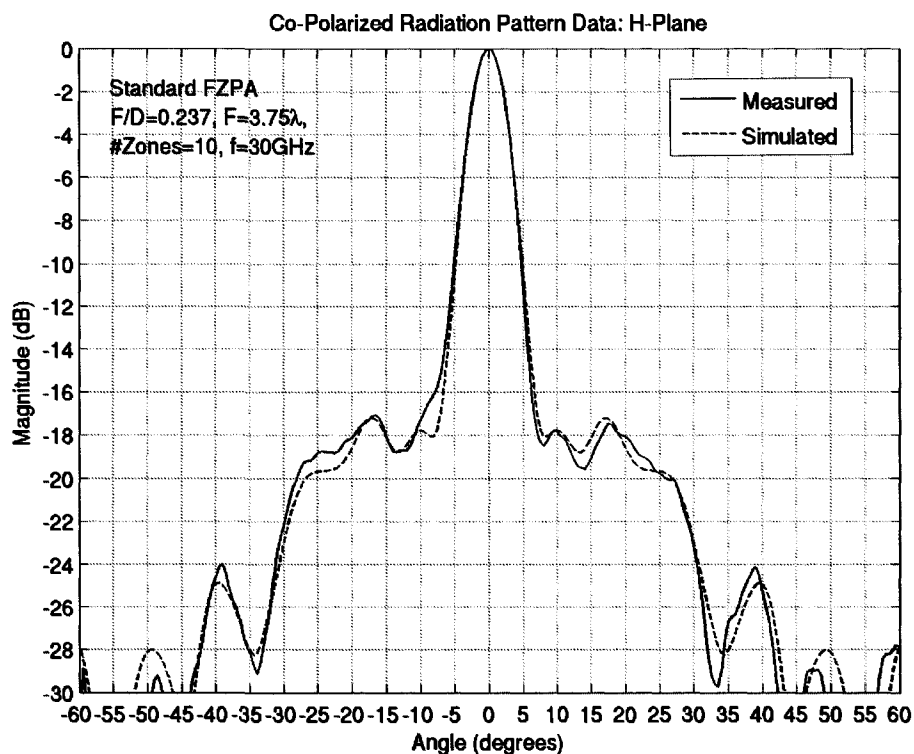


Figure 7-8: Comparison Between Measured and Simulated Results, H-Plane

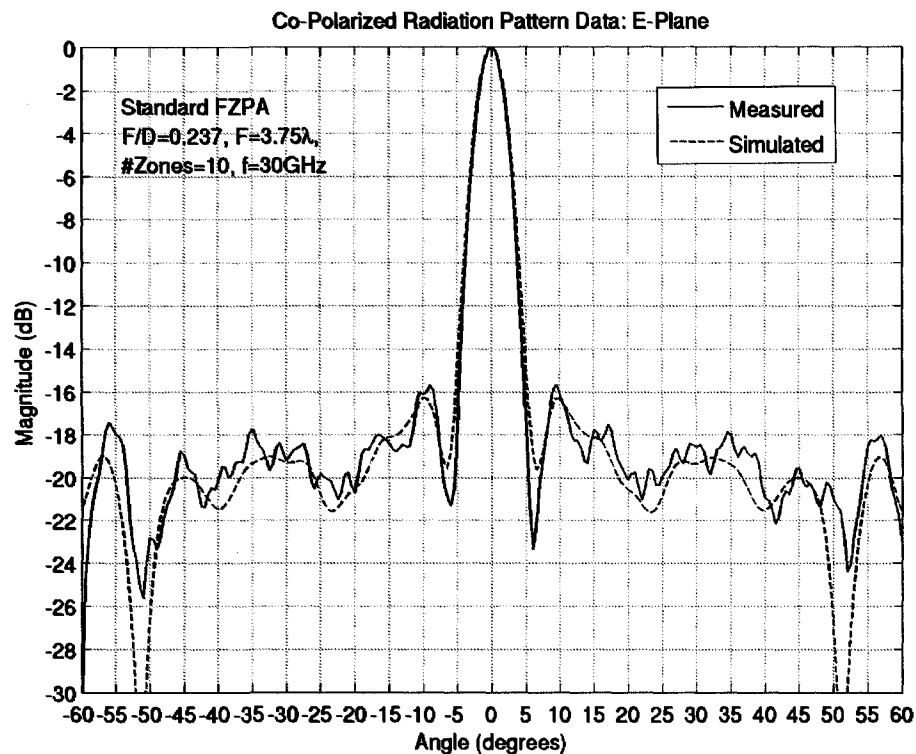


Figure 7-9: Comparison Between Measured and Simulated Results, E-Plane

The minor differences in the gain and sidelobe areas were likely due to the fact that the simulation model did not include either the FR4 material or the test structure. Based on these results, there was a high level of confidence in the FZPA simulations.

7.5 Conclusion

This chapter presented a novel reflector-backed FZPA. The structure was created by placing a ground plane at the aperture of the waveguide feed in order to re-reflect the radiation that was originally reflected off the metal zones of the FZPA. Simulations showed that the FZPA with a reflector, or ground plane, at the aperture of the feed had a higher directivity by about 1.3dB, better overall sidelobes by about 2dB, and an aperture efficiency which improved by about 4%, which is 33% better than the FZPA without the

ground plane. The reflector-backed FZPA has the potential to allow an efficient low-profile design comparable to a microstrip patch array. This would involve using a microstrip antenna feed instead of the waveguide and the FZPA would need a small focal length.

CHAPTER 8

LOW-PROFILE FZPA

8.1 Introduction

Another disadvantage of the FZPA in its conventional configuration is its relatively large physical volume compared to planar arrays. Similar to shaped lenses and parabolic reflectors, the FZPA has a depth dimension due to the location of the feed antenna relative to the aperture. This distance is dictated by the lens focal distance, which is typically several wavelengths long, and significant when compared to a planar array.

This chapter is focused on addressing the large physical volume of the FZPA by examining several lower profile configurations. The focal distance of the FZPA was progressively decreased and the effect on the antenna's radiation patterns, peak directivity, and aperture efficiency was observed [8-1, 8-2]. All structures were simulated in the Ka-band and measurements were performed to verify the simulations. Also, a comparison between the FZPA and the low-profile superstrate antenna will be presented and discussed.

8.2 FZPA with Small Focal Distances

The geometry of the FZPA used for this study was based on the reflector-backed FZPA described in Chapter 7, which incorporates a ground plane at the aperture of the waveguide feed. This structure was chosen since it not only has an improved aperture efficiency, but, more importantly, it offers the best possibility of obtaining a low profile structure.

While studying the effect of reducing the focal distance it was important to determine how small the focal distance could be before the radiation patterns deteriorated excessively. It was expected that the key factors contributing to the degradation would be the aperture illumination and the effect of fields reflecting off the ground plane. The aperture illumination problem arises because the same feed was used for all simulations despite it not providing 10dB edge illumination for all cases. This would mean that the antenna aperture would not be entirely illuminated for the smaller focal distances, as illustrated in Figure 8-1(a). The outer zones of the FZPA would therefore receive less energy and thus may not be required. The number of zones would be an important factor in this part of the study.

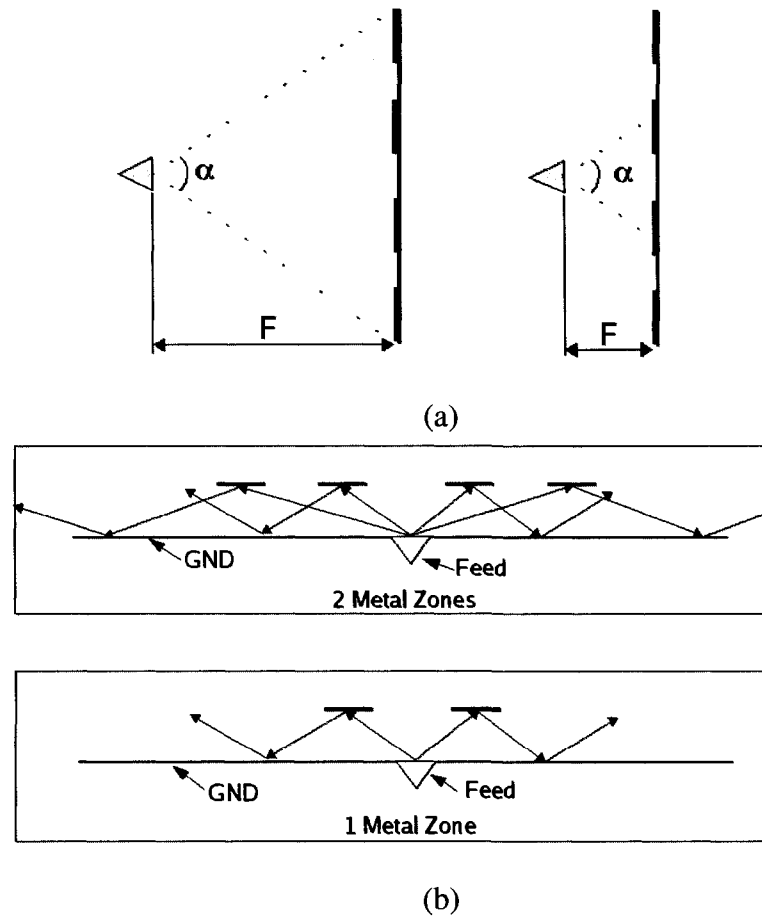


Figure 8-1: (a) Aperture Illumination Issue, (b) Ground Plane Reflection Issue

The presence of the ground plane around the feed results in multiple reflections between the FZPA and ground plane. This multiple reflection effect is also related to the number of zones and occurs because the ground plane in the study was fixed at a certain size for all cases. If there is a small number of zones, then there will be less reflections off the ground plane than if there are more zones where the reflection effect spreads out farther along the ground plane. It was expected that this would cause a change in the effective area of the antenna. Figure 8-1(b) illustrates this concept.

8.2.1 Simulation Model

Similar to models described in previous chapters, the FZPAs were designed at 30GHz and modeled at frequencies from 25GHz to 35GHz with a perfect conductor for the metal zones. Simulations were carried out for FZPAs ranging from one to five metal zones. The focal distance of the FZPA was decreased from 3.75λ to 0.25λ and, for each focal distance, the radii of the metal zones were re-computed using Equation 2-5. As noted in Chapter 2, this equation is only valid for large focal distances. It depends on the principle of ray-tracing, which requires that the rays make small angles with the focal axis so that they can be paraxial. In the case of the small focal distances used in this chapter, the accuracy of Equation 2-5 is unknown and will be tested.

Similar to Chapter 7, a ground plane was placed around an open-ended WR28 waveguide aperture to feed the FZPAs and was placed at the focal point. The ground plane dimensions were chosen to be 15.8cm x 15.8cm where the 15.8cm represents the largest metal zone diameter of the lenses under consideration. The waveguide was oriented such that the electric field vector was along the y-axis, as shown in Figure 8-2. Since the H- and E-field patterns of the waveguide were not symmetrical, it was expected that the patterns of the lens would also not be symmetrical.

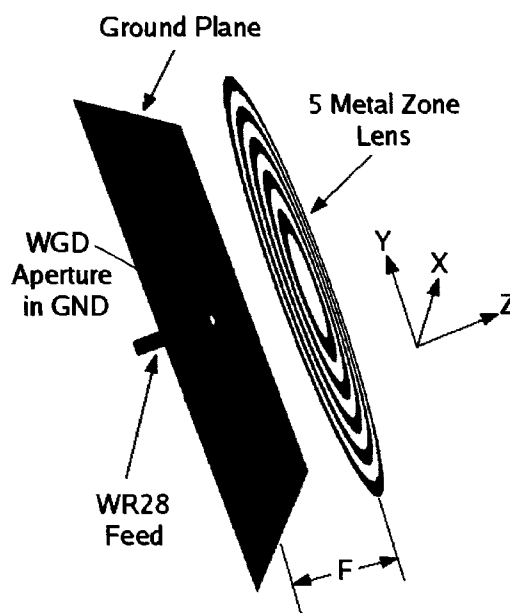


Figure 8-2: FZPA with Ground Plane Surrounding Waveguide Aperture

8.2.2 Focal Spacing Decrement Considerations

It was important to first consider what decrement of focal distance should be used to yield in-phase radiation at 30GHz. A ray-tracing analysis of the structure revealed that spacing with odd multiples of 0.25λ between the feed and the FZPA aperture would enable in-phase radiation. Figures 8-3 and 8-4 illustrate, for the single metal zone case, the peak directivity variance with frequency where the difference between using even (0.5λ , 1.0λ , etc...) and odd multiple (0.25λ , 0.75λ , etc...) of 0.25λ spacing respectively is highlighted. As expected, the peak directivity for focal distance spacings having even multiples of 0.25λ , dropped substantially at 30GHz. This drop was due to the phase cancellation between radiation that diffracted through the air zones directly from the feed and the radiation that reflected off the metal zones, then re-reflected off the ground plane and eventually diffracted back through an air zone. These two types of radiation were 180° out of phase at 30GHz when the spacing between the ground plane and the FZPA aperture was even multiples of 0.25λ .

The focal distances shown in Figure 8-4, which were for odd multiples of 0.25λ , showed no phase cancellation at 30GHz since the reflected and direct radiations were in-phase. This figure also shows phase cancellations at other frequencies, such as 28GHz and 32GHz for the 3.75λ focal distance case, where the focal distance became an even multiple of 0.25λ due to the wavelength change. The band between these phase cancellations increased as the focal distance decreased such that for focal distances below 0.75λ , the cancellations did not occur between 25GHz and 35GHz.

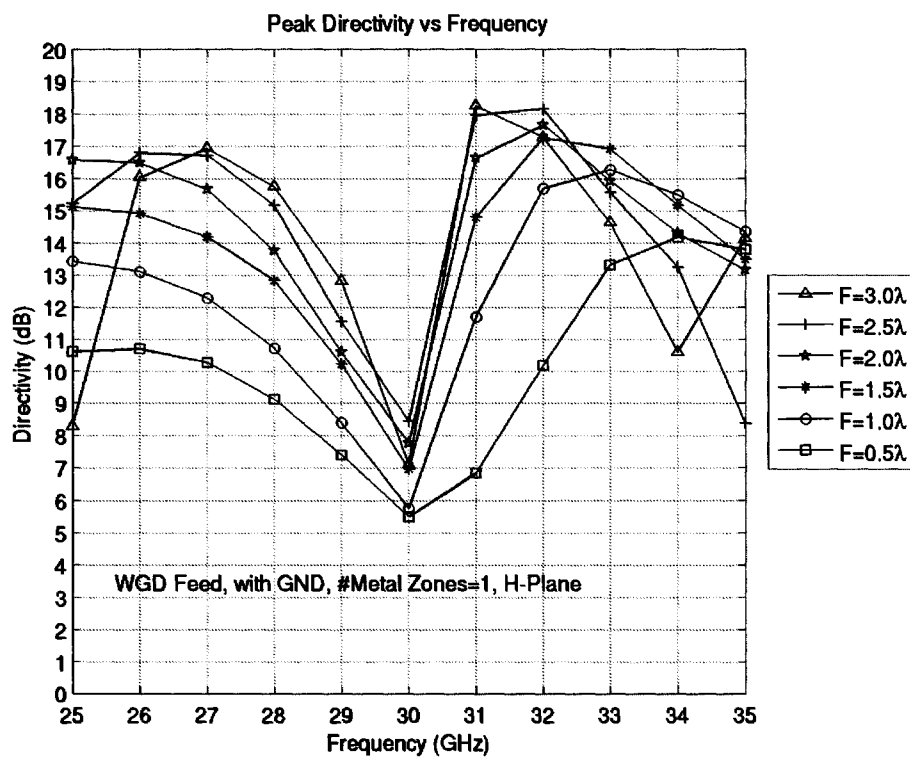


Figure 8-3: Peak Directivity vs. Frequency for F with Even Multiples of 0.25λ

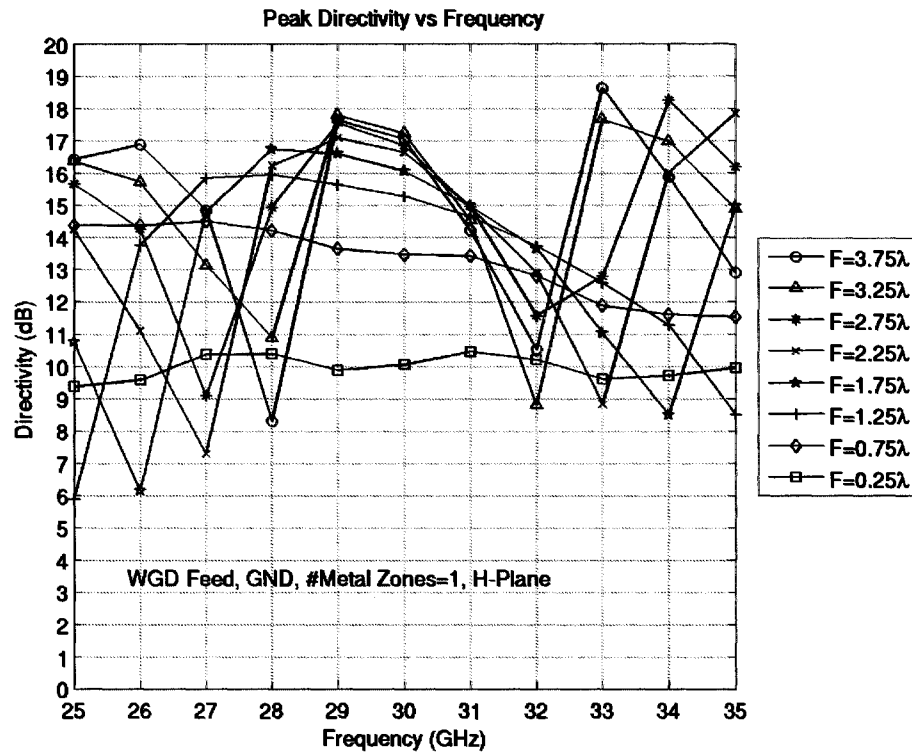


Figure 8-4: Peak Directivity vs. Frequency for F with Odd Multiples of 0.25λ

Figure 8-4 also highlights the fact that the frequency where the maximum peak directivity occurred was not the same for each focal distance. Certain focal distances were therefore more optimal than others for focusing the fields at certain frequencies. This shift in frequency was likely related to the fact that the zone radii were not the proper size to obtain the peak at the designed frequency of 30GHz. This was expected based on the approximation in Equation 2-5 with small focal distances. However, despite this slight shift in frequency, the radii computed based on Equation 2-5 were fairly close to the correct values meaning that Equation 2-5 can be used with only minor tuning required.

8.2.3 Peak Directivity vs. Number of Metal Zones

The effect of the number of metal zones on the peak directivity is shown in Figure 8-5 for focal distances which were decreasing by odd multiples of 0.25λ . The first observation was that the directivity decreased with decreasing focal distance. This was expected since the aperture size was also decreasing due to the relationship between the focal distance and the radii given in Equation 2-5. However, the cases with focal distances below 1.25λ showed directivity decreases at 30GHz which were more than what was expected based on the aperture change. This additional drop was thought to be related mostly to the aperture illumination effect since very little of the aperture was being illuminated at these small focal distances. The inaccurate radii dimensions due to Equation 2-5 being out of range could also be contributing to this additional drop in directivity.

When the focal distance spacing reached 0.25λ , the directivity was only a few decibels higher than that of the feed and the shape of the radiation pattern was very similar to the feed's pattern, which was not the case for the other focal distances. At this small focal distance, components of the near field were involved, which meant that standard interference techniques such as geometrical optics did not apply [5-2]. In this case, the FZPA tended to behave more like a leaky-wave structure [5-3].

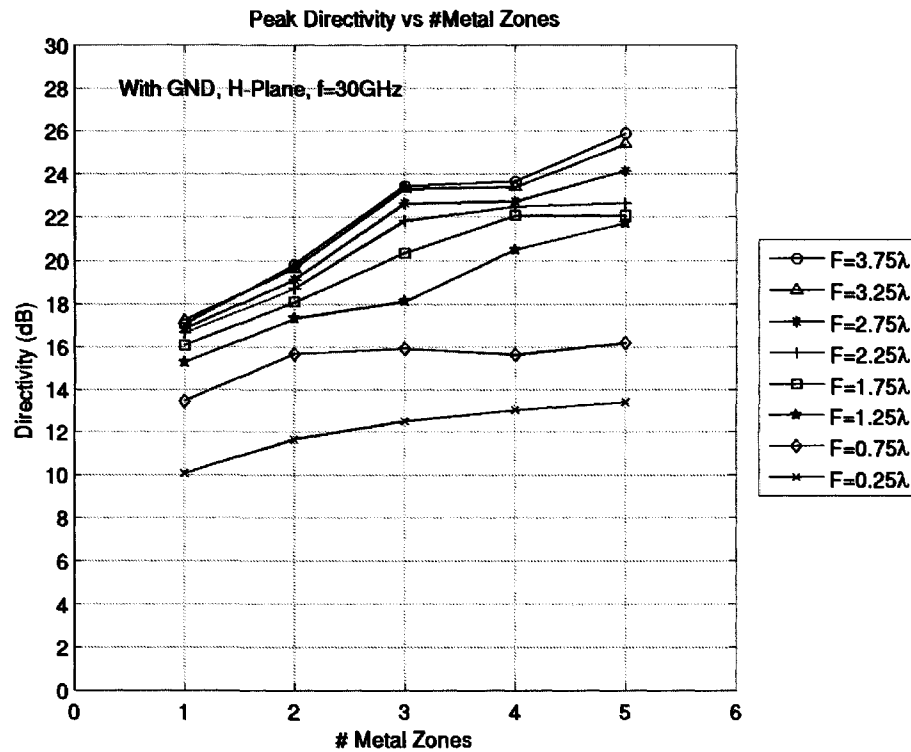


Figure 8-5: Peak Directivity vs. # Metal Zones With Ground Plane

The final observation from Figure 8-5 was that the directivity increased as the number of metal zones increased for nearly all focal distance cases. This indicated that the aperture illumination reduction with the larger number of metal zones was likely compensated for by the aperture area increase as the number of metal zones increased. Also, the curves in Figure 8-5 did not increase monotonically with the number of metal zones, which is a result of the ground plane reflections. When the same curves were generated without the ground plane, they increased monotonically. Figure 8-6 shows this result.

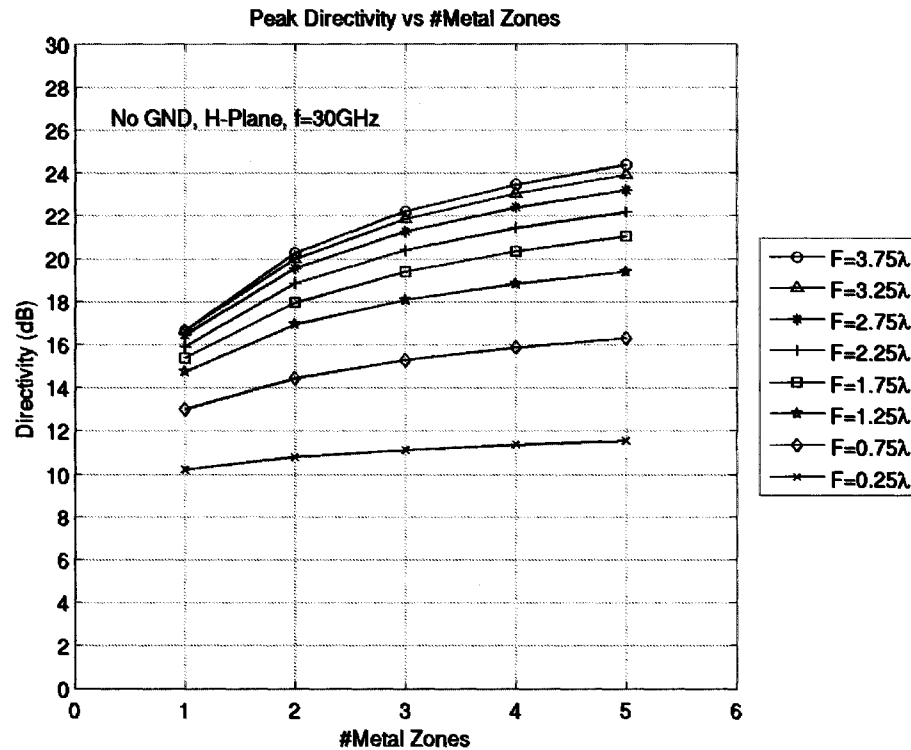


Figure 8-6: Peak Directivity vs. # Metal Zones With No Ground Plane

8.2.4 Peak Directivity Bandwidth

In order to properly observe the variation in directivity with focal distance, the aperture size must remain constant while the focal distance is decreased. Due to the different sizes of metal zone radii for the different focal distances, a direct comparison was only possible for the 3.75λ and 1.25λ focal distance cases, where the aperture diameter was kept constant at about 6λ by having two metal zones in the 1.25λ case and one metal zone in 3.75λ case. Figure 8-7 shows a comparison between these two cases. The smaller focal distance yielded a broader band response and a higher directivity at 30GHz. The frequency sensitivity of the $F=3.75\lambda$ case was caused by the larger separation between the lens and ground plane. This sensitivity was not present when the ground plane was removed.

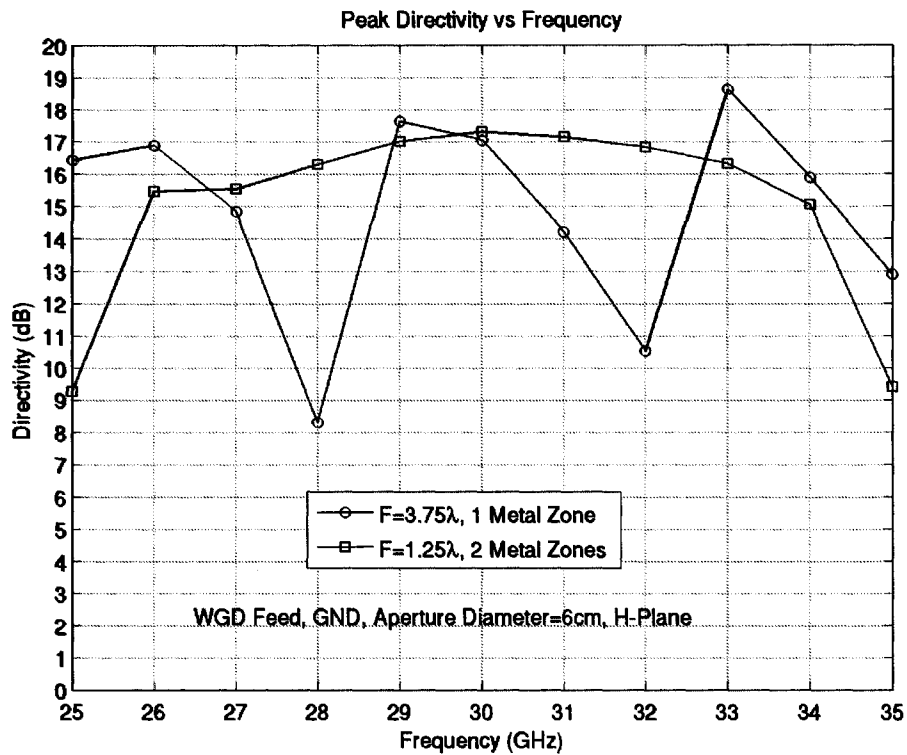


Figure 8-7: Peak Directivity vs. Frequency for $F=3.75\lambda$ and 1.25λ Cases

8.2.5 Aperture Efficiency vs. Number of Metal Zones

Based on the simulated peak directivity values and the physical size of the FZPA apertures, the effective area and antenna aperture efficiency were calculated at 30GHz. Table 8-1 lists these results for the single metal zone case with focal distances which were decreasing by odd multiples of 0.25λ . The highest aperture efficiency was achieved with the $F=1.25\lambda$ case.

Focal Distance (λ)	Lens Diameter (cm)	Peak Directivity (dB)	Effective Area (cm²)	Physical Area (cm²)	Aperture Efficiency (%)
3.75	2.915	17.05	4.03	26.69	15.11
3.25	2.739	17.22	4.19	23.57	17.80
2.75	2.550	16.84	3.84	20.43	18.82
2.25	2.345	16.64	3.35	17.28	21.25
1.75	2.121	16.06	3.21	14.13	22.73
1.25	1.871	15.27	2.67	11.00	24.35
0.75	1.581	13.45	1.76	7.85	22.43
0.25	1.225	10.05	0.80	4.71	17.08

Table 8-1: Single Metal Zone Small Focal Distance Simulation Results

Figure 8-8 shows how the aperture efficiency varied with the number of metal zones. The aperture efficiencies with five metal zones were much lower than with the single metal zone. This trend was the opposite of the directivity variation from Figure 8-5.

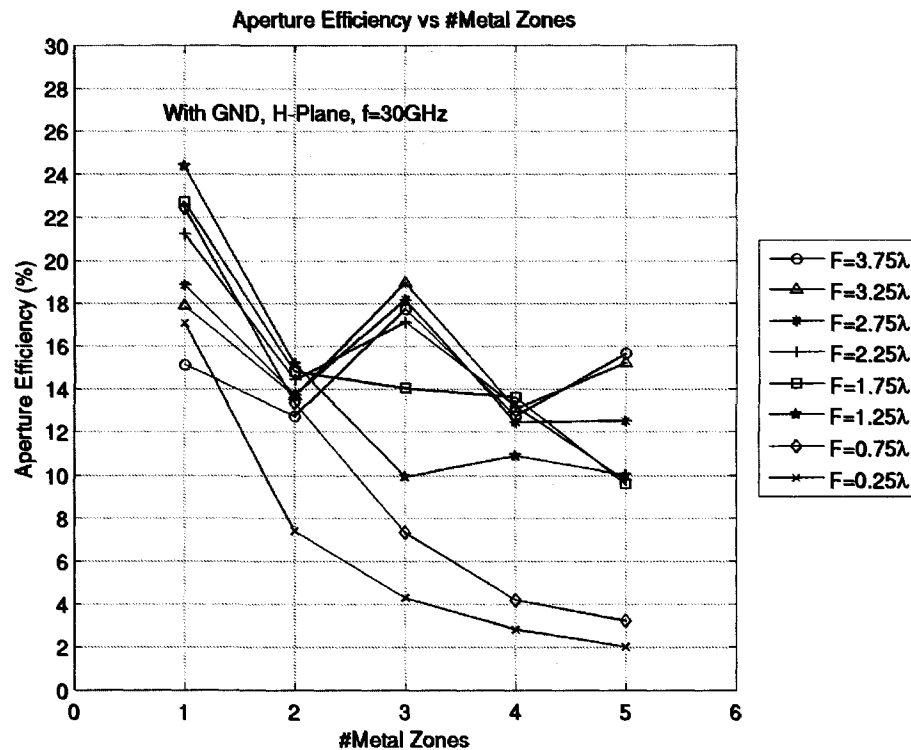


Figure 8-8: Aperture Efficiency vs. # Metal Zones With Ground Plane

The reason that the aperture efficiency decreased while the directivity increased when the number of zones was increased was that the aperture area of the antenna was increasing faster than the directivity as the number of zones increased. This made sense in terms of the inverse relationship between aperture efficiency, physical area, and directivity.

Another observation was that for small focal distances, the aperture efficiency decreased nearly monotonically while this was not the case for the larger focal distances. Over all focal distances and number of metal zones, the highest aperture efficiency occurred for the $F=1.25\lambda$ case with the single metal zone, which was 61% higher than the single zone $F=3.75\lambda$ case.

8.2.6 Discussion

The curves in Figure 8-5 & 8-8 confirm that there is a trade-off to be made between the desired directivity, aperture efficiency and the number of metal zones. Operating below 0.25λ did not yield much more directivity than the feed and the aperture efficiencies were generally below 10%, while operating at 2.75λ produced nearly the same directivity and aperture efficiency as in the 3.25λ and 3.75λ focal distance cases. Also, choosing more metal zones generally resulted in more directivity but less aperture efficiency.

8.3 Single-Zone FZPA Compared with Superstrate Antenna

In this section the single-zone FZPA will be compared to a superstrate antenna since it has an equivalent size to the FZPA. The superstrate antenna is based on a quarter-wave thick superstrate with a high dielectric constant ($\epsilon_r=10$), spaced a half-wave above the ground plane and feed. Figure 8-9 illustrates this structure. A superstrate in this configuration behaves as a leaky-wave antenna and is able to efficiently collimate a beam.

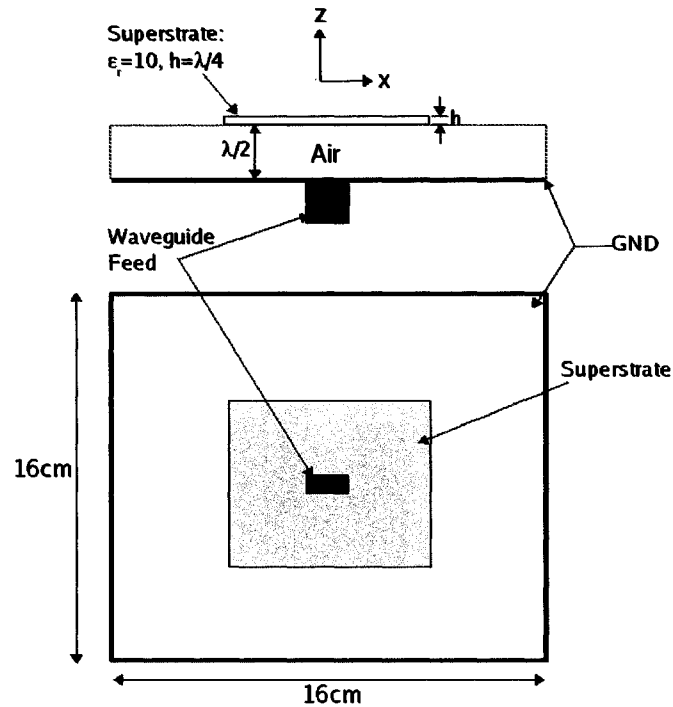


Figure 8-9: $\lambda/4$ Superstrate Spaced $\lambda/2$ Above a Ground plane

In order to make a proper comparison with the FZPA, the focal distance of the FZPA should ideally be 0.5λ since that would correspond to a half-wave spacing between the feed and superstrate. Since there was significant phase cancellation at 30GHz for the $F=0.5\lambda$ case when the ground plane was present, the comparison was made without the ground plane. The superstrate was chosen to have dimensions of 25mm x 25mm, which represented approximately the same area as the outer zone of the single metal zone FZPA with $F=0.5\lambda$.

Figure 8-10 shows a comparison at 30GHz of the H-plane radiation patterns between the superstrate and the single metal zone FZPA with $F=0.5\lambda$. The difference in maximum directivity between the two curves is about 4dB at 30GHz and the 3dB beamwidth of the FZPA is wider. The peak directivity of the FZPA could be improved with the presence of

the ground plane, but, in order to avoid the phase cancellation, the FZPA focal distance would have to be changed to 0.75λ . In this case, the FZPA peak directivity would be about 13.5dB, making the difference between it and the superstrate case only 2.5dB.

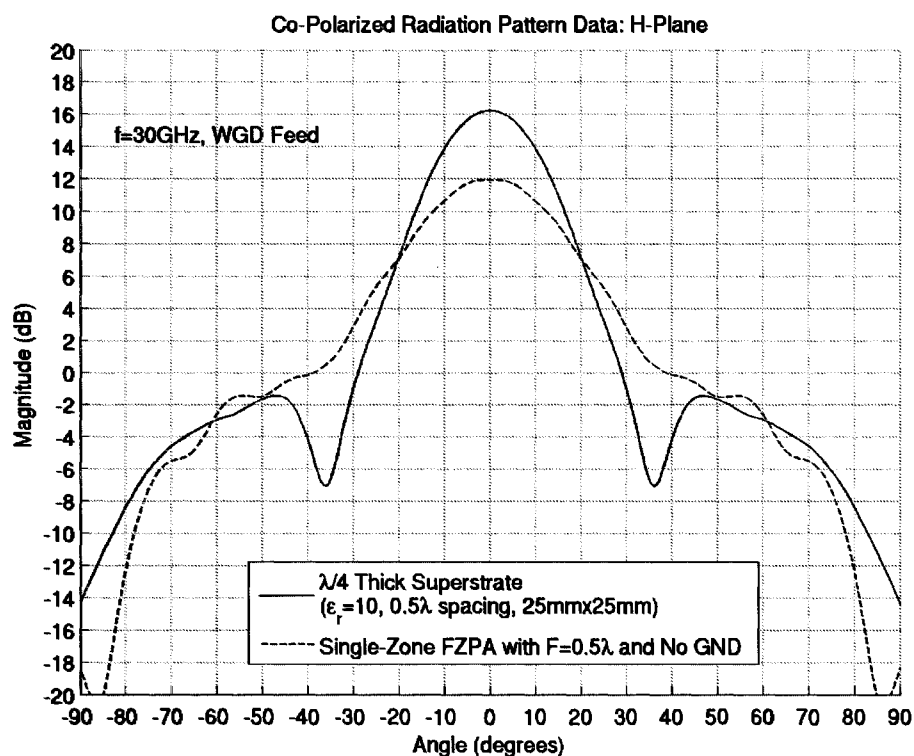


Figure 8-10: Comparison Between FZPA and Superstrate at 30GHz, H-plane

Another aspect for comparison between the two structures is the peak directivity bandwidth where the FZPA has a significant advantage. Figure 8-11 shows the peak directivity versus frequency of each structure. The 3dB bandwidth of the superstrate is about 2.85GHz whereas the 3dB bandwidth of the FZPA is larger than 10GHz.

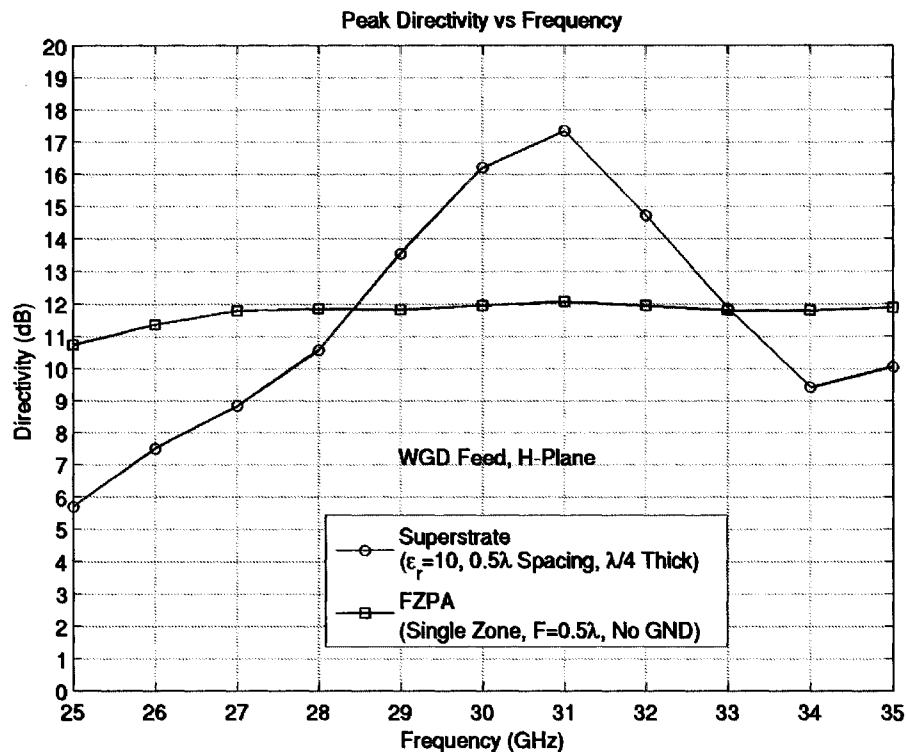


Figure 8-11: Bandwidth Comparison Between the FZPA and the Superstrate

Other advantages of the FZPA over the superstrate are the practicality of the structure at lower frequencies and cost effectiveness of the overall package. The superstrate structure can be very costly due to the expensive microwave material required to obtain a high dielectric constant and low loss tangent. Also, at lower frequencies, the superstrate is not practical due to the large thickness requirements which also serve to further increase the cost.

8.4 Measurement Results

8.4.1 Antenna Fabrication and Test Set-Up

In order to verify the simulated results, several low-profile antennas were selected for fabrication. Two single zone lenses with $F=0.5\lambda$ and $F=3.0\lambda$ respectively were made

using the same zone radii as in the simulations and were etched on a 0.127mm FR4 material. The antennas were attached with tape to pieces of foam that were cut to be the thickness of the focal distance. A steel ground plane was fabricated to be the same dimensions as in the simulations with a rectangular hole in the center for the open-ended WR28 waveguide feed. In this case, the tapered waveguide was not used since the measurements were performed in the far-field chamber and it would not fit on the far-field test fixtures. The foam holding the antenna was attached to the ground plane. The entire structure was then situated on a custom-made test fixture which allowed for measurements both with and without the ground plane. Figure 8-12 shows the test set-up in the far-field anechoic chamber.

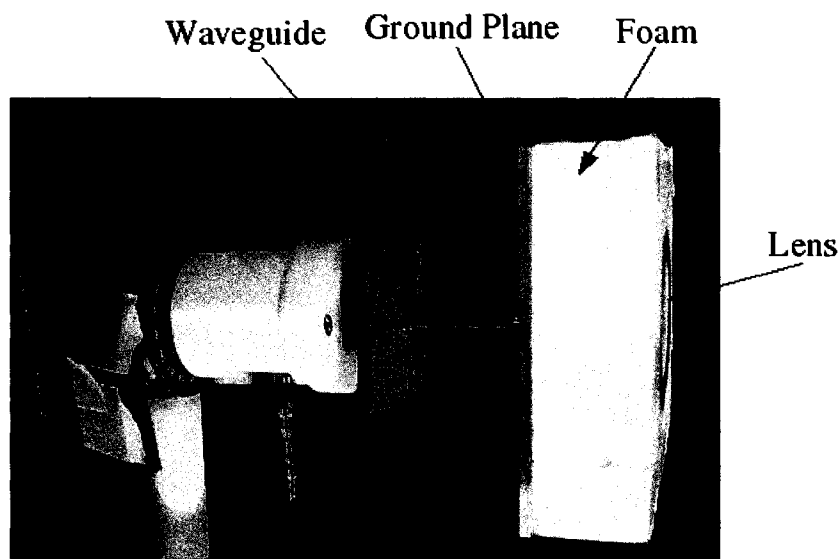


Figure 8-12: FZPA Test Set-Up for $F=3.0\lambda$

A superstrate was also fabricated for testing. The superstrate was made from 0.030" (closest thickness to $\lambda/4$ that was available) Taconic CER material with $\epsilon_r=10$. It was cut to the dimensions 28.28mm x 28.28mm square. The superstrate was taped to the 0.5 λ thick foam and was measured with the ground plane at the aperture of the open-ended

waveguide. Figure 8-13 shows this test set-up.

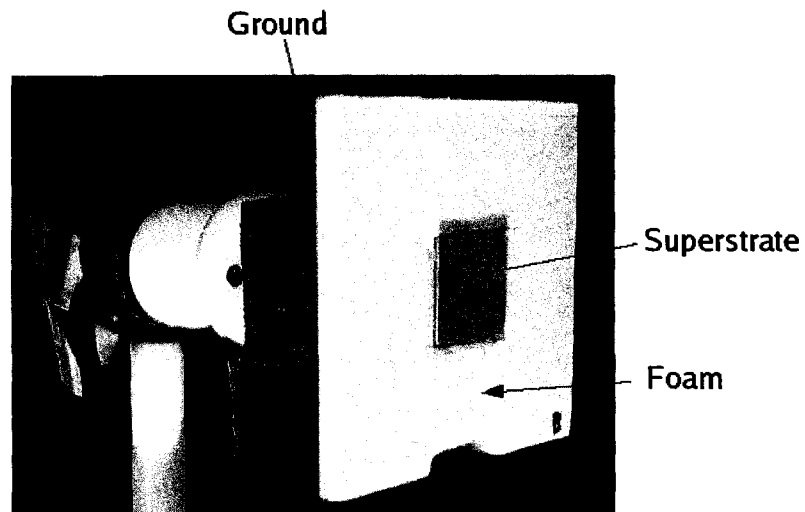


Figure 8-13: FZPA Test Set-Up for the Superstrate

8.4.2 Measurement Test Results

8.4.2.1 Feed Alone

The open-ended WR28 waveguide was measured on its own to compare with the simulated waveguide results. It was found that the simulated results matched very closely to the measurements. Figures 8-14 and 8-15 illustrate these normalized results for the H- and E-plane respectively. The simulated peak gain was about 0.5dB higher than the measured peak gain.

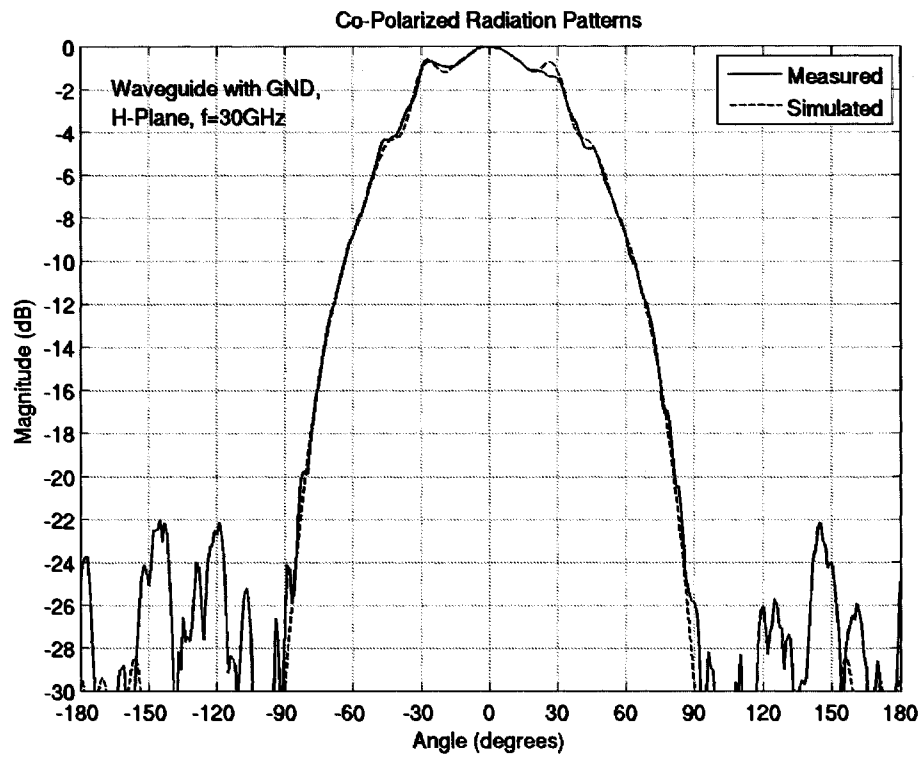


Figure 8-14: Measured and Simulated Results for WR28, H-Plane

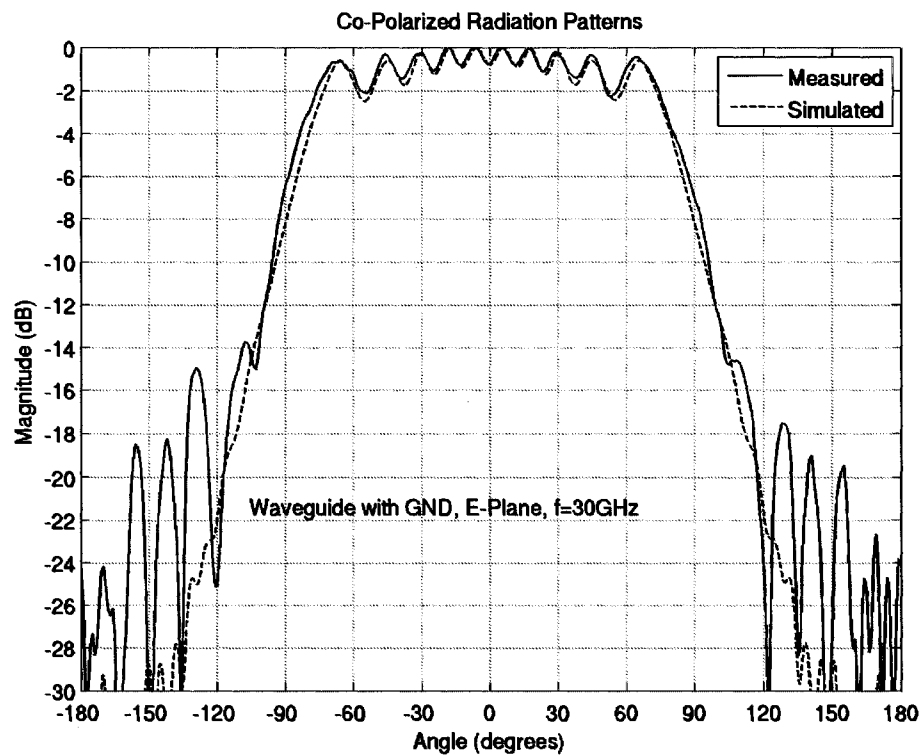


Figure 8-15: Measured and Simulated Results for WR28, E-Plane

8.4.2.2 $F=3.0\lambda$ Single-Zone FZPA With Ground Plane

Figure 8-16 shows a normalized comparison between the measured and simulated results of the single-zone FZPA with $F=3.0\lambda$ in the H-plane. This figure demonstrates how well the software modeled the structures since the two curves are very similar. The measured peak gain for the $F=3.0\lambda$ case was lower than the simulated gain by about 0.2 dB.

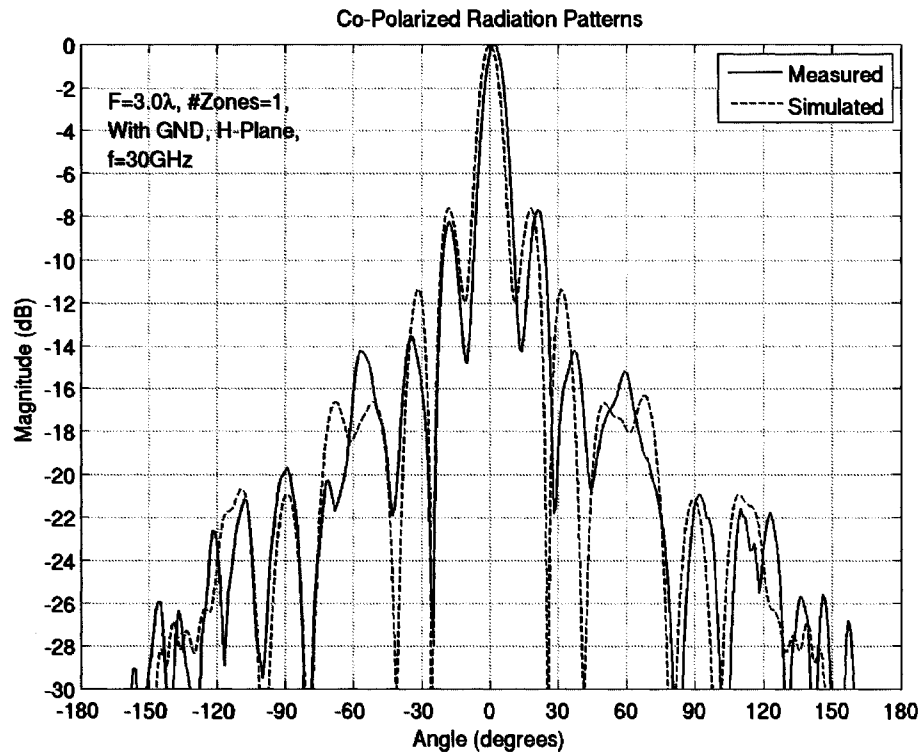


Figure 8-16: Measured and Simulated Results for $F=3.0\lambda$ FZPA, H-Plane

In order to achieve this level of agreement between the measured and simulated results, the effects of the FR4 substrate, foam, and thickness of tape had to be taken into account. These items were not included in the original simulations. It was found that the FR4 substrate and the tape had very little effect on the simulated radiation patterns, but the foam made a significant difference. The original simulations included air ($\epsilon_r=1$) between

the lens and waveguide and the radiation pattern showed a significant drop in directivity at 30GHz due to the phase cancellation. However, since the dielectric constant of the foam was actually closer to 1.03, when the air was changed to have this dielectric constant, the FZPA directivity improved greatly. This result and is shown in Figure 8-17.

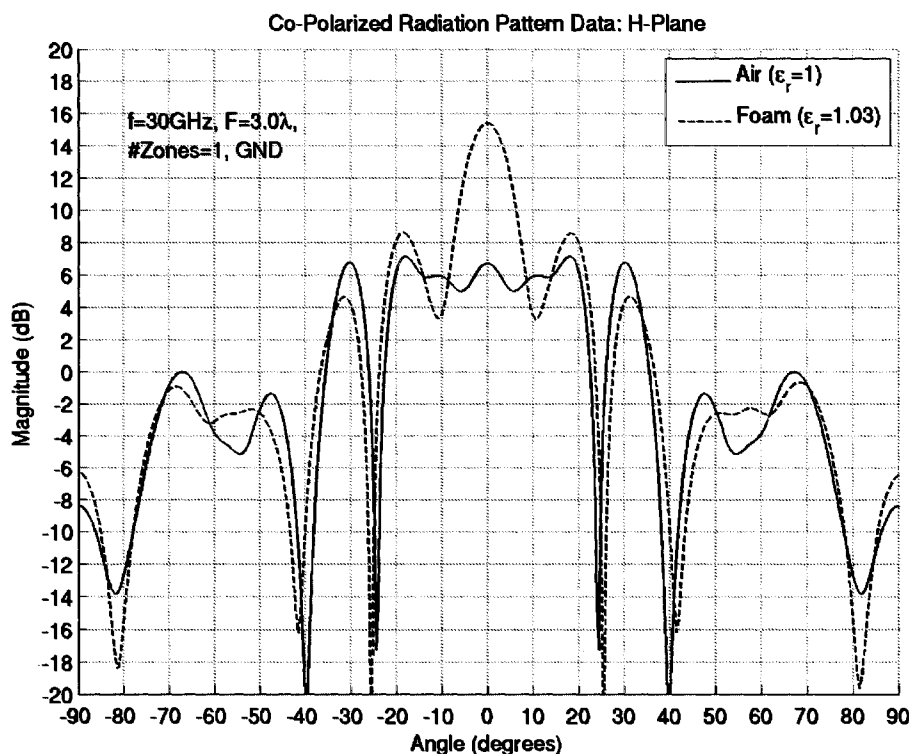


Figure 8-17: Radiation Patterns With and Without Foam for $F=3.0\lambda$, H-Plane

The fact that the lens had poor directivity at 30GHz in the original simulations made sense because of the phase cancellation at $F=3.0\lambda$ when the ground plane was present, as discussed in Section 8.2.2. The fact that a much higher directivity was achieved with the foam having $\epsilon_r=1.03$ meant that the actual properties of the foam shifted the location of the phase cancellation to a lower frequency. Figure 8-18 illustrates this comparison.

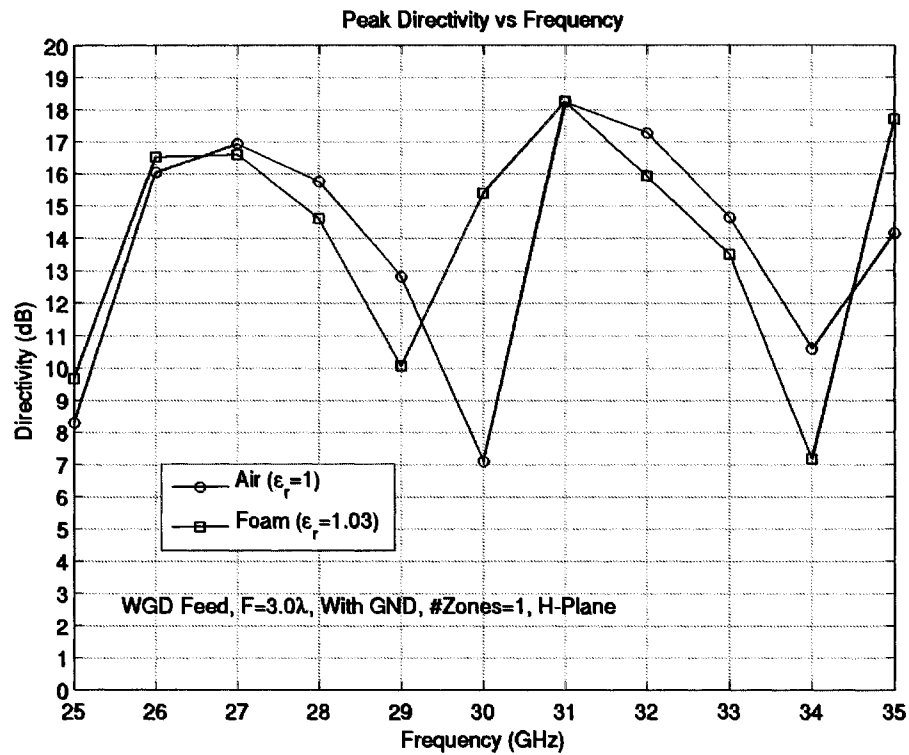


Figure 8-18: Bandwidth Comparison With and Without Foam for $F=3.0\lambda$, H-Plane

This figure highlights the frequency sensitivity of the FZPAs with focal distances on even multiples of 0.25λ . Because of the rapid change in directivity around 30GHz, any small change to the structure would cause a significant change to the directivity. In this case, the phase cancellation that was at 30GHz moved to 29GHz when the dielectric constant of the air was changed to 1.03. Figure 8-19 shows how this frequency sensitivity did not exist when the focal distance was an odd multiple of 0.25λ . The figure compares the $F=1.75\lambda$ (odd multiple of 0.25λ) and $F=2.0\lambda$ (even multiple of 0.25λ) cases. The $F=1.75\lambda$ case shows very little change in directivity when the foam with dielectric constant of 1.03 is added whereas adding the foam in the $F=2.0\lambda$ case makes a significant directivity change at 30GHz.

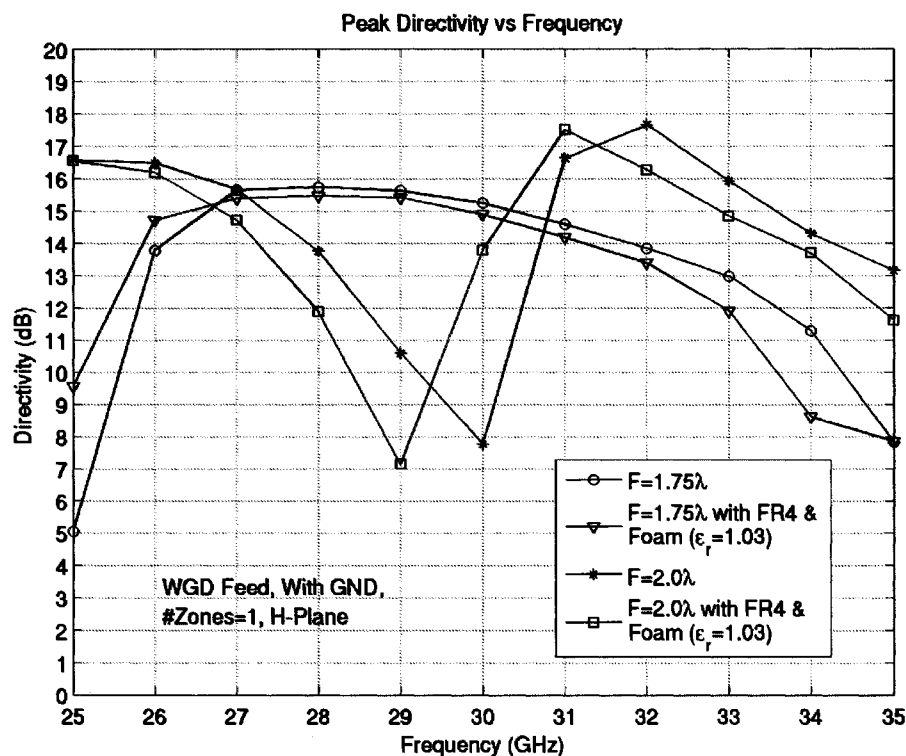


Figure 8-19: Frequency Sensitivity Comparison Between $F=1.75\lambda$ and 2.0λ , H-Plane

After the changes were made to the model, the minor differences that still existed in the gain and sidelobe areas of Figure 8-16 were likely due to fact that the test fixture was not included in the simulations and the exact dielectric constant of the foam and FR4 substrate was unknown. Based on these results, there was a high level of confidence in the simulations.

8.4.2.3 $F=3.0\lambda$ Single-Zone FZPA Without Ground Plane

A comparison between the measured and simulated results for the same antenna as in Section 8.4.2.2 was also performed without the ground plane at the aperture of the waveguide. It was found that the model predicted well the measurement result without the changes to the air as was required when the ground plane was present. Figure 8-20

illustrates this normalized result. The explanation for this was related to the higher quantity of fields between the ground plane and lens compared to the case without the ground plane. Because of the many reflections and re-reflections with the ground plane, the fields were more dense in this area, which made a small change in the dielectric constant have a bigger impact.

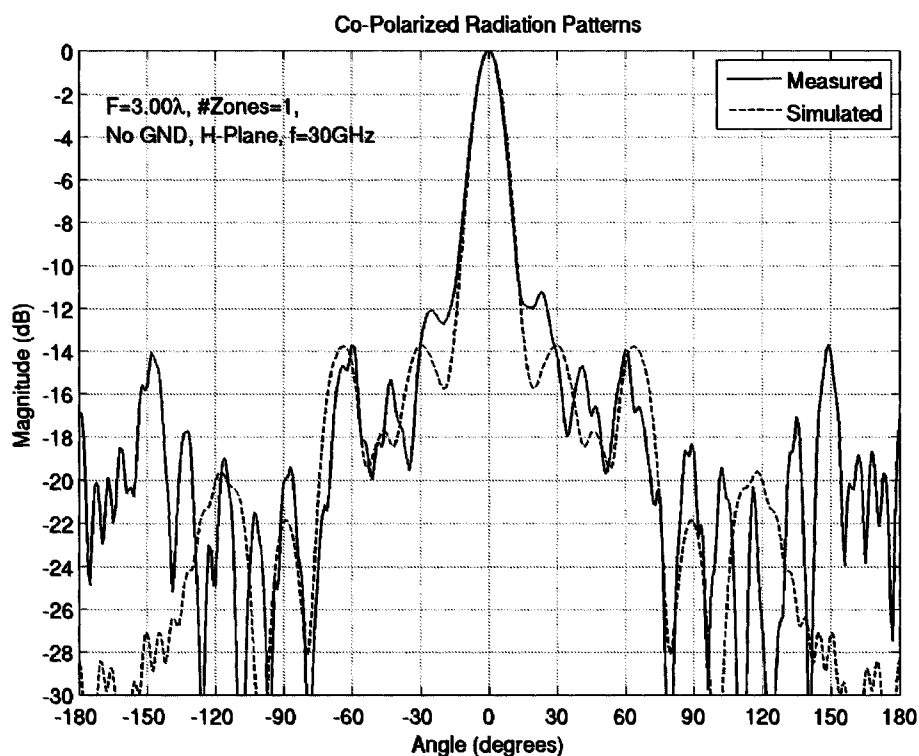


Figure 8-20: Measured and Simulated Results Without Ground plane, $F=3.0\lambda$, H-Plane

8.4.2.4 $F=0.5\lambda$ Single-Zone FZPA With Ground Plane

Figure 8-21 shows a normalized comparison between the measured and simulated results of the single-zone FZPA with $F=0.5\lambda$ in the E-plane. Similar to the $F=3.0\lambda$ case, this figure confirms how well the software modeled the structures since the two curves are again very similar. The measured peak gain was lower than the simulated gain by about

0.7dB in this case.

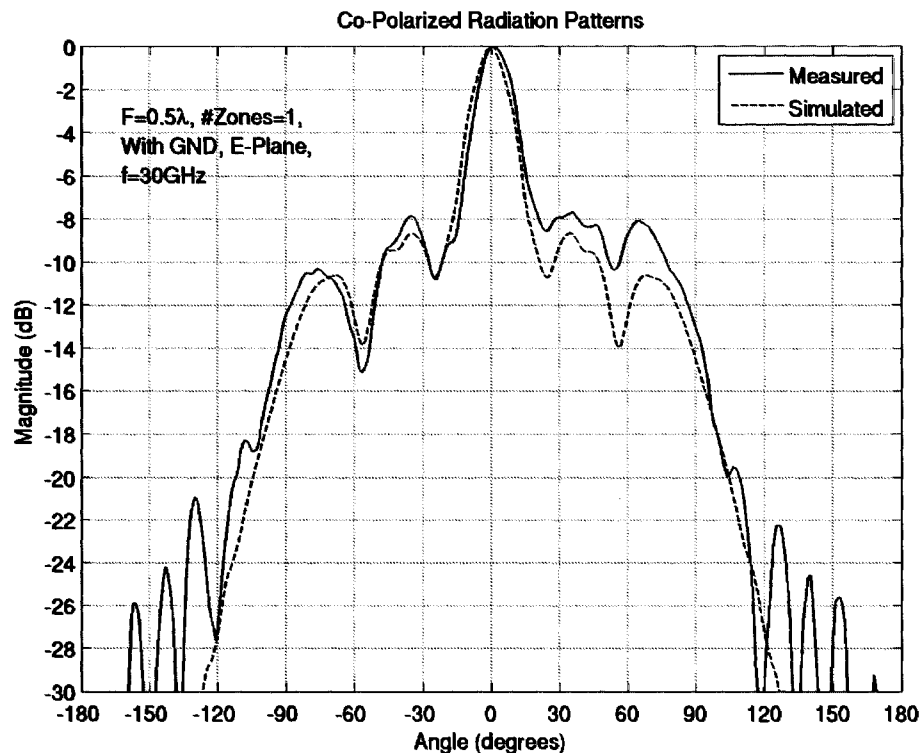


Figure 8-21: Measured and Simulated Results for $F=0.5\lambda$, E-Plane

Again, this high level of agreement was achieved by including in the model the FR4 substrate, foam, and the tape thickness. Similar to the $F=3.0\lambda$ case, it was found that with the ground plane present, the FR4 substrate made very little difference while the foam, having $\epsilon_r=1.03$, had a significant effect on the simulated radiation patterns. However, different from the $F=3.0\lambda$ case, the focal spacing in the simulations needed to be increased to 0.6cm from 0.5cm in order to achieve results closer to the measurements. The extra 1mm was attributed to a combination of experimental inaccuracies including the non-consistent foam thickness (machine shop could not cut the foam at exactly 0.5cm thick), the small air gaps between the lens and foam at the spots where there was no tape,

and the thickness of the double sided tape between the FR4 substrate and foam. In this smaller focal distance case, the dense fields contained between the ground plane and the lens were being forced into a smaller area thus turning small inaccuracies into significant changes in the radiation patterns. Also, it is important to remember that, at this small focal distance, the feed was likely contained within the near fields, which made the results extra sensitive as described in Section 8.2.3.

Similar to the $F=3.0\lambda$ case, the measured and simulated cases without the ground plane matched quite closely without alterations to the model.

8.4.2.5 Superstrate

For the superstrate, similar modifications to what was done with the $F=0.5\lambda$ case needed to be made to the simulation model in order to get good agreement with the measurements. In this case, the focal spacing required was 0.54cm instead of 0.6cm as was required for the $F=0.5\lambda$ case. The lesser spacing change was attributed to the fact that there were less fields contained between the ground plane and the superstrate thus reducing the impact of the experimental inaccuracies. Figure 8-22 shows a comparison in the H-plane between these simulated and measured results.

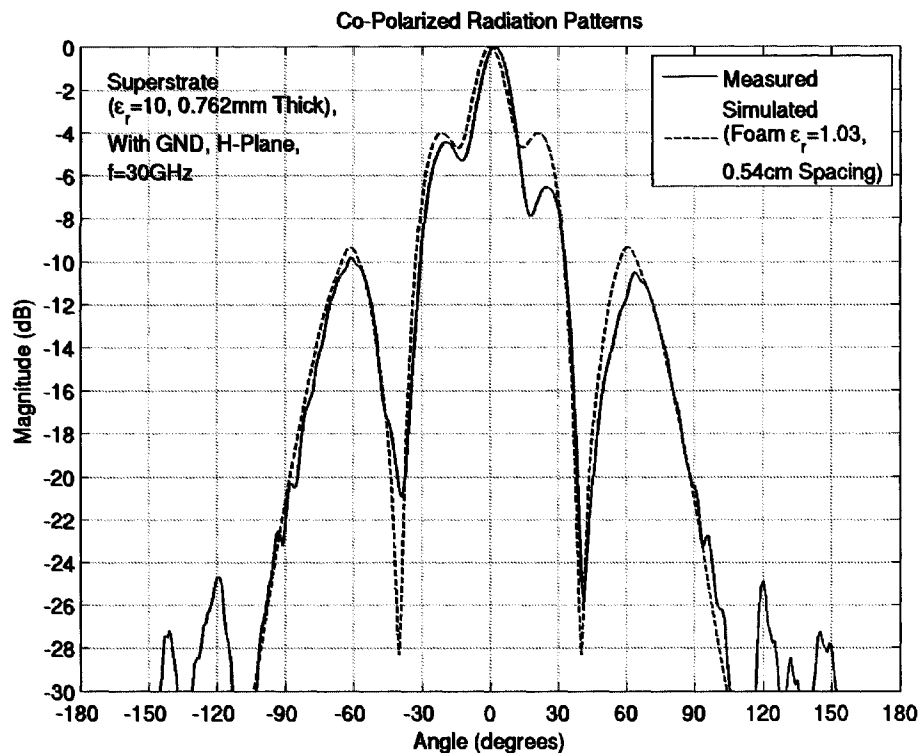


Figure 8-22: Measured and Simulated Results for Superstrate, H-Plane

8.4.3 Discussion

The measurement results described in this section provided interesting insight into the workings of the low-profile FZPA. The dielectric constant of the foam was found to have a significant influence on the radiation patterns of the FZPA when the ground plane was present, particularly when the focal distance was small. This finding was most useful since it revealed that changing slightly the dielectric constant of the material between the antenna aperture and the feed can improve the directivity and radiation patterns. This means that all focal distances can be considered, not just those with odd multiples of 0.25λ .

8.5 Conclusion

A study investigating a low-profile FZPA was presented. The focal distance of the FZPA with a ground plane at the aperture of the waveguide feed, was reduced in steps of 0.25λ until the radiation patterns resembled the feed. It was found that the FZPA could not focus well at distances below 0.75λ . The effect of the reduced focal distance was observed in terms of the peak directivity and aperture efficiency with a varying number of metal zones. It was found that the single metal zone $F=1.25\lambda$ focal spacing yielded the highest overall aperture efficiency of just over 24%. This represented nearly a two-fold improvement over the conventional FZPA.

The FZPA was also compared to a leaky-wave antenna with a $\lambda/4$ superstrate spaced $\lambda/2$ above a ground plane. This comparison revealed that although the superstrate antenna produced a higher peak directivity, the FZPA had a larger directivity bandwidth and would be far more cost effective, especially at lower frequencies.

Measurements were performed to verify the simulated results and revealed that the dielectric constant of the material between the FZPA aperture and the feed was critical when the ground plane was present. When more accurate foam permittivities were included in these simulations, good agreement with the measurements was achieved.

CHAPTER 9

FZPA ARRAYS

9.1 Introduction

A high-gain and low-profile FZPA must be an array. In Chapter 8, it was shown that decreasing the focal distance to achieve a low-profile FZPA decreased the peak directivity. Specifically, to maintain a focal distance of 1.25λ at 30GHz, the single element FZPA with 5 metal zones yields a peak directivity just below 22dB. This value drops to 16dB when the focal distance is further reduced to 0.75λ . Arraying FZPAs is a good way to increase the directivity while maintaining the low profile.

In Section 2.4, the concept of arraying lenses was discussed. It was shown that, by reducing the size of each array element, the focal distance will also be reduced to maintain the same F/D of the original single element lens. This concept applies here in the opposite sense since the focal distances have already been reduced. What remains is to determine the required size of the elements and the relative spacing between them.

This chapter begins by outlining a new method to design the zones of the FZPA based on

the phase of the feed. As will be seen, this method is immune to the issues related to overlapping zones and is more accurate than using Equation 2-5. Sections 9.3 and 9.4 compare these 'modified' zones to the conventional circular zones for various array configurations. Section 9.6 will investigate the results of using different FZPA elements in the array.

Arrays of lenses require a feed for each element. This adds to the complexity of the overall antenna. However, in comparison with a microstrip patch array, the FZPA elements are much bigger and so few elements are required in the array to satisfy the gain specification. Fewer elements means fewer feeds and hence less complexity in comparison. Section 9.6 will investigate this comparison in detail.

9.2 Conversion from Feed Phase to FZPA Zones

The locations of the zones on the surface of the FZPA aperture are determined by the phase of the waves from the feed. As outlined in Section 2.2.4, by knowing the phase values for every point on the surface of the aperture, it is a matter of ray trigonometry to determine the location of the alternate 180° phase sub-zones that need to be metalized. In the case of an array of FZPAs, however, the trigonometry is not so simple. The waves from the multiple feeds interact together and create a pattern of phase contours on the FZPA aperture that are no longer circular and are not easy to predict without modeling software.

In this section, a method of establishing 'modified' zones based on the phase of the FZPA feed will be outlined. This method is easily applied to arrays and will be shown to be

more accurate than the standard zone radii computation (Equation 2-5). For the work in this section, the FZPA focal distance was chosen to be 0.7λ in order to be low profile and simulations were performed at 30GHz.

9.2.1 Phase of a Single Waveguide

The FDTD software Empire [3-3] can easily compute the phase of any component of electric field of any structure that can be drawn and properly discretized. In this case, the fields from a single WR28 waveguide were analyzed alone at a fixed z value away from the waveguide. Figure 9-1 illustrates this geometry where a FZPA aperture is shown at the location where the analysis was performed. In the development of this method, there was no ground plane at the aperture of the feed, but once arrays are considered later in the chapter, the ground plane will be added.



Figure 9-1: Geometry of Single Waveguide for Phase Computation

Since the FZPA feeds used in this thesis were polarized in the y -direction, the E_y field component was used for these phase computations. By looking at the location where the FZPA aperture would be located in the z -direction and cutting through the $y=0$ point in

the x - y plane, the phase plot will resemble that shown in Figure 9-2. In this case, the desired FZPA aperture location was 0.7λ away from the aperture of the waveguide feed.

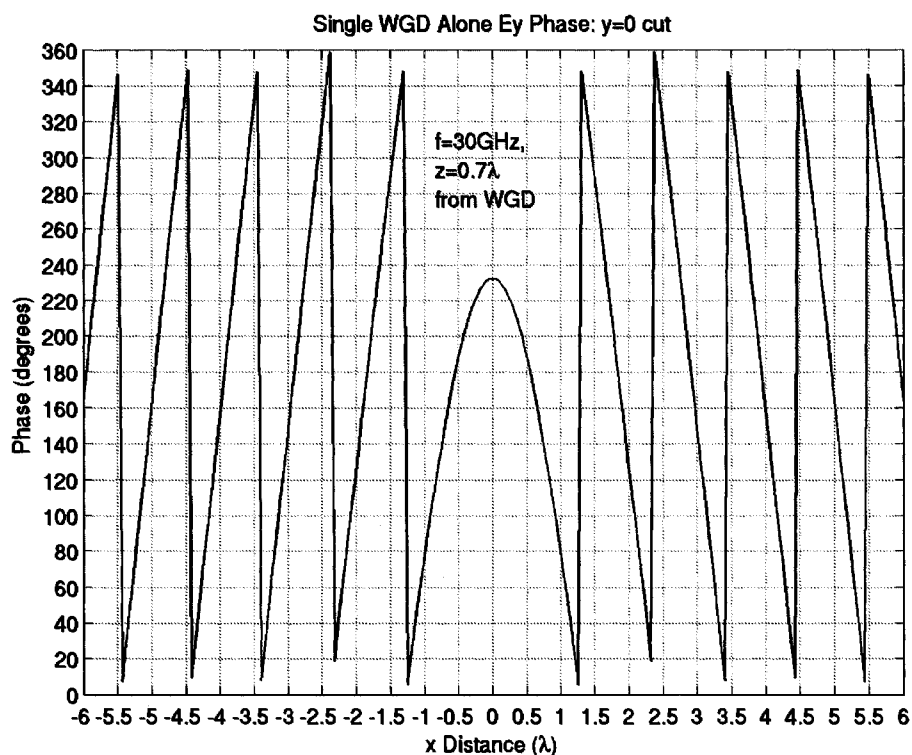


Figure 9-2: E_y Phase at $z=0.7\lambda$ from Waveguide, $y=0$ cut

From this figure, it can be seen that the phase peak at $x=0\lambda$ represents the location of the waveguide. The peak is at 232° at 30GHz. In order to easily determine the points that are 180° away from the peak, this curve must be normalized. Figure 9-3 illustrates the resulting normalized plot and Figure 9-4 represents the same plot but shows only the left portion of the graph.

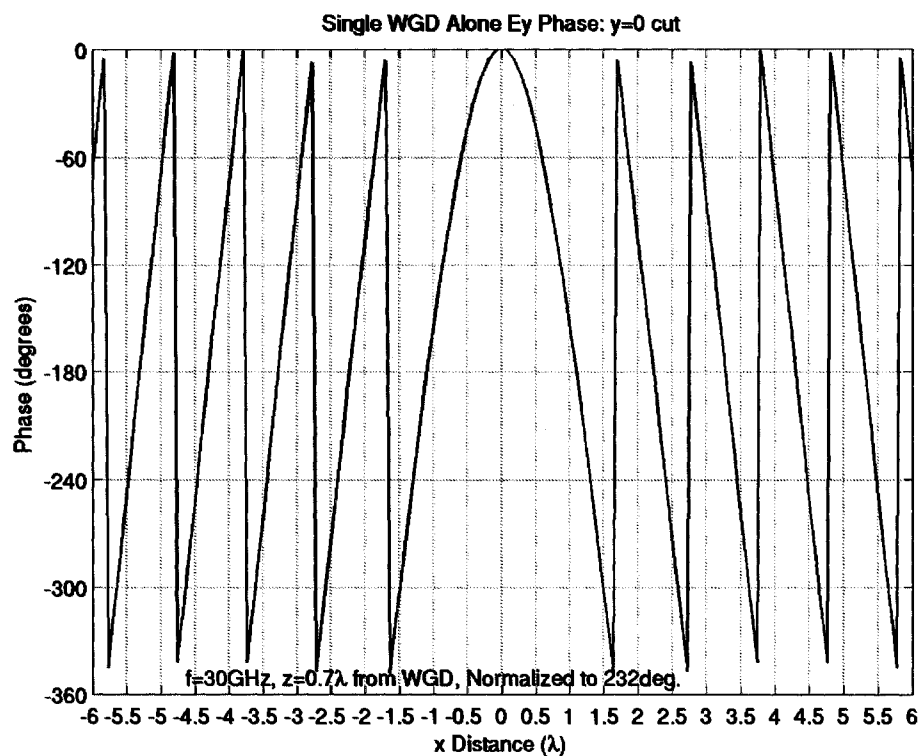


Figure 9-3: Normalized E_y Phase at $z=0.7\lambda$ from Waveguide, $y=0$ cut

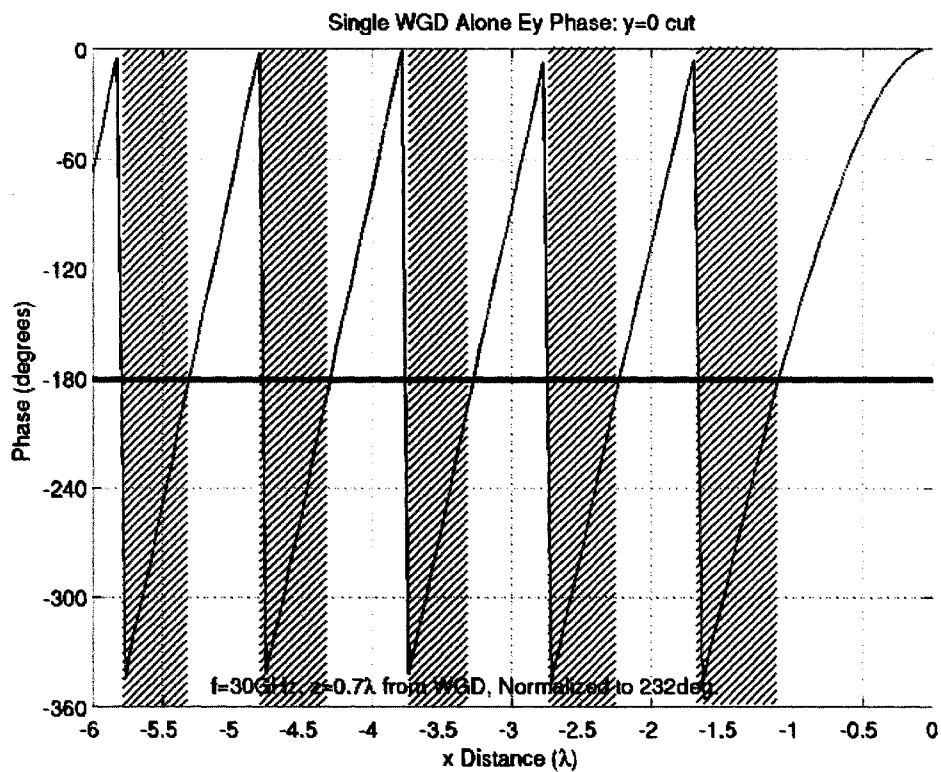


Figure 9-4: Magnified Version of Figure 9-3

The horizontal line in Figure 9-4 is at the 180° phase location. By measuring the x -distance between locations where the horizontal line hits adjacent 180° points, the width of the Fresnel zones can be established as indicated by the rectangular hatched areas. Table 9-1 compares the metal zone widths as measured from Figure 9-4 with those computed using Equation 2-5, which is considered the standard approach.

Metal Zone Number (inside to outside)	Zone Width Figure 9-4 (cm)	Zone Width Equation 2-5 (cm)
1	0.57	0.574
2	0.52	0.522
3	0.49	0.511
4	0.48	0.507
5	0.49	0.504

Table 9-1: Comparison of Metal Zone Widths

These results indicated that the two methods yielded nearly identical results for the first two metal zones and close results for the remaining metal zones. The discrepancy with the outer zones was related to the assumptions associated with Equation 2-5, which require that rays from the feed to the lens be paraxial. The rays from the feed to the inner zones have smaller angles than those going to the outer zones meaning that the paraxial approximation will be better and Equation 2-5 will be more accurate for the inner zones.

9.2.2 Phase Contours

By plotting the same E_y phase data from above in the x - y plane instead of along x only, a set of contours can be observed. Figure 9-5 illustrates the 90° , 180° , and 270° phase contours for the single waveguide case described in the previous section. The red

contours represent the 90° phase locations, the green contours represent the 180° phase locations and the blue contours represent the 270° phase locations. After the blue contours comes a contour which has red, green, and blue overlapping. They all overlap because they are all physically the same phase.

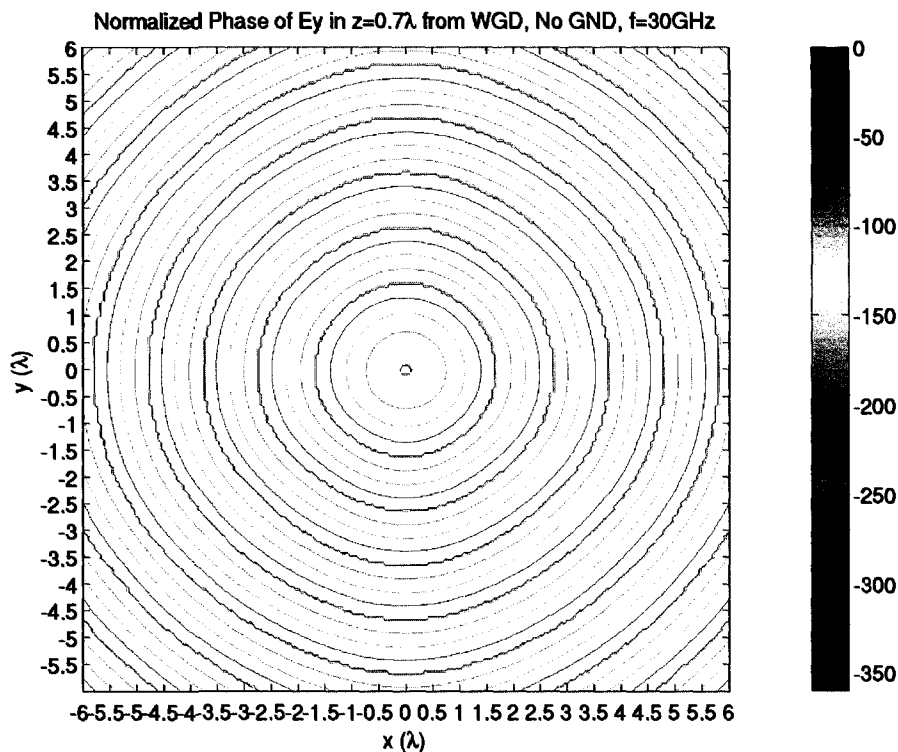


Figure 9-5: Phase Contours in the x - y Plane at $z=0.7\lambda$ from the Waveguide

Since only the 180° phase contours were required to determine the zones of the FZPA, all contours except those that represent the 180° phase locations were removed. The resulting contours thus represent the locations where the metal zones should be placed to create the FZPA. Figure 9-6 shows this result.

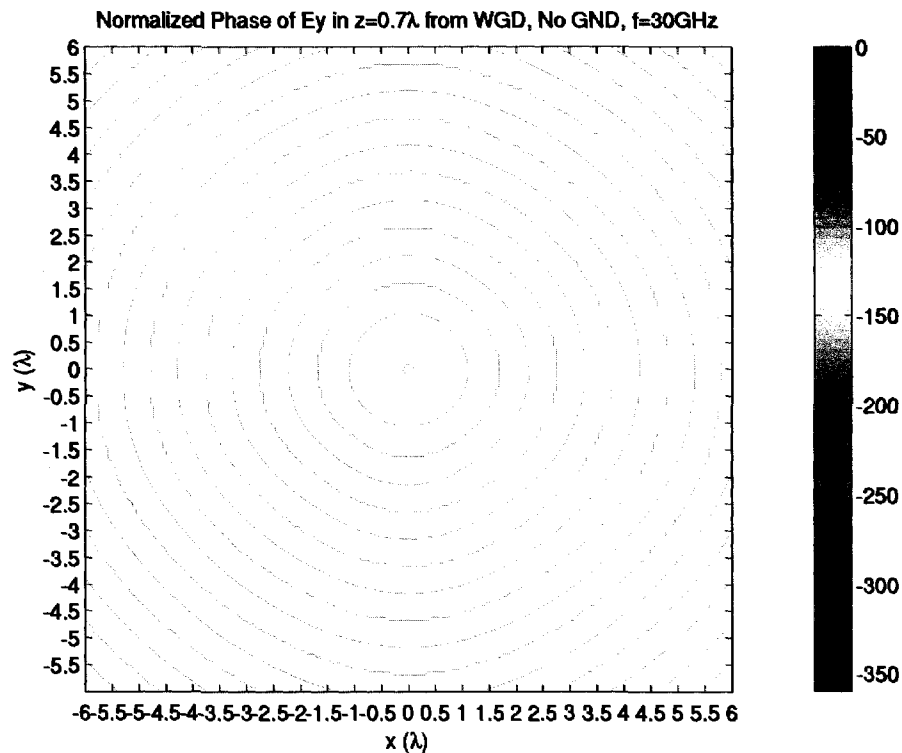


Figure 9-6: 180° Phase Contours from Figure 9-5

These contours were then each extracted into separate files containing listings of (x,y) coordinates so that they can be re-created in Empire.

9.2.3 'Modified' Zones Based on Phase Contours

The 180° contours were imported, one by one, into Empire and placed at the correct z -location in front of the waveguide feed that was previously simulated. The contours were then defined as being either metal or air. Figure 9-7(a) illustrates the resulting FZPA geometry while Figure 9-7(b) shows the 'modified' and circular zone geometries overlaid. The 'modified' zones are more elliptical along the horizontal axis in comparison to the circular zones. This is related to the patterns of the feed not being symmetrical in each plane, which is taken into account in this method.

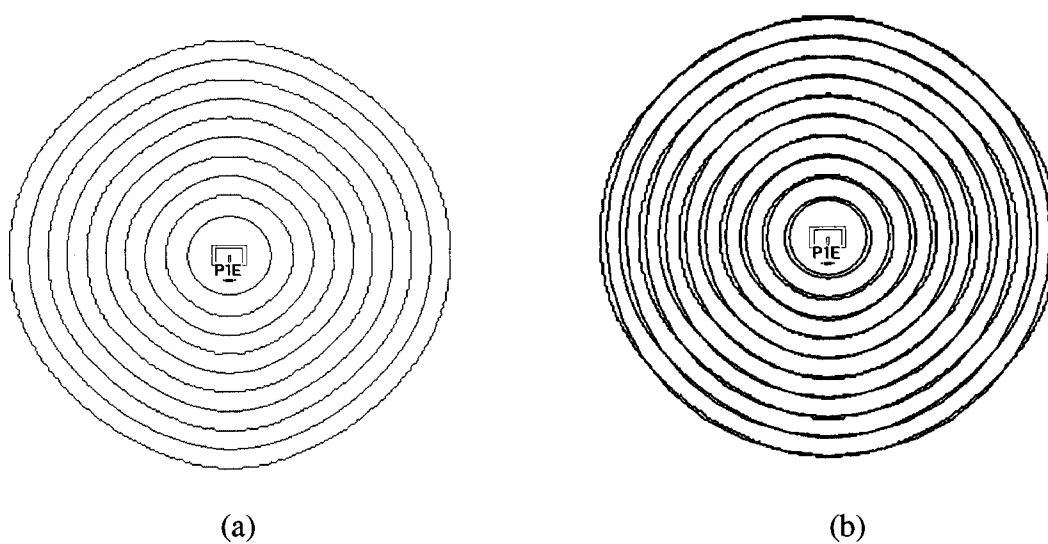


Figure 9-7: (a) 'Modified' Zone FZPA Based on 180° Contours,
(b) 'Modified' and Circular Geometry Comparison

Figures 9-8 and 9-9 show a comparison between the 'modified' and circular zone radiation patterns in the H- and E-planes respectively. The 'modified' zones have higher directivity by about 0.8dB and, in the principle planes, have substantially lower sidelobes in the back of the antenna.

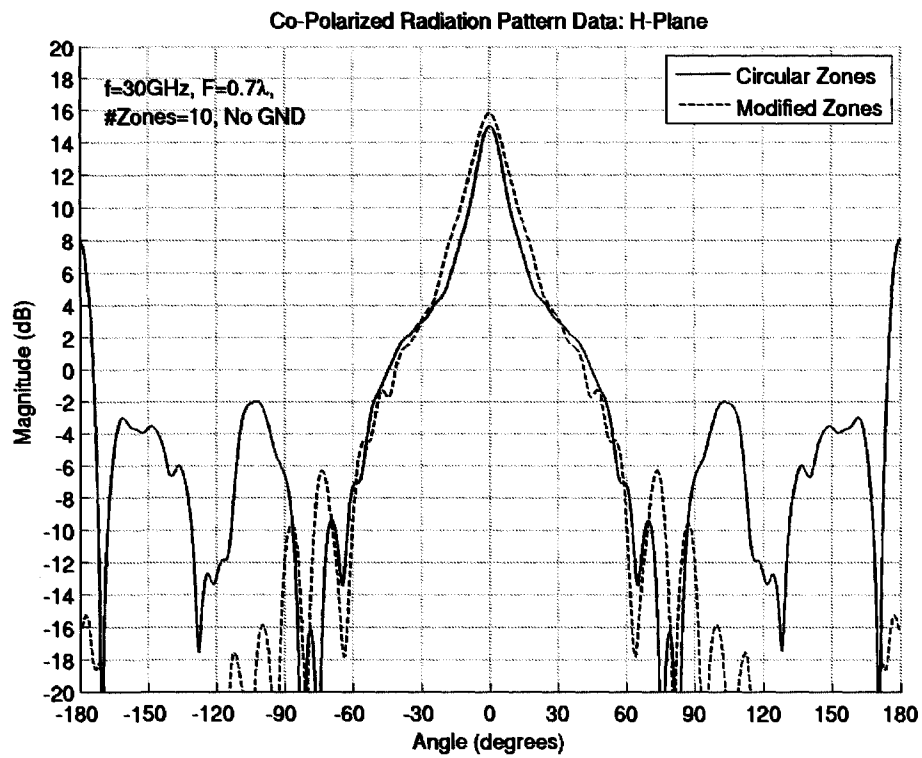


Figure 9-8: Comparison of 'Modified' vs. Circular Zone FZPAs, H-Plane

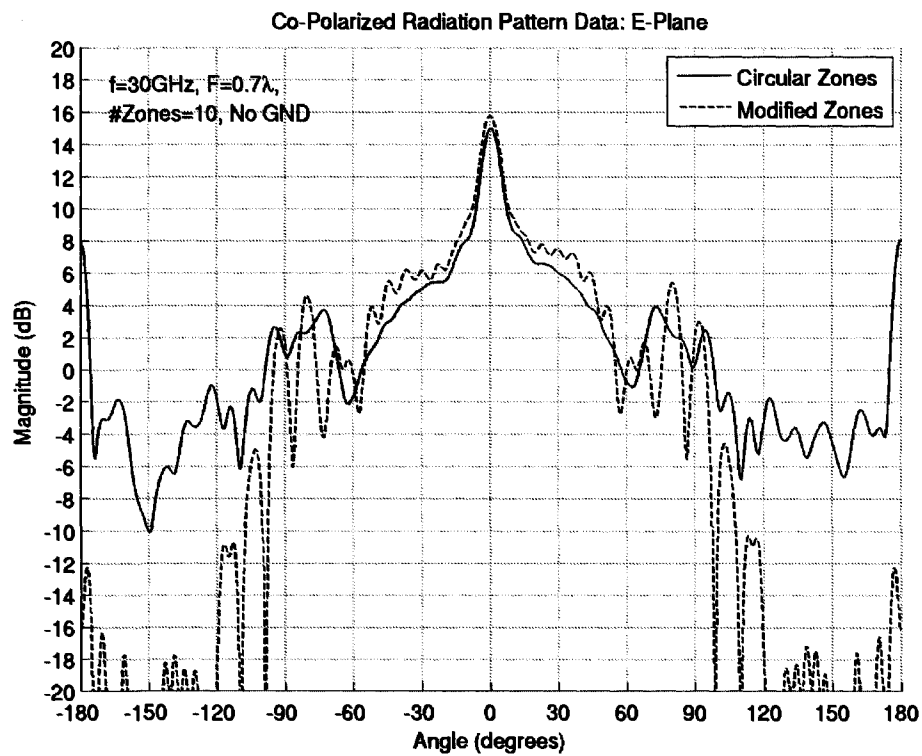


Figure 9-9: Comparison of 'Modified' vs. Circular Zone FZPAs, E-Plane

9.2.4 Discussion

The above described process, compared to using Equation 2-5, is a more accurate approach to defining the location and size of the zones on the FZPA aperture. The method takes into account the exact feed under consideration and models the exact phase generated by the feed at the location of the FZPA aperture. Although the zone locations matched fairly closely with those computed from Equation 2-5, the 'modified' zones are free from assumptions regarding the paraxial approximation and will provide accurate zone locations in the presence of interference between multiple feeds or other metallic objects in the vicinity of the FZPA. This approach will be used in the next sections to model the FZPA arrays.

9.3 FZPA Linear 2-Element Array

The first array considered in this work was a simple linear 2-element array where the elements were arrayed along the x -axis. This was similar to the 2-element arrays presented in [9-1]. However, in [9-1] the idea was to create two separate inclined beams instead of one main beam as in this work.

In order to improve efficiency, a ground plane was placed around the aperture of the waveguide as described in Chapter 7. The separation between the two waveguides was set at 31.62mm for the work in this section. With this spacing the first metal zone of each FZPA, as computed using Equation 2-5 with $F=0.75\lambda$, was just touching, but not overlapping. Other separations were used and the differences will be discussed briefly at the end of this section.

9.3.1 Phase Contours & 'Modified' Zone Determination

The phase contours for the two waveguides with a separation of 31.62mm were obtained using the method outlined in Section 9.2. The E_y phase was plotted in the x - y plane at the location where the FZPA aperture would be placed. This distance was 0.75λ from the aperture of the waveguide at 30GHz.

Although the exact shape of the contours was unknown in advance, it was expected that the 180° phase zones would not be circular due to the interference of the waves from both feeds. Figure 9-10 shows the resulting normalized 180° phase contours. The shape of the contours made intuitive sense. They were more circular to the left and right of the figure where there was less interference, and they were less circular in the middle where there was significant interference.

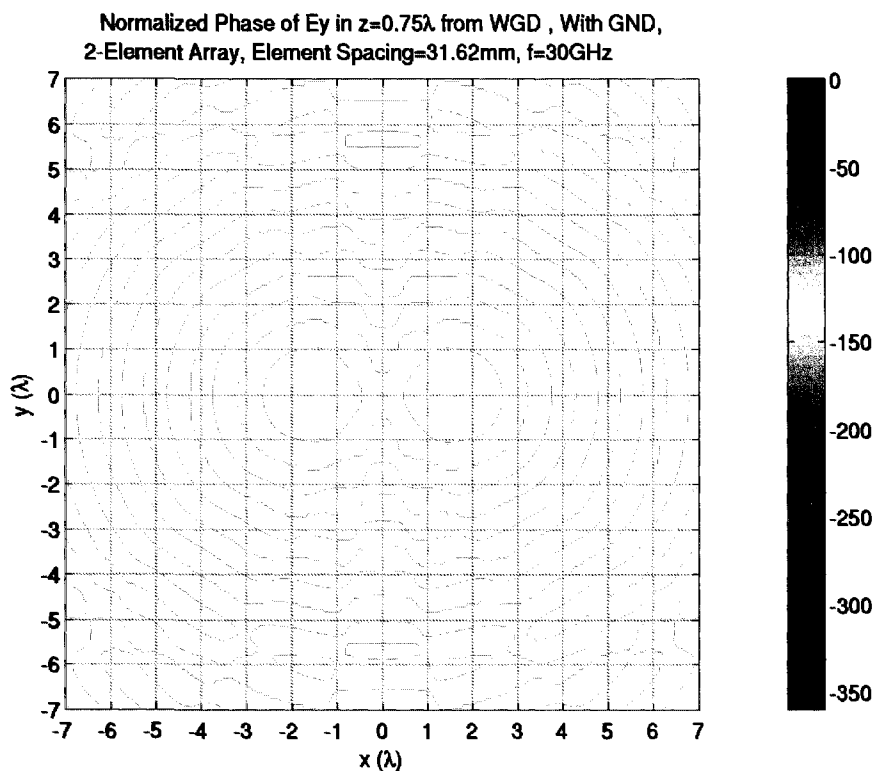
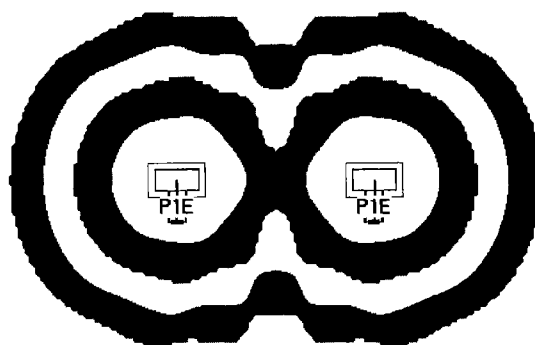
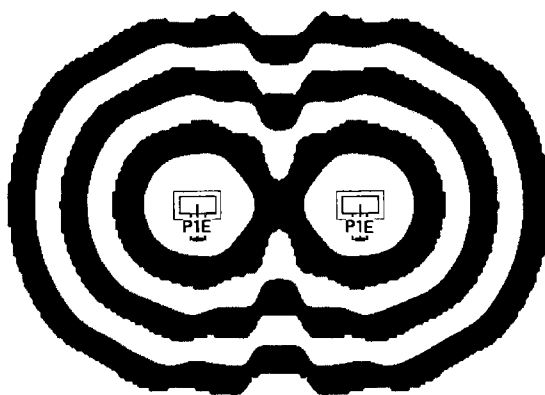


Figure 9-10: 180° Phase Contours of 2 Waveguides with Separation=31.62mm

After extracting these contours to a file and then importing them into Empire, the 'modified' zone FZPA was created for both the 2 and 3 metal zone cases. Figure 9-11 illustrates these two geometries where the waveguide feeds can be viewed at the center of each FZPA. In the model, the waveguides were excited by coaxial ports since Empire does not allow for simulation of multiple internal waveguides in a structure.



(a)



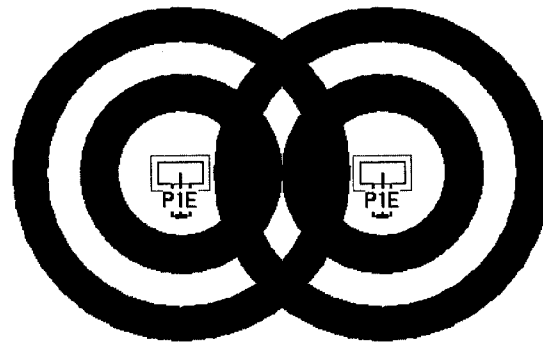
(b)

Figure 9-11: 'Modified' Zone 2-Element FZPA: (a) 2 Metal Zones, (b) 3 Metal Zones

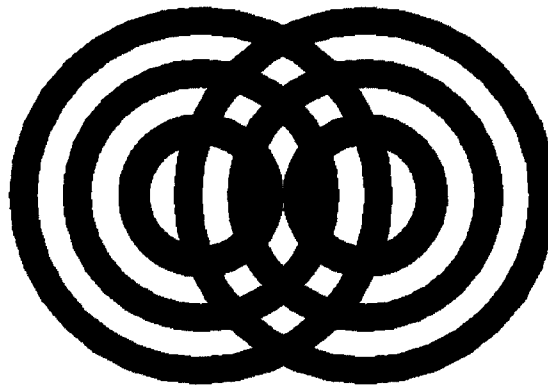
9.3.2 Circular Zone Determination

The circular zone radii for each FZPA were determined using Equation 2-5 with a focal distance of 0.75λ at 30GHz. The zones for each FZPA were placed, as computed, in the

aperture plane (i.e. 0.75λ from the waveguide) with a separation of 31.62mm. The resulting geometry is shown in Figure 9-12 for the 2 and 3 metal zone cases. It can be seen that there are overlapping zones in both cases. In the three metal zone case, a significant portion of the center zone is blocked by the overlapping zones from the other lens.



(a)



(b)

Figure 9-12: Circular Zone 2-Element FZPA: (a) 2 Metal Zones, (b) 3 Metal Zones

In order to study the effect of the center zone being blocked, the 3 metal zone case was modeled using two different methods in Empire. The first method used a ring subtraction technique, which meant that the zones were created by subtracting the air zones from the metal zones, leaving only the metal zones floating in air. With this approach, wherever

there is metal, metal will be simulated. The second method used a priority technique, which meant that each zone was assigned a priority with higher priority zones cutting holes in the lower priority zones. In this approach, the outer zone had the lowest priority and every zone moving inwards was assigned a progressively higher priority. In this way, the outer zones from one lens that would normally be blocking the center zone of the other lens would no longer be blocking since the center zone had a higher priority than the outer zones and would remain as air. Figure 9-13 shows a sketch of how these two approaches affected the resulting geometry in the 3 metal zone case. Using the priority approach yielded zones that more closely resemble the 'modified' zones shown in Figure 9-11(b).

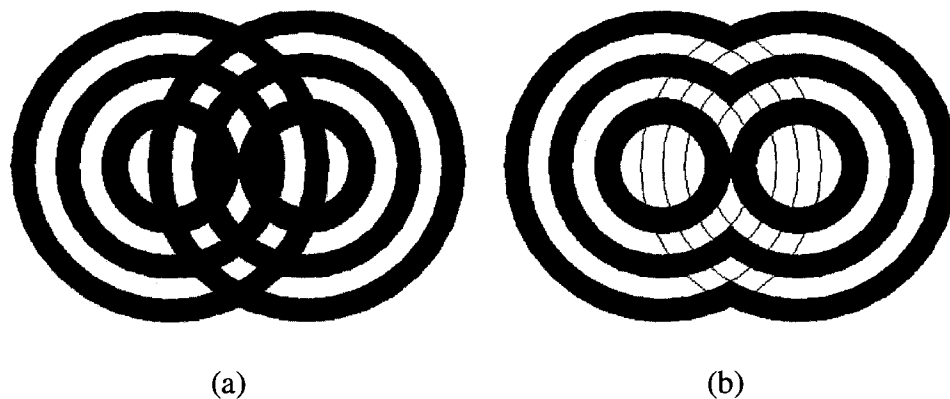


Figure 9-13: (a) Ring Subtraction Approach, (b) Priority Approach

9.3.3 'Modified' and Circular Zone 2-Element Array Patterns

Figure 9-14 shows the radiation patterns of the 2 metal zone case for the 'modified' zones compared to the circular zones. The peak directivity of the 'modified' zone case was 0.1dB higher than the circular zone case. The sidelobe level over all ϕ angles of the 'modified' case was nearly 0.2dB better than the circular case.

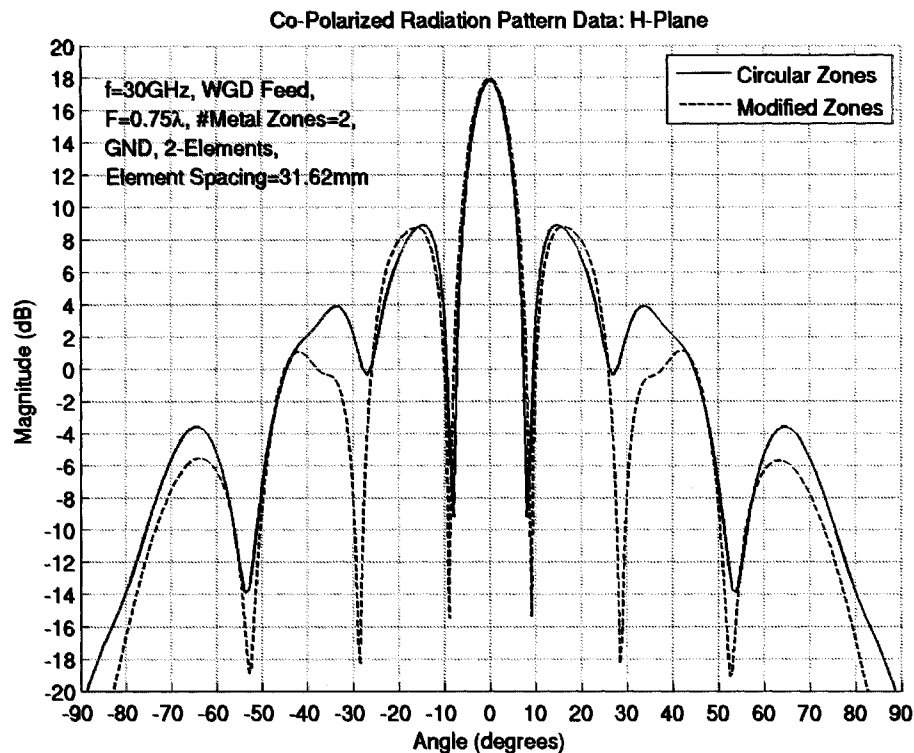


Figure 9-14: 'Modified' and Circular Zone 2-Element Array Patterns:
2 Metal Zones, H-Plane

Figures 9-15 and 9-16 show the normalized radiation patterns for the 3 metal zone case. Figure 9-15 shows the circular zone case with the ring subtraction approach whereas Figure 9-16 shows the circular zone case with the priority approach. The peak directivity of the 'modified' zone case was about 0.8dB higher than the circular zone case when using the ring subtraction approach where the center zone was partially blocked. However, when the center zone was not blocked in the priority approach case, the directivity difference dropped to about 0.1dB. The maximum sidelobe level over all ϕ of the 'modified' zone case was about 1.1dB better than the circular case using ring subtraction, but this difference dropped to about 0.6dB for the priority approach.

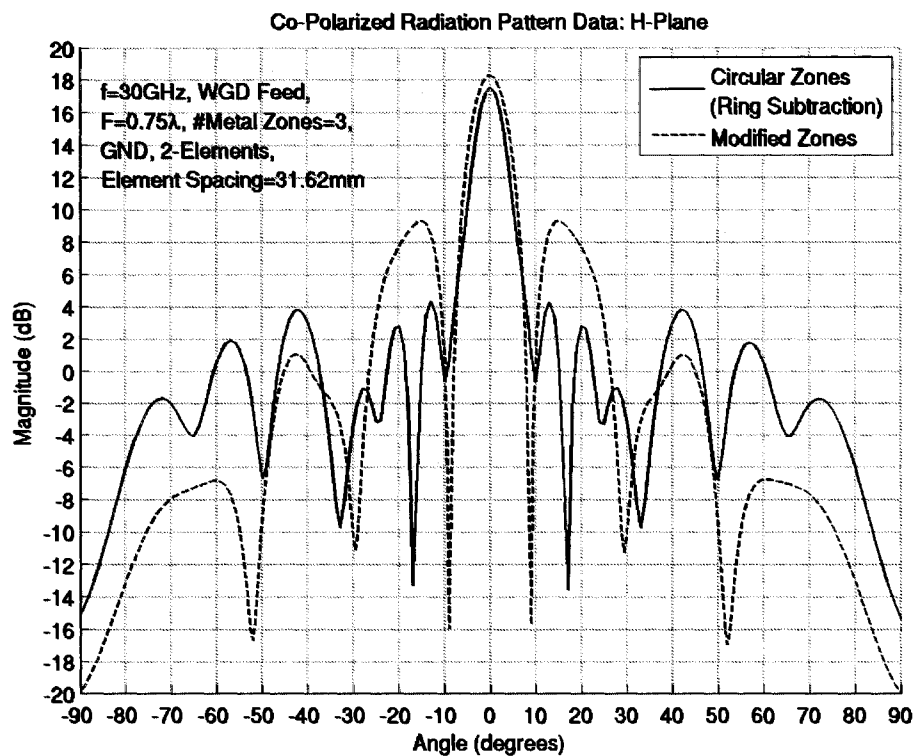


Figure 9-15: 3 Metal Zones with Ring Subtraction Approach for Circular Case, H-Plane

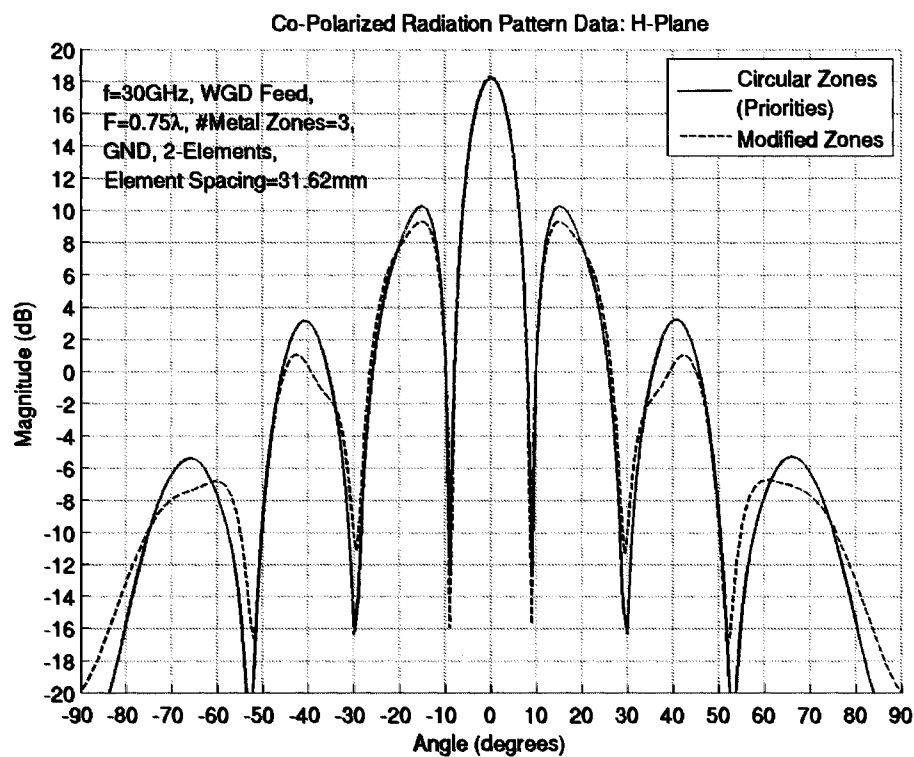


Figure 9-16: 3 Metal Zones with Priority Approach for Circular Case, H-plane

Several other array spacings were also modeled to further verify these findings. As the element spacing was reduced and the center zone blockage increased, the worse the radiation patterns became when using the ring subtraction approach.

9.3.4 Discussion

Generally, the radiation patterns of the 'modified' 2-element FZPA array were very close to those with the circular zones as long as the center zones of the elements were not blocked. The 3 metal zone circular elements, without modification to their overlap areas, do not yield comparable radiation patterns and directivity. In order to make use of the simpler-to-model circular zones, open areas that were being blocked by overlapping zones, particularly the center zone, needed to be removed. When this happened, the resulting zones resembled the 'modified' zones and the radiation patterns matched up more closely. Using the priority approach in the model to avoid this blockage was effective. However, the 'modified' zones still yielded a slightly higher peak directivity and slightly better relative sidelobes over all ϕ angles.

9.4 FZPA Planar Arrays

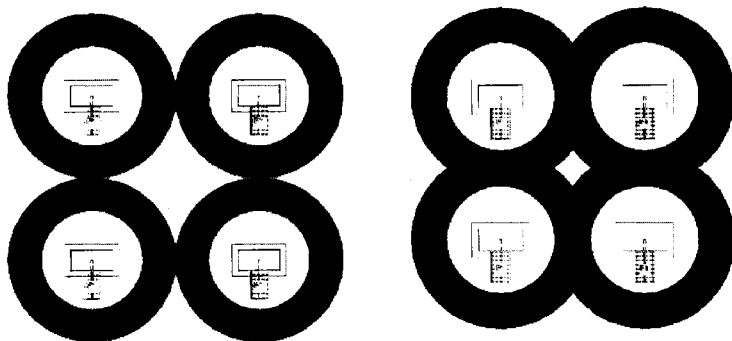
It was important to extend the 'modified' zone concept to larger arrays to further verify the concept. Also, a practical FZPA array would consist of a planar array as opposed to a linear array and would undoubtedly have many more elements. One of the objectives of this part of the study was to see how much directivity could be achieved with these bigger arrays. This was important for later comparisons with microstrip patch array technology. In this study, the 2x2 and 4x4 arrays were investigated.

Planar FZPA arrays are different from most standard arrays in use today. Standard planar

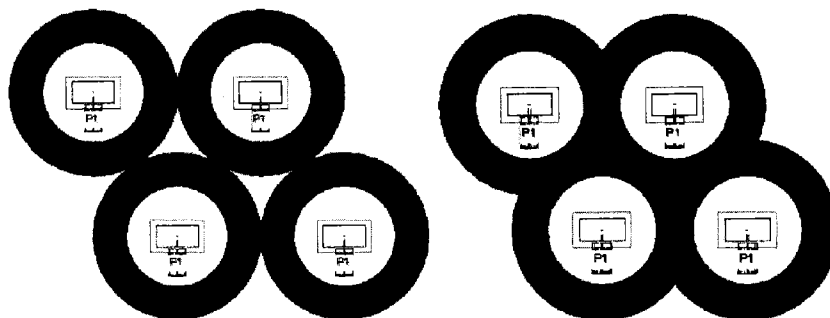
arrays usually consist of low gain elements with spacings of about $\lambda/2$ or λ between them in order to avoid grating lobes. The FZPA elements, on the other hand, have higher gain and, due to their relative sizes, must be spaced several wavelengths apart. This means that grating lobes are inevitable. The other difference with a FZPA is that the elements can be physically overlapped to some degree in order to help reduce the grating lobes. To this end, the element spacing and the array lattice were important aspects of the design to be investigated for the planar arrays.

9.4.1 Array Lattice Determination

Before modeling the 2x2 arrays, it was important to first establish the type of array lattice that would yield the best results. Like standard arrays, there are many ways that the elements can be arranged. This investigation was limited to rectangular and triangular lattices where the triangular lattice was equilateral, meaning that the horizontal and diagonal element spacings were equal. Simulations with identical FZPAs (1 zone, same focal distance, with ground plane at the aperture of the waveguide) and element spacings were performed with both lattice types. Two element spacings were used, the first where there was no overlap between elements, and the second where there was one complete metal zone overlapped. Figure 9-17 illustrates these four lattice configurations.



(a) No Overlap (left) & 1 Metal Zone Overlapped (right)



(b) No Overlap (left) & 1 Metal Zone Overlapped (right)

Figure 9-17: Lattice Configurations: (a) Rectangular, (b) Equilateral Triangular

The normalized radiation patterns for the no overlap case are shown in Figures 9-18 and 9-19 for the H- and E-planes respectively. There was very little difference in directivity (less than 0.1dB), but the rectangular lattice had higher grating lobes, particularly in the H-plane.

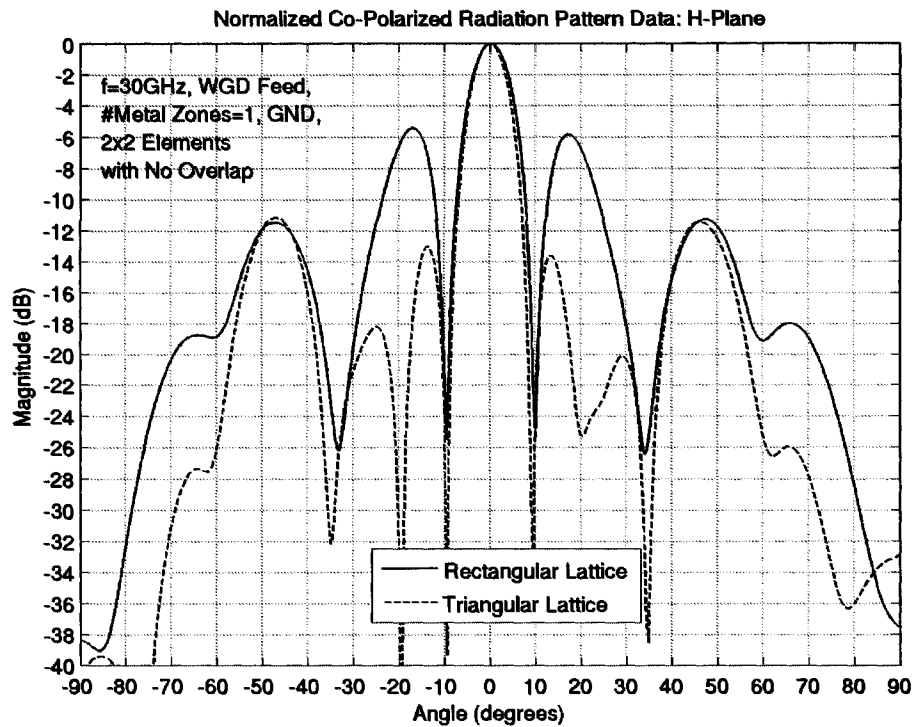


Figure 9-18: Radiation Patterns of No Overlap Case, H-Plane

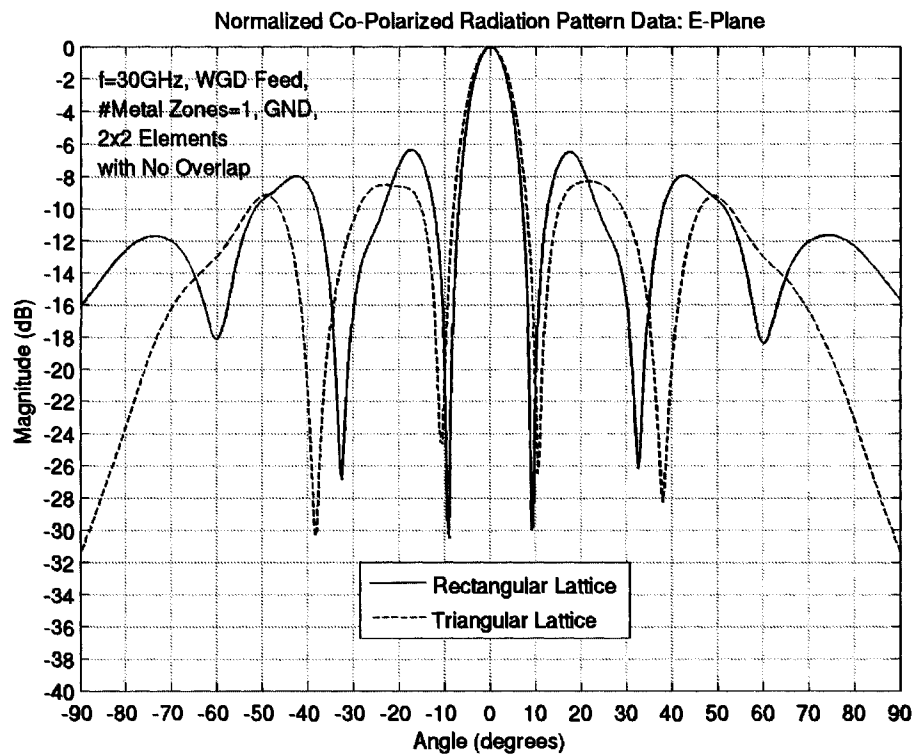


Figure 9-19: Radiation Patterns of No Overlap Case, E-Plane

The normalized radiation patterns for the 1 metal zone overlapped case are shown in Figures 9-20 and 9-21 for the H- and E-planes respectively. Again, there was very little difference in directivity (less than 0.01dB) and again the rectangular lattice had higher grating lobes, particularly in the H-plane. Since the grating lobes were better with the triangular lattice, it was selected for the array designs in thesis.

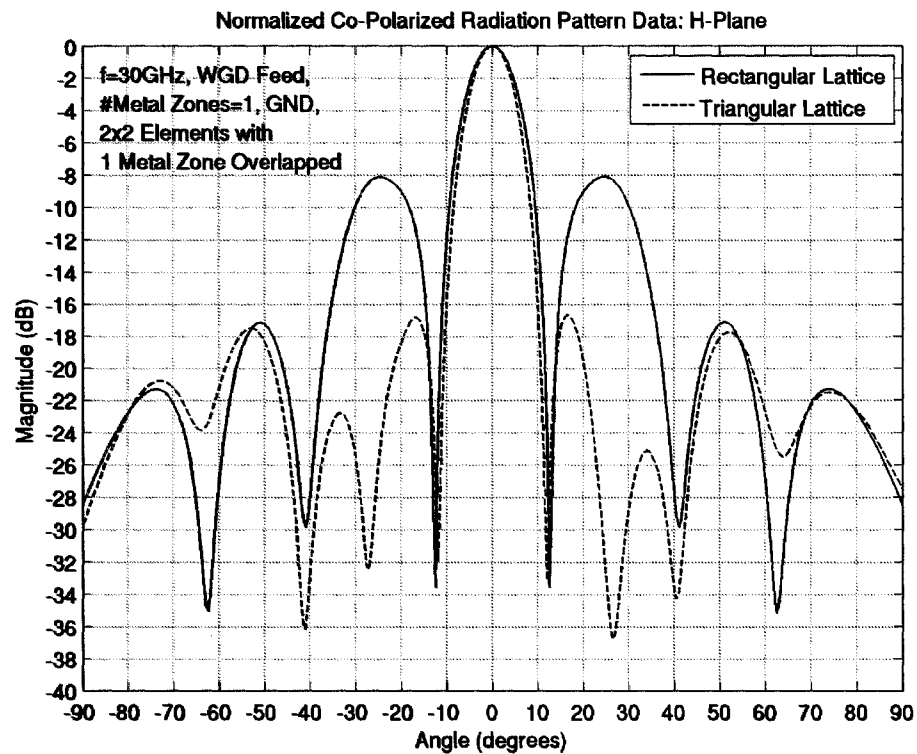


Figure 9-20: Radiation Patterns of 1 Metal Zone Overlapped Case, H-Plane

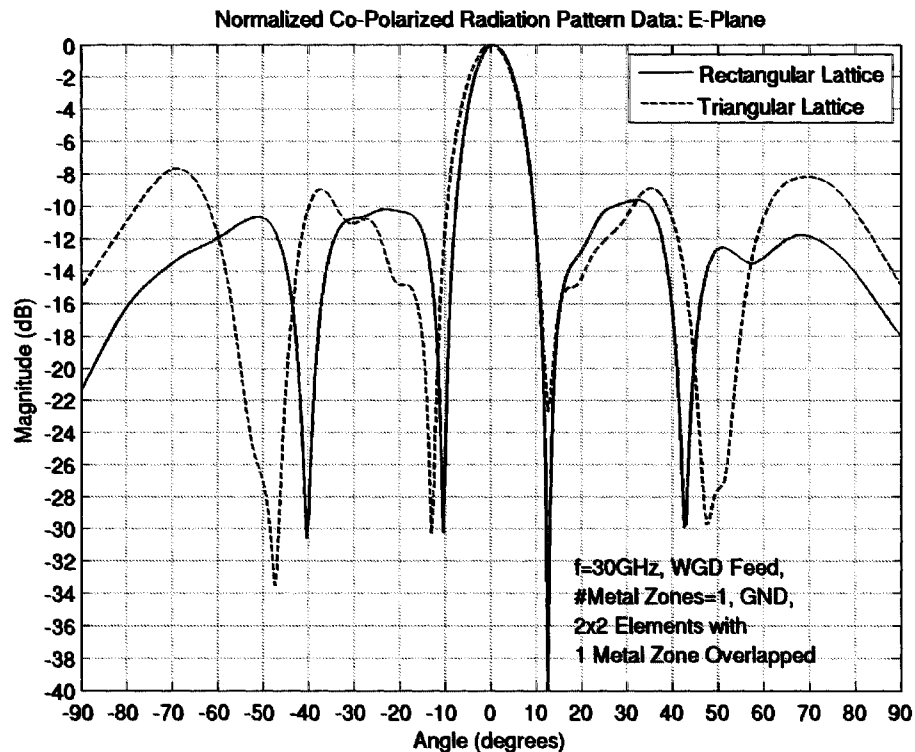


Figure 9-21: Radiation Patterns of 1 Metal Zone Overlapped Case, E-Plane

9.4.2 Grating Lobe Analysis

Since it was desirable to keep the array grating lobes below 10dB down from the array peak, many different element spacings were tested. A short program was written to take the full 3D Empire simulated radiation patterns for the single element FZPA as well as the desired array lattice geometry and compute the array factor and array pattern. From this array pattern, the worst relative grating lobes were determined. However, since this approach did not take into account the mutual coupling between the elements nor the effects of the elements being overlapped, the levels were not expected to be accurate.

Using the equilateral triangular lattice geometry, the FZPA with $F=0.75\lambda$ was again considered with both the 2 and 3 metal zone cases. It was found that for both the 2 and 3 metal zone cases, element spacings less than 3λ would yield grating lobes better than

10dB down from the peak. In order to keep the spacing as large as possible so as to minimize the zone overlap, 3λ was chosen for the element spacing.

9.4.3 Phase Contours & 'Modified' Zone Determination

The phase contours for the 2×2 waveguides with triangular lattice element spacing of 3λ were obtained using the method outlined in Section 9.2. The ground plane at the aperture of the waveguide was shaped and made big enough to just fit around the elements when they were eventually included. In this way, the ground plane size was different for the 2 and 3 metal zone cases. The E_y phase was plotted in the x - y plane at the location where the FZPA aperture would be placed. This distance was 0.75cm from the aperture of the waveguide in order to achieve a focal distance of 0.75λ . After extracting the contours to a file and then importing them into Empire, the 'modified' zone FZPA array was created for both the 2 and 3 metal zones cases. Figure 9-22 illustrates these two geometries where it can be seen that the zones are not circular.

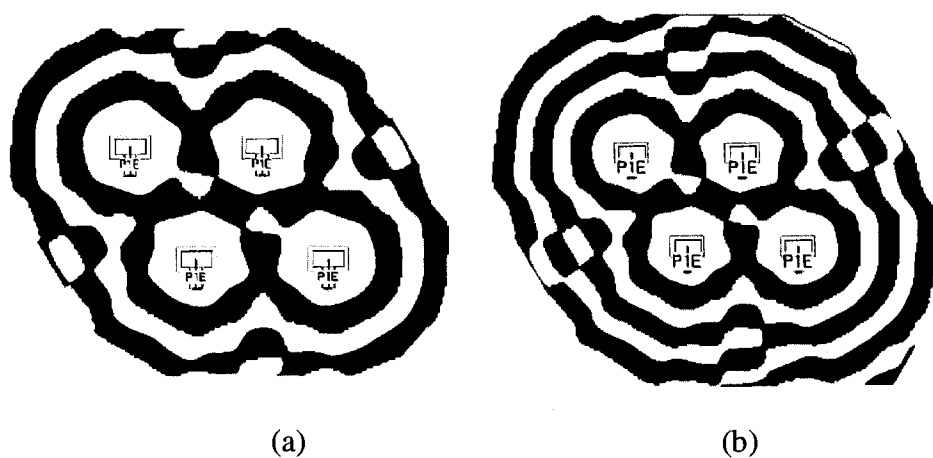


Figure 9-22: 'Modified' Zone 2×2 Element FZPA: (a) 2 Metal Zones, (b) 3 Metal Zones

9.4.4 Circular Zone Determination

The circular zone radii for each FZPA were again determined using Equation 2-5 with a focal distance of 0.75λ at 30GHz. The zones for each FZPA were placed, as computed, in the aperture plane (i.e. 0.75λ from the waveguide) with triangular lattice element spacing of 3λ . The resulting geometry is shown in Figure 9-23 for the 2 and 3 metal zone cases. The same shaped ground planes as used in Section 9.4.3 were used in this case. In order to avoid blockage of the center zone, the priority approach outlined in Section 9.3 was used.

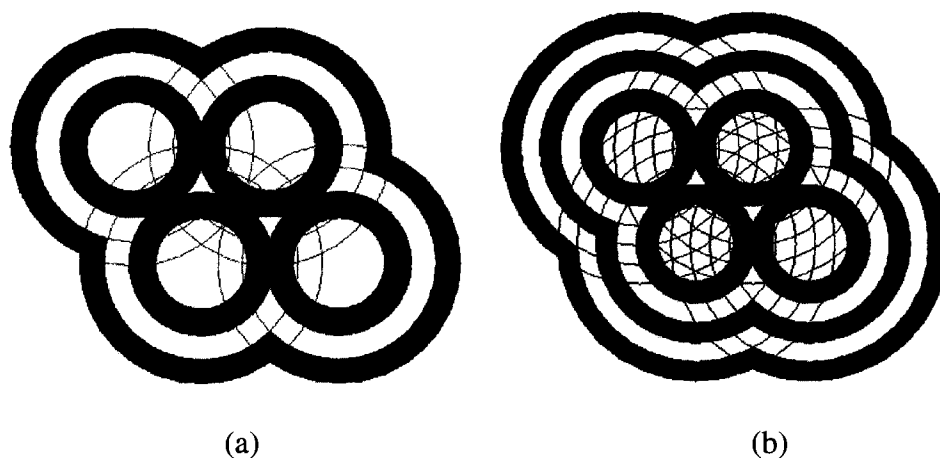


Figure 9-23: Circular Zone 2x2 Element FZPA: (a) 2 Metal Zones, (b) 3 Metal Zones

A comparison between Figures 9-23 and 9-22 revealed that the circular zone array made using the priority approach has a similar resulting zone shape to the 'modified' zones. It should be noted that if the ring subtraction approach were used in the 3 metal zone case, the center zone would be almost completely blocked as evidenced by the blue lines in Figure 9-23(b).

9.4.5 'Modified' and Circular Zone 2x2 Element Array Patterns

The radiation patterns for the 2 metal zone 2x2 element array are shown in Figures 9-24 and 9-25 for the H- and E-planes respectively. Each figure shows a comparison between the 'modified' and circular zone results. The 'modified' zone peak directivity was higher than the circular version by about 0.4dB and the maximum relative sidelobe over all ϕ angles was better for the modified zones by about 0.8dB.

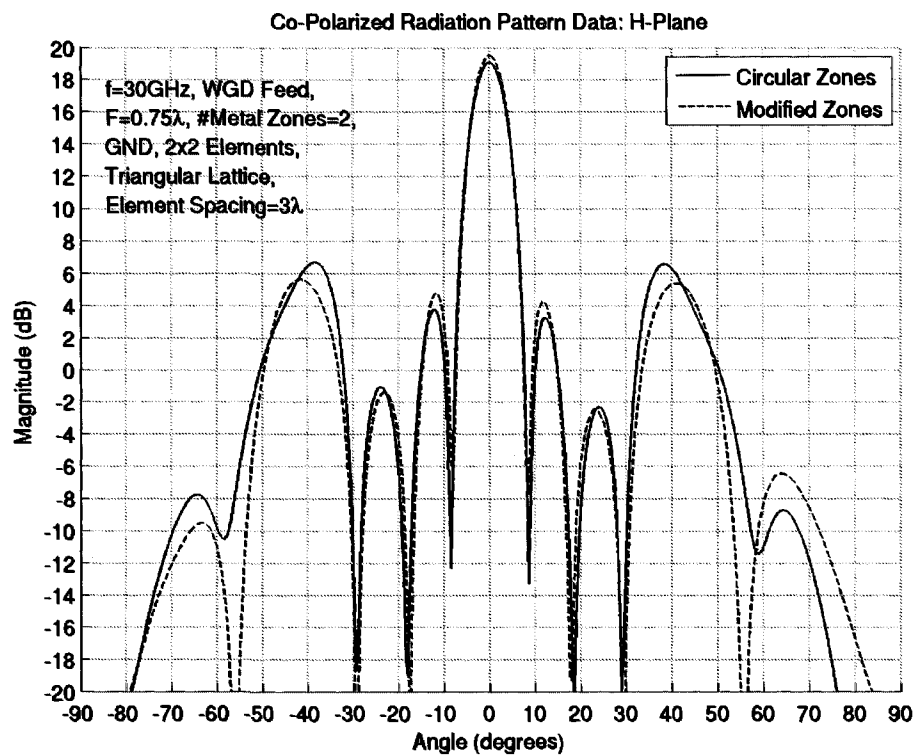


Figure 9-24: Radiation Patterns of 2 Metal Zone 2x2 Array, H-Plane

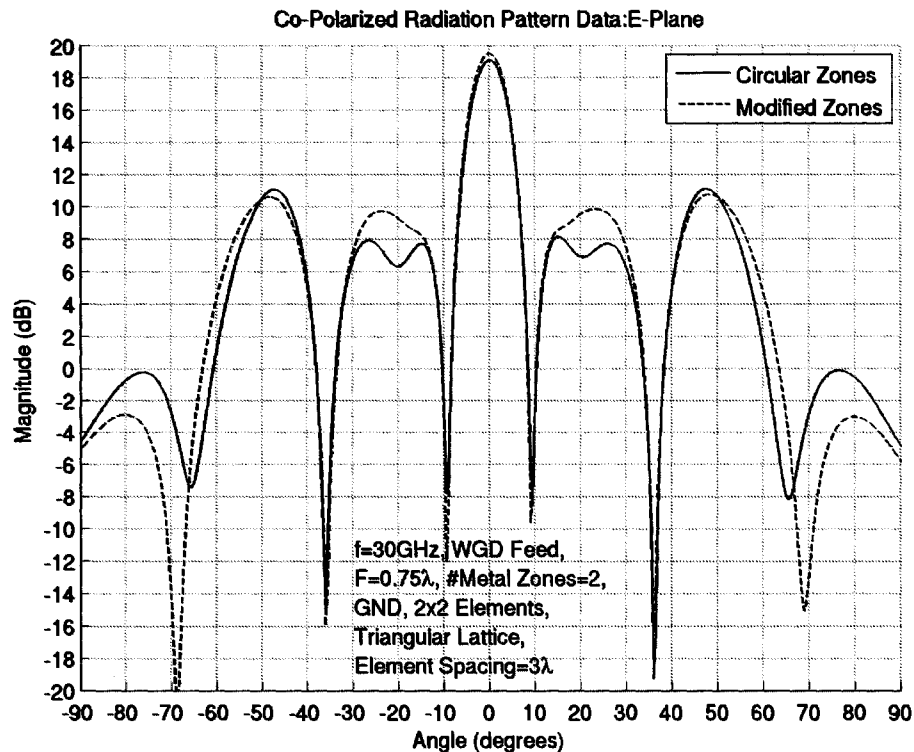


Figure 9-25: Radiation Patterns of 2 Metal Zone 2x2 Array, E-Plane

The radiation patterns for the 3 metal zone 2x2 array are shown in Figures 9-26 and 9-27 for the H- and E-planes respectively. Similar to the 2 metal zone case, each figure shows a comparison between the 'modified' and circular zone results. Again, the peak directivity of the 'modified' zone case was higher by nearly 0.5dB and the maximum sidelobe level over all ϕ angles was better also by about 0.5dB. Although the sidelobe levels in the H-plane of these figures were better than 10dB down from the peak, the maximum relative sidelobe level over all ϕ angles was actually only about 8dB down. In order to meet the desired sidelobe specification, the element spacing would need to be increased despite this being counter intuitive. The reasoning is related to the interference (mutual coupling) between the elements.

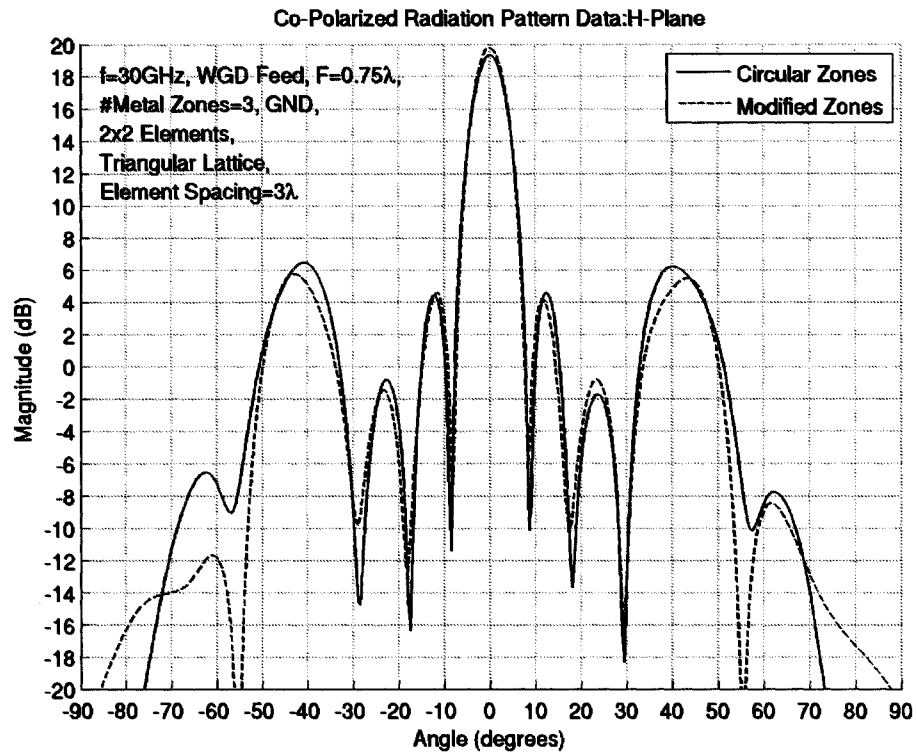


Figure 9-26: Radiation Patterns of 3 Metal Zone 2x2 Array, H-Plane

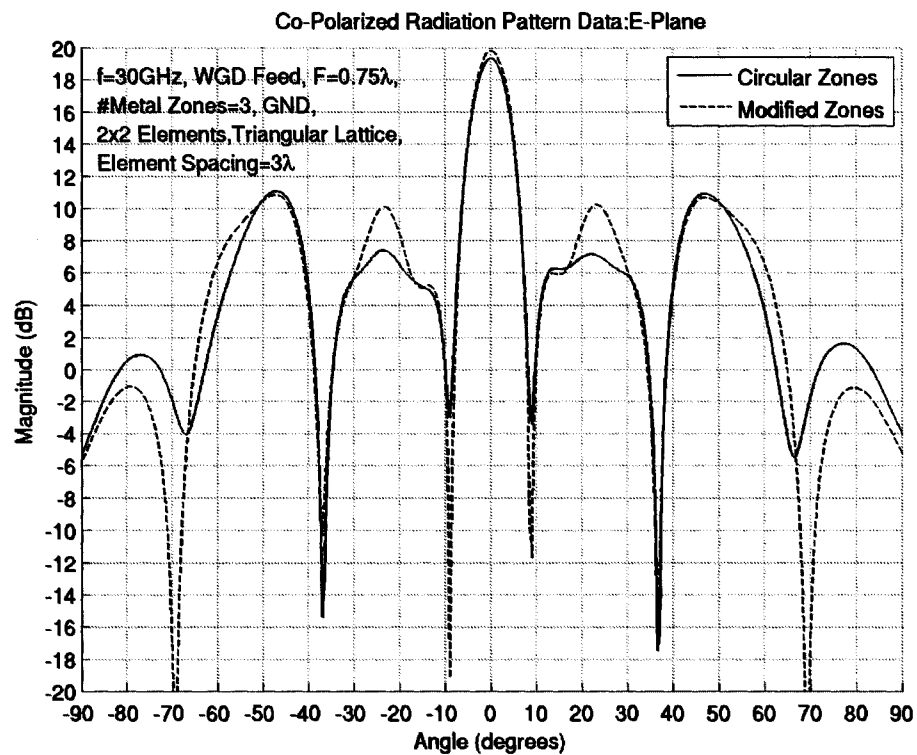


Figure 9-27: Radiation Patterns of 3 Metal Zone 2x2 Array, E-Plane

Similar to the 2-element case, the 'modified' zones performed slightly better than the circular zone array when the circular zone version was modeled using the priority approach. This continued to reflect the fact that the 'modified' zones were derived from the exact phase on the FZPA aperture, thus yielding a more accurate representation of the zone geometry. The circular zones, however, provided a good approximation to the actual zone geometry when modeled with the priority approach.

The 1.25λ focal distance was also modeled in the 2×2 array configuration. Table 9-2 shows a comparative summary of the results at 30GHz for the 0.75λ and 1.25λ focal distances. The table shows only the circular 2 zone cases for simplicity. The maximum relative sidelobe level for the $F=1.25\lambda$ case with 3λ element spacing was better than 10dB down from the peak.

<i>Focal Distance</i> (λ)	<i>Zone Type</i>	<i># Metal Zones</i>	<i>Element Spacing</i> (λ)	<i>Peak Directivity</i> (dB)	<i>Max. Relative Sidelobe Level</i> (dB)
0.75	circular	2	3	17.85	-8.25
1.25	circular	2	2.5	20.25	-7.30
1.25	circular	2	3	20.97	-10.29

Table 9-2: Summary of Simulation Results

9.4.6 4x4 Array

Since the radiation patterns of the circular zones were a fair approximation to the patterns of the 'modified' zones, only the circular zones were used in the 4×4 array analysis for modeling simplicity. Prior to modeling the 4×4 array, a grating lobe analysis was again undertaken to determine an appropriate element spacing to maintain the grating lobes

better than 10dB below the peak. The 4x4 array geometry was set as an equilateral triangle lattice and the analysis was performed for two different focal distances, $F=0.75\lambda$ and $F=1.25\lambda$, both with 2 metal zones. The analysis showed that, in the absence of mutual coupling and interference effects, the element spacing at 30GHz should be about 2λ for the $F=0.75\lambda$ case and 2.5λ for the $F=1.25\lambda$. Figure 9-28 illustrates the two arrays after applying the priority approach.

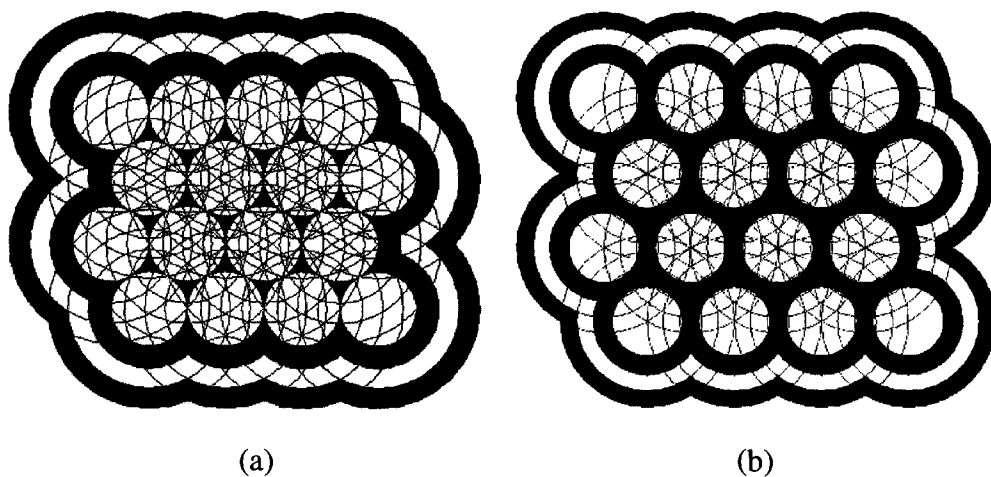


Figure 9-28: 4x4 Array Geometry: (a) $F=0.75\lambda$, (b) $F=1.25\lambda$

Figure 9-29 shows the radiation patterns of the 4x4 array with $F=0.75\lambda$ and 2 metal zones. The grating lobes in the E-plane were very high and were only about 5dB below the main beam peak. This was likely a result of the mutual coupling and interference between elements, which was included in the simulations but not in the grating lobe analysis.

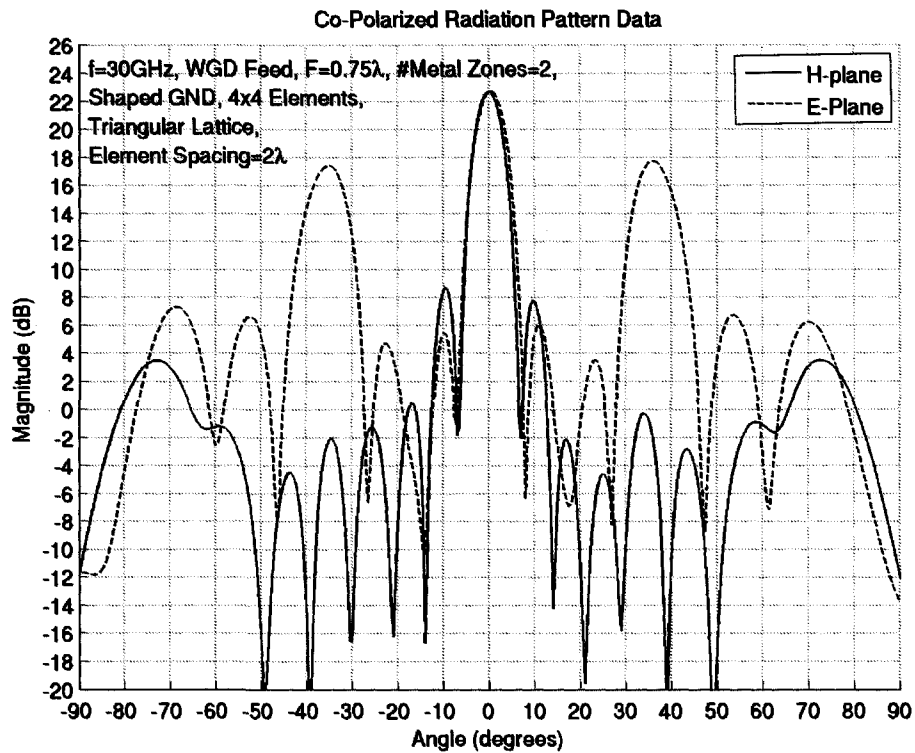


Figure 9-29: Radiation Patterns of 2 Metal Zone $F=0.75\lambda$ 4x4 Array

Figure 9-30 shows the radiation patterns of the 4x4 array with $F=1.25\lambda$ and 2 metal zones. Simulations revealed that the element spacing of 2λ yielded grating lobes that were only about 5.4dB below the main beam peak. The element spacing was increased to 3λ where it was found that the grating lobes in the E-plane were better. They improved to just over 10dB below the main beam peak. The curves in Figure 9-30 are for the 3λ element spacing.

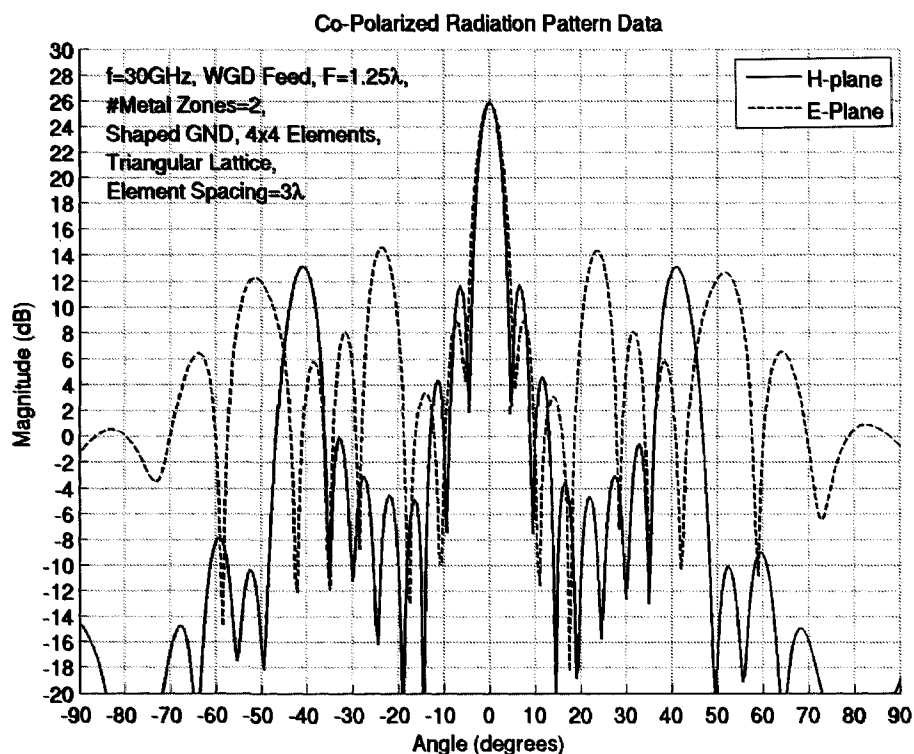


Figure 9-30: Radiation Patterns of 2 Metal Zone $F=1.25\lambda$ 4x4 Array

Table 9-3 summarizes the results for the 4x4 simulated FZPA arrays.

Focal Distance (λ)	Zone Type	# Metal Zones	Element Spacing (λ)	Peak Directivity (dB)	Max. Relative Sidelobe Level (dB)
0.75	circular	2	2	22.68	-4.96
1.25	circular	2	2.5	24.56	-5.41
1.25	circular	2	3	25.87	-10.16

Table 9-3: Summary of Simulation Results

9.4.7 Discussion

The simulations discussed in this section revealed that the 'modified' zones continued to slightly outperform the circular zones. However, when using the priority approach with

the circular zone modeling, the resulting geometry and radiation patterns were very similar to those of the 'modified' zones. Since modeling the circular zones was far less time consuming than modeling the 'modified' zones, the circular zones were chosen for the larger array work. Using equilateral triangular array lattices, it was found that a low profile 4x4 array could yield nearly 25dB directivity and overall grating lobes better than 10dB down from the array peak.

9.5 FZPA Arrays with Different Elements

Typically arrays are comprised of identical elements. This is to facilitate the computation of the array radiation patterns, which can easily be determined through calculation of the array factor when the elements are identical. In this case, the array pattern is the product of the array factor and the element pattern. Equation 9-1 shows the normalized array factor for a planar array where the array consists of N elements, A_n is the magnitude of the n^{th} element, β is the linear phase progression between elements, (x_i, y_i) is the location of the elements, and Ψ_i accounts for the difference in phase arising from the different path lengths from each element to the far-field observation point.

$$af(\Psi) = \frac{\sum_{n=1}^N A_n e^{-j\Psi_n}}{\max \left\{ \left| \sum_{n=1}^N A_n e^{-j\Psi_n} \right| \right\}} \quad (9-1)$$

$$\text{where } \Psi_i = k x_i \sin(\theta) \cos(\phi) + k y_i \sin(\theta) \sin(\phi) + \beta_i$$

When the elements are not identical, the equation for the array pattern is not so straightforward to compute since the individual element patterns would not be same. The

radiation pattern of each element must be taken into account and is far more complex to compute by hand. Modeling software such as Empire [3-3], however, can model such arrays accurately and can account for the mutual coupling between elements.

Although it has always been possible to design arrays with different elements, FZPA arrays are particularly well suited to such designs. This is because of the FZPA structure, which can maintain certain fundamental characteristics while allowing modification of others. In this study, arrays having elements with different reference phases was investigated as well as arrays having elements with different zone rotations.

9.5.1 Arrays with Different Reference Phase Elements

It was expected that applying a reference phase to a FZPA array element would have the same effect as applying an electrical phase to identical elements of an array. To verify this assumption, two test cases were modeled in Empire, one without any applied reference phase and the second with a progressive reference phase from one element to the other around the array. The FZPA elements were kept the same other than the reference phase (5 metal zones, $F=3.75\lambda$, $F/D=0.237$, element spacing= 11λ , equilateral triangular lattice). The array geometry is shown in Figure 9-31 where the elements are numbered clockwise from 1 through 4 starting from the element on the top left.

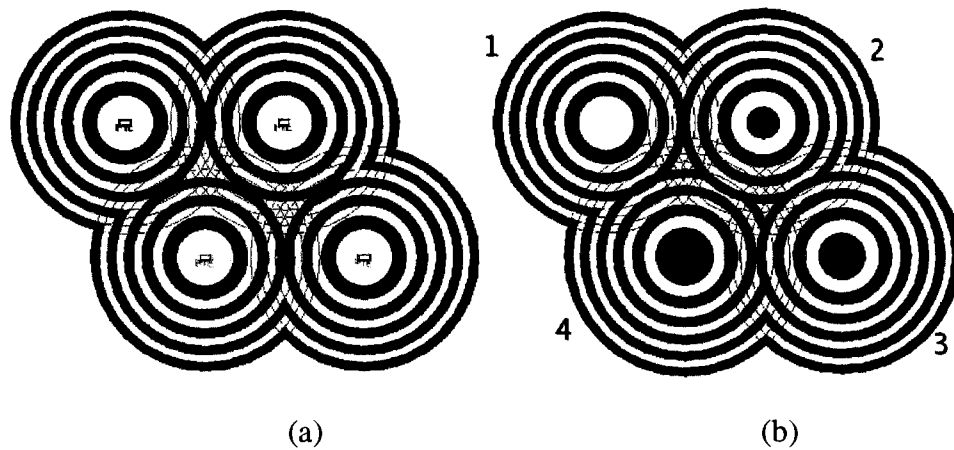


Figure 9-31: Array Geometry: (a) No Reference Phase, (b) Progressive Reference Phase

Figures 9-32 and 9-33 show the resulting radiation patterns in the H-plane for the case without reference phase and the case with a progressive reference phase (1) 0° , (2) 60° , (3) 120° , (4) 180° respectively. The main beam of the radiation pattern in Figure 9-33 is quite different from the one in Figure 9-32. Having the progressive reference phase caused the main beam to split into three unsymmetrical beams.

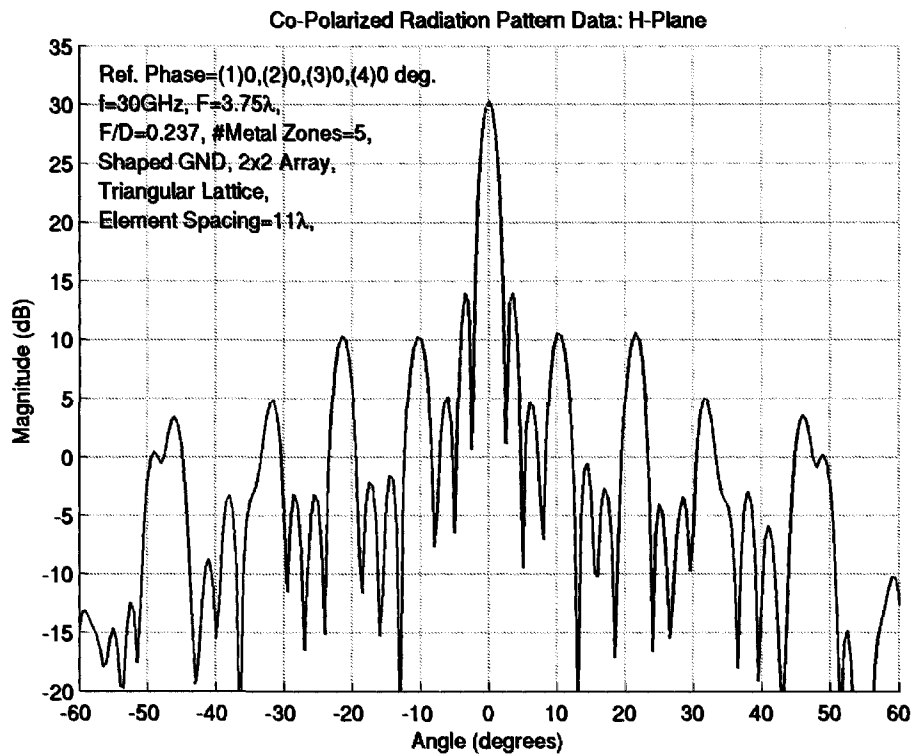


Figure 9-32: All Elements with 0° Reference Phase, H-Plane

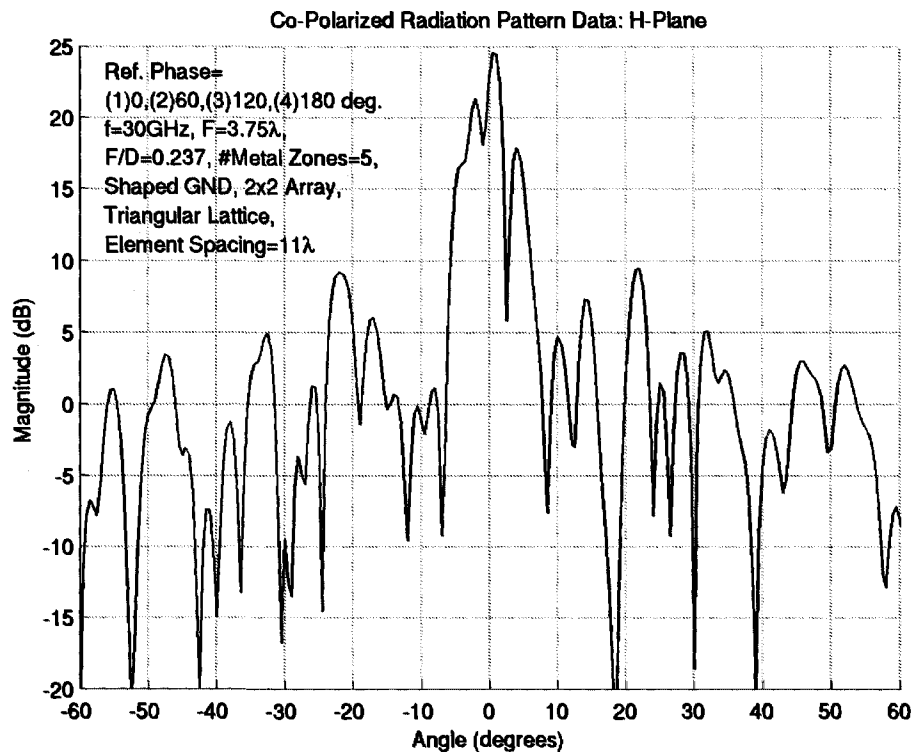


Figure 9-33: Progressive Reference Phase (1) 0° , (2) 60° , (3) 120° , (4) 180° , H-Plane

To better visualize the change to the radiation pattern, Figure 9-34 illustrates a top view of the 3D far-field patterns. The patterns are clipped at the same level from the normalized peak to emphasize the main beam and immediate sidelobes. The two patterns were very different. There was increased sidelobe activity in the pattern with the progressive reference phase and the main beam asymmetry was evident.

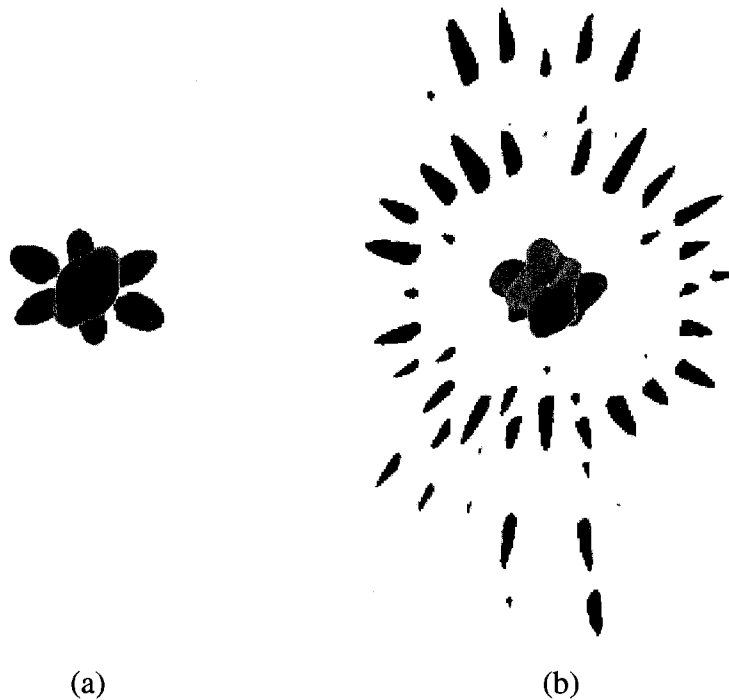


Figure 9-34: 3D Far-Field Patterns: (a) 0° Reference Phase, (b) Progressive Reference Phase (1) 0° , (2) 60° , (3) 120° , (4) 180°

These results indicated that applying different reference phases to the elements of an array will only succeed in skewing the main beam. This was because the elements have such a large spacing between them (11λ in this case) that the phase change caused the grating lobes to be too close to the main beam.

The results with the progressive reference phase were similar to what would have been

achieved by taking the same array lattice and identical single patterns then applying the same progressive electrical phase shift to each element. Figure 9-35 illustrates this result in comparison to the one with modeled reference phase. It can be seen that the two curves are virtually identical, particularly in the area of the main beam.

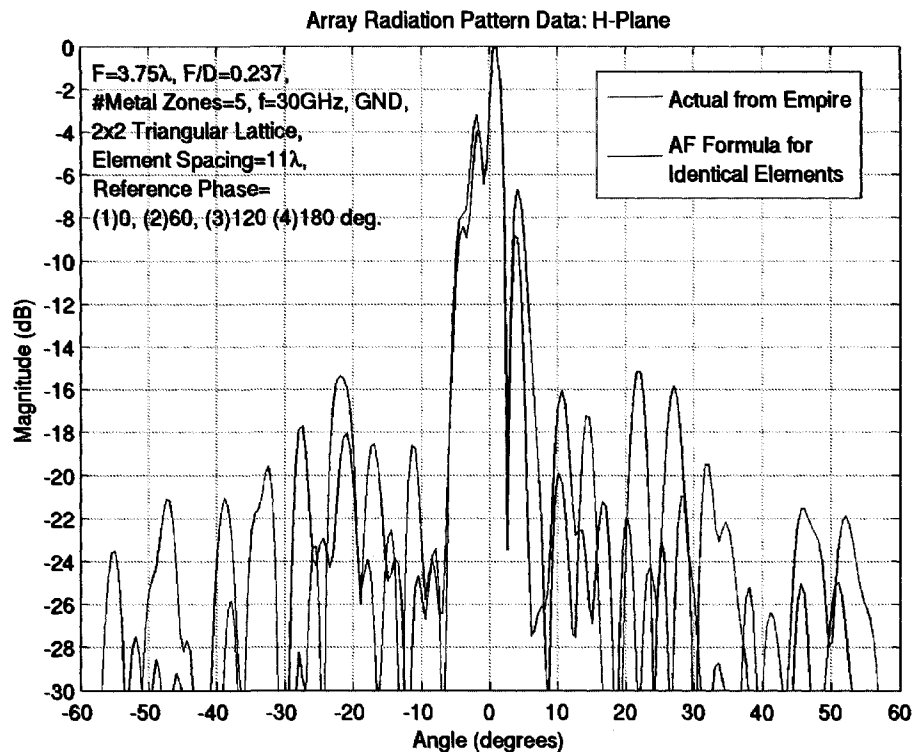


Figure 9-35: Empire vs. Array Factor (AF) Pattern for Identical Elements, H-Plane

This result was important because it showed how assuming the elements were identical in an array was a good approximation. This was true even though the array pattern computation for identical elements did not take into account mutual coupling or interaction between elements. By looking at the element patterns for the various reference phase cases, shown in Figure 9-36, it can be seen that they are very similar within $\pm 5^\circ$ to 10° from boresight. This indicates that when the element patterns of the

non-identical elements are very similar, the identical element array pattern can be used to approximate the patterns for non-identical elements.

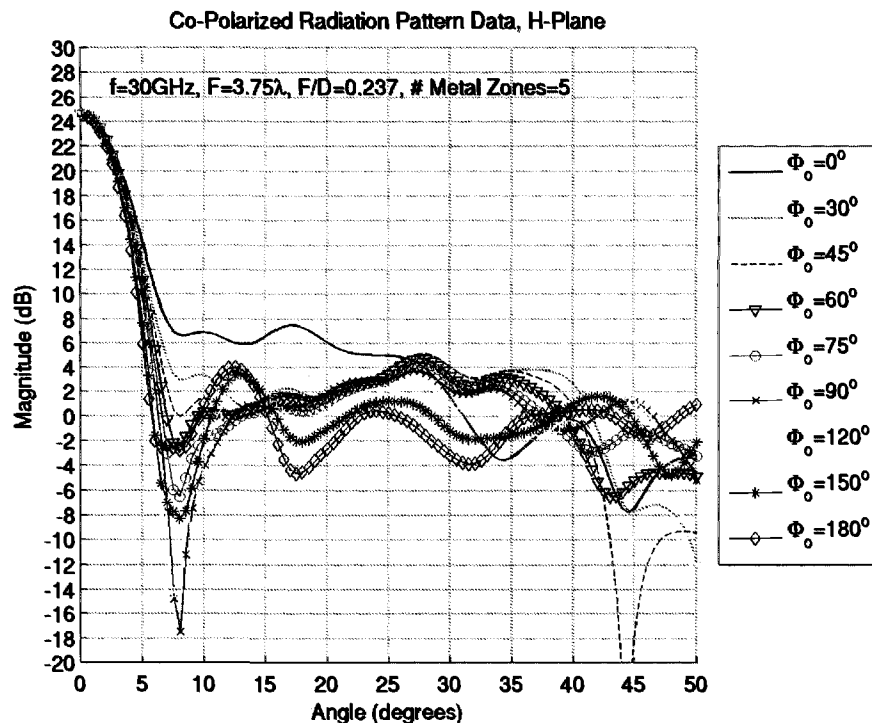


Figure 9-36: Radiation Patterns of Various Reference Phase Cases, H-Plane

9.5.2 Arrays with Rotated Hex-Cut & Hexagonal Elements

It was found in Chapter 6 that rotating the alternating hex-cut zones of the FZPA yielded some degree of control over the sidelobe levels and locations. The intent of this section was to extend the zone rotation concept to FZPA arrays and allow for control over the levels and locations of the sidelobes.

Prior to proceeding with this investigation, the element patterns of various rotated zone configurations were compared to the array factor patterns to verify that the first sidelobe was not being blanketed by the main beam of the element pattern. If the element pattern

main beam was wider than the first sidelobes of the array factor, then the sidelobes of the resulting array radiation pattern would not be affected by any combination of different elements.

Figures 9-37 through 9-39 show examples of different element patterns (5 metal zones, $F=3.75\lambda$, and ground plane at the aperture of the waveguide) compared to the appropriate array factors (2x2 equilateral triangle array lattice having 11λ element spacing). The first case consisted of an element pattern where the zones were all circular, the second was a rotated zone alternating hex-cut case, and the third consisted of rotated hexagonal zones. The element patterns in all three cases were much wider than the first sidelobes in the array factor pattern. This was also found to be true of all alternating hex-cut zone rotation cases with this focal distance.

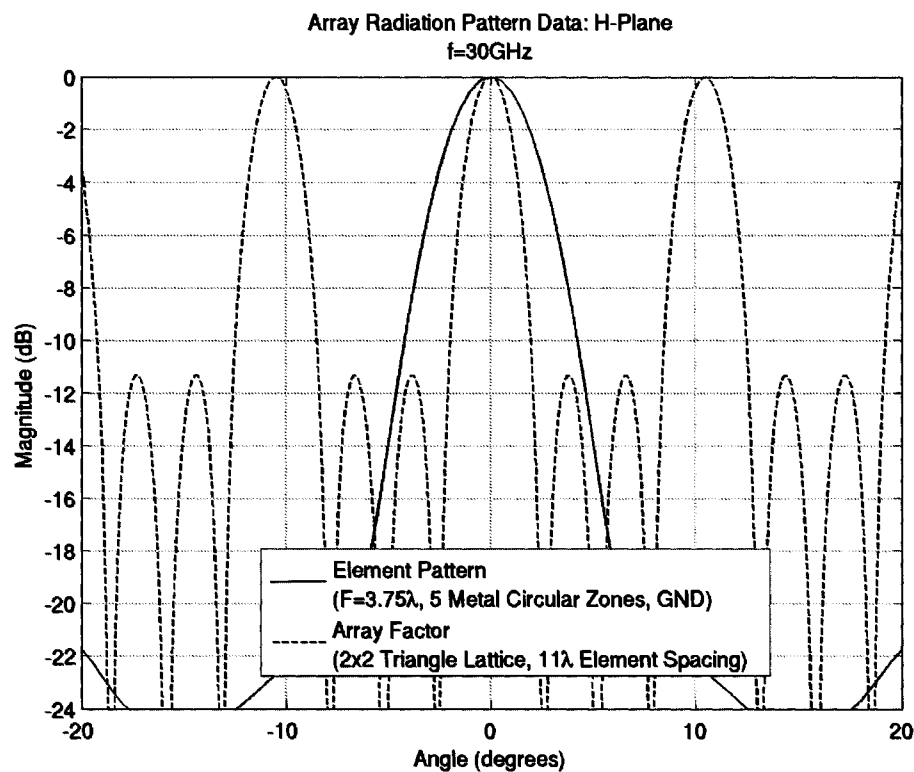


Figure 9-37: Element Pattern (all circular zones) vs. Array Factor, H-Plane

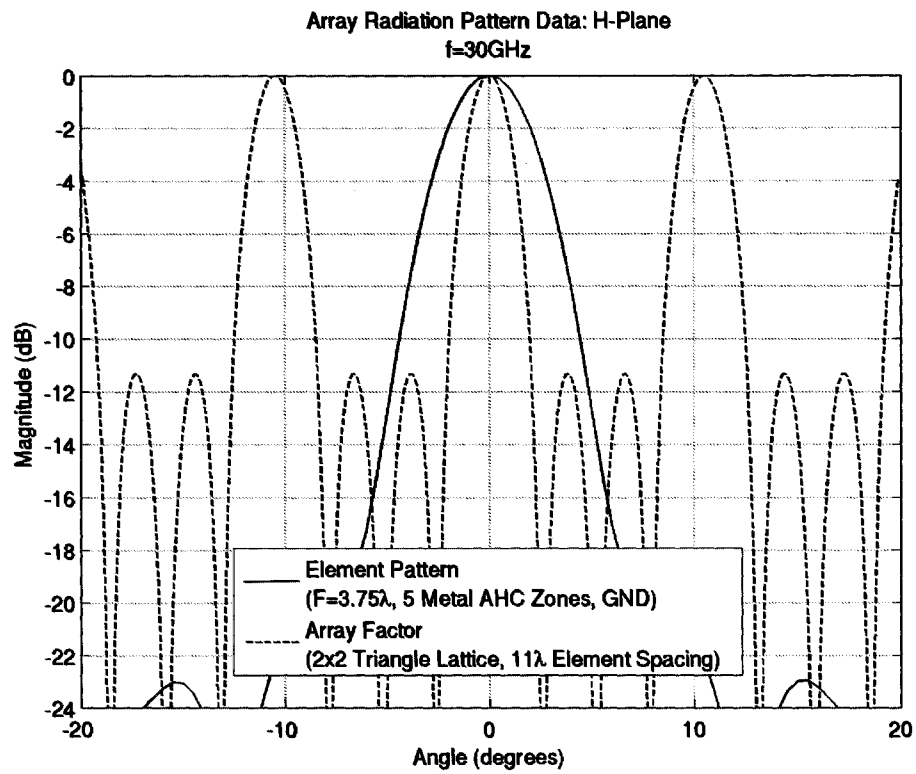


Figure 9-38: Element Pattern (alternating hex-cut zones) vs. Array Factor, H-Plane

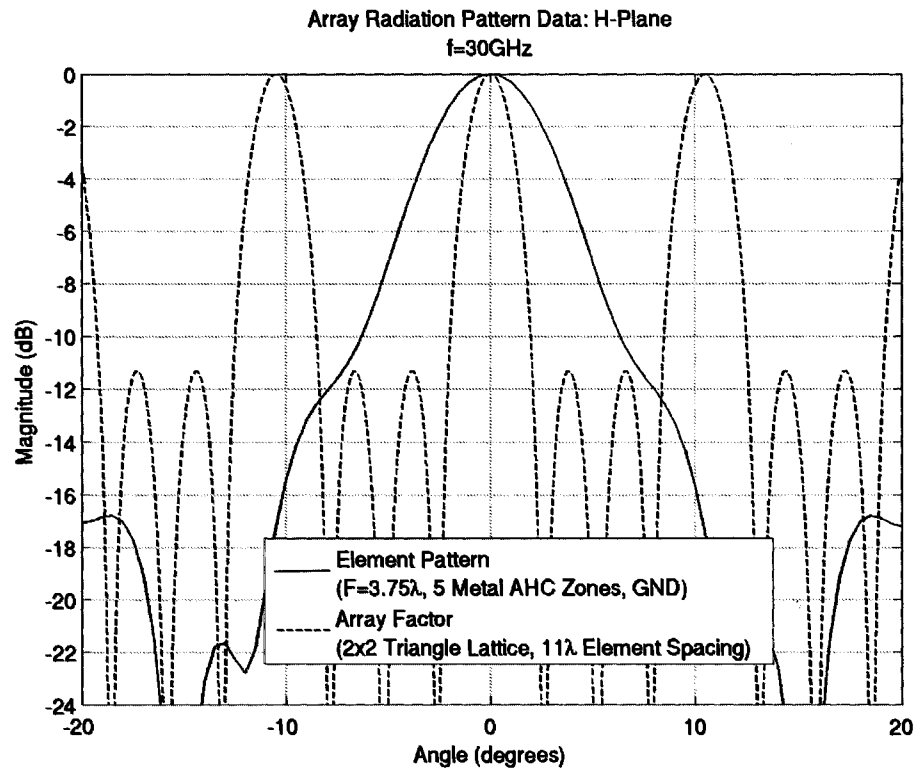


Figure 9-39: Element Pattern (all hexagonal zones) vs. Array Factor, H-Plane

Figures 9-40 and 9-41 show element patterns with smaller focal distances ($F=1.75\lambda$, 2 or 3 metal zones, ground plane at the aperture of the waveguide) and array factors with smaller element spacings (2x2 equilateral triangle array lattice having 3λ element spacing). Each of these two cases has the inner zone rotated by 45° clockwise.

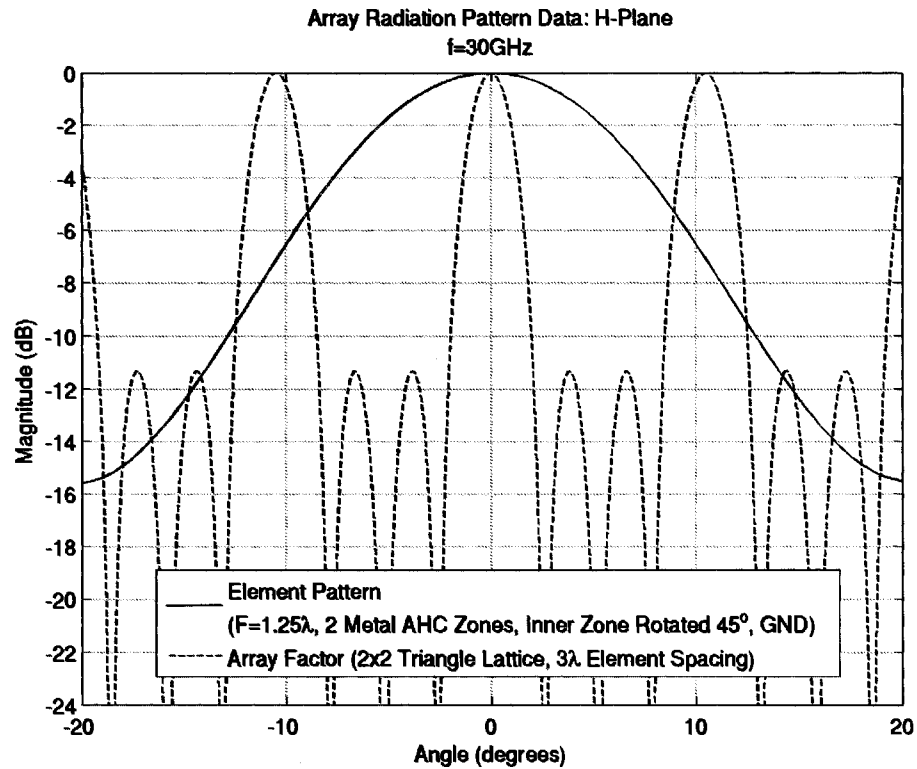


Figure 9-40: Element Pattern (2 alternating hex-cut zones) vs. Array Factor, H-Plane

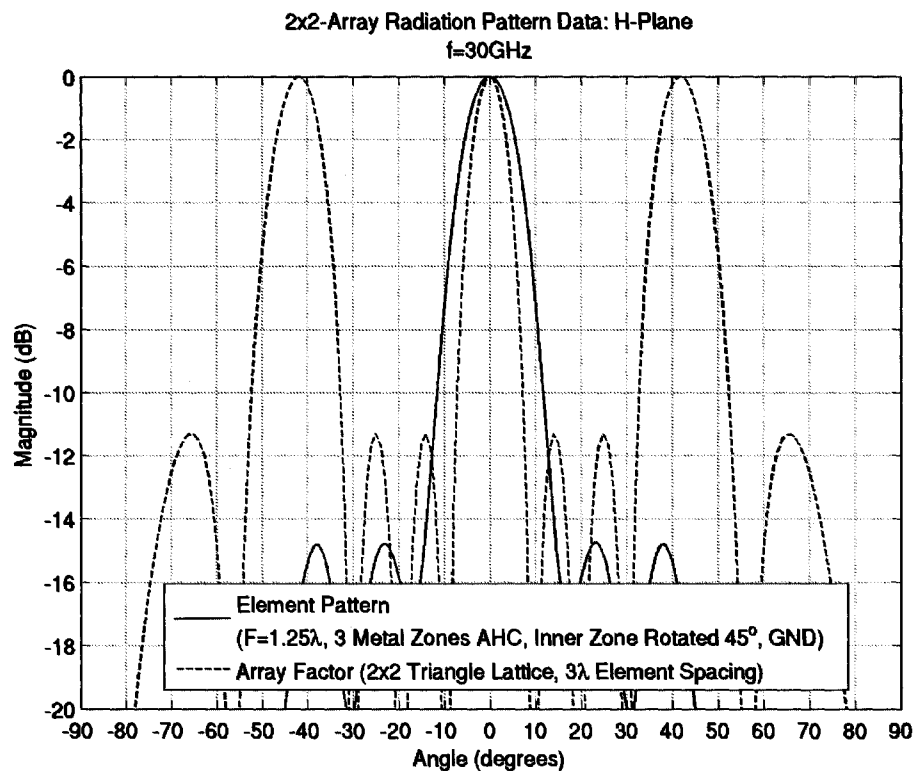


Figure 9-41: Element Pattern (3 alternating hex-cut zones) vs. Array Factor, H-Plane

This time, the element pattern of the 3 metal zone alternating hex-cut case was not as wide as with the $F=3.75\lambda$ case. In fact, the first sidelobes were slightly outside of the element pattern main beam. This case was therefore identified as having potential for array sidelobe control and so was simulated in various array configurations at 30GHz. Table 9-4 summarizes these configurations as well as the results, where the elements are numbered the same as before, clockwise starting on the top left.

	Rotation Configuration (zone rotations from outer to inner metal zones)	#Metal Zones	Peak Directivity (dB)	Max. Relative Sidelobe (dB)	Angle of Max. Sidelobe (degrees)
	No Rotation	3	21.49	-10.77	60
<i>A</i>	All elements with 0°, 0°,45°	3	21.61	-10.79	61
<i>B</i>	(1) 0°,0°,0°, (2) 45°,45°,45°, (3) 0°,0°,0°, (4) 0°,0°,0°	3	21.55	-10.83	-120
<i>C</i>	(1) 0°,0°,0°, (2) 0°,0°,45°, (3) 0°,0°,45°, (4) 0°,0°,0°	3	21.48	-10.78	60
<i>D</i>	(1) 0°,0°,0°, (2) 25°,25°,25°, (3)35°,35°,35°, (4) 45°,45°,45°	3	21.74	-11.02	-120

Table 9-4: Summary of Results for Rotated Alternating Hex-Cut Zone FZPA Array

Table 9-4 shows how, no matter what the rotation configuration, the maximum sidelobe remains in essentially the same spot, either at 60° or -120°. Also, the level of the sidelobe does not change significantly. Figure 9-42 illustrates the top view of the 3D far-field radiation pattern for the array in all five cases from the table. The patterns were all clipped at the same level from the normalized peak to view the impact on the close-in sidelobes of the array. It is clear from this figure that the radiation patterns were virtually identical.

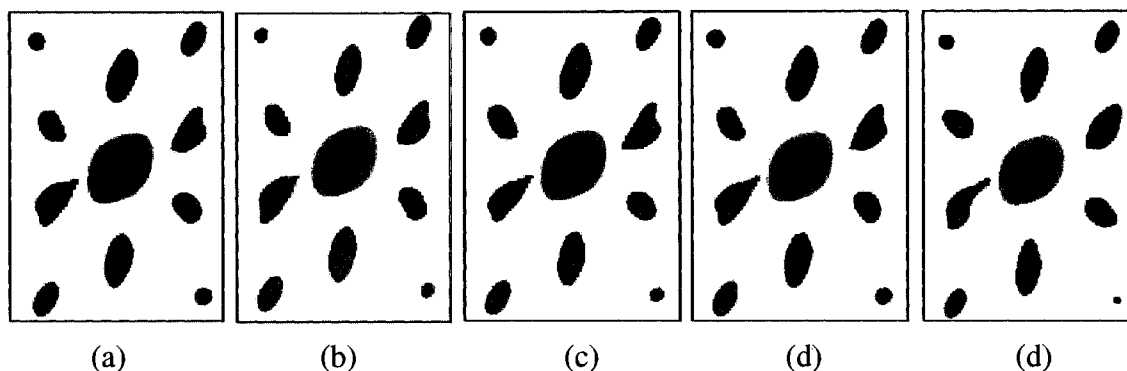


Figure 9-42: 3D Far-Field Patterns: (a) No Rotation, (b) Rotation *A*, (c) Rotation *B*, (d) Rotation *C*, (e) Rotation *D*

These results showed that, even if part of the array factor inner sidelobe was free from the element pattern main beam, it was not enough to create sidelobe movement or rotation in the array pattern. Since no other cases were found where the array factor inner sidelobe was completely free from the element pattern, no further arrays of this type were modeled.

9.5.3 Discussion

This investigation showed that, of the two methods analyzed, neither approach resulted in the desired array sidelobe control. Having different reference phases on each array element only succeeded in affecting negatively the main beam due to the close proximity of the grating lobes to the main beam as a result of the large element spacing. Having different zone rotation configurations on each element in the array also did not provide sidelobe control. In fact, the array radiation patterns were virtually unchanged since the element patterns were all wider than the array factor inner sidelobe. It was shown that even if those inner sidelobes were only slightly covered by the element radiation pattern, there would still be no effect on the overall array radiation pattern.

9.6 FZPA Array & Microstrip Patch Array Losses

Since the FZPA array had higher-gain elements that were several wavelengths in size, it was anticipated that the line losses required in the FZPA array feed network, assumed to be printed, would be less than those for an equivalent microstrip patch array (MPA). This is because the MPA requires many more elements than the FZPA array in the same area and thus would require more feed lines and power splits. This section will estimate the losses in the feed network of the FZPA as well as those for an equivalent MPA.

There are primarily two components to the loss in printed feed networks. The first is the loss associated with the total path length from the initial feed point to any element, and the second is the loss associated with the radiation from the junctions. Both types of loss are related to the operating frequency and feed substrate characteristics and both will be estimated in the subsequent analysis.

9.6.1 Estimated Loss in T-Junctions

To estimate the loss in the junctions, a basic T-junction power splitter was modeled at 30GHz. Two commercially available substrates were considered with parameters as outlined in Table 9-5. It should be noted that neither the permittivities or the loss tangents were specified at 30GHz. A T-junction was designed with each substrate for comparison purposes.

Material	Permittivity	Thickness	Loss Tangent	λ_g
Rogers 3010	10	0.03" (0.762mm)	0.0035	3.86mm
Taconic RF35	3.5	0.03" (0.762mm)	0.0018	6.03mm

Table 9-5: Substrate Material Data

For the substrate with $\epsilon_r=10$ two methods were used to design the T-junction and both were optimized in Empire [3-3]. The one shown in Figure 9-43 represented the best option which minimized the use of wide quarter-wave transformer lines.

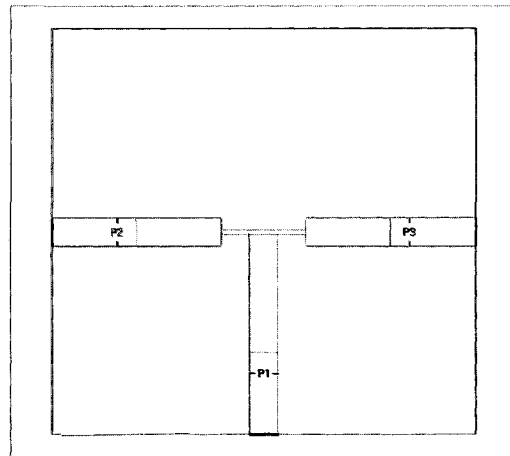


Figure 9-43: Geometry of the $\epsilon_r=10$ T-Junction

For the substrate with $\epsilon_r=3.5$, a similar design was implemented as shown in Figure 9-44. Again, the T-junction was optimized in Empire [3-3].

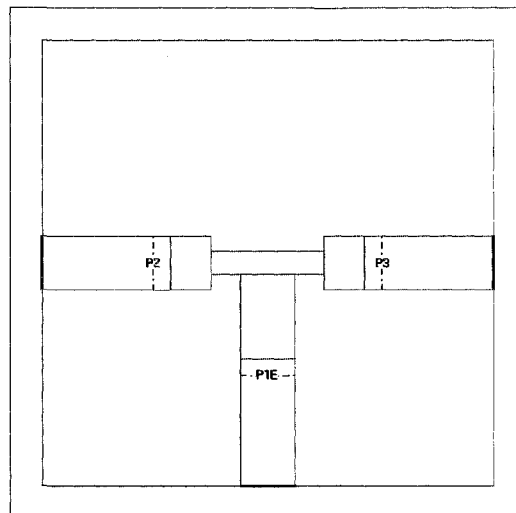


Figure 9-44: Geometry of the $\epsilon_r=3.5$ T-Junction

The return loss (S_{11}) and insertion loss (S_{21}) for both junctions are shown in Figure 9-45. At 30GHz the insertion loss was found to be about 2.2dB for each T-junction. This can be seen from the graph as being 2.2dB below the -3dB level, which is the expected drop in a lossless 2-way power splitter.

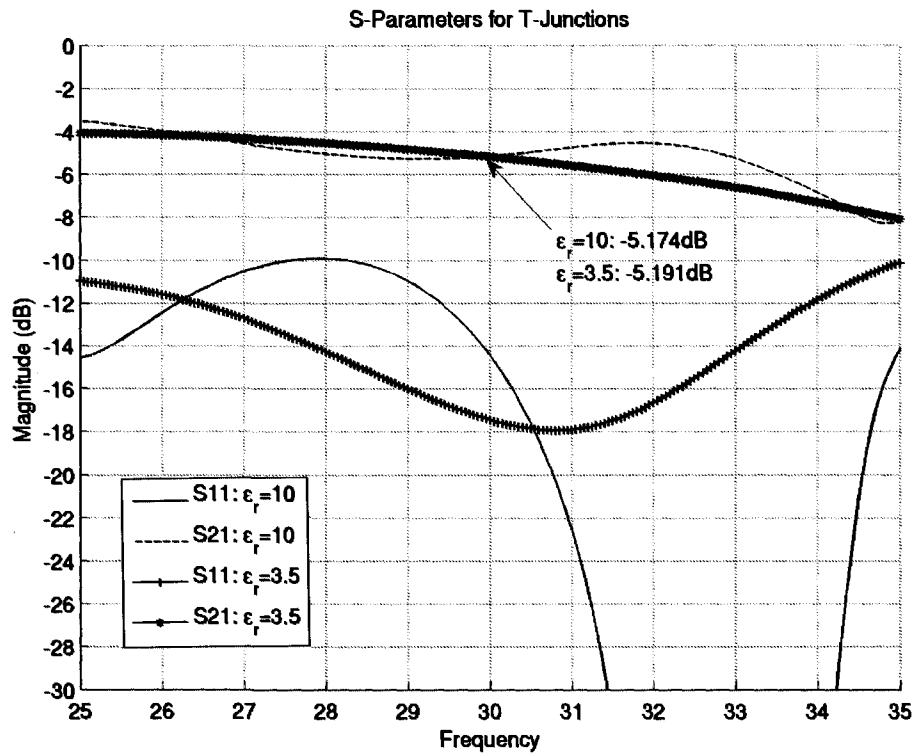


Figure 9-45: Return Loss and Insertion Loss for both T-Junctions

Though beyond the scope of this work, the insertion loss in both designs could be improved by using a Y-junction and by selecting a more optimal substrate with a better combination of dielectric constant and thickness properties. However, it is not clear whether or not there would be room in a microstrip patch feed network for a Y-junction since it takes up more space than the T-junction.

9.6.2 Estimated Path Loss

The path loss for the FZPA array ($F=1.25\lambda$, 2 metal zones, element spacing= 3λ) was estimated by measuring the line lengths from the initial feed point to any of the array elements. Two different array geometries were used, one with 4x4 elements and one with 8x8 elements. In the case of 4x4 elements, the path length was measured to be $9.75\lambda_0$, while the path length for the 8x8 array was found to be $22.25\lambda_0$.

The path loss for the MPA was estimated in the same way as above. The two MPA geometries that corresponded to about the same overall area as the considered FZPA arrays were 32x32 elements and 64x64 elements, each with element spacing of $\lambda_0/2$. In the case of the 32x32 element array, the path length was measured to be $15.5\lambda_0$, while the path length for the 64x64 element array was found to be $31.5\lambda_0$.

Again, similar to the junction loss, the path loss was related to the substrate characteristics. Several commercial substrates were again considered. It was found that for substrates with dielectric constants around three, the loss for a 1mm wide line was typically about 12dB/m. The substrates with dielectric constants around 10, had loss for a 0.25mm wide line of about 39dB/m. The computed losses are shown in the next section.

9.6.3 Total Estimated Loss

The total estimated loss for the FZPA array ($F=1.25\lambda$, 2 metal zones, element spacing= 3λ), and MPA is shown in Table 9-6 for each of the array configurations discussed in the previous section. The calculations were performed at 30GHz, based on the 12dB/m line loss substrates, and the T-junction loss was set at 2.2dB/junction from Section 9.6.1.

<i>Array</i>	<i>Substrate Line Loss (dB/m)</i>	<i>Number of T-Junctions</i>	<i>T-Junction Loss (Total) (dB)</i>	<i>Path Length (λ_0)</i>	<i>Path Loss (dB)</i>	<i>Total Loss (dB)</i>
FZPA 4x4	12	4	8.8	9.75	1.17	9.97
MPA 32x32	12	10	22	15.5	1.86	23.86
FZPA 8x8	12	6	13.2	22.25	2.67	15.87
MPA 64x64	12	12	26.4	31.5	3.78	30.18

Table 9-6: Total Estimated Loss for 12dB/m Line Loss Substrates ($\epsilon_r \approx 3$)

Table 9-7 shows the results for the 39dB/m line loss substrates at 30GHz. The T-junction loss was again 2.2dB/junction from Section 9.6.1.

<i>Array</i>	<i>Substrate Line Loss (dB/m)</i>	<i>Number of T-Junctions</i>	<i>T-Junction Loss (Total) (dB)</i>	<i>Path Length (λ_0)</i>	<i>Path Loss (dB)</i>	<i>Total Loss (dB)</i>
FZPA 4x4	39	4	8.8	9.75	3.80	12.6
MPA 32x32	39	10	22	15.5	6.04	28.04
FZPA 8x8	39	6	13.2	22.25	8.68	21.88
MPA 64x64	39	12	26.4	31.5	12.28	38.68

Table 9-7: Total Estimated Loss for 39dB/m Line Loss Substrates ($\epsilon_r \approx 10$)

As expected, the total loss of the FZPA array feed network was less than the MPA for all array configurations and substrate line losses considered. Also, the loss difference between the FZPA array and the MPA did not increase by much when changing to the larger array. This was because the path loss increased nearly proportionally for each case.

9.6.4 Gain vs. Loss/Junction

Even though the total loss in the feed network of the FZPA array was much less than that of the MPA, the MPA had a much higher radiation efficiency than the FZPA array and so the loss advantage may not make up for the FZPA's low aperture efficiency. This was determined by observing the array gain with all the losses included. Since the junction loss depended highly on the design of the junction, it was decided to plot the gain versus the junction loss to see at what junction loss the FZPA array gain would exceed that of the MPA.

Figure 9-46 shows the gain of the 4x4 FZPA and the 32x32 MPA, with the same parameters as defined previously, plotted against the junction loss while keeping the substrate line loss constant at 12dB/m. The 39dB/m line loss was omitted from further consideration since the losses were too high to be practical. The MPA was assumed to be 70% efficient, on average, based on the published results from Section 2.5.1 and the FZPA array was assumed to be 16% efficient based on the best efficiency achieved for the reflector-backed FZPA element in Chapter 7.

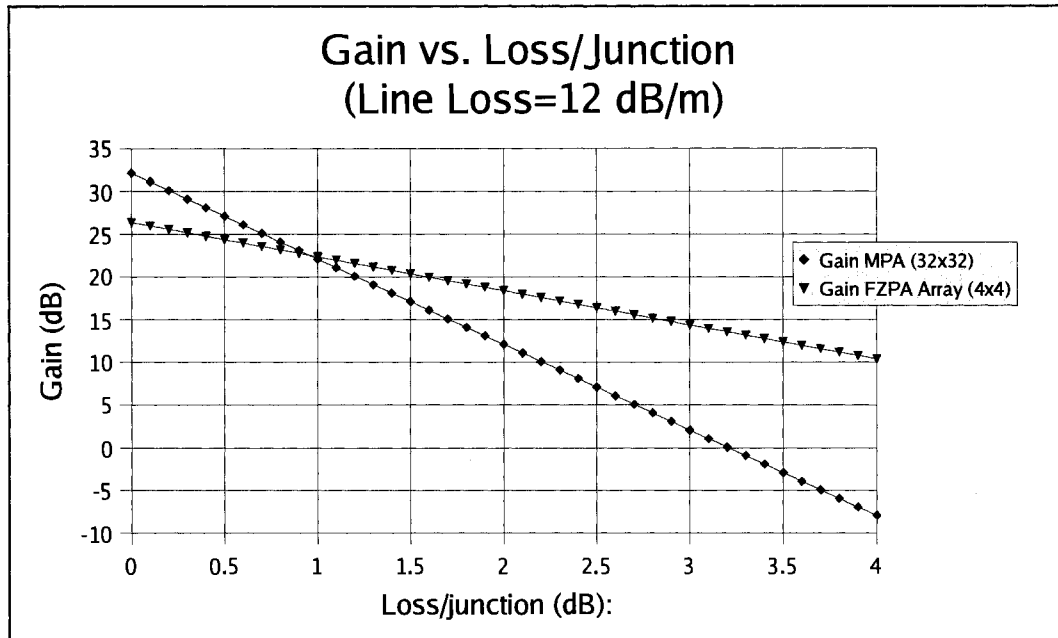


Figure 9-46: Gain vs. Junction Loss for 12dB/m Line Loss ($\epsilon_r \approx 3$)

With the 12dB/m line loss, the junction loss must be greater than about 1dB in order for the FZPA array gain to exceed that of the MPA. Given the results from Section 9.6.1 for loss in T-junction designs of 2.2dB, the FZPA array gain well exceeds the MPA gain at this value of T-junction loss. However, if a Y-junction was used, the junction loss required could be less than 1dB.

For comparison purposes, the parameters of the FZPA array were changed to reduce the number of junctions. Instead of using $F=1.25\lambda$, 2 metal zones, and 3λ element spacing, the parameters were changed to $F=3.75\lambda$, 5 metal zones, and 11λ elements spacing. With these new parameters, a 2×2 FZPA array would fit into the same area as the 32×32 element MPA and the 4×4 FZPA array would fit into the same area as the 64×64 element MPA. Table 9-8 summarizes these results for the 12dB/m line loss cases.

<i>Array</i>	<i>Number of T-Junctions</i>	<i>Path Length (λ_0)</i>	<i>Junction Loss where FZPA Array Gain= MPA Gain (dB)</i>
FZPA 2x2	2	13.75	1.1
MPA 32x32	10	15.5	
FZPA 4x4	4	35.75	1.25
MPA 64x64	12	31.5	

Table 9-8: Total Estimated Loss for 12dB/m Line Loss ($\epsilon_r \approx 3$)

These results illustrated how reducing the number of junctions in the FZPA array by changing the antenna focal parameters and size did not make much of a difference in terms of the amount of junction loss required for the FZPA array gain to exceed the MPA gain. This was because, the larger FZPA elements required a much larger element spacing in the array, which in turn increased the path length dramatically. In the 4x4 FZPA array case, the path length actually exceeded the path length of the equivalent MPA.

9.6.5 Discussion

This investigation has shown that, although the total loss in the FZPA array feed network is much less than the total loss in the MPA feed network, the MPA gain would still exceed that of the FZPA array if the loss per junction was less than about 1dB. This was primarily due to the efficiency differences between the two structures. A significant improvement in losses is required for the FZPA array to overcome the low aperture efficiency and become comparable to the MPA.

9.7 Conclusion

This chapter began by presenting a new approach to creating FZPA zones based entirely on the phase from the feed. This method was shown to be free from assumptions related to the the feed and the paraxial approximation and would produce accurate zone shapes regardless of the interference between multiple feeds. It was shown that these 'modified' zones yielded more accurate results than the conventional circular zone FZPAs.

Using the 'modified' zone technique to model 2-element and 2x2 element arrays yielded similar conclusions about the new approach. The 'modified' zone method provided better radiation characteristics than the equivalent circular zone version, particularly when the circular elements were overlapped through the center zone. However, a modeling approach for the circular overlapping zones, which used priorities, enabled the circular zone radiation patterns to more closely resemble those of the 'modified' zones. The priority approach effectively freed up the otherwise blocked center zone and resulted in a zone geometry which was very similar to the 'modified' zone geometry. Since this approach was much simpler to model, it was used for the larger array simulations.

The 4x4 FZPA array modeling in this chapter revealed that low-profile, small FZPA arrays achieved directivities between 22dB and 25dB depending on the exact focal distance. The element spacing was not optimal in all of these simulations though since the grating lobe levels were typically only about 5dB down from the peak. One case with $F=1.25\lambda$ and 3λ element spacing yielded a maximum relative sidelobe level just over 10dB down from the array peak.

In Section 9.5, arrays with different elements were explored as a means to potentially control the sidelobe levels. Two types of different elements were modeled. The first had elements with different reference phases. In this case, it was found that the proximity of the grating lobes to the main beam, due to the large element spacing, affected negatively the main beam instead of enabling control over the sidelobe levels. It was concluded that this technique would not yield the desired sidelobe control in the array. The second case involved different rotated zone configurations on the elements in the array. It was found that this technique would not affect the sidelobes due to the width of the element pattern main beam relative to the array factor sidelobes. The element patterns were too wide. Many simulations were performed to verify this conclusion.

Finally, in Section 9.6, a loss comparison between FZPA arrays and MPAs was presented. It was found that, although the FZPA array had less total loss at 30GHz, the gain of the MPA could still be higher depending on the junction loss. This was because of the significant difference in aperture efficiencies of the two structures. The FZPA element was analyzed with a 16% efficiency whereas the MPA was analyzed with an aperture efficiency of 70%. However, it was found that, if the junction loss was around 1dB or greater, the FZPA array gain would exceed the MPA gain for typical $\epsilon_r=3$ substrates.

CHAPTER 10

CONCLUSIONS & FUTURE RESEARCH

10.1 Summary of Conclusions

The overall objective of this thesis was to explore the possibility of making the FZPA a viable and attractive alternate antenna option for future satellite communication systems in the Ka-band. To address this objective, a list of specific questions was established in Chapter 1 which required investigation. The following list highlights the concluding response to each question based on the work of this thesis:

1. *Are there any properties of the FZPA that can add enhanced capability?* The reference phase property was found to improve sidelobe levels of the FZPA. It was shown in Chapter 4 that it was possible to improve the inner sidelobe levels by as much as 9.3dB in the H-plane without affecting the other radiation characteristics.
2. *What is the resolution of the low-profile FZPA?* The resolution of the FZPA was found to be less than 0.5λ with sub-wavelength focal distances. Chapter 5 showed

that this resolution was actually close to what can be achieved for a dielectric phase correcting Fresnel antenna at the same frequency.

3. *Is there a more desirable FZPA zone shape in terms of performance?* FZPA zones that were trimmed by a hexagon and then rotated with respect to each other were found to achieve control over the sidelobe levels and their locations in the radiation pattern. Chapter 6 showed that this control was achieved while still maintaining the radiation performance of the conventional FZPA.
4. *Can the efficiency of the FZPA be improved without increasing the profile?* A reflector-backed FZPA was conceived and investigated as a method to improve the aperture efficiency of the FZPA while also removing the need for an arm to support the feed. Chapter 7 showed that the aperture efficiency of the reflector-backed FZPA was improved to 16% which was 33% better than the FZPA without the reflector at the aperture of the feed.
5. *How low profile can the FZPA be made?* It was found in Chapter 8 that the FZPA focal distance, and hence the profile of the overall antenna, could be reduced to 0.75λ while still maintaining the ability to focus. At 30GHz, this represents a thickness 0.75cm. Since there would also be a printed feed network, which would be around 1mm thick, this yields an overall profile of about 1cm. This thickness is close to the planar printed array profiles described in Section 2.6.1 and is significantly lower profile than traditional lenses or reflectors.
6. *How does FZPA element overlap affect array performance?* Overlapping zones in a FZPA array were shown to be detrimental to the radiation characteristics when

the center zones of the elements were blocked. Chapter 9 outlined a new approach that avoids this problem.

7. *How do different elements perform in a FZPA array?* Having elements in a FZPA array with different reference phase was found to negatively affect the main beam. Also, having a FZPA array with different zone rotation configurations on each element was found to have no effect on the radiation patterns. Chapter 9 outlined this investigation.
8. *How does the loss of the FZPA array compare to an equivalent planar array?* The feed network loss for the FZPA array was found to be less than that of the planar printed array antenna at 30GHz. Chapter 9 showed that this was due to the fact that the FZPA array required less feed antennas than the equivalent planar technology. A junction loss of more than 1dB was required before the FZPA array gain would exceed that of the planar printed array.
9. *What is the relative cost of the FZPA compared to an equivalent planar array?* The cost of the FZPA fed via a printed array would be less than the planar printed array antenna if the planar array was of the aperture-coupled type. It was presumed that the cost of the feed substrate would be the same for each. The difference would be in the cost of the foam and FR4 substrate for the FZPA element substrate versus the expensive microwave grade substrate required for the printed array elements.

10. *What is the relative weight of the FZPA compared to an equivalent planar array?*

It was estimated that the weight of the FZPA array and the planar printed array antenna would be comparable. This is because both contain a feed network made from similar materials and it is debatable whether the weight of the element substrate for the planar printed array would weigh more than the combination of the FZPA FR4 substrate and foam.

11. *What is the aesthetic and relative fabrication complexity of the FZPA?* The

fabrication complexity and the aesthetic of each antenna would likely be the same since they would both require similar circuit board etching and bonding, and could both be packaged in similar radomes.

10.2 Thesis Contributions

The primary contributions of this thesis research are summarized below:

1. A systematic study of varying reference phase in the design of circular FZPAs [4-3]. The first sidelobe level can be reduced substantially without impact on the directivity, beamwidth, or cross-polarization of the antenna.
2. An investigation into the spatial resolution of the FZPA with sub-wavelength focal distances [5-1]. Resolutions comparable with the dielectric phase correcting Fresnel lens were achieved.
3. The conception of a FZPA with alternating hex-cut zones [6-2]. The zones can be

rotated with respect to each other to yield some degree of sidelobe control without significant impact to the directivity.

4. The design of a new reflector-backed FZPA [7-1]. It has an improved directivity and aperture efficiency compared to the conventional circular FZPA and it also enables a method to achieve a low-profile antenna package.
5. An investigation into reducing the focal distance of the FZPA [8-2]. The focal distance can be reduced down to 0.75λ before losing the ability to focus.
6. The creation of a technique to accurately determine the FZPA zones. It takes into account the interference between multiple feed antennas and is free from assumptions related to the feed and the paraxial approximation.

10.3 Future Research

Although this thesis covered many topics pertaining to improving the FZPA, further research is required. Some immediate future research areas are:

1. Innovative methods to improve FZPA aperture efficiency are required. This is the primary area in which the FZPA does not compare as well to existing planar printed technology. Several of the methods that were highlighted in Chapter 2 could be explored in terms of the FZPA array for efficiency improvement. Fundamentally, a method is required that provides phase correction without an increase in thickness, complexity, or cost of the antenna.

2. Throughout this thesis a waveguide was used to feed the FZPA. However, a waveguide is not ideal for a practical low-profile FZPA package. A microstrip patch array feed would be a better low profile option. The reflector-backed FZPA used a ground plane at the aperture of the waveguide in order to mimic the effect of the ground plane present in the microstrip patch array feed. An important next step in achieving a marketable FZPA array would therefore be to model and test the array with the microstrip patch array feed instead of the waveguide feed.
3. An investigation into using materials other than air between the feed and the FZPA aperture. This could yield lower profile structures wherein the feed and aperture are integrated on the same substrate as in [2-24].
4. Finally, since it has been established that FZPAs can achieve spatial resolutions of less than 0.5λ , they are attractive for spatial power combining applications at Ka-band. The FZPA is already an interesting candidate for these applications because it is physically large, requires less elements and power, has better thermal properties, and is less complex than an equivalent planar microstrip patch technology.

REFERENCES

Chapter 2:

- [2-1] Petosa, A., Ittipiboon, A., "Fresnel Lens Antenna for Microwave Communication Applications", *CRC Report No. 2004-003*, Ottawa, Nov. 2004.
- [2-2] Wiltse, J.C., "History and Evolution of Fresnel Zone Plate Antennas for Microwaves and Millimeter Waves", *IEEE Antennas and Propagation Int, Symp. 1999*, Special Section "Status and Future of Fresnel Zone Plate Antennas", Orlando FL, July 11-16, 1999, Symp. Digest Vol.2, pp.722-725.
- [2-3] Sobel, F., Wentworth, F.L., Wiltse, J.C., "Quasi-Optical Surface Waveguide and Other Components for the 100- to 300-Gc Region", *IRE Transactions on Microwave Theory and Techniques*, pp.512-518, November 1961.
- [2-4] Reid, D., Smith, G.S., "A Full Electromagnetic Analysis of Grooved-Dielectric Fresnel Zone Plate Antennas for Microwave and Millimeter-Wave Applications", *IEEE Transactions on Antennas and Propagation*, Vol. 55, No. 8, pp. 2138-2146, August 2007.

- [2-5] Balanis, Constantine, A. *Advanced Engineering Electromagnetics*. John Wiley & Sons, New York, c1989.
- [2-6] Hristov, Hristo, D. *Fresnel Zones in Wireless Links, Zone Plate Lenses and Antennas*. Artech House Inc., Boston, MA, c2000.
- [2-7] Fresnel, A, "Calcul de l'Intensite de la Lumiere au Centre de l'Ombre d'un Ecran et d'une Ouverture Circulaires Eclairée par un Point Radieux", *Oeuvres d'Augustin Fresnel*, Vol.1, Note 1, pp.365-372 (1866). Reprinted in J. Ojeda-Castanada and C. Gomez-Reino, *Selected Papers on Zone Plates*, SPIE Milestone Series Vol. MS 128 (1996).
- [2-8] Guenther, Robert. *Modern Optics*. John Wiley & Sons Inc., New York, c1990.
- [2-9] Boivin, A., Dion, A, Koenig, H.P., "Etude Experimentale de la Diffraction des Micro-Ondes Par Des Ouvertures a Symetrie de Revolution," *Canadian Journal of Physics*, Vol. 34, pp. 166-178, 1956.
- [2-10] Buskirk, L.F., Hendrix, C.E., "The Zone Plate as a Radio Frequency Element", *IRE Transactions on Antennas and Propagation*, Vol. 9, pp. 319-320, May1961.
- [2-11] Sanyal, G.S., Singh, M., "Fresnel Zone Plate Antenna", *Journal of the Institution of Telecommunications Engineers*, Vol. 14, pp.265-281, 1968.
- [2-12] Guo, Y., J., Barton, S., K., "On the Sidelobe Performance of Fresnel Zone Plate

Antennas”, *IEEE Antennas and Propagation Symposium*, 1992, pp.2175-2178.

- [2-13] Baggen, L.C.J., Herben, M.H.A.J., “Design Procedure for Fresnel-Zone Plate Antenna”, *International Journal of Infrared and Millimeter Waves*, Vol. 14, No. 6, pp. 1341-1351, 1993.
- [2-14] Baggen, L. C. J., Jeronimus, C. J. J., Herben, M. H. A. J., “The Scan Performance of the Fresnel-Zone Plate Antenna: A Comparison with the Parabolic Reflector Antenna”, *Microwave and Optical Tech. Letters*, Vol. 6, No. 13, pp. 769-774, Oct. 1993.
- [2-15] Guo, Y.J., Barton, S.K., *Fresnel Zone Antennas*, Kluwer Academic Publishers, Boston, 2002.
- [2-16] Zhang, Wen-Xun, “An Improved Zoning Rule of the Fresnel Zone Plate”, *Microwave and Opt. Tech Lett.*, Vol. 23, No. 2, October 20 1999.
- [2-17] Guo, Y.J., Barton, S.K., Wright, T.M.B., “Focal Field Distribution of Fresnel Zone Plate Antennas”, *Proceedings of the International Conference on Antennas and Propagation – ICAP 1991*, York UK, April 1991, pp.6-8, 1991.
- [2-18] Minin, O.V., and Minin, I.V., *Diffractional Optics of Millimeter Waves*, Institute of Physics Publishing, Bristol, U.K., 2004.
- [2-19] Born, M., Wolf, E., *Principles of Optics 7th Edition*, Cambridge University Press,

Cambridge, U.K., 1999.

- [2-20] Goldsmith, P.F., *Quasioptical Systems*, IEEE Press, Piscataway, N.J., 1998.
- [2-21] Kearey, P.D., Klein, A.G., "Resolving Power of Zone Plate," *Journal of Modern Optics*, Vol. 36, No.3, pp. 361-367, 1989.
- [2-22] Minin, I.V., and Minin, O.V., Gagnon, N., Petosa, A., "Investigation of the Resolution of Phase Correcting Fresnel Lenses with Small Focal Length-to-Diameter Ratios and Subwavelength Focus", *Electromagnetic Theory Symposium (EMTS)*, Ottawa, On, Canada, July 26-28, 2007, CDROM.
- [2-23] Huder, B., Menzel, W., "Flat Printed Reflector Antenna for mm-Wave Applications", *Electronics Letters*, Vol. 24, No. 6, pp. 318-319.
- [2-24] Gouker, M. A., Smith, G. S., "A Millimeter-Wave Integrated-Circuit Antenna Based on the Fresnel Zone Plate", *IEEE Trans. Microwave Theory and Techniques*, Vol. 40, No.5, pp. 968-977, May 1992.
- [2-25] Fujita, M., Yu, J., "Design and Analysis of a Folded Fresnel Zone Plate Antenna", *Int. Journal of Infrared and Millimeter Waves*, Vol. 15, No.8, pp. 1385-1406, 1994.
- [2-26] Jiang, G. Z., Zhang, W.X., "The Effect of Layer Spacing on the Properties of Double-Layer Fresnel Zone Plate Lens", *IEEE Antennas and Propagation*

Symposium, 1997, pp.472-475.

- [2-27] Jiang, G. Z., Zhang, W.X., Liu, T.H., "New Types of Fresnel Zone Plate Lens with Lower Backward Radiation", *IEEE Antennas and Propagation Symposium*, 1998, pp.166-169.
- [2-28] Guo, Y.J., Barton, S.K., "Offset Fresnel Zone Plate Antennas", *International Journal of Satellite Communications*, Vol. 12, pp.381-385, 1994.
- [2-29] Guo, Y.J., Sassi, I.H., Barton, S.K., "Offset Fresnel Zone Plate Antenna", *IEE Proceedings on Microwaves, Antennas and Propagation*, Vol., 141, No. 6, pp. 517-522, December 1994.
- [2-30] Guo, Y.J., Sassi, I.H., Barton, S.K., "Multilayer Offset Fresnel Zone Plate Reflector", *IEEE Microwaves and Guided Wave Letters*, Vol. 4, No. 6, pp.196-198, June 1994.
- [2-31] Hoashi, T., Onodera, T., Kimura, E., "Offset Characteristics of Elliptic Fresnel-Zone-Plate Lens", *ANTEM 1998*, Ottawa Canada, pp.563-566, August 1998.
- [2-32] Onodera, T., Hoashi, T., "A Design Method of Offset Fresnel Zone Plate Reflector", *IEEE Antennas and Propagation Symposium*, 1999, pp.750-753.
- [2-33] Janicijevic, L. J., "Diffraction Characteristics of Square Zone Plates", *Journal of Optics (Paris)*, Vol. 13, No. 4, pp.199-206, 1982.

- [2-34] Gonzalez, F.J., Alda, J., Ilic, B., Boreman, G.D., "Infrared Antennas Coupled to Lithographic Fresnel Zone Plate Lenses", *Applied Optics*, Vol. 43, No. 33, pp.6067-6073, November 20, 2004.
- [2-35] Minin, I.V., Minin, O.V., Danilov, E.G., Lbov, G.S., "Parameters Optimization Algorithm of a New Type of Diffraction Optics Elements", *Proceedings of the 5th IEEE-Russia Conference MEMIA*, Novosibirsk, Russia, pp.177-185, Dec. 13-15, 2005.
- [2-36] Minin, I.V., Minin, O.V., Petosa, A., Thirakoune, S., "Improved Zoning Rule for Designing Square Fresnel Zone Plate Lenses", *Microwave and Optical Technology Letters*, Vol. 49, No.2, pp. 276-278, February 2007.
- [2-37] Alda, J., Boreman, G., "Optimization of Polygonal Fresnel Zone Plates", *Microwave and Optical Technology Letters*, Vol. 50, No.2, pp. 536-541, February 2008.
- [2-38] Jahns, J., Walker, S.J., "Two-Dimensional Array of Diffractive Microlenses Fabricated by Thin Film Deposition", *Applied Optics*, Vol. 29, No. 7, pp. 931-936, March 1, 1990.
- [2-39] Carcole, E., Campos, J., Bosch, S., "Diffraction Theory of Fresnel Lenses Encoded in Low-Resolution Devices", *Applied Optics*, Vol. 33, No. 2, pp. 162-174, January 10, 1994.

- [2-40] Bett, T.H., Dnason, C.N., Jinks, P., Pepler, D.A., Ross, I.N., Stevenson, R.M., “Binary Phase Zone-Plate Arrays for Laser-Beam Spatial-Intensity Distribution Conversion”, *Applied Optics*, Vol. 34, No. 20, pp. 4025-4036, July 10, 1995.
- [2-41] Petosa, A., Ittipoon, A., Thirakoune, S., “Array of Perforated Dielectric Fresnel Lenses”, *URSI International Symposium on EM Theory, EMTS 2004*, Pisa, Italy, May 23-27, 2004, pp. 969-971.
- [2-42] Petosa, A., Thirakoune, S., Minin, I.V., Minin, O.V., “Array of Hexagonal Fresnel Zone Plate Lens Antennas”, *Electronics Letters*, Vol. 42, No. 15, pp. 834-836, July 20 2006.
- [2-43] Williams, J.C., “A 36GHz Printed Planar Array”, *Electronics Letters*, Vol. 14, No. 5, pp. 136-137, March 2, 1978.
- [2-44] Weiss, M.A., “Microstrip Antennas for Millimeter Waves”, *IEEE Transactions on Antennas and Propagation*, Vol. 29, No.1, pp. 171-174, January 1981.
- [2-45] Feresidis, A.P., Vardaxoglou, J.C., “High Gain Planar Antenna Using Optimized Reflective Surfaces”, *IEE Proc. Microwave and Antennas Propagation*, Vol. 148, No.6, December 2001.

Chapter 3:

- [3-1] Goodman, J.W., *Introduction to Fourier Optics 2nd Edition*, McGraw-Hill,

Boston, 1996.

- [3-2] Yee, K. S., "Numerical Solution of Initial Boundary Value Problems Involving Maxwell's Equations in Isotropic Media," *IEEE Transactions on Antennas and Propagation*, Vol. 14, No. 3, pp. 302-307, May 1966.
- [3-3] EmpireTM: 3D EM Field Simulator by IMST GmbH, Germany. Website: www.empire.de.
- [3-4] Kim, T.Y., Kagawa, Y., Chai, L. Y., "Modeling of a Circular Fresnel Zone Plate Lens for Electromagnetic Wave Antenna Application", *International Journal of Numerical Modeling: Electronic Networks, Devices and Fields*, Vol. 18, pp. 429-439, 2005.
- [3-5] Reid, D. R., Smith, G.S., "A Full Electromagnetic Analysis for the Soret and Folded Zone Plate Antennas", *IEEE Transactions on Antennas and Propagation*, Vol. 54, No. 12, pp. 3638-3646, December 2006.

Chapter 4:

- [4-1] Minin, I.V., Minin, O.V., Webb, G., "Flat and Conformal Zone Plate Antenna with New Capabilities", *Proceedings International Conference on Applied Electromagnetics and Communications – ICECOM 2005*, Dubrovnik, Croatia, Oct. 11-14, pp.405-408.

- [4-2] Minin, I.V., Minin, O.V., “Control of Focusing Properties of Diffractive Elements”, *Sov. J. Quantum Electron.* Vol. 20, No. 3, pp.198-199, 1990.
- [4-3] Stout-Grandy, S., Petosa, A., Minin, I.V., Minin, O.V., Wight., J.S., “A Systematic Study of Varying Reference Phase in the Design of Circular Fresnel Zone Plate Antennas”, *IEEE Transactions on Antennas and Propagation*, Vol. 54, No.12, Dec 2006, pp 3629-3637.

Chapter 5:

- [5-1] Stout-Grandy, S., Petosa, A., Minin, I.V., Minin, O.V., Wight., J.S., “Recent Advances in Fresnel Zone Plate Antenna Technology”, *Microwave Journal* on-line publication ([http://www.mwjournal.com/](http://www.mwjjournal.com/)), March 2008.
- [5-2] Merlin, R., “Radiationless Electromagnetic Interference: Evanescent-Field Lenses and Perfect Focusing”, *Science*, Vol. 317, August 17, 2007.
- [5-3] Johnson, R.C. (Ed.). *Antenna Engineering Handbook*, 3rd Edition. McGraw-Hill, 1993.

Chapter 6:

- [6-1] Stout-Grandy, S., Petosa, A., Minin, I.V., Minin, O.V., Wight., J.S., “Hexagonal Fresnel Zone Plate Antenna”, *ANTEM 2006*, Montreal, Canada, pp. 511 – 514, July 2006.

- [6-2] Stout-Grandy, S., Petosa, A., Minin, I.V., Minin, O.V., Wight., J.S., “Fresnel Zone Plate Antenna with Hexagonal-Cut Zones”, *Microwave and Optical Technology Letters*, Vol. 50, No.3, pp. 672-676, March 2008.

Chapter 7:

- [7-1] Stout-Grandy, S., Petosa, A., Minin, I.V., Minin, O.V., Wight, J.S., “A Novel Reflector-Backed Fresnel Zone Plate Antenna”, *Microwave and Optical Technology Letters*, Vol. 49, No.12, pp. 3096-3098, Dec.2007.

Chapter 8:

- [8-1] Stout-Grandy, S., Petosa, A., Minin, I.V., Minin, O.V., Wight., J.S., “Investigation of Low Profile Fresnel Zone Plate Antenna”, *URSI North American Radio Science Meeting*, Ottawa Ontario, July 23, 2007, CDROM.
- [8-2] Stout-Grandy, S., Petosa, A., Minin, I.V., Minin, O.V., Wight., J.S., “Low Profile Fresnel Zone Plate Antennas”, *Microwave and Optical Technology Letters*, Vol. 50, No. 8, August 2008.

Chapter 9:

- [9-1] Minin, I.V., Minin, O.V., Pedreira, A., Vassal'lo, J., “Some Fundamental Principles of the FZP-Like Antenna Developments”, *Proceedings of the 6th Int. Conf. on Actual Problems on Electronics Instrument Engineering, APIEE-2002*, vol. 1, pp. 176-177, Novosibirsk, Sept. 23-26, 2002.